NOVEL DEVICE ARCHITECTURES FOR PEROVSKITE SOLAR CELLS



Maximilian Tobias Hörantner

Linacre College

Department of Physics

University of Oxford

This dissertation is submitted for the degree of Doctor of Philosophy

March 2017

This thesis is dedicated to my parents, who allowed me to dream without limits and who supported me to follow these dreams.

Der Weg ist das Ziel.

~ Unknown Author

ABSTRACT

The aim of the work presented in this thesis is to study the opto-electronic properties of semi-conducting perovskite materials when being used in unconventional solar cell device configurations. Being a young technology, perovskites as solar cell materials have seen an unparalleled rise in the research community which has driven the fastest performance inflation to power conversion efficiencies competing with the ones of long established single crystalline technologies. The ability to process perovskites inexpensively makes them the new hope in the fight against climate change. Herein device architectures were developed with a special focus on potential commercial applications.

Initially the work in this thesis has been motivated by the interest in crystal growth and morphology of perovskite thin-films, which has led to the study of confined crystal growth within microstructures. Controlling the crystal domain geometry enabled the fabrication of enhanced semi-transparent devices. More efforts were directed into the improvement of specifically neutral colour semi-transparent devices, which could be improved via a simple treatment of selectively attaching shunt-blocking layers. Furthermore, a back-contacted perovskite device design was introduced, which allows not only for the fabrication of a new type of perovskite solar cell, but also represent a great material testing platform to study perovskite and electrode characteristics. This led to the discovery of charge transport distances, that exceed those of other thin-film devices.

Finally, perovskite-on-silicon tandem solar cell designs were analysed through a rigorous optical model to estimate the expected real world energy yield from such systems. Important implications include the fact that two terminal tandem solar cells come close to four-terminal configurations and can overall compete, in relative terms, well with established single junction silicon cells.

ACKNOWLEDGEMENTS

I want to deeply thank my supervisor, Professor Henry Snaith, for the opportunity to carry out research in his group during a time which couldn't have been any more exciting in the field of perovskite solar cells. He supported me with every project idea and gave me all the freedom I wanted to explore this field in various areas. Moreover, Henry's enthusiasm is contagious and his optimisms can sometimes make the impossible feel possible again. I have learned a lot from his character and he will always be a great inspiration who made me find my biggest strengths.

Aside from Henry, the entire group of Snaithlings has made every single day at the office or lab so much fun that I couldn't imagine a better team to work with. In no particular order I would like to give my special thanks to Konrad Wojciechowski for challenging every single statement and being a great friend, Tomas Leijtens for the same and for teaching me a lot about the spectroscopy magic, James Ball and Sam Stranks for great scientific and life discussions, Wei Zhang for training me to become a lab ninja, Giles Eperon for his inputs and recipes, Pabitra Nayak for teaching me device physics and Nakita Noel as well as Martina Congiu for helping me out whenever most needed and for keeping the lab efficient and tidy. More thanks go to all the other present and past colleagues and friends: Severin, Jacob, Olivia Hakes, Alexandra, Michael, Sandeep, Bernard, Grey, Ivan, Giulio, Song and Clara. More thanks go to my Cambridge collaborators in Professor Richard Friend's group, Luis Pazos-Outon, Felix Deschler, Johannes Richter and Gregory Tainter.

My Oxford social life wouldn't have been the same without these very special people: The Icelanders (Einar and Asgeir), Mike and Swissl, Derek Hollman, David McMeekin, Federico Pulvirenti, Jongjul Lim and Alba Pellaroque.

Without the continuous support of my family I would have never made here. And finally, I thank Stefi for her love, and great company during the last couple of years.

PUBLICATIONS

1. Hörantner, M. T.; Zhang, W.; Saliba, M.; Wojciechowski, K.; Snaith, H. J. Templated Microstructural Growth of Perovskite Thin Films via Colloidal Monolayer Lithography. *Energy Environ. Sci.* **2015**, 8, 2041–2047.

2. Wojciechowski, K.; Leijtens, T.; Siprova, S.; Schlueter, C.; Hörantner, M. T.; Wang, J. T.-W.; Li, C.-Z.; Jen, A. K.-Y.; Lee, T.-L.; Snaith, H. J. C 60 as an Efficient N-Type Compact Layer in Perovskite Solar Cells. *J. Phys. Chem. Lett.* **2015**, 6, 2399–2405.

3. Ball, J. M.; Stranks, S. D.; Hörantner, M. T.; Hüttner, S.; Zhang, W.; Crossland, E. J. W.; Ramirez, I.; Riede, M.; Johnston, M. B.; Friend, R. H.; et al. Optical Properties and Limiting Photocurrent of Thin-Film Perovskite Solar Cells. *Energy Environ. Sci.* **2015**, 8, 602–609.

4. Zhang, W.; Saliba, M.; Moore, D. T.; Pathak, S. K.; Hörantner, M. T.; Stergiopoulos, T.; Stranks, S. D.; Eperon, G. E.; Alexander-Webber, J. A.; Abate, A.; et al. Ultrasmooth Organic–inorganic Perovskite Thin-Film Formation and Crystallization for Efficient Planar Heterojunction Solar Cells. *Nat. Commun.* **2015**, 6, 6142.

5. Saliba, M.; Wood, S. M.; Patel, J. B.; Nayak, P. K.; Huang, J.; Alexander-Webber, J. A.; Wenger, B.; Stranks, S. D.; Hörantner, M. T.; Wang, J. T. W.; *et al.* Structured Organic-Inorganic Perovskite toward a Distributed Feedback Laser. *Adv. Mater.* **2016**, *28*, 923–929.

6. Choi, J.; Song, S.; Hörantner, M. T.; Snaith, H. J.; Park, T. Well-Defined Nanostructured, Single-Crystalline TiO2 Electron Transport Layer for Efficient Planar Perovskite Solar Cells. *ACS Nano* **2016**, 10, 6029–6036.

7. Hörantner, M. T.; Nayak, P. K.; Mukhopadhyay, S.; Wojciechowski, K.; Beck, C.; McMeekin, D.; Kamino, B.; Eperon, G. E.; Snaith, H. J. Shunt-Blocking Layers for Semitransparent Perovskite Solar Cells. *Adv. Mater. Interfaces* **2016**, 3, 1500837.

8. Song, S.; Moon, B. J.; Hörantner, M. T.; Lim, J.; Kang, G.; Park, M.; Kim, J. Y.; Snaith, H. J.; Park, T. Interfacial Electron Accumulation for Efficient Homo-Junction Perovskite Solar Cells. *Nano Energy* **2016**, 28, 269–276.

9. Sutton, R. J.; Eperon, G. E.; Miranda, L.; Parrott, E. S.; Kamino, B. A.; Patel, J. B.; Hörantner, M. T.; Johnston, M. B.; Haghighirad, A. A.; Moore, D. T.; et al. Bandgap-Tunable Cesium Lead Halide Perovskites with High Thermal Stability for Efficient Solar Cells. *Adv. Energy Mater.* **2016**, 6, 1502458.

10. McMeekin, D. P.; Sadoughi, G.; Rehman, W.; Eperon, G. E.; Saliba, M.; Horantner, M. T.; Haghighirad, A.; Sakai, N.; Korte, L.; Rech, B.; *et al.* A Mixed-Cation Lead Mixed-Halide Perovskite Absorber for Tandem Solar Cells. *Science* **2016**, *351*, 151–155.

11. Song, S.; Hörantner, M. T.; Choi, K.; Snaith, H. J.; Park, T.; Kojima, A.; Teshima, K.; Shirai, Y.; Miyasaka, T.; Kim, H. S.; *et al.* Inducing Swift Nucleation Morphology Control for Efficient Planar Perovskite Solar Cells by Hot-Air Quenching. *J. Mater. Chem. A* **2017**, *131*, 6050.

12. Zhang, L.; Hörantner, M. T.; Zhang, W.; Yan, Q.; Snaith, H. J. Near-Neutral-Colored Semitransparent Perovskite Films Using a Combination of Colloidal Self-Assembly and Plasma Etching. *Sol. Energy Mater. Sol. Cells* **2017**, 160, 193–202.

13. Noel, N. K.; Habisreutinger, S. N.; Wenger, B.; Klug, M. T.; Hörantner, M. T.; Johnston, M. B.; Nicholas, R. J.; Moore, D. T.; Snaith, H. J. A Low Viscosity, Low Boiling Point, Clean Solvent System for the Rapid Crystallisation of Highly Specular Perovskite Films. *Energy Environ. Sci.* **2017**.

14. Cannavale, A.; Hörantner, M. T.; Eperon, G. E.; Snaith, H. J.; Fiorito, F.; Ayr, U.; Martellotta, F. Building Integration of Semitransparent Perovskite-based Solar Cells: Energy Performance and Visual Comfort Assessment. *Applied Energy (accepted)*

15. Hörantner, M. T.; Snaith, H. J. Predicting and Optimising the Energy Yield of Silicon-Perovskite Tandem Solar Cells under Real World Conditions. *(in preparation)*

16. Hörantner, M. T.; Pazos-Outon, L.; Tainter, G.; Richter, J.; Manenti, R.; Deschler, F.; Leijtens, T.; Friend, R. H.; Snaith, H. J. Extraordinary Charge Carrier Behaviour in Back-contacted Perovskite Thin-Films. *(in preparation)*

CONTENTS

1 INTRODUCTION 1

1.1 MOTIVATION – THE CLIMATE CHANGE DILEMMA 1

1.2 STRUCTURE AND AIM OF THE THESIS 4

2 BACKGROUND 8

2.1 SEMICONDUCTORS 8

2.1.1 ENERGY BANDS AND FERMI LEVEL 8

2.1.2 ABSORPTION AND RECOMBINATION 13

2.1.3 P-N AND P-I-N JUNCTIONS 17

2.1.4 SOLAR CELL PERFORMANCE CHARACTERISTICS 18

2.2 MODELLING OF SOLAR CELLS 20

2.2.1 EQUIVALENT CIRCUIT MODEL 20

2.2.2 DETAILED BALANCE 23

2.2.3 TRANSFER MATRIX MODEL 25

2.2.4 SOLAR RADIATION 29

2.3 PEROVSKITE SOLAR CELLS 36

2.4 SEMI-TRANSPARENT SOLAR CELLS 40

2.5 TANDEM SOLAR CELLS 42

2.6 BACK CONTACT SOLAR CELLS 45

2.7 MICRO- AND NANOLITHOGRAPHY TECHNIQUES 47

2.7.1 UV-PHOTOLITHOGRAPHY 48

2.7.2 COLLOIDAL LITHOGRAPHY 50

2.7.3 SELF-ASSEMBLED MONOLAYERS 51

3 METHODS 53

3.1 PEROVSKITE SOLAR CELL FABRICATION 53

3.1.1 SUBSTRATE PREPARATION 54

3.1.2 Bottom n-type or p-type layer deposition 54
3.1.3 Honeycomb oxide structuring 56
3.1.4 Back-contacting electrode fabrication 56
3.1.5 Perovskite absorber layer deposition 58
3.1.6 Shunt-blocking layer for semi-transparent perovskite device 59
3.1.7 Perovskite surface passivation of back-contacted solar cells 59
3.1.8 Hole-transporting layer deposition 60
3.1.9 Anode fabrication 60
3.2 Solar cell characterization 61
3.3 Optical characterisation 61
3.3.1 UV-Vis Transmission and reflection measurements 61
3.3.2 Photoluminescence measurements 61
3.3.3 Photocurrent and photoluminescence spatial mapping measurements 62
3.3.4 Photoluminescence quantum yield measurements 62
3.4 Microscopy 63
3.4.1 Optical microscope imaging 63
3.4.2 Scanning electron microscopy imaging 63
3.4.3 Atomic force microscopy 63
3.5 Further material characterization 64
3.5.1 Film thickness measurements 64
3.5.2 X-ray diffraction 64
3.6 Energy yield simulations and optimisation 64

4 TEMPLATED MICROSTRUCTURAL GROWTH OF PEROVSKITE THIN FILMS VIA COLLOIDAL LITHOGRAPHY 70

4.1 Context and summary 70
4.2 Introduction 71
4.3 Results and discussion 73
4.3.1 Microsphere monolayer formation and oxide honeycomb fabrication 73

4.3.2 Perovskite structuring 75
4.3.3 Semi-transparent solar cell development 79
4.4 Conclusion and outlook 85

5 SHUNT-BLOCKING LAYERS FOR SEMI-TRANSPARENT PEROVSKITE SOLAR CELLS 86

5.1 Context and summary 86
5.2 Introduction 87
5.3 Results and Discussion 90
5.3.1 Self-assembly of shunt-blocking layer 90
5.3.2 Solar cell fabrication 95
5.3.3 Larger active-area solar cells 101
5.3.4 Fully transparent device fabrication 102
5.4 Conclusion and outlook 104

6 EXTRAORDINARY CHARGE CARRIER BEHAVIOUR IN BACK-CONTACTED PEROVSKITE THIN-FILMS 106

6.1 Context and summary 106
6.2 Introduction 107
6.3 Results and Discussion 110
6.3.1 Optical model for absorption improvement estimation 110
6.3.2 Architecture and fabrication 111
6.3.3 Regular device improvements 114
6.3.4 Charge transport phenomena 118
6.3.5 Inverted devices 125
6.3.6 Surface passivation 126
6.4 Conclusion and outlook 127

7 PREDICTING AND OPTIMISING THE ENERGY YIELD OF PEROVSKITE-ON-SILICON TANDEM SOLAR CELLS UNDER REAL WORLD CONDITIONS 129

7.1 CONTEXT AND SUMMARY 129

7.2 INTRODUCTION 130

7.3 RESULTS AND DISCUSSION 135

7.3.1 INDIVIDUAL CELL PERFORMANCE MODELLING 135

7.3.2 OPTIMISATION FOR PCE IN LAB CONDITIONS 138

7.3.3 ENERGY YIELD SIMULATIONS 141

7.3.4 EFFICIENCY DERATING FACTOR 149

7.4 CONCLUSION AND OUTLOOK 151

8 CONCLUSIONS AND OUTLOOK 153

9 REFERENCES 157

LIST OF TABLES

Table 4.1: Solar cell performance parameters of best performing devices without (dewet perovskite films) and with SiO_2 honeycomb scaffolds fabricated from different perovskite precursor concentrations. Values in brackets represent mean values for tested set of devices with standard deviation. Conc. is perovskite precursor solution concentration; AVT is average visible transmission between 380 to 780 nm; AL AVT is the Active Layer AVT, which excludes absorption losses in the FTO/c-TiO_2 anode. 83

Table 5.1: Average and maximum performance parameters of OTS treated (n = 39) and untreated (n = 28) semi-transparent perovskite devices. 97

Table 7.1: Tabulated geographic and meteorological data for locations Golden, Seattle and Mohave desert. Data was derived from NREL NSRDB[136] for the year 2015. 142

LIST OF FIGURES

Figure 1.1: Development of annual energy consumption of different energy sources[7].....2

Figure 2.1: Illustration of valence and conduction band, separated by bandgap 9

Figure 2.2: Density of states function, Fermi function at T = 0 and T > 0 and number density of electrons for typical semi-conductor. 12

Figure 2.3: Schematic band diagram and Fermi energies of intrinsic, p-type and n-type semiconductors. 13

Figure 2.4: Schematic of photon absorption leading to charge generation and thermalisation.....14

Figure 2.5: Different recombination mechanisms: radiative band-to-band, non-radiative via trap state and Auger recombination. 16

Figure 2.6: Representations of p-n junction and p-i-n junction with (solid bands) and without (dashed bands) extended electric field. 18

Figure 2.7: Typical J-V curve and corresponding power curve with indicated maximum power point parameters. 19

Figure 2.8: The one diode equivalent circuit model of a solar cell with series and shunt resistances. 21

Figure 2.9: Influence of series resistance (left) and shunt resistance (right) on the shape of J-V curve. 23

Figure 2.10: Multilayer structure of m layers being surrounded by ambient and showing propagating forward and backward travelling electric fields. 26

Figure 2.11: Illustration of solar irradiation with different air mass values. 30

Figure 2.12: Plot of global horizontal irradiance spectra and their ratio at two different times in Seattle 2007. 31

Figure 2.13: Illustration of the sky dome with descriptive angles for solar position and panel orientation and tilt. 33

Figure 2.14: Illustration of fixed, 1-axis and 2-axis solar panel tracking systems. 34

Figure 2.15: Typical normalized diffuse light radiance distribution over sky dome. 35

Figure 2.16: Cubic ABX_3 perovskite crystal structure. 37

Figure 2.17: Evolution from mesoporous oxide based architecture to planar heterojunction architecture of perovskite solar cells. 38

Figure 2.18: Working principle of perovskite solar cell as p-i-n junction. 40

Figure 2.19: Schematic of different semi-transparent solar cell design concepts with selective absorption layer, thin-film absorber and reduced coverage absorbing layer. 42

Figure 2.20: Concept of tandem solar cell in which a perovskite solar cell absorbs within the low wavelength region and the silicon solar cell in the high wavelength region of the solar power spectrum. 43

Figure 2.21: Four terminal and two terminal tandem solar cell configurations. 44

Figure 2.22: Combined tandem power conversion efficiency for different top cell and bottom cell bandgap combinations in 4T and 2T configurations. 45

Figure 2.23: Schematic comparison of layered contact and back contact solar cell. 46

Figure 2.24: Processing steps for patterning metal with negative photoresist. 49

Figure 2.25: Illustration of the processing steps of sacrificial colloidal lithography. A colloidal monolayer and a gap filling material are deposited via spin-coating and subsequently the microspheres are degraded to leave behind a patterned layer. 51

Figure 2.26: Sketch of self-assembled monolayer with head group, tail and functional group. 52

Figure 3.1: Illustration of different device architectures with the included components and corresponding materials used. 53

Figure 3.2: Simulation process for PCE calculation of tandem solar cell stack. 66

Figure 3.3: Illustration of the pre-processing method used for the modelling of real world solar spectra needed for the input of energy yield simulations of solar cells. 67

Figure 3.4: Simulation process for annual energy yield calculation of tandem solar cell stack. ...69

Figure 4.1: SEM images (with magnified insets, scale bar 1 µm) showing a typical highly ordered monolayer of 1 µm diameter PS microspheres (a), cured TiO_2 (b) and SiO_2 (c) honeycomb structure. SEM images of colloidal monolayer (d, f) of PS microspheres with 0.37 and 0.6 µm diameter and corresponding SiO_2 honeycomb scaffold (e, g).....74

Figure 4.2: AFM measured 3D profile of 15 Ohm/square FTO glass before (left) and after (right) deposition of c-TiO_2. The root mean square roughness was calculated to be 10.5 and 5.2 nm. 75

Figure 4.3: AFM measured 3D profile of TiO_2 honeycomb structure (left). Line profile of TiO_2 honeycomb structure with indicated level of 300 nm thick perovskite filling. 76

Figure 4.4: SEM images (top view) showing perovskite film formations within TiO_2 (a) and SiO_2 (b) honeycomb scaffolds, on a c-TiO_2 layer (c) and on a mesoporous SiO_2 scaffold of 400 nm thickness (d) produced with 20 wt% perovskite precursor solution. Detailed top view and cross-section SEM images show the filling characteristic of TiO_2 scaffold with 20 wt% (e, f) and 40 wt% (g, h) perovskite precursor solution. 77

Figure 4.5: XRD patterns of perovskite films within SiO_2 honeycombs (top) or on top of FTO/c-TiO_2 substrates (bottom) deposited from 20 wt% precursor solution. The patterns are showing good similarity with the typical tetragonal $CH_3NH_3PbI_3$ patterns and lattice parameters (a=8.884, c=12.61 and a=8.874, c=12.62) were determined via a Rietveld refinement with χ^2=4.7 and χ^2=9.8). By Scherrer equation, crystallite sizes were estimated to be equal to around 110-120 nm (top) and 150-190 nm (bottom), respectively. 78

Figure 4.6: Total transmission measurements (a) within the visible spectrum of FTO/c-TiO_2 substrates (solid red line), compared to FTO/c-TiO_2 substrates covered with the SiO_2 honeycomb scaffold (dashed green line) and TiO_2 honeycomb scaffold (dotted blue line). Total transmission measurements (b) within the visible spectrum of top-electrode less devices with (dashed lines) and without SiO_2 honeycomb scaffolds (solid lines) and absorbing layers

fabricated with 10 (blue lines), 15 (magenta lines) and 20 wt% (green lines) perovskite solutions. 79

Figure 4.7: J-V characteristic curve for a SiO_2 honeycomb structured perovskite solar cell fabricated with 30 wt % precursor solution, scanning from forward bias to short circuit direction with a scan rate of 0.15 V/s.....80

Figure 4.8: Schematic illustration of the device architecture with oxide honeycomb scaffold (a). Colour enhanced cross-section SEM image of a complete device fabricated from the micro-structured SiO_2 honeycomb with 20 wt% perovskite precursor solution (b). Perovskite (purple) is shown in cup-shape SiO_2 scaffold pores (green) and covered with hole transporting layer, spiro-OMeTAD (yellow), below a silver top-electrode (white). Measured (symbols) and one-diode model fitted (lines) J-V characteristics of devices fabricated with and without SiO_2 honeycomb scaffolds and covered with perovskite films processed from 10 and 20 wt% precursor solutions (c). The arrows indicate the obvious change of shape that results in higher open-circuit voltages and fill factors for the SiO_2 honeycomb scaffold devices. The current voltage curves were scanned from forward bias to short-circuit at a rate of 0.15 V/s.....81

Figure 4.9: J-V characteristic curves for forward and backward scan (scan rate 0.15 V/s) of SiO_2 honeycomb structured perovskite solar cell fabricated with 10 and 20 wt% perovskite precursor solution (left). Stabilized current density and PCE of a SiO_2 honeycomb device fabricated from 20 wt% perovskite precursor solution, held at the maximum power voltage of 0.74 V for 120 seconds (right). This device shows a J_{SC} of 10.5 mA/cm^2, a PCE of 7.5 %, a FF of 0.77 and a V_{OC} of 0.9 V in the J-V measurement scanning from forward bias to short circuit direction under simulated AM1.5 100 mWcm^{-2} simulated sun light.....84

Figure 5.1: Representation of the $CH_3(CH_2)_{17}SiCl_3$ chemical structure (a). Schematic of the dip-coating process for the selective assembly of the Silane blocking layer (b). Sketch of the components of the island-structured perovskite device with siloxane blocking layer between perovskite domains (c). Conventional (d) and conductive (e) AFM images of dewet perovskite domains on top of compact TiO_2 layer without OTS treatment. Conventional (f)

and conductive (g) AFM images of compact TiO_2 layer after OTS treatment and subsequent removal of perovskite domains via DMF immersion. All AFM images represent a 40 x 40 µm scanned area. 90

Figure 5.2: Contact angle measurement image of OTS treated FTO/c-TiO_2 surface showing contact angle of around 112 °. 91

Figure 5.3: AFM (left) and conductive-AFM (right) after OTS treatment. 92

Figure 5.4: Absorption spectrum taken with a Fourier transform infrared (FTIR) spectrometer of the OTS treated substrates. 93

Figure 5.5: Time-resolved photoluminescence response measurement of dewetted semi-transparent perovskite cells without a quenching layer (left) and with Spiro-OMeTAD as a quenching layer (right). 94

Figure 5.6: Contact angle measurement images of bare compact TiO_2 covered FTO substrates (top row) and compact TiO_2 covered FTO substrates with dewetted low-coverage perovskite (bottom row) before and after different concentrations of OTS treatment. 95

Figure 5.7: Histograms and fitted normal distributions of the measured V_{OC} of semi-transparent dewet perovskite cells before (a) and after (b) OTS treatment. Histograms and fitted normal distributions of the measured PCE of semi-transparent dewet perovskite cells before (c) and after (d) OTS treatment. Averaged J-V curves of 15 semi-transparent perovskite solar cell devices with non-transparent Au top-electrode before (magenta) and after (red) OTS treatment (including all devices above 0.1% PCE). J-V curves (scan speed: 0.38 V/s, scan direction: forward bias to short-circuit) of best preforming semi-transparent perovskite solar cell devices with non-transparent Au top-electrode before (cyan) and after (blue) OTS treatment (e). Total transmittance UV-vis spectra of top-electrode less semi-transparent before (red) and after (blue) OTS treatment (f). 96

Figure 5.8: Top view SEM image of the dewetted perovskite islands on top of c-TiO_2 coated FTO glass. 98

Figure 5.9: J-V characteristic curves of OTS treated device (left) scanned with a speed of 0.38V/s from forward bias to short circuit (black line with squares: J_{SC} = 10.2 $mAcm^{-2}$, V_{OC} = 0.89 V, FF = 0.60, PCE = 5.5%) and from short circuit to forward bias (red line with circles: J_{SC} = 10.2 $mAcm^{-2}$, V_{OC} = 0.80 V, FF = 0.54, PCE = 4.4%) showing hysteresis. J-V characteristic curves of untreated device scanned with equal parameters (black line with squares: J_{SC} = 9.9 $mAcm^{-2}$, V_{OC} = 0.63 V, FF = 0.69, PCE = 4.3%) and from short circuit to forward bias (red line with circles; J_{SC} = 9.9 $mAcm^{-2}$, V_{OC} = 0.63 V, FF = 0.58, PCE = 3.6%) showing anomalous hysteresis. 98

Figure 5.10: Graph showing the current-density (black squares) and PCE (blue squares) measured over time at maximum power point voltage (0.68 V) determined from the reverse scan curve. 99

Figure 5.11: Combined J-V curves of untreated and OTS treated semi-transparent perovskite cells and one-diode model fitting comparison.....100

Figure 5.12: Left, J-V curves of a spiro-OMeTAD-compact/OTS/c-TiO_2 diode (black) and spiro-OMeTAD-compact/c-TiO_2 diode (red), fabricated in the same way as the perovskite solar cells but without perovskite layer. Calculated combined J-V curves of a measured fully-covered perovskite cell[173] with the OTS treated diode (dashed orange) and with the untreated diode (dashed purple) by assuming a coverage of 45%. Right, potential equivalent circuit diagram of perovskite solar cell with shunting path through spiro-OMeTAD-compact/c-TiO_2 diode (1) or through spiro-OMeTAD-compact/OTS/c-TiO_2 diode (2).....101

Figure 5.13: J-V curves (scan speed: 0.38 V/s, scan direction: forward bias to short-circuit) of optimized OTS treated semi-transparent perovskite cells with $TiCl_4$ post treatment of the compact TiO_2 layer (black line with squares; J_{SC} = 11.9 $mAcm^{-2}$, V_{OC} = 0.92 V, FF = 0.68, PCE = 7.4 %) or IPFB passivation treatment (red line with circles; J_{SC} = 10.0 $mAcm^{-2}$, V_{OC} = 0.98 V, FF = 0.67, PCE = 6.6 %).....102

Figure 5.14: J-V curves (scan speed: 0.38 V/s, scan direction: forward bias to short-circuit) of semi-transparent solar cells with (black line with squares; J_{SC} = 10.8 $mAcm^{-2}$, V_{OC} = 0.89 V,

FF = 0.54, PCE = 5.2%) and without OTS treatment (red line with circles; J_{SC} = 11.0 mAcm^{-2}, V_{OC} = 0.69 V, FF = 0.55, PCE = 4.2%) on 0.71 cm^2 exposed devices. 103

Figure 5.15: Characteristic J-V curve (scan speed: 0.38 V/s, scan direction: forward bias to short-circuit) of best performing semi-transparent dewet perovskite solar cell after OTS treatment with transparent top-electrode (a). Total transmittance UV-vis spectrum of best performing semi-transparent perovskite cell after OTS treatment with transparent top-electrode (b). Photograph of best performing neutral colour semi-transparent device with transparent top-electrode. 104

Figure 6.1: Optical model results for absorption in perovskite if covered by PEDOT and ITO as in a commonly found sandwiched devices or covered by PMMA as in a back contacted device. 111

Figure 6.2: Illustration of the back contacted perovskite solar cell architecture. 112

Figure 6.3: Illustration of the processing steps for back contacted perovskite solar cells. 112

Figure 6.4: Semi-cross sectional SEM image of patterned and developed photoresist with visible undercut profile (a). 10x (b), 100x (c) magnified optical microscope image of patterned finger electrodes. 113

Figure 6.5: Cross sectional SEM image of back contacted perovskite solar cell with Au as anode (a). J-V characteristic of Au based back contacted perovskite solar cell (b). 115

Figure 6.6: Illustrations of designs to modify top electrodes for better hole-selectivity. First design uses evaporated NiO as HTM and insulating SAM to block exposed Au sides (a). Second design incorporates a NiO shell around Ni electrode as HTM (b). 116

Figure 6.7: J-V characteristics of back contacted devices with oxidised Nickel shell from annealing and O_2 plasma treatment in light and dark. 117

Figure 6.8: Spatially resolved projected EQE (a, b) and PL intensity (c, d) of back contacted devices with oxidised Nickel shell from annealing (a, c) and O_2 plasma treatment (b, d). 118

Figure 6.9: Normalised spatially resolved photocurrent when exciting beyond the last p-type electrode. 119

Figure 6.10: Illustration of back-contacted device with extended pitch (a). Short current density of devices with 1 µm, 5 µm, 10 µm and 20 µm pitch (b). Optical microscope image of patterned electrodes with 5 µm (c), 10 µm (d) and 20 µm (e) pitch. 120

Figure 6.11: Sketch of proposed mechanism for long-distance hole diffusion. 121

Figure 6.12: Normalised transient PL decay of perovskite thin-films on top of spin-coated TiO_2, spin-coated SnO_2 and spray-coated TiO_2 electron extraction layers on FTO coated class (a). Normalised current density for devices incorporating electron transporting materials of spin-coated TiO_2, spin-coated SnO_2 and spray-coated TiO_2 with various pitch (b). 123

Figure 6.13: Illustration of spatial mapping technique of large pitch device (a). Top view microscope image of spatially analysed area (b). Photocurrent map of device with 20 µm pitch (c) and equivalent photoluminescence map (d) with indicators of the location where photoluminescence decay in (f) was measured. Plot of normalised mapped photocurrent, photoluminescence and estimated lifetime from photoluminescence decay of analysed area in horizontal scan direction. Plot of photoluminescence decay above TiO_2 and NiO electrodes at location indicated in (d). 124

Figure 6.14: J-V characteristic of inverted back contacted device with 1 µm pitch in forward (SC to OC) and reverse (OC to SC) scan direction. 125

Figure 6.15: Illustration of back contacted perovskite solar cell with surface passivation layer (a). J-V characteristic of surface passivated and un-passivated devices, as well as ionic liquid treated devices (b) in reverse scan direction. Transient PL decay measurements and corresponding PLQEs of passivated and un-passivated SnO_2 and spray coated TiO_2 devices (c). 127

Figure 7.1: Illustration of the 2T/4T tandem stacks and the HIT solar cell, including all materials and layer thicknesses. 136

Figure 7.2: Simulated EQE spectrum (a) and J-V characteristic with performance parameters (b) of single junction perovskite solar cell. 137

Figure 7.3: Simulated EQE spectrum (a) and J-V characteristic with performance parameters (b) of optimised single junction HIT solar cell. 138

Figure 7.4: Shifted extinction coefficients and corresponding Kramers-Kronig transformed refractive index spectra (a). PCE for optimised 2T and 4T tandem device stacks with C_{60} as ETL for shifted perovskite band-gaps (b). PCE for optimised 2T tandem devices with different ETL for perovskite bandgaps of 1.55 eV and 1.70 eV. 140

Figure 7.5: Simulated EQE spectrum (a) and J-V characteristic with performance parameters (b) of optimised 2T perovskite-on-silicon (1.7 eV) solar device. Table of optimised layer thicknesses (c). 141

Figure 7.6: Diffuse horizontal irradiance and global horizontal irradiance spectrum with 25^{th} - 75^{th} and 5^{th} – 95^{th} percentile representation in Golden (a), Seattle (b) and Mohave desert (c). Comparison of DHI and GHI spectra of all three locations at correct scale (d) and DHI and DNI spectra of all three locations at normalised scales (e). Plot of the fractions of GHI spectra pairs to demonstrate non-constant scaling (f). 143

Figure 7.7: Global horizontal irradiance spectrum in Mohave desert on July 4^{th} at 12:00 p.m. (a) and simulated corresponding J-V characteristic of HIT cell (b) and 2T tandem device optimised for $AM_{1.5}/0°$ (c). Global horizontal irradiance spectrum in Seattle on July 4^{th} at 2:00 p.m. (d) and simulated corresponding J-V characteristic of HIT cell (e) and 2T tandem device (f). 145

Figure 7.8: Angle dependence of normalised PCE for HIT device and 2T tandem device compared to cosine dependence (a). Angle dependent relative difference in normalised PCE of 2T tandem to HIT device (b). 146

Figure 7.9: PCE and energy yield of optimised 2T and 4T tandem solar cells depending on perovskite bandgap, optimised and calculated with fixed, 1-axis and 2-axis tracking at locations Golden (a), Mohave desert (b) and Seattle (c). Highest achievable annual energy

yield for optimised devices with varying tracking system at different locations (d). Relative energy yield gain of devices optimised for energy yield compared to devices optimised for $AM_{1.5}$/0° PCE. 148

Figure 7.10: Efficiency derating factors for tandem devices with varying tracking systems at different locations. 150

1 INTRODUCTION

1.1 Motivation – The Climate Change Dilemma

The unlimited thirst for energy has been one of the driving forces for the industrialization for the past century and keeps growing in a steady rate. Growth of gross domestic product (GDP), one of the most important indicators for economic performance of a country, is in close correlation with energy consumption[1]. Due to economic growth saturation, the energy consumption of industrialized regions such as the USA or Europe, has slowed down to an almost constant amount. However, the understandable gigantic economic catch-up of some heavily populated Asian countries, has caused an ongoing steep rate for the consumption of energy. Low prices for fossil fuels, a sluggish and powerful industry behind them and their particularly high energy density, has caused humans to burn fossil fuels as their primary source of energy production (see Figure 1.1). In this way, the enormous amount of hydrocarbons that have been captured underground over hundreds of millions of years get released into the atmosphere as CO_2 within a comparatively shock takingly short time frame[2]. Nowadays it is generally accepted within the scientific community[3] and the public that CO_2 acts as a greenhouse gas within our atmosphere and that we must pay the high price of a changing climate that is causing catastrophic

environmental effects[4]. In recent years, we started to experience disgracefully melting pole caps and glaciers, rising sea levels that make people having to relocate their lives, dying coral reefs and storms that leave behind cities unrecognizable[5,6]. New records of measured temperatures are an annual experience and statistical data analysis shows that such effects are extremely likely to be caused by the emission of greenhouse gases. Arguably humans have never influenced the environment of this planet more. One of the possible reasons for the little counteracting to these effects by governments is the fact that the unpleasant implications of climate change are occurring too slowly so some individuals are still able to deny the cause by human actions.

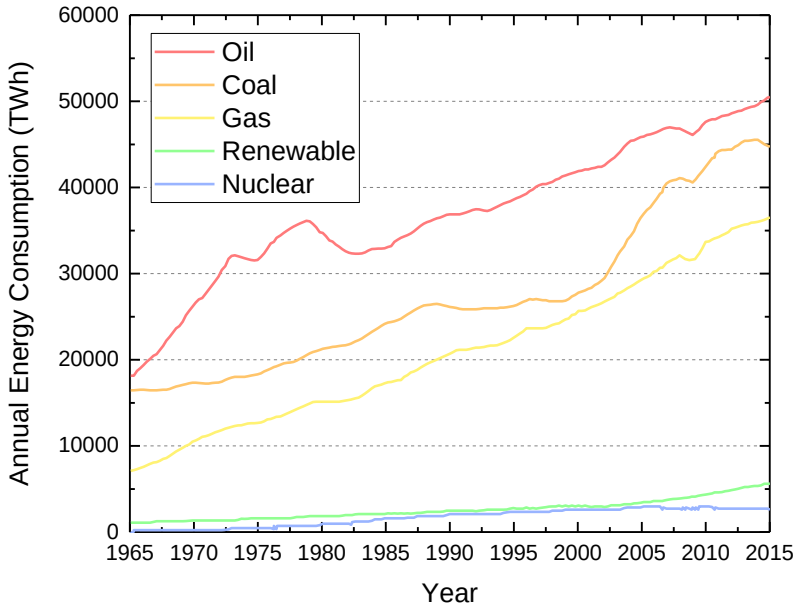


Figure 1.1: Development of annual energy consumption of different energy sources[7].

Recently, at the 2015 United Nations Climate Change Conference (COP21) in Paris the biggest milestone of global climate change policy making has taken place, when the Paris agreement was signed by 195 countries worldwide to do their best to "keep global warming well below 2 °C". The consequence taking policies are starting to appear on the international horizon and most of them involve the creation of financial incentives for the

implementation of renewable energy producing systems and the introduction of a carbon tax.

Despite some uncertainties about the coming United States policy making direction, the private sector has fortunately also come to realise that the use of clean energy is economically beneficial, which has recently been termed "The irreversible momentum of clean energy" by leaving president Barack Obama[8]. Energy production from renewable sources has gone up year over year with mostly wind and hydro taking the biggest shares in electricity generation[9]. Various technologies exist, which all have their own advantages and disadvantages depending on the energy needs and on the location where they are deployed. Solar energy, which has currently the highest growth rate[9], plays a particularly interesting role, as relatively high irradiance of sunlight is distributed well across the planet, especially in areas of high population[10]. To meet the world's energy demand in 2050 (estimated to ca. 25 TW_p[10]), we would only require an area slightly larger than the United Kingdom and cover it with mediocre performing solar panels. Many materials that are used for photovoltaic modules are abundant and produced in high volume. Recently the price of silicon based solar panels has dropped tremendously to values as low as 0.5 \$/W[11], which makes it in many locations an energy source cheaper than the cost for energy from the grid (known as grid parity). However, due to large capital expenditure cost for production equipment, the economies of scale don't have a strong enough effect to bring the prices for solar modules down enough to make solar energy cost competitive in all regions without implementing government incentives. High investments are needed, which drive up the minimum sustainable price of modules and hinder new manufacturers to enter the market[12]. Furthermore, installation cost of current photovoltaic systems make up a significant part of the overall cost[13].

Thin-film materials and particularly perovskites of organic-inorganic hybrids represent very promising candidates to disrupt the solar technology market and make a significant contribution to limit climate change in the future. Perovskites have often been described as a "wonder material" due to their almost ideal opto-electronic properties for photovoltaic applications. The materials are abundant, cheap to produce, simple to process via solution or vapour deposition methods, strongly absorbing, they have relatively long diffusion lengths and tuneable bandgaps to name some of the characteristics. These allow for low capital expenditure manufacturing processes as well as lightweight, flexible thin-film products or even the use as top absorbers in tandem solar cell applications. One could imagine solar cell products that have never been feasible to be implemented before. No wonder that the scientific community has become hugely interested in the past four years, which has also helped to bring the solar cell power conversion efficiency records in the labs up to 22% with a rate that has never been seen before with any other photovoltaic technology[14].

There is barely anything more motivating than carrying out research on a material, which has such a great potential to contribute to the saving of the planet. Still, many fundamental scientific questions remain to be answered and new concepts for devices for mass production to be found, which the work of this thesis is trying to contribute to.

1.2 Structure and aim of the thesis

This thesis aims to provide the reader with a broader motivation for the work that has been carried out, the introduction into perovskite solar cells and the background information necessary to understand the concepts of the research covered by the thesis. While the research results are discussed in much detail and most of the fundamental concepts are included to provide the required basics to understand the scientific methodology and the

implications as well as the broader context, the general reader might need to find additional information in specialised text books and published journal articles.

The structure of the thesis follows a contextual order to guide the reader from the first to the last page with clarity. The following background chapter varies widely from the fundamental scientific concepts of semiconductors, with their energy band theory, the absorption and recombination mechanisms and then leading to the working principle of solar cells in general. This content was added since the following chapters will mention or touch upon theories that make use of these basic concepts. The later used modelling techniques are explained starting with the standard equivalent circuit model, the detailed balance theory of radiation and emission, transfer matrix method and all the essentials about solar radiation to understand the optical modelling under real world conditions. For the familiarization of the underlying technology, which is being used throughout the thesis, a short review of perovskite solar cells is presented by familiarizing the reader with the material properties, important findings and the device architecture developments over time. As the later chapters contain three different concepts of perovskite solar cell device designs, the basics of semi-transparent, tandem and back-contacted solar cells are discussed. The device designs were realized through different lithography and self-assembly techniques, which are then defined in more detail to help the reader put them into the context of other fabrication processes. A continuing methods chapter tries to cover all the experimental and modelling details that were used to gather the later discussed results. The sections are categorized by the type of experiments.

Even though the field of perovskite solar cells has had a huge amount of attention from the scientific community, it is still a young field and a lot is left to learn about the fundamentals and also the more applied scalable processing techniques of this material. Every research project presented in this thesis has been motivated by looking at the potential practical use

cases for future applications. The development of new device designs could possibly lead to a different and maybe even simpler manufacturing processes.

The control of thin-film formation, including the entire process of crystal seeding and crystal growth, has been a highly-studied topic since the very beginning of this research field and still is arguably one of the most important aspects that can help to make high performing perovskite solar cells. At the time of conducting the research presented in Chapter 4, it has not been demonstrated to pattern perovskites in a controlled way. It was the curiosity about the possibility to confine the crystal growth of perovskite thin-films that drove the efforts to develop a templated perovskite device, that could later be used as a semi-transparent solar cell. Through the course of this project it was discovered that the self-assembly of perovskite island domains by dewetting[15] would present a simpler fabrication technique to make neutral colour semi-transparent devices. However, these suffered from shunting paths occurring through the uncovered areas between the perovskite domains. Consequently, the discussed project of chapter 5, builds upon the knowledge of chapter 4, and semi-transparent solar cells could be improved with the introduction of a selectively-attaching shunt-blocking layer. This simple process showed to be reproducible and lead effectively to higher open-circuit voltages.

Chapter 6 presents an entirely new architecture for perovskite solar cells, as it introduces back-contacts as alternative to sandwiched devices. The motivation originally emerged from the interest to study lateral diffusion characteristics of perovskite thin-films with a specifically designed device. When it was realised that charge carriers in perovskites have long enough diffusion lengths, the idea was born to try to develop devices that would mirror back-contacted devices from the silicon solar cell field to maybe create the perovskite cell of the future.

As latest reports have demonstrated that perovskites represent great candidates as top cell absorbers in tandem applications, a lot of research efforts have shifted into this direction. Even though the potential is undeniable, it is not yet clear, how such applications would compare to conventional single-junction devices in real world conditions. Furthermore, the community doesn't seem to agree, if a four-terminal or a two-terminal configuration is preferable for feasible future applications. With these questions in mind an extensive optical model was developed to simulate the energy yield of such systems being deployed in different locations under various solar irradiation conditions. The results are presented in Chapter 7.

Finally, a concluding Chapter 8 summarizes the important implications gotten from the results of this work and offers an outlook for future paths that should be explored for the improvement of perovskite solar cell applications.

2 BACKGROUND

This chapter is meant to give an overview of the fundamental concepts that are needed to understand the contents of the following chapters of the thesis. It starts with an introduction into semiconductors, the operating principle of solar cells with a specific emphasis on perovskite solar cells. Furthermore, the design aspects of perovskite solar cells are introduced, nano-lithography methods are explained and finally the theoretical backgrounds behind the optical modelling of Chapter 7 are given.

2.1 Semiconductors

The fundamental building block of every photovoltaic system is a semi-conducting material, which is defined as having an influenceable conductivity somewhere in the range between a metal and an insulator.

2.1.1 Energy Bands and Fermi level

The semi-conducting characteristic of a material can be explained with distinct energy states that electrons (e^-) can occupy. The dynamic behaviour of the electron within a material can be described with the quantum mechanical wave function ψ, which can be derived by solving the time-independent Schrödinger equation for the molecular system that the electron is embedded into. While solving this equation is beyond the scope of this thesis, the reader can find analytical solutions for crystalline systems with periodic potentials in standard textbooks[16] or numerical density functional theory solutions for more complex crystal structures (i.e. hybrid-organic perovskites[17,18]) in recent publications. The solution describes the relationship between the electron's energy and the momentum and

therefore defines allowed energy levels that an electron can occupy. While in a single atom, these are only discrete energy levels, but when atoms are brought together and interact as in crystalline solids, these degenerate energy levels will be separated into many energy levels. Due to the very close separation, they may be seen as a continuous band of allowed energy states. The highest energy band that is fully occupied by electrons at T = 0 K is the so called valence band and the band above, which is fully empty at T = 0 K is called the conduction band. All other bands below the valence band are presumed to be fully occupied and the bands above the conduction band, to be empty. Figure 2.1 shows an example of the two energy bands that are separated by a gap of forbidden energies, the so called band-gap (E_g). The band-gap is defined as the difference between the lowest energy of the conduction band E_C and the highest energy of the valence band E_V, hence $E_g = E_C - E_V$.

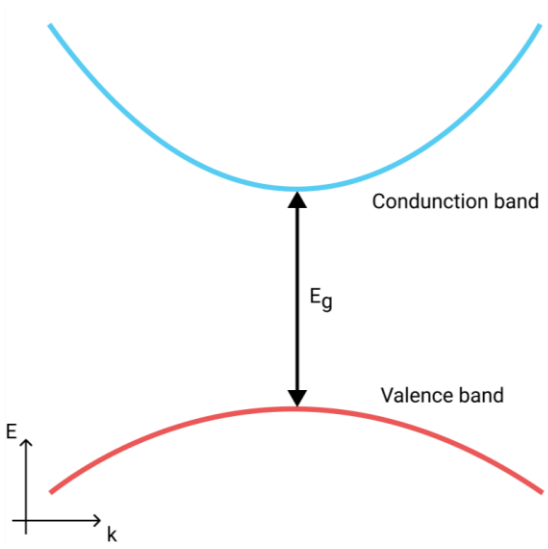


Figure 2.1: Illustration of valence and conduction band, separated by bandgap

Charge transport can only occur in not completely filled bands where electrons have space to move because the overall momentum of the electrons needs to be preserved[19]. Within a semiconductor, electrons in the valence band must be excited with an energy $E > E_g$ in order to cause a transition into the conduction band from which the electrons can contribute to charge transport and they leave behind a hole (h^+) in the valence band.

An important concept for the description of semiconductors is the introduction of the effective mass (m^*). It allows us to treat electrons within complex potential landscapes with quasi-mechanical concepts as it represents the analogous of the electron mass of a free electron but includes the many forces that act upon the electron within an energy band and should therefore not generally be seen as a constant. The effective mass is defined by the reciprocal curvature of the energy band in k-space:

$$m^* = \frac{1}{\hbar^2}\frac{\partial^2 E}{\partial k^2} \tag{2.1}$$

Where $\hbar$ represents the reduced Planck constant and k the wave vector. Now this allows us to approximate the dynamics of the electron (subscript n) motion and equivalently the motion of a hole (subscript p) within a semiconductor. After using the effective mass and some further quantum mechanical derivations[20], the density of states for the conduction (c) and the valence (v) band is given by:

$$g_C(E) = \frac{m_n^*\sqrt{2m_n^*(E - E_C)}}{\pi^2\hbar^3}, \tag{2.2}$$

$$g_V(E) = \frac{m_p^*\sqrt{2m_p^*(E_V - E)}}{\pi^2\hbar^3} \tag{2.3}$$

Generally, the density of states defines the number of available states at each energy. The above derived expression, allows us to determine the number of available states that electrons with energy E can occupy in the conduction or valence band. Furthermore, the probability of an electron occupying a particular energy state can be described by Fermi-Dirac statistics, or the so-called Fermi function:

$$f(E) = \frac{1}{1 + e^{(E-E_F)/k_BT}} \tag{2.4}$$

E_F is the Fermi level, defined as the energy for which the Fermi function is 0.5, k_B is the Boltzmann constant and T is the temperature. The quantitative electron occupation of the energy bands in equilibrium can be described by the integral of the product of density of

states *g(E)* and the probability of an electron occupying a state, over all possible energies, and therefore we can derive it for electrons (*n*) as well as for holes (*p*) in equilibrium as follows (used Boltzmann approximation with the assumption that $E - E_F > 3k_BT$):

$$n = \int_{E_C}^{\infty} g_C(E) f(E) dE = 2\left(\frac{2\pi m_n^* k_B T}{h^2}\right)^{\frac{3}{2}} exp\left(-\frac{E_C - E_F}{k_B T}\right) \tag{2.5}$$

$$p = \int_{-\infty}^{E_V} g_V(E)[1 - f(E)] dE = 2\left(\frac{2\pi m_p^* k_B T}{h^2}\right)^{\frac{3}{2}} exp\left(-\frac{E_F - E_V}{k_B T}\right) \tag{2.6}$$

We define the effective density of states as N_C and N_V:

$$N_C = 2\left(\frac{2\pi m_n^* k_B T}{h^2}\right)^{3/2}, \quad N_V = 2\left(\frac{2\pi m_p^* k_B T}{h^2}\right)^{3/2} \tag{2.7}$$

The Fermi function at temperatures above absolute zero will divert from the step function and causes the effect of some electrons being present in the conduction band at thermal equilibrium, which is illustrated in Figure 2.2.

In an intrinsic semiconductor at thermal equilibrium, the number of electrons in the conduction band is equal to the number of holes in the valence band and the intrinsic carrier concentration (n_i) can be described by:

$$n_i = \sqrt{np} = \sqrt{N_C N_V} exp\left(-\frac{E_g}{2k_B T}\right) \tag{2.8}$$

This leads us to the expression of the Fermi level of an intrinsic semiconductor $E_i = E_F$, given by

$$E_i = \frac{E_V + E_C}{2} + \frac{k_B T}{2} ln\left(\frac{N_V}{N_C}\right) \tag{2.9}$$

which is usually very close to the middle of the bandgap.

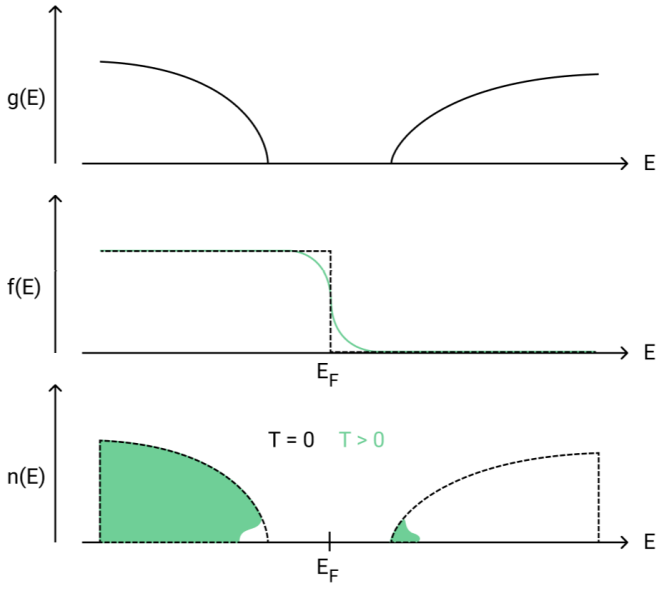


Figure 2.2: Density of states function, Fermi function at T = 0 and T > 0 and number density of electrons for typical semi-conductor.

Generally, the conductivity (σ) of intrinsic photoconductors is quite low due to the low number of intrinsic charge carriers but this property can be changed by introducing impurities or dopants that act as electron donors (subscript *D*) or electron acceptors (subscript *A*). Adding a controlled amount of charged ions can introduce additional electronic states to the semiconductor that are usually between the energy gap so that the Fermi level becomes:

$$E_{F,n} = E_i + k_B T ln\left(\frac{N_D}{n_i}\right) \tag{2.10}$$

for an n-type semiconductor in which the electrons are the main carriers of charge, and

$$E_{F,p} = E_i + k_B T ln\left(\frac{N_A}{n_i}\right) \tag{2.11}$$

for a p-type material in which the holes are the main carriers of charge. Figure 2.3 shows the energy bands for different types of materials with their representative Fermi-levels.

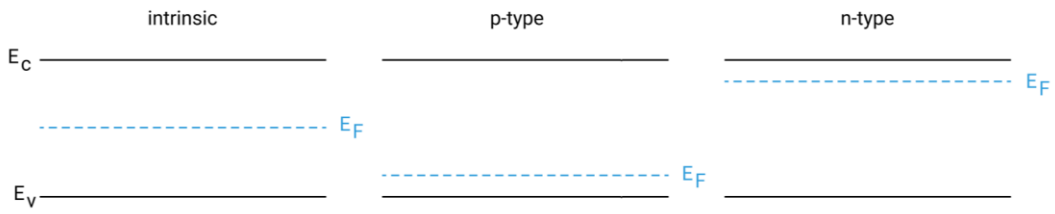


Figure 2.3: Schematic band diagram and Fermi energies of intrinsic, p-type and n-type semiconductors.

2.1.2 Absorption and Recombination

Known from the quantum mechanical dualism of light, apart from treating photons as particles, they can also exhibit wavelike character with a photon energy defined by the product of the Planck constant and the photons frequency (f) as $E = hf$.

In a solar cell, the charge generation mechanism works as shown in the simplified illustration of Figure 2.4. Photons impinge on a semi-conducting material and in case their energy is larger than the bandgap of the absorbing material ($hf > E_g$) they transfer their energy to the electron, which can be excited from the valence band to the conduction band. The excited electron leaves behind a positively charged hole in the valence band, and in an ideal case the electron in the conduction band diffuses and reaches the electron-collecting electrode while on the opposite site the hole is collected by the hole-collecting electrode and thereby creating an electric current. Typically, an electron transporting layer (ETL) and respectively a hole transporting layer (HTL) help the diffusion and stop the recombination which will transfer the excited electron back to the valence band and not contribute to charge generation. In this way, the energy of the photon gets transferred into electrical energy, however photons with higher energies than the band gap will excite the electrons to higher energy states and will cause a quick thermalisation back to the conduction band energy level. This energy difference is lost into thermal dissipation and

cannot contribute to a higher power conversion efficiency, which explains why materials with the lowest bandgaps do not lead to the most efficient solar cells.

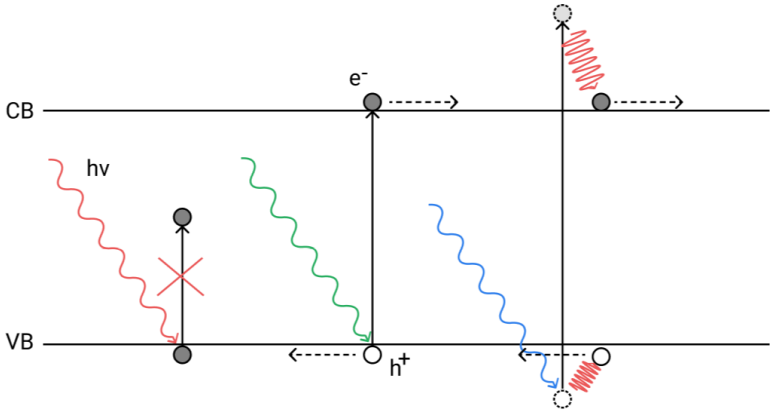


Figure 2.4: Schematic of photon absorption leading to charge generation and thermalisation.

The optical absorption plays a crucial role in the electricity conversion in a photovoltaic system. The more photons get absorbed, the more electrons can be excited and therefore the efficiency of a cell is closely related to the absorption characteristics. There are three possible mechanisms that can occur when an incident photon approaches a material. It is either transmitted through the film (maybe with a change of direction coming from scattering effects), it can be reflected by the surface of the film or it will be absorbed. Neglecting reflection, the absorption strength of a material can be described with the so-called absorption coefficient (α) that determines the amount of light that is being absorbed within a certain depth x of a material by the following relation:

$$I(x) = I_0 e^{-\alpha x} \tag{2.12}$$

Where $I(x)$ is the intensity of light at depth x and I_0 being the intensity at the surface of the material. The absorption coefficient depends on the wavelength of the incoming photon and is closely related to the extinction coefficient (k) of the material by:

$$\alpha = \frac{4\pi k}{\lambda} \tag{2.13}$$

Once photons get absorbed and generate electron hole pairs, they must be transported through the material and collected at the appropriate electrodes. The motion is governed by a combination of drift, dependent on the electric field (E) across the material, and diffusion due to a statistically random spreading force of charges across space. The resulting current (J) is consequently described by the one-dimensional drift-diffusion equation:

$$J = q(n\mu_n + p\mu_p)E + q\left(D_n\frac{dn}{dx} + D_p\frac{dp}{dx}\right) \tag{2.14}$$

Where μ and D are the material specific charge carrier mobility and diffusion coefficient, which are in low-field conditions directly related via the Einstein relation:

$$\mu = \frac{qD}{k_B T} \tag{2.15}$$

It can happen that the electron and the formed hole recombine before they are collected by the electrodes after the diffusion. While there is only one dominant mechanism of charge carrier generation, there are three possible recombination processes[21] (see Figure 2.5):

The unavoidable recombination mechanisms that are due to intrinsic material properties include spontaneous radiative band-to-band recombination and a process called Auger recombination in which the excited carrier relaxes to the valence band as well but passes on its energy to another carrier within the conduction band. This carrier eventually thermalizes back to the conduction band edge and the kinetic energy is lost in thermalisation. Radiative recombination might lead to another charge carrier generation if the emitted photon is absorbed (known as photon recycling). Furthermore, there exists an avoidable recombination process due to the existence of defects in the material that cause the relaxation through a trap state within the band-gap. This so-called Shockley-Read-Hall (SRH) recombination causes the charge carriers to recombine non-radiatively and therefore lead to energy loss in the process. Another formalism is often used in which the

recombination processes are classified into monomolecular recombination, bimolecular recombination and trimolecular recombination. Monomolecular recombination involves only one type of charge carrier, which recombines through a recombination centre (i.e. SRH recombination is monomolecular). Bimolecular recombination involves two free charge carriers, such as in band-to-band recombination. And any process involving three charge carriers, such as Auger recombination, is called trimolecular recombination.

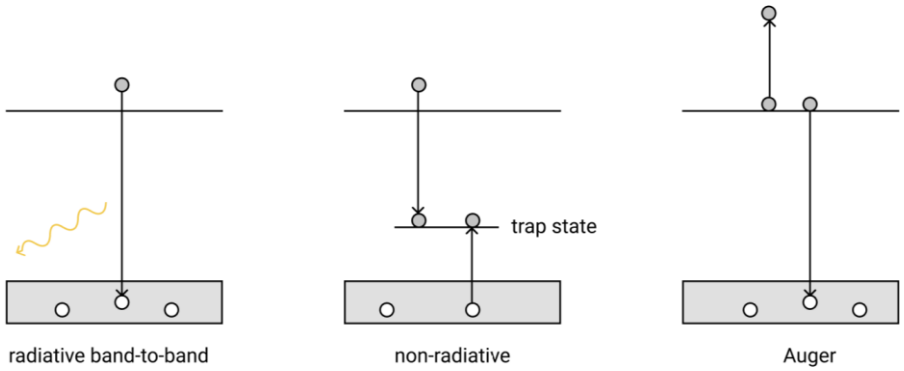


Figure 2.5: Different recombination mechanisms: radiative band-to-band, non-radiative via trap state and Auger recombination.

The recombination can be quantified with the net recombination rate (R), which is derived through charge carrier relaxation statistics and is heavily dependent on the minority carriers in the semiconductor material. The recombination rate is related to the charge carrier lifetime (τ), an intrinsic material property that defines how long it takes on average for an excited charge carrier until it recombines (or in other words the time it takes for the charge population *N* to reach *exp(-1)*):

A general recombination rate equation is used to describe the recombination rate through mono-, bi- and trimolecular recombination pathways with their specific recombination rate coefficients (a, b, c):

$$R = -\frac{dn}{dt} = a * n + b * n^2 + c * n^3 \qquad \textbf{(2.16)}$$

This equation can be used to quantify different recombination mechanisms when spectroscopic data (i.e. from transient photolumiscence measurements) are available. A non-neglectable contribution of SRH recombination arises at crystal grain boundaries and at the surface of the material. Defects between crystal grains introduce disturbances within the energy band and can lead to trap states that serve as recombination centres. Therefore, perfectly single crystalline materials will suffer less from such effects. However, they are prone to surface defects that can be a result of unpassivated dangling bonds and extrinsic impurities introduced by interfacing materials. Surface recombination can therefore be suppressed by passivating the surface area or improving the interfacial materials. If only bulk recombination pathways are considered, total bulk recombination lifetime can be described as the combined lifetimes as:

$$\frac{1}{\tau_{bulk}} = \frac{1}{\tau_{rad}} + \frac{1}{\tau_{SRH}} + \frac{1}{\tau_{Auger}} \tag{2.17}$$

Combined with the diffusion coefficient, we can define the average diffusion length *L* of charge carriers as:

$$L = \sqrt{D\tau} \tag{2.18}$$

2.1.3 p-n and p-i-n Junctions

When an interface is created between an n-type and a p-type semiconductor, a p-n junction is created (see illustration on the left in Figure 2.6). The Fermi levels align and so the different work functions of the materials lead to a difference in electrostatic potential, which builds up an electric field at the junction that creates a drift of photo generated electrons to the n side and holes to the p side. Consequently, the junction region is depleted of charge carriers and presents a barrier to majority carriers (electrons in n-type) and a low resistance path for minority carriers (holes in n-type). When operated as a solar cell device,

photo-generated minority carriers from both materials are reaching the junction by diffusion and are then contributing to the photocurrent.

A slight variation to the p-n junction is the inclusion of an intrinsic semi-conductor between the n-type and p-type materials (see illustration on the right in Figure 2.6). In this configuration, the electric field is either extended over a wider distance (illustrated as solid bands), which helps in materials with shorter diffusion lengths that need more drift driven charge collection. Otherwise, in high injection conditions or due to charged impurities the electric field can fall to zero within most of the intrinsic region, which requires that charge transport to the electrodes is preferentially driven by diffusion.

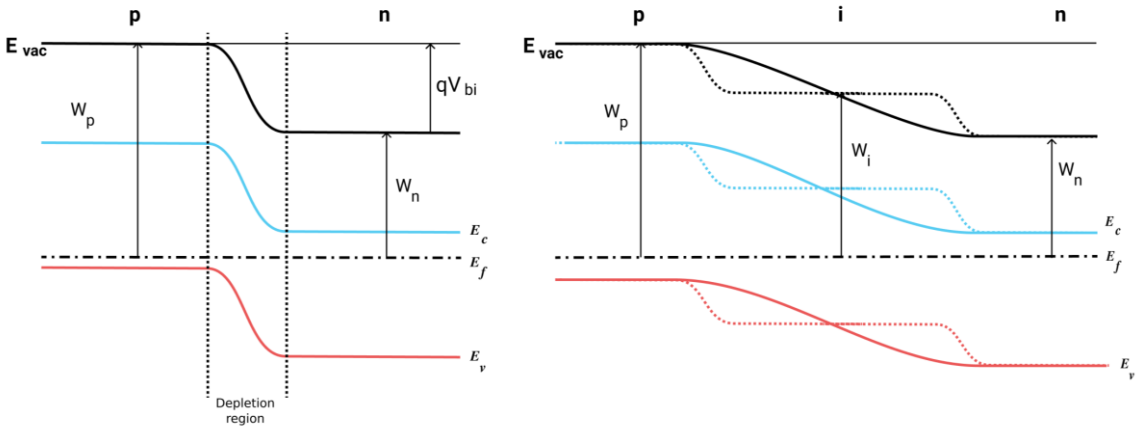


Figure 2.6: Representations of p-n junction and p-i-n junction with (solid bands) and without (dashed bands) extended electric field.

It needs to be noted that the above description assumes homo-junctions with perfectly aligned band-gaps. In the opposite case of hetero-junctions there will be emerging discontinuities between the bands, which introduces potential steps that can lead to more complex charge transport characteristics.

2.1.4 Solar cell performance characteristics

The performance of a solar cell can be well characterized by the measurement of its current density dependence upon applied bias voltage (V) and light. A typical current density-

voltage (J-V) curve is depicted in Figure 2.7 and can be measured by a process discussed in Section 3.1. The important characterization parameters are the short circuit current (J_{SC}), measured when the voltage across the device is zero, and the open circuit voltage (V_{OC}), which is the maximum attainable voltage from a solar cell. Figure 2.7 also shows the power (P) curve that comes from the product of the current and the voltage:

$$P = J * V \tag{2.19}$$

The fraction of the maximum attainable power (maximum power point in Figure 2.7) to the product of J_{SC} and V_{OC} define the third most important characterization value, the fill factor (FF):

$$FF = \frac{J_{mmp} * V_{mmp}}{J_{SC} * V_{OC}} \tag{2.20}$$

The fill factor describes the "squareness" of the J-V curve and is generally influenced by recombination and parasitic resistances (will be described in Section 2.2.1), which can lead to parallel current flow into the opposite direction.

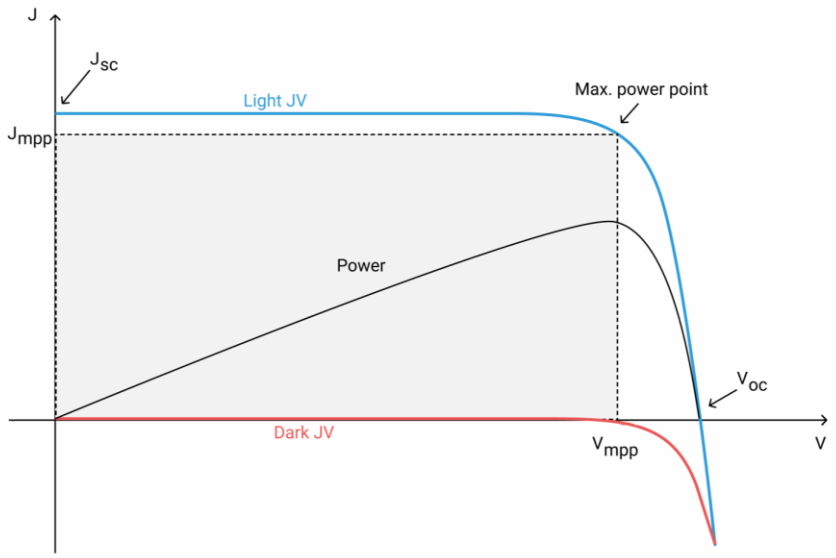


Figure 2.7: Typical J-V curve and corresponding power curve with indicated maximum power point parameters.

Together with the $J_{SC,}$ V_{OC} and irradiation power (P_{in}) it can be used to formulate the power conversion efficiency (PCE):

$$PCE = \frac{J_{SC} * V_{OC} * FF}{P_{in}} \tag{2.21}$$

The theoretical limit for PCE that can be reached with single-junction photovoltaic applications has been established by Queisser and Shockey[22]. The theory will be described in Section 2.2.2 and predicts that the maximum attainable PCE (known as the Shockley-Queisser (SQ) limit) for a single-junction solar cell equals approximately 33.7 % and requires a band-gap of 1.34 eV. One way to overcome this limit is by using multi-junction tandem solar cell applications, which is described in Section 2.5.

2.2 Modelling of solar cells

There are many aspects of the solar cell device mechanisms that can be modelled to predict the operation of solar cells in real world conditions. In this work, we have limited the efforts to equivalent circuit device models, optical models and the description of solar radiation in order to offer sufficient background information for the understanding of the methods used in Chapter 7.

2.2.1 Equivalent Circuit Model

The electric working principle of a solar cell can be explained with a simple equivalent circuit model shown in Figure 2.8. The current density (J) of the cell is dependent on the voltage (V) applied and defined as the difference of the photocurrent density at short circuit (J_{SC}), the so called dark current (J_{dark}) and the shunt current (J_{shunt}):

$$J(V) = J_{SC} - J_{dark}(V) - J_{shunt}(V) \tag{2.22}$$

The J_{SC} depends on the absorption characteristic and several other parameters that will be explained in a later section in more detail. We can relate it to the incident spectrum by integrating the external quantum efficiency (EQE_{PV}) of the solar cell, multiplied with the photon flux of solar spectrum (ϕ_{sun}) over the entire spectrum of photon energies, to get the number of generated electron- current-voltage pairs. Multiplied with the unit charge (q), this leads to the J_{SC}:

$$J_{SC} = q \int_0^\infty EQE_{PV}(E)\phi_{sun}(E)dE \tag{2.23}$$

The $EQE_{PV}(E)$ is the probability of a photon with energy E to be absorbed to then contribute one electron as charge output. Another value that is often used to describe the efficiency of absorbed charges to extracted charges is defined as the internal quantum efficiency (*IQE*), which can be determined by dividing the *EQE* by the light harvesting efficiency (LHE):

$$IQE = \frac{EQE}{LHE} \tag{2.24}$$

LHE can be defined as the effective light that gets absorbed by the material and therefore as all light that is not resulting in reflection (R) nor transmission (T): $LHE = 1 - R - T$.

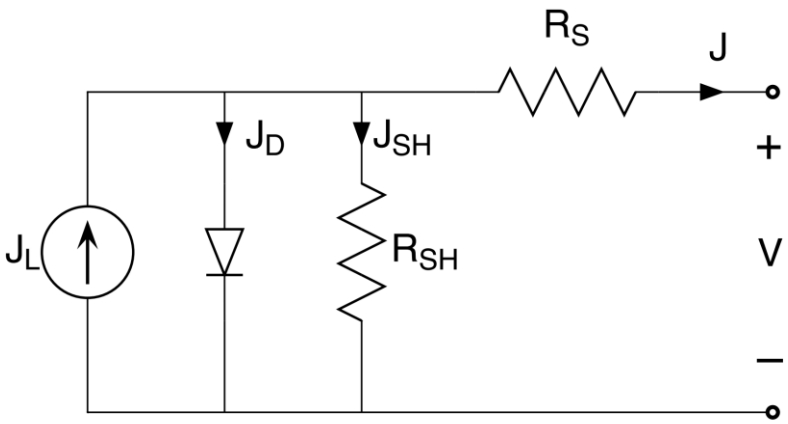


Figure 2.8: The one diode equivalent circuit model of a solar cell with series and shunt resistances.

Under load, a potential difference between the terminals of the solar cell generates a current flowing into the opposite direction of the photocurrent. This so called dark current density can be modelled by assuming the cell behaves as a diode in which J_0 is known as the material specific reverse saturation current density that occurs when a reverse bias is applied to the diode:

$$J_{dark}(V) = J_0\left(e^{\frac{qV}{mk_BT}} - 1\right) \tag{2.25}$$

The exponential term depends on the charge energy and the thermal energy of the electron. The elementary charge is symbolized as q and the ideality factor (m) is used to account for the unideal behaviour of the diode. The shunt current density is defined by the fraction of the voltage across all components and the shunt resistance (R_{SH}). The voltage across the components is comprised as the sum of the voltage across the output terminal and the voltage across the series resistor (R_S):

$$J_{shunt} = \frac{V + J(V)R_S}{R_{SH}} \tag{2.26}$$

The shunt current is lost from the generated net current density, which then becomes:

$$J(V) = J_{SC} - J_0\left(e^{\frac{q(V+J(V)R_S}{mk_BT}} - 1\right) - \frac{V + J(V)R_S}{R_{SH}} \tag{2.27}$$

The way the shunt and series resistances influence the shape of the J-V curve (and therefore the performance of the solar cell) is presented in Figure 2.9.

In the ideal solar cell device (with $m = 1$, $R_S \to 0$ and $R_{SH} \to \infty$), the current density becomes:

$$J(V) = J_{SC} - J_0\left(e^{\frac{qV}{k_BT}} - 1\right) \tag{2.28}$$

We can then determine the V_{OC} (assuming only radiative recombination) by setting $J = 0$ and solving for *V*:

$$V_{OC} = \frac{k_B T}{q} ln\left(\frac{J_{SC}}{J_0} + 1\right) \tag{2.29}$$

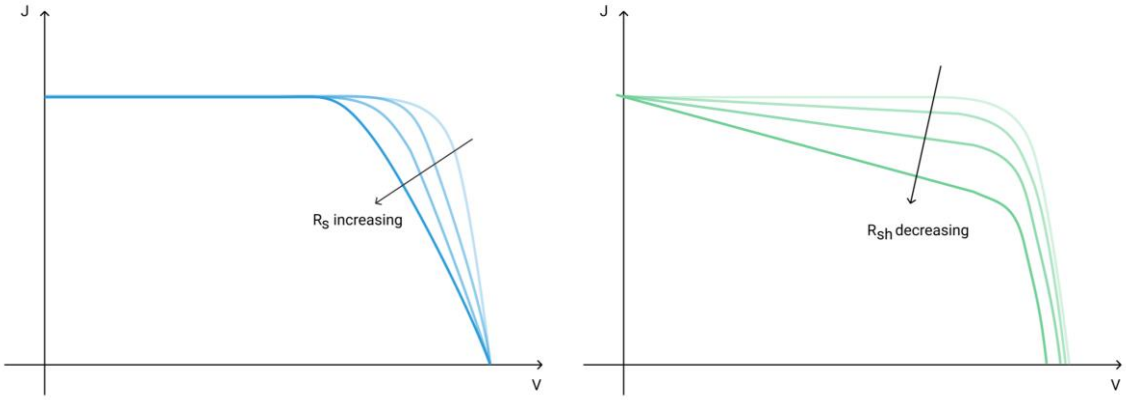


Figure 2.9: Influence of series resistance (left) and shunt resistance (right) on the shape of J-V curve.

2.2.2 Detailed balance

Shockley and Queisser[22] postulated the thermodynamic equilibrium between absorption and emission and introduced the famous Shockley-Queisser efficiency limit for a single band gap semiconductor in the case for which only radiative recombination occurs. The theory is based on the consideration that a solar cell is under constant irradiation from the ambient and this photon flux (ϕ_{BB}) can be described by the radiation from a black body with ambient temperature T_0, also known as Planck's law:

$$\phi_{BB}(E) = \frac{1}{4\pi^2 \hbar^3 c^2} \frac{E^2}{exp\left(\frac{E}{k_B T_0}\right) - 1} \tag{2.30}$$

Kirchhoff's law states that this irradiation needs to be in equilibrium with the emission from the solar cell[23]. Consequently, we can formulate an expression for the current density that is absorbed and emitted in equilibrium:

$$J_{abs,0} = q\int_0^\infty EQE(E)\phi_{BB}(E)\,dE = J_{rad,0} \tag{2.31}$$

In an ideal solar cell, we assume that no carriers are lost due to non-radiative recombination (what we call the radiative limit). Thus, the only loss of energy comes from the equilibrium correlated radiative recombination. Under light, we introduce additional charges to the conduction band, which will change the probability of photons being spontaneously emitted by already introduced Fermi statistics:

$$J_{em}(V) = J_{rad,0}e^{\frac{qV}{k_BT}} - J_{rad,0} \tag{2.32}$$

Since the spontaneously emitted photons will be lost from the net photocurrent, we have derived an expression for the dark current during operation:

$$J_{dark} = q\int_0^\infty EQE(E)\phi_{BB}(E)\,dE * \left(e^{\frac{eV}{k_BT}} - 1\right) \tag{2.33}$$

Together with equation 2.28 we arrive at a general *J(V)* representation depending on the measurable $EQE_{PV}(E)$:

$$\begin{aligned} J(V) = q\int_0^\infty EQE_{PV}(E)\phi_{sun}(E)dE \\ - q\int_0^\infty EQE_{PV}(E)\phi_{BB}(E)\,dE * \left(e^{\frac{eV}{k_BT}} - 1\right) \end{aligned} \tag{2.34}$$

In order to account also for non-radiative recombination, the reciprocity of absorption and emission contributes to a more generalized theory originally developed by Rau[24]. Consequently, we can assume that the emission process is not ideal and we can measure this efficiency (EQE_{EL}) by operating the solar cell as a light emitting diode (LED) driven by an injection current (J_{inj}):

$$J_{em}(V) = EQE_{EL} * J_{inj}(V) \tag{2.35}$$

In solar cell operation mode, the injection current becomes the photocurrent and we use equations 2.28, 2.32 and 2.35 to find the *J(V)* with accounted non-radiative recombination:

$$J(V) = J_{ph} - \frac{J_{rad,0}}{EQE_{EL}}\left(e^{\frac{eV}{k_B T}} - 1\right) \tag{2.36}$$

Another way of modelling a realistic *J(V)* relation can be achieved by assuming an EQE_{EL} of 100% and using the characteristic J-V parameters *m*, R_{sh} and R_s which can be indirectly obtained by fitting existing J-V curves with equation 2.27[25].

2.2.3 Transfer Matrix Model

Photocurrent is generated when energy from an optical electric field gets absorbed by the semiconducting material. In a stack of several materials, which a solar cell usually consists of, there are multiple interfaces from which the incident electromagnetic waves are reflected or transmitted into and throughout the layers. Fresnel equations, fully consistent with the rigorous electrodynamics framework of Maxwell, describe the behaviour of light at the interface and consequently can be used to find the field intensity and change of field propagation direction within two media. The complex Fresnel coefficients for reflection and transmission can be derived with Snell's law and depend on the polarization of the incidence waves. For light with the field perpendicular to the plane of incidence (s-polarized) we get for the interface between layer *j* and layer *k*:

$$r_{jk}^{s} = \frac{q_j - q_k}{q_j + q_k} \tag{2.37}$$

and for the case of light with the field parallel to the plane (p-polarized) we get:

$$r_{jk}^{p} = \frac{\tilde{n}_k^2 q_j - \tilde{n}_j^2 q_k}{\tilde{n}_k^2 q_j + \tilde{n}_j^2 q_k} \tag{2.38}$$

$$t_{jk}^{p} = \frac{2\tilde{n}_j \tilde{n}_k q_j}{\tilde{n}_k^2 q_j + \tilde{n}_j^2 q_k} \tag{2.39}$$

With

$$q_j = \tilde{n}_j cos\theta_j = \left[\tilde{n}_j^2 - n_0^2 sin{\theta_0}^2\right]^{1/2} \tag{2.40}$$

where $\tilde{n} = n + ik$ is the complex refractive index, θ_j is the angle of refraction in layer *j*, n_0 is the refractive index of the ambient medium and θ_0 is the angle of incidence.

The transfer matrix method now allows us in an elegant way to generalize the Fresnel equations into a stack of multiple layers of different materials by using linear algebra[26]. If we consider a stack of *m* layers between a semi-infinite ambient medium from which the plane electromagnetic wave propagates and a semi-infinite ambient medium (see Figure 2.10), where layer *j* (where *j = 1,2,..,m)* has a thickness d_j and the material specific wavelength dependent refractive index $\tilde{n}_j(\lambda)$.

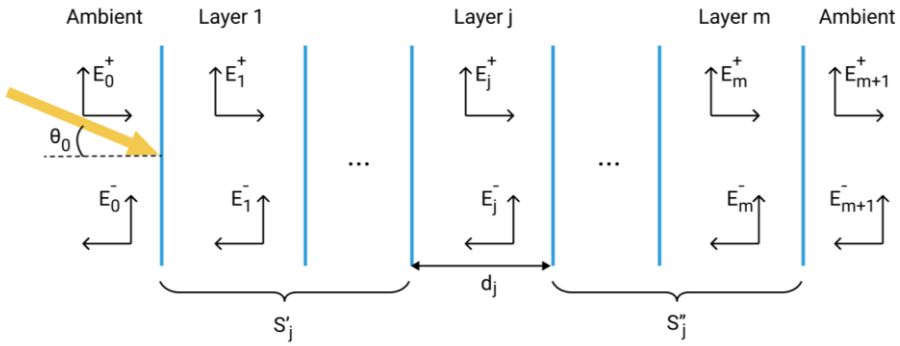


Figure 2.10: Multilayer structure of m layers being surrounded by ambient and showing propagating forward and backward travelling electric fields.

We can resolve the electric field, described by its forward and backward propagating components $\boldsymbol{E}_j^+(x)$ and $\boldsymbol{E}_j^-(x)$ at every position *x* within layer *j*. In a first step, we define an interface matrix at every interface of the multilayer stack:

$$\boldsymbol{I_{jk}} = \frac{1}{t_{jk}}\begin{bmatrix} 1 & r_{jk} \\ r_{jk} & 1 \end{bmatrix} \tag{2.41}$$

Furthermore, we introduce a layer matrix describing the propagation through layer *j* by:

$$\boldsymbol{L_j} = \begin{bmatrix} e^{-i\xi_j d_j} & 0 \\ 0 & e^{i\xi_j d_j} \end{bmatrix} \tag{2.42}$$

where $\xi_j d_j$ is defined as the phase shift that acts on the plane travelling though layer *j*, and ξ_j being defined as:

$$\xi_j = \frac{2\pi}{\lambda} q_j \tag{2.43}$$

We can formulate a total system transfer matrix[27], which relates the electric fields at both ends of the multilayer by:

$$\begin{bmatrix} E_0^+ \\ E_0^- \end{bmatrix} = \boldsymbol{S} \begin{bmatrix} E_{m+1}^+ \\ E_{m+1}^- \end{bmatrix} \tag{2.44}$$

$\boldsymbol{S}$ is then defined as:

$$\boldsymbol{S} = \begin{bmatrix} S_{11} & S_{12} \\ S_{21} & S_{22} \end{bmatrix} = \left(\prod_{v=1}^{m} \boldsymbol{I_{(v-1)v}} \boldsymbol{L_v} \right) \cdot \boldsymbol{I_{m(m+1)}} \tag{2.45}$$

Now it is possible to calculate the complex reflection and transmission coefficients of the entire stack by using the calculated scattering matrix elements:

$$r = \frac{E_0^-}{E_0^+} = \frac{S_{21}}{S_{11}} \tag{2.46}$$

$$t = \frac{E_{m+1}^-}{E_0^+} = \frac{1}{S_{11}} \tag{2.47}$$

If we are now interested in the internal electric field of layer *j*, we describe the partial system of transfer matrices that relates the left boundary electric fields $E_0^{+,-}$ with the right boundary electric fields $E_j'^{+,-}$ by:

$$\begin{bmatrix} E_0^+ \\ E_0^- \end{bmatrix} = \boldsymbol{S_j'} \begin{bmatrix} E_j'^+ \\ E_j'^- \end{bmatrix} \tag{2.48}$$

$$\boldsymbol{S_j'} = \begin{bmatrix} S_{j11}' & S_{j12}' \\ S_{j21}' & S_{j22}' \end{bmatrix} = \left(\prod_{\boldsymbol{v=1}}^{\boldsymbol{j-1}} \boldsymbol{I_{(v-1)v} L_v} \right) \cdot \boldsymbol{I_{(j-1)j}} \tag{2.49}$$

and

$$\begin{bmatrix} E_j''^{+} \\ E_j''^{-} \end{bmatrix} = \boldsymbol{S_j''} \begin{bmatrix} E_{m+1}^{+} \\ E_{m+1}^{-} \end{bmatrix} \tag{2.50}$$

$$\boldsymbol{S_j'} = \begin{bmatrix} S_{j11}'' & S_{j12}'' \\ S_{j21}'' & S_{j22}'' \end{bmatrix} = \left(\prod_{\boldsymbol{v=j+1}}^{\boldsymbol{m}} \boldsymbol{I_{(v-1)v} L_v} \right) \cdot \boldsymbol{I_{m(m+1)}} \tag{2.51}$$

Now we can find again the complex reflection and transmission coefficients for layer *j* by using the partial matrix elements:

$$r_j' = \frac{S_{j21}'}{S_{j11}'} \tag{2.52}$$

$$t_j' = \frac{1}{S_{j11}'} \tag{2.53}$$

$$r_j'' = \frac{S_{j21}''}{S_{j11}''} \tag{2.54}$$

$$t_j'' = \frac{1}{S_{j11}''} \tag{2.55}$$

The linearity of the system now allows us to combine the coefficients to relate the two incident plane waves in forward and backward propagating direction to the internal electric field in layer *j* at the interface (*j-1*) and *j*:

$$t_j^{+} = \frac{E_j^{+}}{E_0^{+}} = \frac{t_j'}{1 - r_{j-}' r_j'' \cdot e^{i2\xi_j d_j}} \tag{2.56}$$

$$t_j^{-} = \frac{E_j^{-}}{E_0^{+}} \frac{t_j' r_j'' e^{i2\xi_j d_j}}{1 - r_{j-}' r_j'' \cdot e^{i2\xi_j d_j}} = t_j^{+} r_j'' \cdot e^{i2\xi_j d_j} \tag{2.57}$$

Finally, we arrive at the description of the total electric field at position *x* (for $0 \leq x \leq d_j$) within a layer *j* by:

$$E_j(x) = E_j^+(x) + E_j^-(x) = \left[t_j^+ e^{i\xi_j x} + t_j^- e^{-i\xi_j x}\right] E_0^+ \\ = t_j^+ \left[e^{i\xi_j x} + r_j'' e^{i\xi_j (2d_j - x)}\right] E_0^+ \tag{2.58}$$

Or in terms of S-matrix elements:

$$E_j(x) = \frac{S_{j11}'' \cdot e^{-i\xi_j (d_j - x)} + S_{j21}'' \cdot e^{i\xi_j (d_j - x)}}{S_{j11}' S_{j11}'' \cdot e^{-i\xi_j d_j} + S_{j12}' S_{j21}'' \cdot e^{i\xi_j d_j}} E_0^+ \tag{2.59}$$

In order to calculate the fraction of absorbed light within layer *j*, we can use the electric field intensity $\left|E_j(x)\right|^2$ to describe the dissipated energy at position *x*:

$$Q_j(x) = \tfrac{1}{2} c \epsilon_0 \alpha_j n_j \left|E_j(x)\right|^2 \tag{2.60}$$

where c is the speed of light, ϵ_0 is the permittivity of free space and α_j the absorption coefficient:

$$\alpha_j = \frac{4\pi k_j}{\lambda} \tag{2.61}$$

An introduction of the complex pointing vector definition for the forward and backward propagating electric fields can lead to a simple calculation of the energy reflectivity (*R*) and transmittance (*T*) for different polarization directions. Furthermore, the treatment of incoherent layers in a multilayer stack requires the substitution of the electric field with its amplitude square $U = |E|^2$ and was rigorously developed as a generalized matrix method by Centurioni[28], which the reader is referred to for a complete explanation.

2.2.4 Solar radiation

The energy, and therefore the photon flux, emitted from the sun at its surface can be described with already introduced Planck's law (stated in equation 2.33). As we are interested how much of this energy reaches the earth, we introduce a geometrical factor

$F_S = \pi * sin^2\theta_{sun}$, which accounts for the angular integration over the emitting hemisphere from the sun and the angle θ_{sun} of the part that can be seen from the earth:

$$\phi_{sun}(E) = \frac{F_S}{4\pi^2\hbar^3c^2}\frac{E^2}{exp\left(\frac{E}{k_BT_0}\right)-1} \qquad (2.62)$$

As θ_{sun} is very small (0.26°), the irradiance from the sun emitted at 5760 K loses a lot of its initial power, which is then very close to the values we can measure at the surface of the atmosphere of the earth (shown in Figure 2.11).

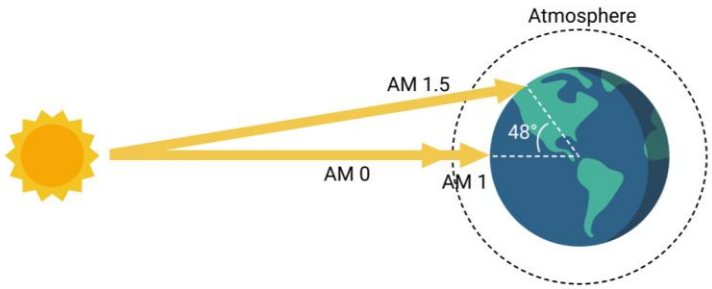


Figure 2.11: Illustration of solar irradiation with different air mass values.

The atmosphere, due to its high density of gases and particles, plays a crucial role for the filtering of the solar spectrum at the surface of the earth. Therefore, we quantify this attenuation by defining the air mass factor (*AM*) as a fraction of the optical path length to the sun and the optical path length if the sun was directly overhead, in other terms:

$$AM = cosec\ \psi_{sun} \qquad \textbf{(2.63)}$$

Where ψ_{sun} is the solar elevation angle. The standard we have defined for very typical air mass conditions is $AM_{1.5}$, or $\psi_{sun} = 42°$. As the integrated solar spectrum (by using the Stefan Boltzmann law) would then only yield around 900 W/m^2, the standardised $AM_{1.5}$ spectrum is normalised to 1000 W/m^2. This spectrum is crucial for the classification of solar cells because it is used to determine the power conversion efficiency under "standard conditions".

Real world conditions differ substantially from the $AM_{1.5}$ spectrum and vary permanently in time. Depending on the location and the weather situation, the sun positional changes, appearing clouds can partially block and scatter the solar radiation and different chemical compositions in the local atmosphere might also have an impact. To demonstrate this effect, Figure 2.12 shows the possible variations of the solar irradiance spectrum by making visible the effects of wavelength dependent reflection from clouds or other atmospheric particles that can result in shifts of the radiative power. The ratio of both spectra shows that the scaling of power is far from constant over the wavelength spectrum.

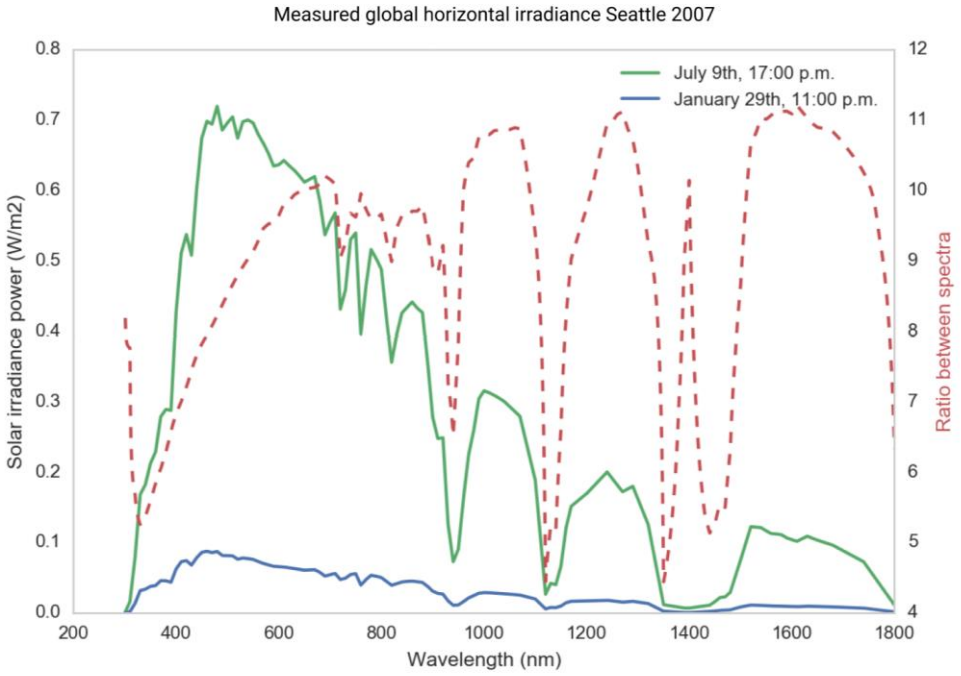


Figure 2.12: Plot of global horizontal irradiance spectra and their ratio at two different times in Seattle 2007.

The position of the sun on the sky dome (defined by solar elevation α and azimuth angle φ as illustrated in Figure 2.13) can be calculated at every moment of the year by using the latitude (LAT) and the vertical altitude of the installation site via[29,30]:

$$\alpha = sin^{-1}[sin\,\delta\,sin\,LAT + cos\,\delta\,cos\,LAT\,cos\,HA] \tag{2.64}$$

$$\varphi = cos^{-1}\left[\frac{sin\,\delta\,cos\,LAT - cos\,\delta\,sin\,LAT\,cos\,HA}{cos\,\alpha}\right] \tag{2.65}$$

Where δ is the solar declination coming from the tilt of the earth and can be approximated to about 1° accuracy with the day number of the year (d):

$$\delta = sin^{-1}[.39795 * cos[.98563 * (d - 173)]] \tag{2.66}$$

Furthermore, HA is the solar hour angle, which is found with the solar time t_s:

$$HA = 15(t_s - 12) \tag{2.67}$$

The solar time is based on the standard time for which the sun points directly south at 12:00 o'clock. Consequently, this depends on the geographical longitude, as the solar time will vary substantially within the same time zone and a correction algorithm can be found in literature[31].

Modelling the local time depending solar irradiance spectra is hardly possible since real world weather conditions are impossible to predict. Several semi-empirical models were developed[32,33] that take multiple measured parameters as input to model the clear-sky or even overcast-sky irradiance spectra. Nowadays many meteorological gaging stations exist around the world which measure the solar irradiance accurately with pyranometers. The irradiance is defined by three components that help to describe the composition. Global horizontal irradiance (GHI) is the total irradiance that reaches a flat plane over the entire hemisphere. One part of the GHI comes from diffuse horizontal irradiance (DHI), which is comprised of the direction-less diffuse light which stems from scattered light by the atmosphere and is summed over the entire hemisphere onto a flat plane. The other part comes from the direct normal irradiance (DNI), which describes the beam irradiance that is radiating directionally from the sun onto a plane directly pointed at the sun. Generally

direct irradiance is significantly higher than the diffuse component but it depends on the location.

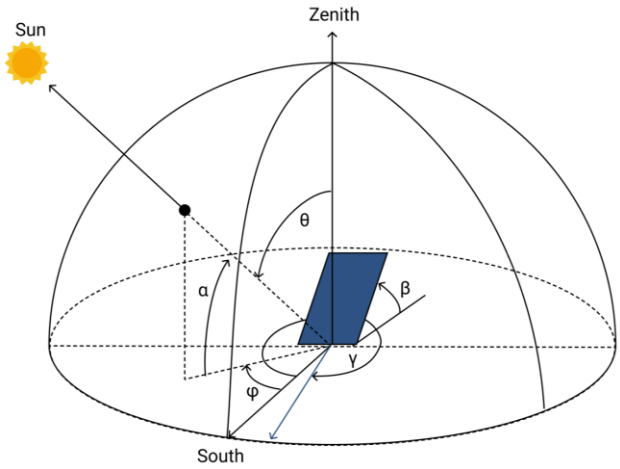


Figure 2.13: Illustration of the sky dome with descriptive angles for solar position and panel orientation and tilt.

The absorption characteristic of a solar panel at larger solar incidence angles depends on the refractive index of the material due to reflections but generally it is advantageous to tilt the panel optimally towards the sun. Anti-reflective coating can help to overcome this effect and is heavily used for Silicon solar cell applications due to the non-ideal refractive index. Furthermore, Lambert's cosine law states that the irradiance reaching the panel will be reduced by the cosine of the angle of incidence:

$$I_{surface} = I_{beam} \cos\theta \tag{2.68}$$

For this reason, the use of tracking systems can have a very beneficial impact on performance for deployed solar panels. As generally the cost of such systems is high, several designs were developed that track either one or two axes. The different concepts are presented in Figure 2.14. One-axis trackers can have three different designs, either a fixed tilt angle with rotation around the vertical axis, a horizontal rotation axis, or a tilted rotation axis. The ideal tilt and rotation angles are depending on the location and time are well described in literature[30].

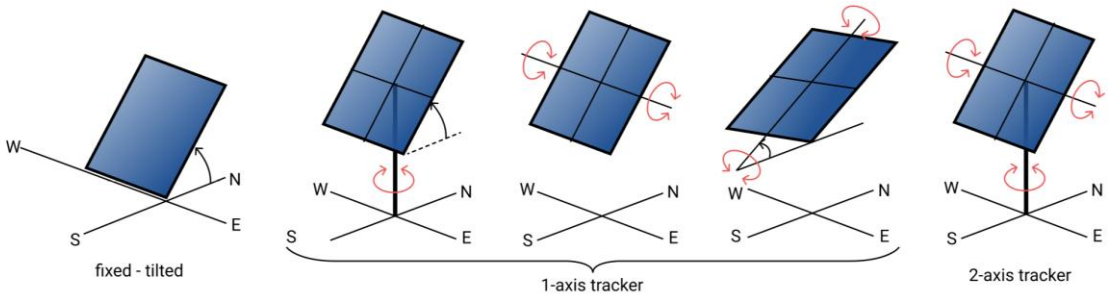


Figure 2.14: Illustration of fixed, 1-axis and 2-axis solar panel tracking systems.

These systems have been reported to have annual energy yield improvements of over 30 % for 1-axis trackers and over 40 % for 2-axis trackers[34]. Specifically, 2T tandem solar cells are benefitting from tracking systems due to the performance loss from unmatched currents at varying angles. This will be further discussed in Chapter 7.

The diffuse light spectrum is more complex than the direct beam irradiance, as it is distributed over the entire sky dome. Many models have been developed to describe it in more detail[35–39]. Most models assume that the diffuse light irradiance is comprised of four components. The isotropic irradiance from the entire sky dome ($I_{d,iso}$), the concentrated circumsolar radiation around the sun from the forward scattered light ($I_{d,cs}$), brightened radiation around the horizon ($I_{d,hb}$) and reflected radiation from the ground ($I_{d,g}$) in case the panel is tilted:

$$I_d = I_{d,iso} + I_{d,cs} + I_{d,hb} + I_{d,g} \tag{2.69}$$

Simple models assume an isotropic distribution of radiation over the hemisphere[35,37]. Logically the intensity of radiation depends on the solar position, position on the sky-dome and the atmospheric conditions and should therefore be described as anisotropic[38,40,41]. Currently the semi-empirical Perez model[42,43] is accepted as a good description of diffuse irradiation. Alternatively to modelling the total DHI, the development of a distributed radiance model over the hemisphere is crucial when performing energy yield calculations, as the solar cell's performance depends strongly on the angle of incidence of the light

beam. Brunger and Hooper[44] introduced a semi-empirical model, which allows to determine the radiance $L(\theta,\varphi)$ depending on the position of the sun, the cloud ratio k (fraction of DHI to GHI) and the clearness index k_t (fraction of GHI to horizontal extra-terrestrial irradiation) as:

$$L(\theta,\varphi) = DHI\left[\frac{a_0 + a_1\cos\theta + a_2 exp(-a_3 * \Psi)}{\pi\left(a_0 + \frac{2a_1}{3}\right) + 2a_2 I(\theta_s, a_3)}\right] \qquad (2.70)$$

The coefficient a_0 accounts for the constant isotropic component, the horizontal brightening and the circumsolar irradiance are modelled with a cosine function and an exponential function respectively. The fitting coefficients a_0, a_1, a_2, a_3 are tabulated for corresponding values of k and k_t. Ψ is the angular distance between the direction of the sun and the direction of the sky dome element, which is simply calculated with the two pairs of positioning angles. Furthermore, $I(\theta_s, a_3)$ is a function also simply evaluated with the use of all previously mentioned parameters and can be found in the corresponding publication. Figure 2.15 shows a typical anisotropic distribution of radiance over the entire hemisphere modelled with the Brunger model.

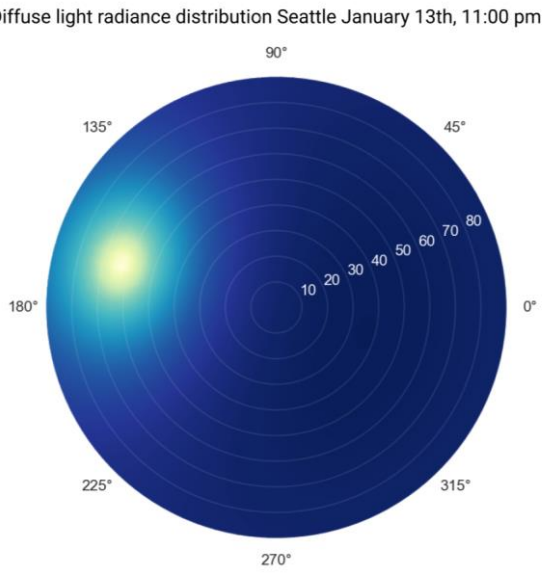


Figure 2.15: Typical normalized diffuse light radiance distribution over sky dome.

2.3 Perovskite Solar Cells

Perovskite is the name for the class of materials that adopt the same crystal structure as calcium titanate ($CaTiO_3$). This general ABX_3 structure, as shown in Figure 2.16, consists of a cation A, a second but smaller cation B and is surrounded by octahedra of X anions. The stable three-dimensional ABX_3 can only be formed if the components fulfil certain size criteria. For that reason, a tolerance factor t has been introduced[45], which takes the ionic radii ($r_{A,B,X}$) of the molecules into account:

$$t = \frac{r_A + r_B}{\sqrt{2}(r_B + r_x)} \qquad (2.71)$$

This tolerance factor can be used to characterize the structural stability of the crystal lattice. The closer the value is to 1, the more stable it will be, but it has been observed that values between 0.8 and 1 lead to the typical cubic structure, values between 0.7 and 0.8 lead to formations of the lower symmetry lattices with tetragonal, trigonal, rhombohedral and hexagonal structures. Tolerance factors greater than 1 usually lead to the formation of two-dimensional sheets of B-X octahedra that are separated by the A cations. Most perovskites currently used for photovoltaic applications and talked about in this thesis contain the organic $CH_3NH_3^+$ (methylammonium or MA), $H_2NCNH_2^+$ (formamidinium or FA) or the inorganic Cs^+ or combinations of all of them as A cations. B site cations are usually Pb_2^+ or Sn_2^+ and the X site halides most commonly used are I^-, Br^-, Cl^-.

Many more perovskites have been investigated and showed a plethora of advantageous material properties including high static stabilities, superconductivity, anti-ferromagnetism and thermoelectricity. The search for solution processable semiconductors lead Mitzi et al.[45] in the early 90's to carry out extensive research on the semiconducting and opto-electronic characteristics of organic-inorganic perovskite materials.

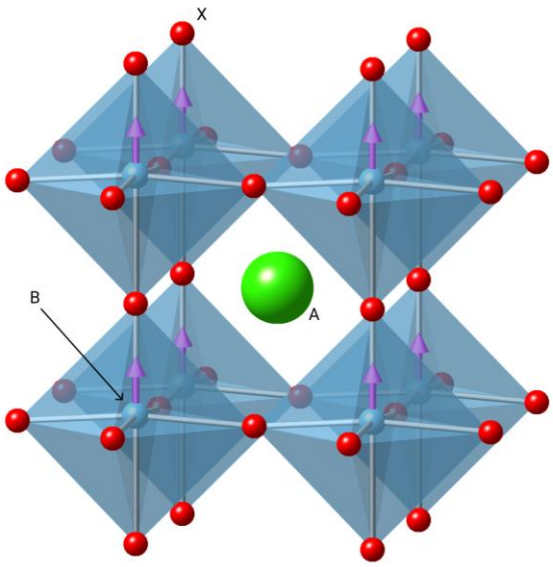


Figure 2.16: Cubic ABX_3 perovskite crystal structure.

It was discovered that these materials exhibit string excitonic features, which could lead to light emitting-diodes and solar cell applications. While various deposition methods through solution, two-step conversion or vapour sublimation have been developed and are currently being reused, the focus was mainly set on the two-dimensional layered perovskite films and a thin-film solar cell remained to be demonstrated for almost two more decades.

The first perovskite solar cells appeared between 2006 and 2009[46,46,47] through the efforts to replace the dye in dye sensitized solar cells by the strongly absorbing hybrid perovskites $CH_3NH_3PbI_3$ or $CH_3NH_3PbBr_3$ as light absorbing layer in combination with iodide triiodide electrolytes. The rapid degradation of the perovskite absorber due to dissolution in the liquid electrolyte hindered remarkable device performances. The big breakthrough came about with the replacement of the liquid electrolyte by a solid-state hole conductor. Almost simultaneously Kim et al.[48] and Lee et al.[49] developed stable perovskite solar cells with power conversion efficiencies around 10% by using (2,2(7,7(- tetrakis- (N,N-di-pmethoxyphenylamine)9,9(-spirobiuorene) (short spiro-OMeTAD) as hole-transporting material. The remarkable discovery by Lee et al. was that an insulating mesoporous oxide scaffold (Al_2O_3) would lead to equally well performing devices as by using the well-known

semiconducting TiO_2 mesoporous scaffold, essential for the electron extraction in dye sensitized solar cells[50]. This suggested long diffusion lengths within the bulk of the perovskite thin-film, which were later quantified via photoluminescence (PL) time decay measurements to be on the order of 1 µm[51,52] and allowed the evolution of planar heterojunction devices, away from the original architecture with mesoporous oxide scaffolds[53,54] (see Figure 2.17). The planar heterojunction design removes a lot of the fabrication complexities and together with the flexibility of perovskite materials to be easily deposited via solution processes or various vapor deposition techniques, this presents a very promising route to commercialization.

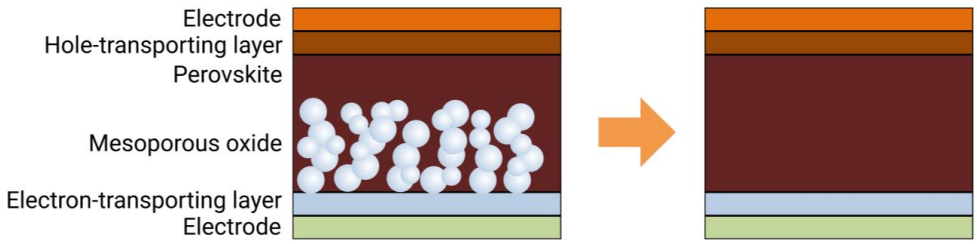


Figure 2.17: Evolution from mesoporous oxide based architecture to planar heterojunction architecture of perovskite solar cells.

The origin of the long diffusion lengths was investigated to come from exceptionally high electron and hole mobilities close to the value of 20 $cm^2V^{-1}s^{-1}$ [55–58], as well as low radiative and non-radiative recombination rates[56]. Apart from the long diffusion lengths and the short absorption depths on the order of 100 - 200 nm[51,52], the introduced perovskite materials show more semiconductor properties that qualify them as almost ideal materials for solar cells. Slow charge recombination rates ensure a high open circuit voltage relatively close to the maximum achievable voltage in the radiative limit[59,60]. Furthermore, the small Urbach energies that have been reported[61], point towards a low energetic disorder and allow again for higher achievable voltages. The exciton binding energy, which defines how much energy is needed to split the electron-hole charge pair apart once it was generated, was optically determined with big variations to be in the wide range of 2-

150 meV[62–66]. Recent rigorous magneto-optic measurements by Miyata et al. supported the small values of only a few meV at room temperature[67]. Since this is well below the thermal energy at room temperature (ca. 26 meV) we can assume that most photoexcited carriers are present as free charge and not as excitons, which is the case in organic photovoltaic materials.

Another extraordinary property of perovskites is the possibility to change the bandgap by introducing different compounds into the crystal lattice. It was shown early on that the bandgap can be increased from the ca. 1.55 eV of the common $CH_3NH_3PbI_3$ by replacing some of the halide sites with Br^- [68] and additionally changing the A cation with FA^+ [69]. A similar effect into the opposite direction (decreasing the bandgap) was discovered by introducing different Sn^- concentrations[70,71]. The problems revealed with these X site mixtures was that they lead to some instabilities within the crystal and would either not form stable films, or degrade within short periods of time. Later the introduction of Cs^+ and FA^+ at the right concentrations would lead to much better intrinsic stability of the perovskite films at almost perfectly adjustable bandgaps in the high[72–74] and the low energy region[75].

A plausible working principle of perovskite solar cells can be explained with a p-i-n junction (as introduced in section 2.1.3), in which perovskite represents the relatively thick intrinsic layer in which most of the light is absorbed and the excited charge pairs are separated instantly as an effect of the low exciton binding energy. Due to this high injection concentration of free charge carriers, the electric field is screened throughout most of the perovskite bulk. The charge carriers are mostly driven by diffusion over long distances within the intrinsic layer, which is contacted by the energetically optimally chosen n-type and p-type interface materials that will extract the electrons and respectively the holes and transfer them into the electrodes. A simplified scheme (without band bending and assumed

relative energy levels) is presented in Figure 2.18. It demonstrates the process that the charge pairs undergo from absorption to charge extraction.

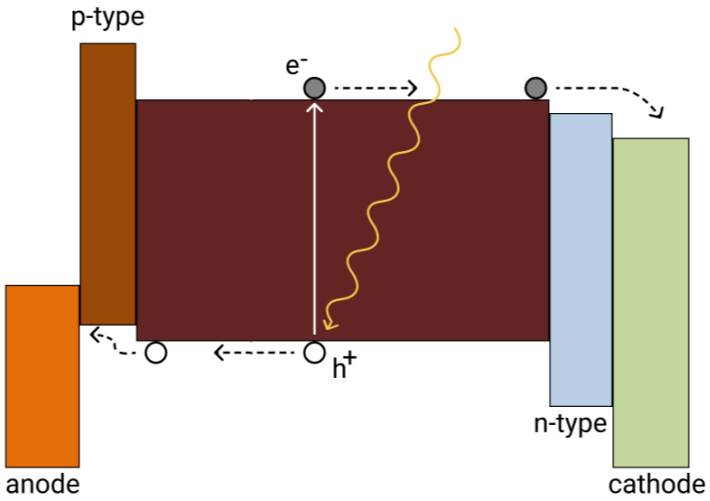


Figure 2.18: Working principle of perovskite solar cell as p-i-n junction.

2.4 Semi-transparent Solar Cells

Photovoltaic cells that convert energy from only partially absorbed sun light and which allow to transmit visible light will have a transparent appearance to the eye. So-called semi-transparent solar cells could represent a very important technology in the future of building integrated photovoltaics as well as the battery charge extension in consumer electronics or vehicles. Therefore, industrial efforts are increasing to introduce such products to the market.

There are currently three different ways of achieving transparent or semi-transparent solar cells, which are shown in the schematic of Figure 2.19. One promising approach makes use of photoactive semi-conducting material that absorb weakly in the wavelength regions of visible light but strongly in the low energy infra-red (IR) or high energy ultraviolet (UV) regions. Organic photovoltaic absorbers[76] and dyes used in dye sensitized solar cells[77] were shown to absorb only light invisible to the human eye. When an IR absorber and a UV absorber are combined in a tandem solar cell (described in the next section), as has been

demonstrated by Chen et al. within a tandem polymer cell achieved 6.4 % efficiency at an average visible transmittance (AVT) of 43 %[78].

Another approach leading to semi-transparent solar applications is realized by employing conventional absorbing materials as very thin films. The reduced thickness leads to a decreased probability of a photon to excite an electron and therefore more photons will be transmitted through the film. As photons with more energy will be more likely absorbed, more of the lower energy photons are transmitted, resulting in a device appearing red coloured. Reports from previous research on semi-transparent perovskite solar cells showed PCEs/AVT ration as high as 10.2 % / 25 %[79] and 7.8 % / 37 %[80] with the use of extremely thin absorbers. In order to fabricate such thin perovskite films with good morphologies, co-evaporation[81,82] or gas assisted spin-coating techniques[83] have to be used.

The third route to develop a semi-transparent solar cell involves a decreased coverage of the active layer to transmit more light. The idea behind it is to structure the active material in micro-scale to decrease the coverage such that a fraction of the photons will pass the areas that are not covered by the semiconductor but small enough to not be visible to the bare eye. The advantage is the colour appearance of such films, which remains neutral coloured due to a flat transmission spectrum[15]. However, the drawback comes from the fact that the uncovered regions between the absorbing domains allow for shunting paths that significantly influence the device performance. Furthermore, scattering of the micro-structured domains needs to be reduced to develop a semi-transparent solar cell with clear view and no haze effect. Successful applications of this design have been reported by Eperon et al. with PCEs up to 5.2 % at AVT of 28 %[15,84] and could be improved by using shunt-blocking layers to 6.1 % PCE with 38 % AVT[85]. Chapter 5 will describe this development in much detail.

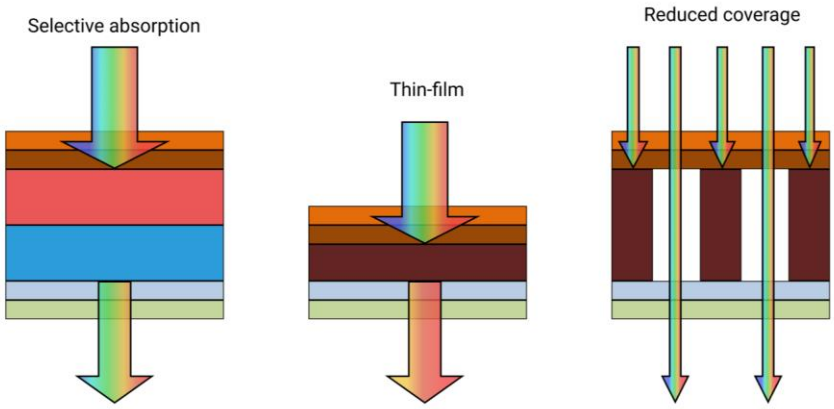


Figure 2.19: Schematic of different semi-transparent solar cell design concepts with selective absorption layer, thin-film absorber and reduced coverage absorbing layer.

All the above stated technologies only lead to transparent solar cells if the other layers in the device are equally highly transparent. This can be a challenging problem in case of the charge conducting electrodes which often come with the trade-off between increased sheet resistance and high transmittance. Despite the use of transparent conducting oxides such as ITO, micro-meshes of nickel[86], Ag[87] and spray coated silver nanowires[80] were shown to be promising solutions as well.

2.5 Tandem Solar Cells

The thermodynamic efficiency limit of single junction solar cells has been derived with the balanced equilibrium theory, introduced in Section 2.2.2, to equal 33.7 %. There are several methods to surpass this efficiency by either increasing the concentration of radiation with Fresnel lenses or by reducing the kinetic energy loss of electrons due to photons that have higher energies than the bandgap of the absorbing semiconductor. One practical approach is the introduction of multiple absorbers with different band-gaps to absorb photons with different energies. While this effect can be made possible via spectral splitting with dichroic mirrors onto different absorbers, a more convenient method is to stack different band-gap absorbers vertically.

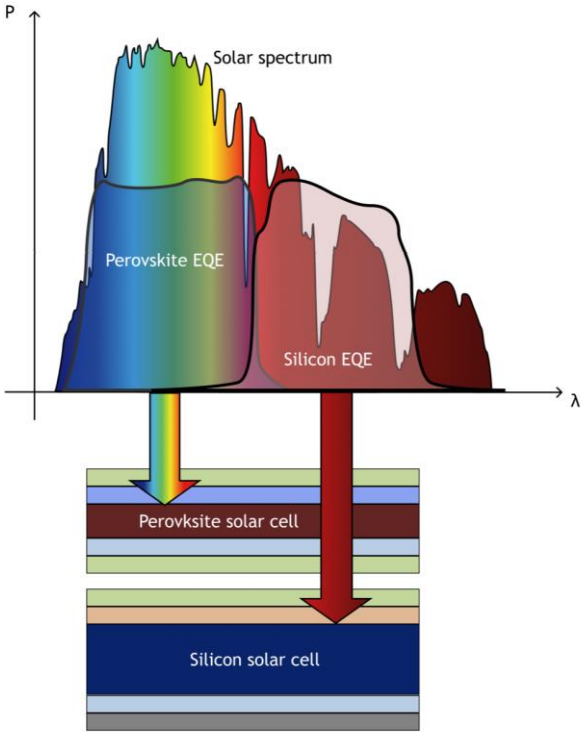


Figure 2.20: Concept of tandem solar cell in which a perovskite solar cell absorbs within the low wavelength region and the silicon solar cell in the high wavelength region of the solar power spectrum.

The spectral response of typical complimentary wide and narrow bandgap absorbers (in this case perovskite and silicon solar cells) is shown together with the solar power spectrum in Figure 2.20.

In case two absorbing layers are implemented into a tandem solar cell, two architectures for the interconnection of the layers are common (shown on Figure 2.21): In the four-terminal (4T) architecture the two absorbers are independently electrically connected and can therefore be optimised individually to yield the highest efficiency. However, an easier design can be achieved within a two-terminal (2T) architecture by connecting the two cells together in series. This design requires the matching of currents to operate at optimal conditions and is therefore difficult to maximize in real world conditions. Despite the simplicity due to the absence of two additional transparent electrodes, the electronic

material optimization becomes challenging due to the need of a so called tunnel junction or recombination layer between the semiconductors.

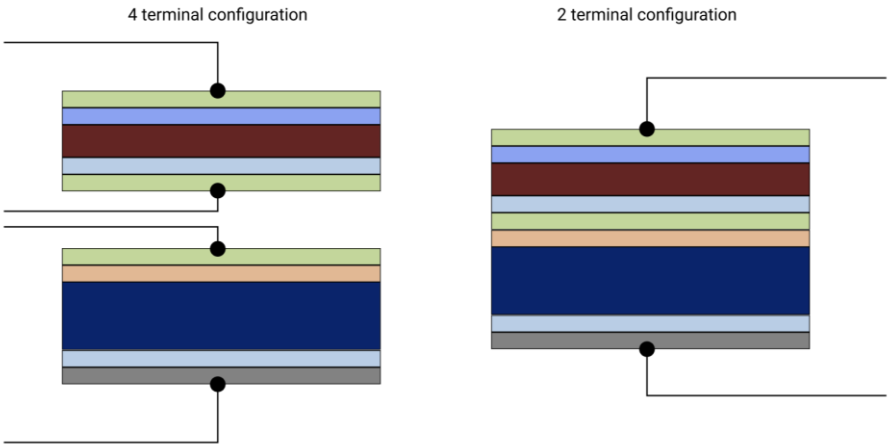


Figure 2.21: Four terminal and two terminal tandem solar cell configurations.

Detailed balance theory can be used to calculate the efficiency limits that are possible to achieve with the tandem device architectures[21,88]. When assuming perfect spectral splitting, the maximum efficiency for different bandgap combinations in a 4T configuration is plotted on the left of Figure 2.22 and demonstrates that a PCE of up to 46 % is achievable with bandgaps of 0.93 eV and 1.73 eV. Analogously, in a 2T configuration the currents need to be matched and due to reduced numerical resolution of the bandgaps, the voltages are not set at the absolute maximum power point, which leads to slightly smaller efficiencies and a different optimal bandgap combination for the absorbing layers as depicted on the right in Figure 2.22. However, in reality, spectral splitting is not perfect and depends on the absorption tails of the absorbing semiconductors, furthermore recombination losses are common and reported record performances are substantially lower at around 31 %[14,89]. Chapter 7 will discuss the real world implications of tandem solar cells in more detail.

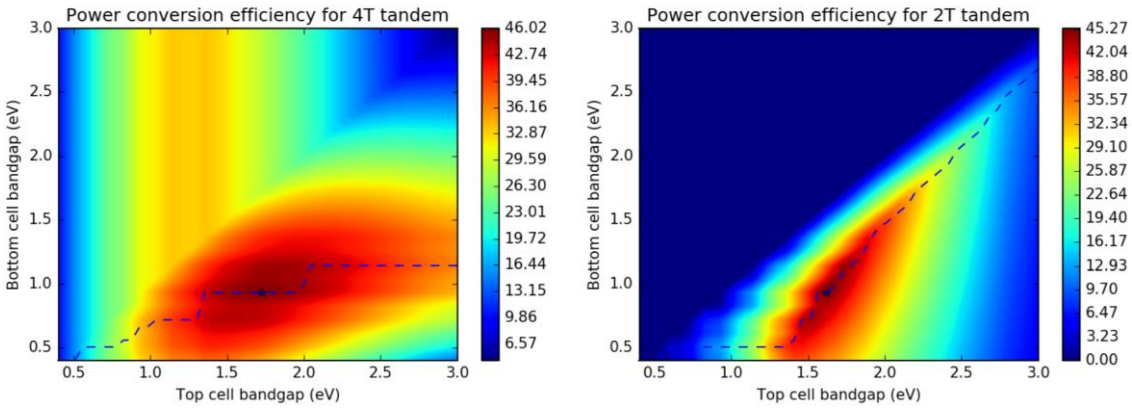


Figure 2.22: Combined tandem power conversion efficiency for different top cell and bottom cell bandgap combinations in 4T and 2T configurations.

2.6 Back Contact Solar Cells

The intuitive design choice for thin-film solar cell devices includes the anode and cathode electrodes to be connected in a layered manner due to the relatively short diffusion lengths and short enough absorption depth of the semiconducting materials. The charges that are generated within an inner absorbing layer are extracted through electrodes at the top and the bottom of the solar cell stack. Since the light is typically entering the stack from the top or from the bottom, one of the electrodes is required to allow a maximum number of photons to pass. In short diffusion length materials (most thin-film solar cells), this is generally achieved with the use of transparent conductive oxides. Materials with longer diffusion lengths allow for metal electrode grids that cover a minimum area to reduce shading losses but offer lower resistance. This has been for a while and still is the most common design for silicon solar cells on the market. The trade-off between maximizing the transmission of light into the device while maintaining large enough conductivity to not induce series resistance losses played an important role for device designs that are used in modules.

An alternative device architecture incorporates both electrodes on the back side, opposite of the radiation side, as shown in Figure 2.23. This leads to minimized shading and reflection losses that would come from front contacts and allow at the same time to cover almost the entire backside area with conductive electrodes[90]. As all charge collection components are placed on the backside, a closely packed interconnection of modules is possible, which all leads to enhanced overall efficiencies. Another substantial benefit of the use of rear contacts comes from the reduced contact area that these electrodes take up, which leads to lower recombination velocities at the interface and allows to optimally passivate all other surfaces to minimise surface recombination and therefore lead to higher performances. Originally this design was invented by Schwartz et al.[91] in 1975 for concentrated solar cells in which the series resistance effect and surface recombination plays an even more import role due to higher photo current densities and larger charge carrier concentrations. Due to the advantages of back contact solar cells, all recent record efficiencies of silicon solar cells were achieved with such a design[92–94]. Specifically the recently reported record efficiency of 26.33 % from Kaneka Corporation was realised with a back contacted architecture in combination with the well absorbing heterojunction with intrinsic thin-layer (HIT) silicon solar cell design[95].

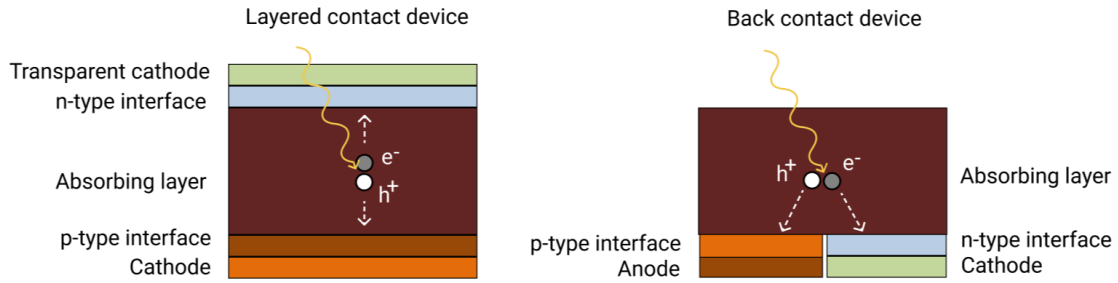


Figure 2.23: Schematic comparison of layered contact and back contact solar cell.

Implications of this design need to be considered and hence when photons are absorbed in the top region close to the surface of incidence, a long diffusion length is required to

efficiently transport all the charges to the back contacts. Highly crystalline materials with low defects are needed for this matter so that recombination in the bulk is hindered. One of the main limiting aspects on the performance of back contacted silicon devices is non-radiative recombination, which is dominated by the lifetime of minority carriers. In crystalline silicon, a typical film needs a thickness in the order of 100 µm to achieve effective absorption in the active material. This puts a strain on the necessary high quality of crystalline silicon, for it needs to allow excitations to travel all the way to the back electrodes with minimal recombination. Solutions for this have been found, such as the emitter wrap through design developed by Gee et al.[96]. This reduces the average distance that a minority carrier needs to travel to reach an electrode. Furthermore, surface recombination velocities play an important role and to suppress these, passivation techniques need to be applied. These specific requirements are not fulfilled by many materials or would require difficult fabrication processes on shorter length scales, which would explain the few demonstrations of other back contacted solar technologies. However, there have been reports of demonstrations in CdS/CdTe[97–99], dye sensitized[100], and even organic photovoltaics[101]. Perovskites fulfil some of the requirements and Chapter 6 introduces a device architecture that could pave the way for efficient back contacted perovskite solar cells.

2.7 Micro- and Nanolithography Techniques

Since the invention of microchips, methods for the patterning and structuring of materials on the micro- and nano-scale below 100 µm have become extraordinary important, which lead to enormous research efforts in this field. In contrast to macroscopic engineering, the development of simple structures can be very complex, since different physical laws and forces are governing the materials. Additionally, visual aid is limited and requires some special apparatuses. A plethora of solutions has emerged to overcome these difficulties and

most of which can be categorized into so-called bottom-up or top-down techniques[102]. The top-down methods of micro- and nanolithography have become essential for the semiconductor industry as well as many other research fields, because it allows the structuring below 10 nm with extremely high accuracy and through put. Several lithographic techniques, such as UV-photolithography, E-beam lithography, ion-beam lithography, nano-imprint lithography and colloidal lithography[102] have been developed with the same working principle of removing well defined portions of a thin film. The two techniques focused on in this work are UV-photolithography and colloidal lithography.

2.7.1 UV-photolithography

Photolithography describes the process in which UV light is used to expose particular areas of a photo-active thin-film material (resist) to make it either soluble or insoluble to a particular solvent (developer). The most common way to pattern a resist is to use a photomask which allows the UV light to pass only through certain areas. Three different types of photoresist materials exist. Positive resists become soluble in the areas that get exposed. The exposed areas of negative photoresists analogously become insoluble when immersed into the developer. A third type, called image reversal photoresist, needs to be first exposed as a positive photoresist but becomes reversely insoluble upon heat treatment and a second high energy flood exposure. It offers advantages in achieving higher resolution and so called undercut profiles that are advantageous for lift-off processes.

The process steps for masked photolithography of a negative resist with subsequent lift-off are depicted in Figure 2.24. The procedure involves a cleaned substrate (1), which is the basis for the deposition of the resist film that usually needs thermal curing for activation (2), then the exposure through an aligned mask (3), development to dissolve the un-crosslinked volumes (4), evaporation of the metal film (5), and lift-off in a solvent to remove the rest of the resists including the covering metal bits (6).

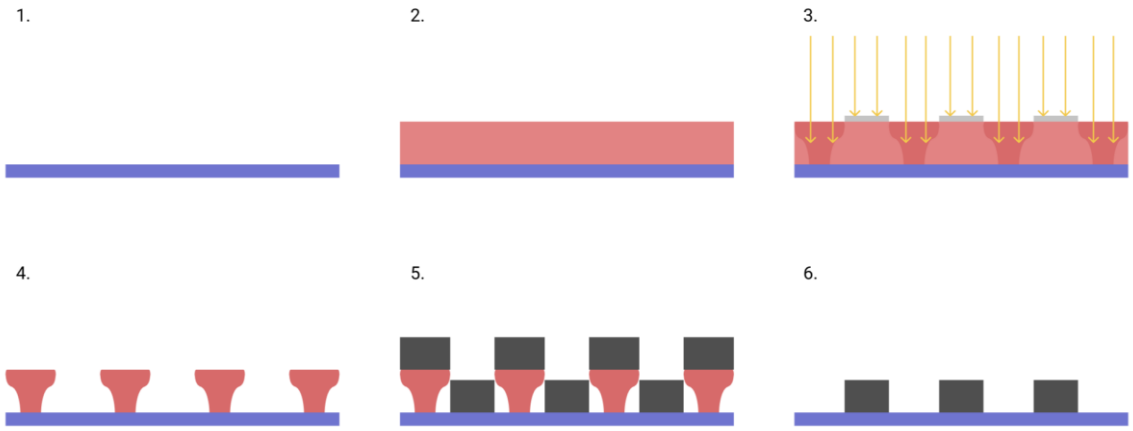


Figure 2.24: Processing steps for patterning metal with negative photoresist.

The resolution of masked photoresists is somewhat limited by the wavelength of the UV light used for exposure. The minimum feature size that is limited by optical diffraction is defined as[103]:

$$l_{min} = k_1 * \frac{\lambda}{NA} \tag{2.72}$$

Where k_1 is the process related factor that includes all precision factors of the process and is usually somewhere around 0.8 in research lab facilities or down to 0.4 in industrial production. λ is the wavelength of the light source and NA is the numerical aperture of the lens as seen from the substrate (it depends on the mask distance). The other competing parameter is the so-called depth-of-focus, which describes the depth into the resist layer for which the exposure radiation is well focused, hence leading to higher resolution. It is defined by:

$$DOF = k_2 * \frac{\lambda}{(NA)^2} \tag{2.73}$$

Here, k_2 is another process specific constant that is usually quoted to equal 0.5. The consequence that follows from the depth-of-focus dependence on the wavelength is the trad-off between reducing wavelengths for higher resolution but sacrificing focal depth at the same time.

The resolution of simple masked photolithography in experimental labs with conventional 365 nm i-line UV light sources and NA of typically 0.35 is limited length scales around 1 µm. This value has been enormously reduced by techniques such as using deep UV light and computational lithography, in which a computer optimizes the exposure diffraction[104]. The microchip industry has introduced methods titled as next generation lithography techniques that include extreme ultraviolet lithography with wavelengths as low as 10 nm to reach for lower resolutions in the order of a few nanometres. Alternatively, electron beams that can be well focused and directed or even X-rays are used for the exposure as they have wavelengths well below the nanometre range. Cost and therefore processing speed are crucial factors for industrial fabrication, which is the reason for the exploration of a promising advancement in which a physical pattern is mechanically pressed into the resist layer, and can be done at single nanometre resolutions with high speeds, even on a roll-to-roll basis[105,106]. This method is known as nano-imprint lithography.

2.7.2 Colloidal Lithography

Colloidal lithography defines the nano-fabrication process that makes use of monolayers of colloidal crystals. Two and three dimensional structures with high periodicity can be patterned though this efficient and inexpensive method. 2D ordered structures are fabricated through the self-assembly of mono-disperse micro- or nano-spheres in hexagonal-close-packed monolayers (MLs) via several strategies. Depending on the microsphere diameter, feature sizes ranging from tens of nanometres to several micrometers[107]. Densely packed monolayers of microspheres can be produced by drop-casting[108], dip-coating[109], spin-coating[110], electrophoretic deposition[111] or water interface transfer of the monolayer onto a substrate[112]. To date, this has been successfully applied in a plethora of fields where precise domain size control is required, including bio-sensing via surface enhanced Raman scattering[113], photonic crystals[114,115], or surface plasmon

applications[116]. The spacing and geometry can be tweaked by the fabrication of non-close packed MLs via etching to shrink the spheres or stretching flexible substrates to increase the distance.

The assembled microspheres can be used as protecting domains in a directional etching process to pattern the underlying substrate. Another typical application for colloidal lithography is the use of the MLs as sacrificial volumes by filling the surrounding spacing with another material to be subsequently patterned by selectively dissolving or decomposing the colloids at high temperatures (the processing steps are visualized in Figure 2.24). This technique enabled the patterning of metal structures via evaporation between the microspheres. Oxides and other materials were structured in a similar manner[117].

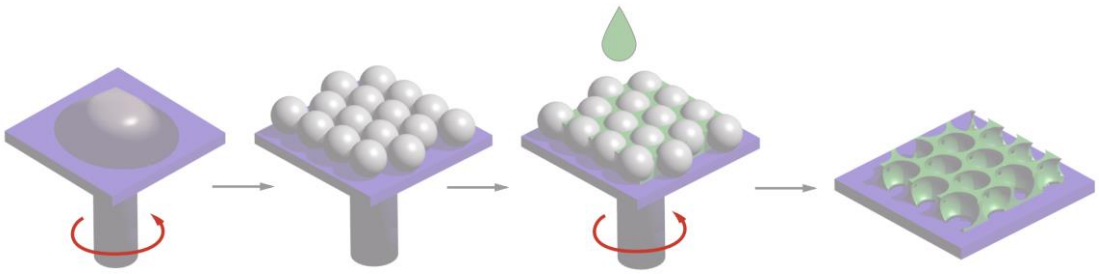


Figure 2.25: Illustration of the processing steps of sacrificial colloidal lithography. A colloidal monolayer and a gap filling material are deposited via spin-coating and subsequently the microspheres are degraded to leave behind a patterned layer.

2.7.3 Self-assembled Monolayers

A self-assembled monolayer (SAM) defines a molecular assembled layer of organic molecules that attaches spontaneously onto a substrate in a pre-defined manner[118]. Such molecules generally consist of a head group that attaches preferentially to the surface of the substrate, a tail carbon atom chain of arbitrary length and an optionally attached functional group (depicted in Figure 2.26). The head groups are strongly bound to the

surface of the substrate by chemisorption, which lowers the surface free-energy of the substrate[119]. This assembly process can happen in the liquid or in the vapour phase and depending on the concentration of molecules and the time duration, a closely packed monolayer forms with the tail groups standing up. Common head groups include silanes, phosphonates or thiols and depending on the chemisorption, strong covalent bonds can be formed.

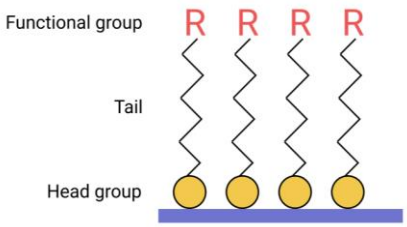


Figure 2.26: Sketch of self-assembled monolayer with head group, tail and functional group.

SAMs are often used for micro- and nano-patterning by using micro-contact printing via pre-patterned elastomeric stamps, by printing them via AFM tips, or by locally removing molecules via scanning tunnelling microscopy, AFM or UV-light (similar to UV-lithography)[120].

3 METHODS

3.1 Perovskite solar cell fabrication

The fabrication of the various perovskite solar cell devices involved different steps that are described in the following sections. Some of the processing steps are optional or interchangeable, depending on the device architecture. The three main different architectures are illustrated in

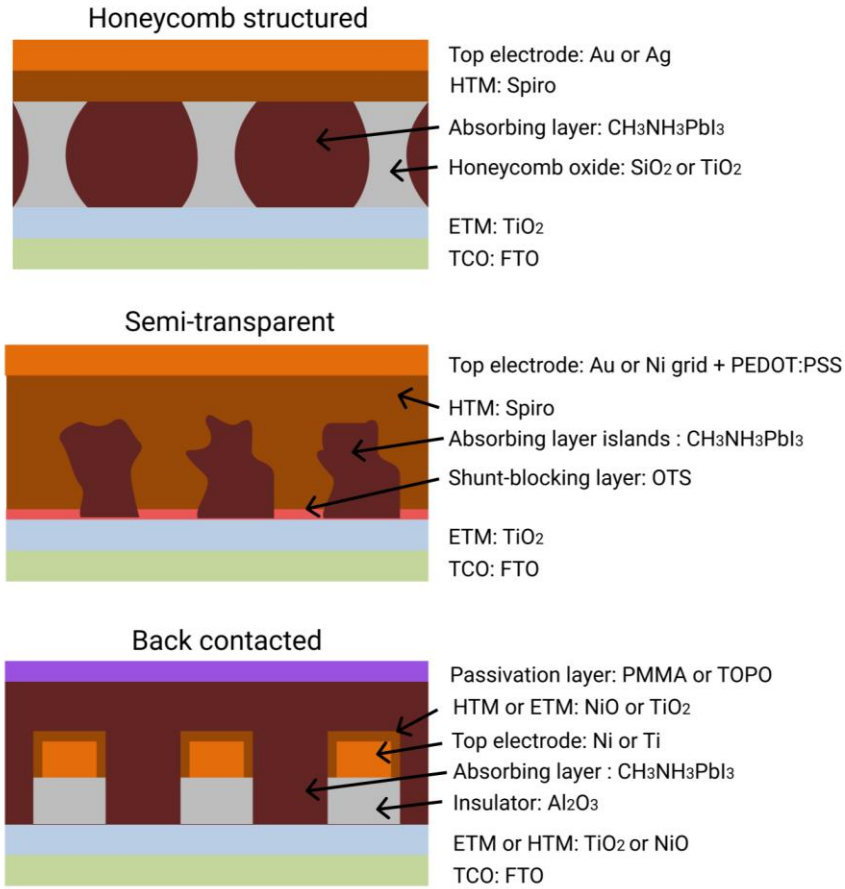


Figure 3.1: Illustration of different device architectures with the included components and corresponding materials used.

3.1.1 Substrate preparation

The glass substrates have been purchased from Pilkington Inc. with a coated fluorinated tin oxide (FTO) layer of 7 or 15 Ω/sq. FTO was partially removed from the substrate via etching with zinc powder and 2 M HCl to create non-conductive stripes for later needed counter-electrode fabrication. The etched substrates were rinsed in deionized (DI) water and cleaned rigorously by brushing Hellmanex solution with a toothbrush before rinsing again in a stream of DI water. N_2 was used to dry the substrates that were then subsequently rinsed in Acetone and 2-Propanol and then etched for 10 min in O_2 plasma.

3.1.2 Bottom n-type or p-type layer deposition

Spin-coated TiO_2 n-type layer:

The n-type TiO_2 compact layer was formed by spin-coating a solution of 0.71 g titanium isopropoxide and 0.07 g of 2 M HCl in 8 ml of Ethanol with 2000 rpm for 45 seconds and then annealed at 500 °C for 45 minutes.

Spin-coated and chemical bath treated SnO_2 n-type layer:

The SnO_2 layer was prepared by following the method described by Anaraki et al.[121]. 0.05 M $SnCl_4 \cdot 5H_2O$ was dissolved over 30 min of stirring in 2-Propanol and then spin-coated in volumes of 200 µl onto the cleaned and etched glass/FTO substrates with 3000 rpm for 30 seconds and 200 rpm/s acceleration. The substrates were then dried for 10 min at 100 °C and 60 min at 180 °C. In the meanwhile, a chemical bath was prepared by mixing 40 ml DI water with 500 mg of urea, 500 µl of HCl (37 wt%), 10 µl of 3-Mercaptopropionic acid and 108 mg of $SnCl_2 \cdot 2H_2O$ (for a final concentration of 0.012 M). The cooled down, spin-coated substrates were then immersed into the chemical bath to be well covered by solution and a lid was placed onto the beaker to prevent evaporation. The

bath was kept at 70 °C within an oven for 180 min and afterwards the samples were sonicated for 2 min in DI water. The substrates were dried under a stream of dry air and then put onto a hotplate at 180 °C for 60 min.

Spray-coated TiO_2 n-type layer:

A uniform TiO_2 compact layer was obtained by initially heating the cleaned and etched glass/FTO substrates to 450 °C on a hotplate. Titanium diisopropoxide bis(acetylacetonate) was diluted in anhydrous Ethanol in a concentration of 1:10 (v:v). 15 ml of this solution was homogenously sprayed with a handpump over the hot substrates that were placed closely together with a total area of 11.4 cm x 22.4 cm. The sprays were carried out by spraying for 10 seconds and then waiting for 20 seconds. The substrates were kept for another 50 minutes at 450 °C and then cooled down slowly over 60 minutes.

Bottom NiO p-type layer deposition:

For the fabrication of inverted devices (light passes through the transparent anode first), the hole-selective p-type layer needed to be deposited onto the glass/FTO substrate. 1 mmol of Nickel Nitrate hexahydrate was fully dissolved in 1 ml of ethylene glycol before 1 mmol of ethylenediamine was added to the solution. The smoke was blown out with compressed air before capping. After shaking the solution vigorously, it was put into a syringe and filtered through a 0.2 µm filter directly onto the substrate to avoid agglomeration. The substrate was spin-coated at 5000 rpm for 50 seconds and then dried at 100 °C on a hot plate for 10 minutes. Finally, the films were annealed at 300°C for 1 h.

3.1.3 Honeycomb oxide structuring

The fabrication of a closely packed monolayer of polystyrene microspheres followed the modified spin-coating procedure after Hulteen *et al.*[122] and Cheung *et al*[123]. The diameters of employed microspheres varied between 0.37 to 1 µm and were ordered from Fischer-Scientific (10 wt%). The particle solution was mixed in a 10:1 (v/v) dilution with a 1:400 (v/v) solution of Triton X-100 in methanol. The resulting solution was dispersed for 10 minutes in a sonication bath and then filtered with a 2.7 µm filter. The multi-step spin-coating involved a first step of 300 rpm for 10 seconds, a second step at 600 rpm for two minutes and an additional step of 2000 rpm for 10 seconds. The self-assembled polystyrene monolayer was dried at room temperature in air for about 3 hours. The oxide honeycomb was fabricated by spin-coating a solution of titanium isopropoxide in ethanol (the same as previously used for the spin-coated TiO_2 compact layer) or a solution of 20 nm pre-made SiO_2 particles in ethanol[124] onto the polystyrene monolayer. Subsequently the monolayer was sintered in multiple steps (drying at 80 °C for 2 hours, quick heating to 250 °C for polystyrene degradation for 30 minutes, then increasing to 500 °C within 2 hours and sintering for 30 minutes) to form a stable oxide honeycomb structure.

3.1.4 Back-contacting electrode fabrication

Photoresist patterning:

The image reversal photoresist AZ 5214 E was spin-coated at 5000 rpm for 45 seconds and baked for 50 seconds at 110 °C according to the datasheet provided by the manufacturer. UV-light exposure with a wavelength of 265 nm and 25 mJ intensity through a chrome patterned glass photomask and subsequent image reversal, by baking for 120 seconds at 120 °C and applying a 250 mJ dose of UV exposure, lead to the solubility of the regions designed for the fingers of the rear contacts. These were dissolved through

immersion for roughly 40 seconds in a developer bath of AZ 726 MIF, resulting in a patterned photoresist layer.

Al_2O_3 + Ni + NiO shell hole conducting electrode:

The patterned photoresist layer was coated with 100 nm of insulating Al_2O_3 and 100 nm of Nickel through e-beam evaporation. The lift-off of the remaining photoresist regions was performed in an 80 °C heated bath of Dimethylsulfoxide (DMSO). The Ni based devices were subsequently annealed at 300 °C for 20 minutes to create a shell of oxidized Ni as a p-type electron blocking layer.

Al_2O_3 + Au + NiO + Thiol blocking layer for hole conducting electrode:

The patterned photoresist layer was coated with 100 nm of insulating Al_2O_3 and 100 nm of Au and 10 nm of NiO through e-beam evaporation. The lift-off of the remaining photoresist regions was performed in an 80 °C heated bath of DMSO. The substrates with the patterned Au electrodes were then immersed in beakers containing 1 mM 1-Dodecanethiol ($C_{12}H_{26}S$) solutions in ethanol for 24 h. After removal, the substrates were thoroughly rinsed with ethanol and blow dried with nitrogen.

Al_2O_3 + Al + Ti + TiO_2 shell electron conducting electrode for inverted back-contact device:

The patterned photoresist layer was coated with 100 nm of insulating Al_2O_3 and 50 nm of Al + 50 nm of Ti through e-beam evaporation. The lift-off of the remaining photoresist regions was performed in an 80 °C heated bath of DMSO. The Al + Ti based devices were

subsequently annealed at 300 °C for 20 minutes to create a shell of oxidized Al as blocking layer around the Al and a shell of TiO_2 as a n-type hole blocking layer.

Ionic liquid coating:

0.01 wt% of 1-butyl-3-methylimidazolium tetrafluoroborate (ionic liquid IL) was dissolved in methanol and the solution was spread onto the patterned electrodes after the lift-off and annealing process, then spin-coated at 4000 rpm for 20 seconds to be then dried at 80 °C for 10 minutes on a hotplate before perovskite deposition.

3.1.5 Perovskite absorber layer deposition

Perovskite layer deposition for honeycomb structured solar cells:

Initially a 3:1 molar ratio of CH_3NH_3I:$PbCl_2$ was dissolved in Dimethylformamide (DMF) with a concentration of 10 wt%, 15 wt% and 20 wt% and stirred for 120 min at 50 °C to prepare the well dissolved pre-cursor solution. Filling the oxide honeycombs with perovskite was realized via spin coating the fresh pre-cursor solution of $CH_3NH_3PbI_{3-x}Cl_x$ onto the patterned substrates. This was carried out in a N_2 filled glove box at spin speed of 2000 rpm for 60 seconds. The perovskite layer was then annealed for 150 min at 100 °C.

Perovskite layer deposition for semi-transparent solar cells:

Perovskite layers with low coverage were deposited after the technique developed by Eperon et al. [15]. 38 wt% CH_3NH_3I and 22 wt% $PbCl_2$ were dissolved subsequently in DMSO and stirred for 60 min. 250 µl of the solution was spin-coated on the substrates with

2000 rpm for 45 seconds and then annealed at 130 °C for 20 minutes. Spin-coating and annealing was done in air with 20 % controlled humidity.

Perovskite layer deposition for back-contacted solar cells:

For back-contacted solar cells, the 3:0.98:0.02 molar ratio of CH_3NH_3I:$PbCl_2$:PbI_2 was well dissolved in DMF with a concentration of 38.5 wt% and spin-coated onto the substrates with patterned electrodes at 2000 rpm for 45 seconds in a dry air atmosphere. The drying of the deposited solution was performed under a weak air flow for 30 seconds before letting the substrates rest for 15 min at room temperature and an additional drying step for 15 min at 70 °C on a hotplate. The films were then annealed in an oven for 90 min at 100 °C and 15 min at 120 °C.

3.1.6 Shunt-blocking layer for semi-transparent perovskite device

Octadecyl-trichloro silane (OTS) is added to toluene (10 µl per ml of toluene) and the substrates with partially covered perovskite layers were immersed into the solution, which is kept in a petri dish. After 10 minutes of incubation at room temperature, the substrates are rinsed with toluene followed by blow drying with N_2 and heating at 60 °C on a hotplate.

3.1.7 Perovskite surface passivation of back-contacted solar cells

In back-contacted devices, the surface of the perovskite does not require an additional coating to function as a solar cell, but depositing an additional layer can help with the improvement of stability due to moist protection or electronic passivation. Consequently, after the perovskite annealing procedure and the cooling of the substrates to room temperature, a layer of Poly(methyl methacrylate) (PMMA) was deposited by spin-coating a solution of 15 mg PMMA, dissolved in 1 ml of chlorobenzene, with 2000 rpm for 45 seconds.

Alternatively, trioctylphosphine oxide (TOPO) with 99 % purity was dissolved with a concentration of 0.025 M in anhydrous chlorobenzene. 100 µl of this solution was spread on the surface of the perovskite layer and then spin-coated for 60 seconds at 2000 rpm.

3.1.8 Hole-transporting layer deposition

For the fabrication of sandwiched solar cell devices, the hole-transporting layer was deposited on top of the perovskite films by spin-coating a solution with 8.5 wt% or 10 wt% spiro-OMeTAD in chlorobenzene and 30 mol% lithium bis(trifluoromethane-sulfonyl)imide and 80 mol% 4-tert-butylpyridine as additives, at 2000 rpm for 60 seconds in the N_2 atmosphere. The sample was dried overnight in a light-sealed desiccator.

3.1.9 Anode fabrication

Opaque anode:

50 nm Au, or 120 nm Ag was thermally evaporated on top of spiro-OMeTAD as the top-electrode. The pressure was ca. 10^{-6} Torr and the evaporation rate close to 0.1 nm/s.

Transparent electrode:

The hole-transporting layer was spray-coated with a PEDOT:PSS layer by keeping the substrate at 50 °C while spraying and for 10 seconds after the deposition. The solution was prepared by mixing a commercial blend (Hereaus GSD1330S) with ethanol and isopropanol in a 1:1:1 volume ratio. Subsequently flexible nickel microgrid sheets (Epimesh 300 from Epigem) of roughly 90 µm thickness were tape-casted with an adhesive mixture of 1:1.34 (w:w) Styccobond:(PEDOT:PSS). After drying the films at 60 °C for 15 min and 120 °C for 5 min the grids were then laminated onto the prepared substrates using finger pressure.

3.2 Solar cell characterization

For measuring the performance of the solar cells, simulated AM 1.5 sunlight was generated with a class AAB ABET solar simulator. It was calibrated to give simulated AM 1.5, of 100 $mWcm^{-2}$ equivalent irradiance, using an NREL-calibrated KG5 filtered silicon reference cell. The mismatch factor was calculated to be 1.065 between 300 - 900 nm, which is beyond the operating range of both the KG5 filtered silicon reference cell and the perovskite test cells[125]. The current-voltage curves were recorded with a sourcemeter (Keithley 2400, USA). The solar cells were masked with a metal aperture defining the active area (0.0625 cm^2, 0.0929 cm^2 and 0.73 cm^2). The back-contacted solar cells were not masked as the active are is defined as the area covered by the patterned electrodes, which measures 0.09 cm^2.

3.3 Optical characterisation

3.3.1 UV-Vis Transmission and reflection measurements

The transmission and reflection measurements were carried out with an internally coupled integrated sphere in a Varian Cary 300 UV-visible spectrophotometer. The average visible transmittance was calculated by averaging over all total transmittance values within the visible spectrum (400 – 780 nm).

3.3.2 Photoluminescence measurements

Steady state and time resolved photoluminescence measurements were carried out on a time-correlated single photon counting (TCSPC) setup (FluoTime 300, PicoQuant GmbH). A 507 nm laser head (LDH-P-C-510, PicoQuant GmbH) was used to excite the samples with pulse frequencies of 0.3 – 10 MHz, a pulse duration of 117 ps and fluence of 3 $\mu J/cm^2$

– 30 nJ/cm^2. The emitted light was detected with a high resolution monochromator and hybrid photomultiplier detector assembly (PMA Hybrid 40, PicoQuant GmbH).

3.3.3 Photocurrent and photoluminescence spatial mapping measurements

The photocurrent and photoluminescence spatial mapping experiments were carried out by Luis Pazos-Outón and Gregory Tainter at the Cavendish Laboratory at University of Cambridge. A WITec alpha 300 s setup was used together with a 405 nm continuous wave (CW) laser (Coherent CUBE) as excitation source, which was locked into a frequency of 840 Hz with a Stanford Research SR 540 Lock-In amplifier. The light was coupled into a microscope with 60 x Nikon lens. The samples were mapped precisely by moving them with a X-Y piezo stage (controlled by WITec ScanCtr Spectroscopy Plus software) underneath a microscope lens (60 x magnified, Nikon) into which the laser light was coupled. Emitted light form PL was detected through the same objective using a spectrometer with additional CCD detector. The excitation signal remained undetected by using a low pass filter before the detector. Photocurrent measurements were acquired by using a Stanford Research SR 570 pre-amplifier in connection with a Stanford Research SR 830 lock-in amplifier, which was locked into the chopped excitation source. All measurements were performed in N_2 atmosphere.

3.3.4 Photoluminescence quantum yield measurements

The photoluminescence quantum efficiency (PLQE) measurements were carried out by Johannes Richter at the Cavendish Laboratory, University of Cambridge. The technique developed by de Mello et al.[126] was used. A CW laser with 532 nm served as the excitation source for a sample kept in an integrating sphere. The scattered PL signal was detected using an Andor iDus DU490A InGaAs detector.

3.4 Microscopy

3.4.1 Optical microscope imaging

Optical microscope images were acquired in reflection and transmission mode with a Nikon Eclipse LV100 base in combination with 10x, 20x, 50x and 100x magnified objectives. Polarization filters, dark field and bright field modes were applied for different visualisations of the film morphologies and microstructure analysis.

3.4.2 Scanning electron microscopy imaging

Top surface and cross-sectional imaging of various films and device stacks was carried out with a Hitachi S-4300 field emission scanning electron microscope (SEM). Most of the measurements were performed with an electron beam voltage of 3 kV. Insulating materials were sputter-coated with 3 nm of Pt for better imaging quality.

3.4.3 Atomic force microscopy

The atomic force microscopy (AFM) images were obtained using a ThermoMicroscope M5 in non-contact mode and scanning over a range of 5 x 5 μm to 20 x 20 μm at a resolution of 256 x 256 data points. The surface roughness was measured as the root mean-squared roughness over the scanning area.

The conductive AFM measurements were carried out with environment control SPM system (Solver P47, NT-MDT, Zelenograd, Russia) under constant N_2 flow purge (< 4% relative humility) in combination with Pt-coated Si probes (HQ:DPER-XSC11/D; NanoAndMore GmbH).

3.5 Further material characterization

3.5.1 Film thickness measurements

Film thicknesses of unstructured layers with thicknesses above 50 nm were measured using a Veeco Dektak 150 surface profilometer.

3.5.2 X-ray diffraction

X-ray diffraction (XRD) spectra were collected from perovskite films deposited on FTO/glass substrates with the use of a Panalytical X'Pert Pro X-ray diffractometer by Cu K-alpha radiating with a wavelength of 0.154 nm.

3.6 Energy yield simulations and optimisation

Power conversion efficiency and annual energy yield simulations have been carried out for perovskite-on-silicon tandem device stacks and the results are presented in Chapter 7. The simulation process consists of various steps which are illustrated in Figure 3.2 for the calculation of the power conversion efficiency and Figure 3.3, Figure 3.4 for the simulation of the expected annual energy yield in real world conditions. The core of the optical model is based on the generalized transfer matrix method[26,127]. The constant refractive index of every material of the layers must be known, and together with the thicknesses of the layers and the incident radiation angle as parameters, the model output is the electric field distribution within the entire stack. This is used to calculate the fraction of transmitted and reflected light as well as the absorption within each layer. The model was implemented with the python programming language with heavy usage of the numerical computation package numpy. By calculating the absorption for every wavelength within the solar spectral range and assuming an internal quantum efficiency of 100%, which is feasible to

do for perovskites solar cells according to published results[66,128], we end up with the external quantum efficiency for the absorbing layers.

The material specific refractive index data for the applied materials was adopted from tandem modelling literature[129]. Changes of the bandgap for the perovskite layer have been simulated by assuming a perfect horizontal shift of the published absorption coefficient[130] along the energy axis. McMeekin et al.[131] have demonstrated that the absorption spectrum behaves in such a way in reality when different perovskite material compositions are used. The shifted absorption coefficient α(λ) can then be rearranged to calculate the extinction coefficient k(λ) via,

$$k = \frac{\alpha\lambda}{4\pi} \qquad \textbf{(3.1)}$$

which can be transformed to the refractive index n(λ) via the Kramers-Kronig transformation[132,133]:

$$n(E) - 1 = \frac{2}{\pi}\int_0^\infty \frac{E'k(E')}{E'^2 - E^2}\,dE' \qquad \textbf{(3.2)}$$

The EQE's of both absorbing layers can further be used to determine the modelled J(V) characteristic with detailed balance theory introduced in section 2.2.2. Following the single diode equivalent circuit model described in section 2.2.1, we can derive the J(V) characteristic representation as in equation 2.35. All of the specific equivalent circuit parameters (m, R_S, R_{SH}) were extracted from reported J(V) curves in literature by fitting the currently highest performing solar cell to the equation above. The used values for a perovskite cell[73] were $R_S = 3.5*10^{-5}$ Ω, R_{SH} = 5 MΩ and m = 2.35 and for the silicon HIT cell[94] $R_S = 5.5*10^{-5}$ Ω, R_{SH} = 100 MΩ and m = 1.0. Since equation 2.30 is an implicit function, the method presented by Jain et al.[134] was used to derive an analytical solution for an explicit equation that can be calculated numerically by using the W-function.

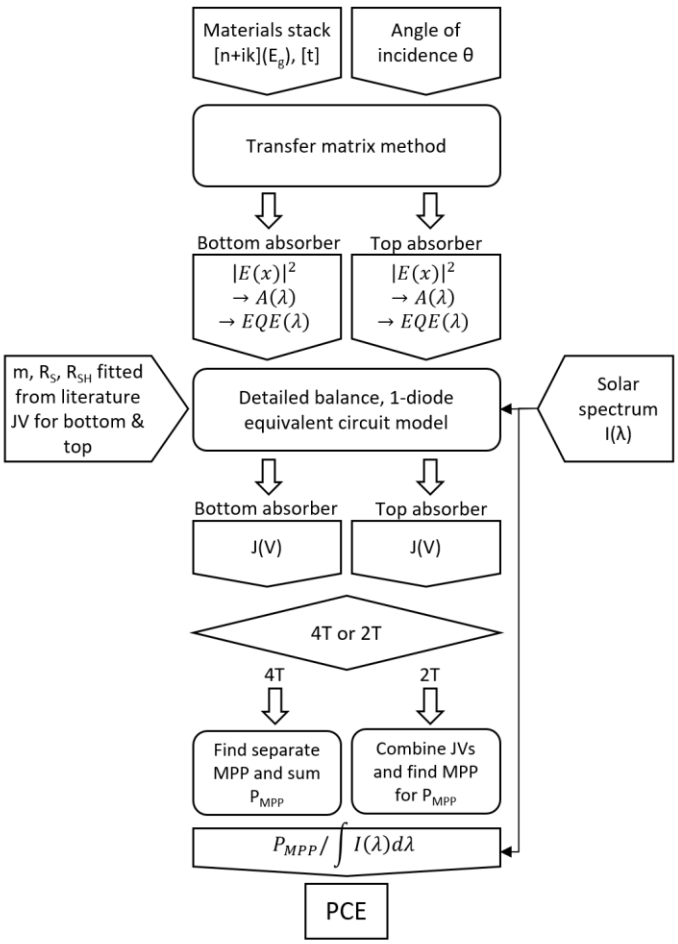


Figure 3.2: Simulation process for PCE calculation of tandem solar cell stack.

Depending on the interconnection of the tandem stack, the maximum power output was calculated in two different ways. In a 2-terminal tandem device the J(V) curves of both absorbing layers are combined by taking the lower current producing cell and calculating the corresponding limited current J(V) characteristic of the other cell[135]. Subsequently the power at maximum power point of the combined J-V curve was determined. In a 4-terminal device the maximum power point of each cell J(V) was determined separately and then the powers were added up. The PCE was then determined by dividing the tandem stack power output with the integrated power from the solar spectrum. It has to be noted that no optical penalty has been introduced for 4T devices (they were treated as if they were connected seamlessly together). Furthermore, no additional series resistance losses or power electronics losses were accounted for.

The annual energy yield (EY) calculations were carried out by using typical meteorological year (TMY) spectral data from NREL. They can be found in a well-organized database (NSRDB) for many locations in the USA[136]. The TMY data includes the global horizontal irradiance spectrum as well as the direct normal irradiance spectrum in the wavelength region from 300 – 1800 nm for every hour of a typical meteorological year. In a pre-processing step, for every hour of the year, the incident angle of the direct irradiance beam towards the panel is determined. It depends on the location and on the tracking mechanism, which can be a fixed panel (at an optimal fixed tilt angle[137]), a one-axis (with tilted rotation axis), or a two-axis sun tracking system as intruded in section 2.2.4. The fixed tilt angles of 33.33 °, 39.19 ° and 29.16 ° were chosen for the locations Golden (CO), Seattle (WA) and Mohave desert (CA). Furthermore, the diffuse light distribution is modelled with the motivation to create a real world scenario, therefore instead of assuming isotropic distribution, the entire hemispherical distribution (broken into a grid of 900 nodes for numerical approximation) of the diffuse light radiance is calculated with the Brunger-Hooper model[44] and the data is grouped for accurate incidence angles of the distributed sky elements towards the fixed or tracked panel (see Figure 3.3).

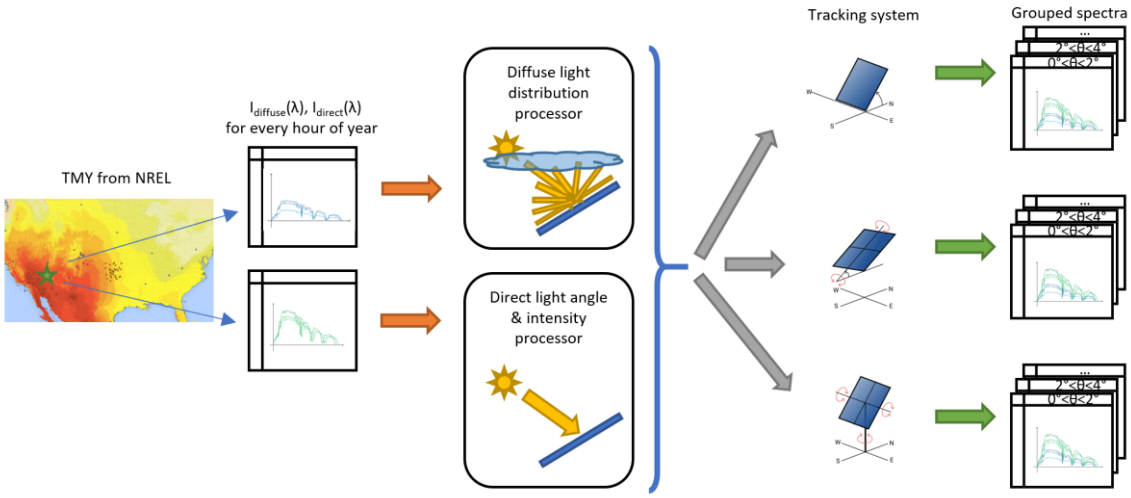


Figure 3.3: Illustration of the pre-processing method used for the modelling of real world solar spectra needed for the input of energy yield simulations of solar cells.

The pre-processed irradiances and their corresponding incidence angles were then fed into the previously described transfer matrix model and a maximum power output was calculated by summing up all hemispherical contributions. Repeating this process for every hour of the year and summing up the hourly power outputs multiplied with 3600 seconds/hour (for hourly energy yield), returns the annual energy yield for a particular tandem solar cell stack (2T or 4T) at a particular location in the USA with one of the three tracking solutions.

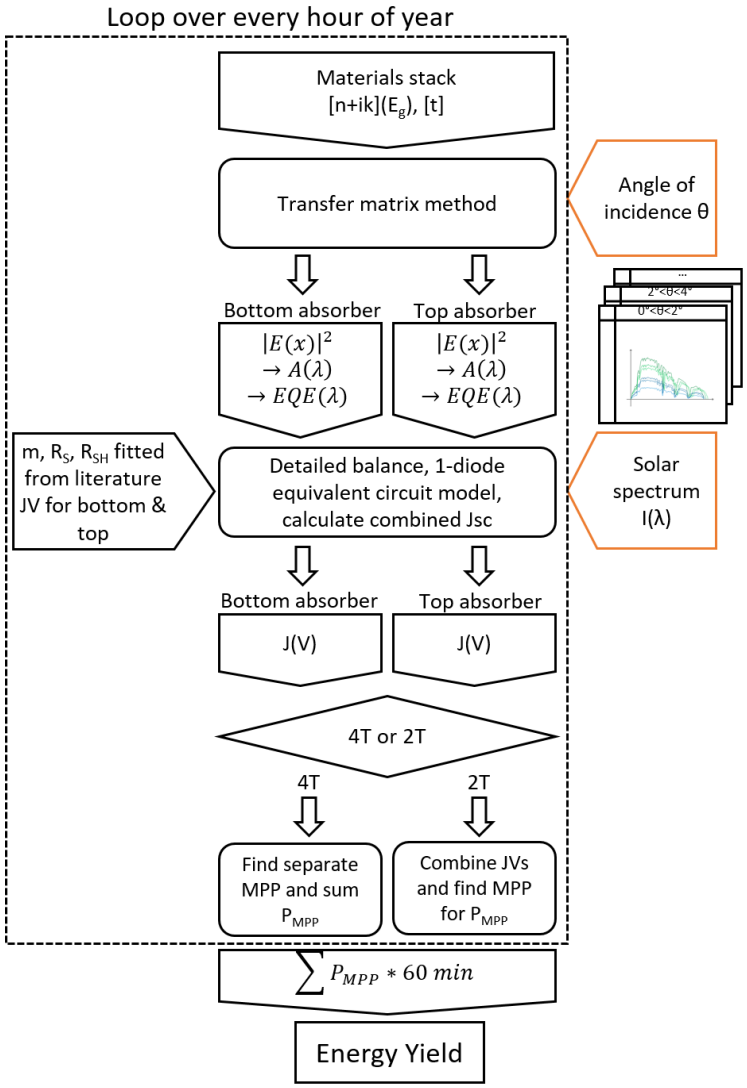


Figure 3.4: Simulation process for annual energy yield calculation of tandem solar cell stack.

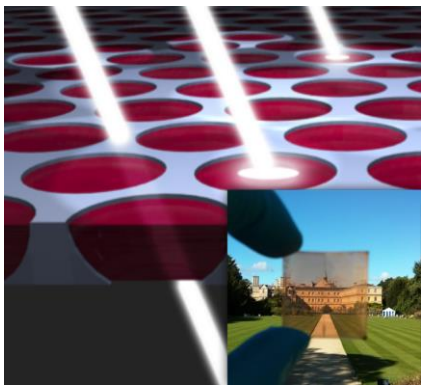
In order to not only calculate the annual energy yield but to optimise the entire material stack for maximum energy yield, the code had to be optimized and the algorithm parallelized for cluster computation. For the global optimisation, a differential evolution algorithm[138] was used, which is inherently faster than a brute force optimisation. However, some optimisations were also calculated with the latter for local and global maxima analysis.

.

4 TEMPLATED MICROSTRUCTURAL GROWTH OF PEROVSKITE THIN FILMS VIA COLLOIDAL LITHOGRAPHY

The work presented in this chapter has been published in:

Hörantner, M. T.; Zhang, W.; Saliba, M.; Wojciechowski, K.; Snaith, H. J., "Templated Microstructural Growth of Perovskite Thin Films via Colloidal Monolayer Lithography", *Energy Environ. Sci.* **2015**, *8*, 2041–2047.



4.1 Context and summary

In addition to solar cells, perovskites show remarkable suitability for lasing and light emitting diode (LED) applications. Such utilisations benefit from well-defined geometries of opto-electronic materials. Here, perovskite crystal domain size and microstructure is controlled by guiding the growth through a highly-ordered metal oxide honeycomb

structure, which is formed via colloidal monolayer lithography. The organic–inorganic perovskite material fills the holes of the honeycomb remarkably well leading to fully controlled domain size with tuneable film thickness. The honeycomb region is predominantly transparent, whereas the perovskite crystals within the honeycomb are strongly absorbing. Consequently, semi-transparent perovskite solar cells are fabricated to demonstrate the feasibility of this structuring, which leads to enhanced open-circuit voltage and fill factor in comparison to unstructured partially dewet perovskite thin films. Power conversion efficiencies of up to 9.5 % are achievable with an average visible transmittance through the active layer of around 37 %. The controlled microscopic morphology of perovskite films opens up a wide range of possible investigations, from charge transport optimization to optical enhancements and photonic structuring for photovoltaic, light emitting and lasing devices.

4.2 Introduction

Organic-inorganic perovskite materials have attracted increasing attention over the past two to three years leading to high performance solar cells with recorded power conversion efficiencies exceeding 20%[47,49,53,139–141], as well as demonstration in other optoelectronic applications, such as thin-film transistors, lasers and light emitting diodes[142–145]. For many optoelectronic applications, the introduction of periodic structures on the photonic length scale can be important to control the interaction between light and matter. For instance, lasers require optical feedback[146–148] and LEDs require control over the angular emission of light[149–151]. Specifically for perovskite solar cells, in addition to achieve high performance, another important application of controlling the optical properties of the active layer is the fabrication of semi-transparent solar cells for building integrated

photovoltaics (BIPV)[152]. Previously, the surface coverage of the absorbing perovskite layer was reduced by forming randomly distributed islands of perovskite upon the planar n-type charge collection electrode in a perovskite solar cell. The average visible transparency of the fabricated films can be controlled from close to 0 to 80% with neutral colour and reasonably high photovoltaic performance still being preserved[15]. However, the presence of regions in the solar cell where the p-type and n-type charge collection materials make contact, in between the perovskite islands, leads to the formation of a "shunt diode", lowering the open-circuit voltage. In addition, the non-uniform shape of the perovskite islands leads to scattering of light, which is non-ideal.

Previously, long before the perovskite solar cell research pandemic, Kagan *et al.*[153] demonstrated that layered organic-inorganic perovskite films can be structured on the 3-10's of micrometer length scale via imprinting a substrate with a self-assembled monolayer of functional groups, which induce a strong contrast in the surface energy between patterned and non-patterned regions. Subsequent coating of the surface energy patterned films with the layered perovskite $(C_6H_5C_2H_4NH_3)_2SnI_4$ led to structuring of the perovskite, where the material was absent from the hydrophobic regions. The 3D crystalline $CH_3NH_3PbX_3$ perovskite (where X is one or more halides), which show good PV performance and high luminescence efficiency, have a very strong tendency to crystalize into large domains, often on the 10's of microns length scale[154]. For the surface energy patterning to be successful on a length scale shorter than the natural crystalline domain size, the surface interaction must be very strong, and dominate over the inherent tendency to form large unbound domains. Thus far, surface energy patterning has proven to be challenging to replicate structures at the photonic length scale into the optoelectronically relevant perovskite materials. There is therefore a pressing need for a new approach to structure these perovskite materials with periodic length scales close to the wavelength of light.

Colloidal monolayer lithography (CML) represents an efficient and low-cost technique for the fabrication of large area, highly ordered, structured arrays. The various fabrication techniques and application examples have been introduced in section 2.7.2. Furthermore, incorporating insulating oxides, such as SiO_2, has been proven to work well in perovskite solar cells[155] and as insulating buffer layers in solid state dye sensitized solar cells[156,157].

In this chapter a double templating approach is demonstrated to introduce periodic structure into perovskite thin films. The successful usage of a colloidal monolayer of polystyrene (PS) microspheres as a sacrificial template to fabricate micro-structured SiO_2 honeycomb films is shown. With subsequent coating and infiltration of the SiO_2 honeycomb with a perovskite precursor solution, precisely controlled perovskite domains are achieved. As an example of their use, these patterned perovskite films are incorporated into semi-transparent perovskite solar cells, which exhibit high levels of transparency and reasonably high efficiencies due to increased fill factors and open circuit voltages as compared to semi-transparent perovskite solar cells fabricated from disordered perovskite islands.

4.3 Results and discussion

4.3.1 Microsphere monolayer formation and oxide honeycomb fabrication

The fabrication method for patterning the oxide structures has already been introduced in section 2.7.2. A schematic illustration of the processing steps is also shown in Figure 2.25. The colloidal PS monolayers is uniformly deposited onto the FTO/compact TiO_2 (c-TiO_2) coated substrate via spin-coating (step 1 and 2), and then subsequently the gaps of the hexagonal closely packed PS microspheres are filled with either a TiO_2 precursor solution or a SiO_2 nanoparticle solution (step 3). Finally, the films are sintered at 500℃ to remove the polymer template, leaving behind the inverse porous honeycomb structure (step 4).

Fabrication of PS monolayers has been previously reported on smooth surfaces such as glass (root mean square roughness ~ 2 nm), and silicon wafers (root mean square roughness < 0.5 nm)[122]. Nevertheless, a uniform distribution of microspheres (see Figure 4.1a) is achievable on the FTO/c-TiO_2 surface with a measured root mean square roughness of 5.2 nm (measured via AFM as seen in Figure 4.2). Two different oxides were employed to fabricate the scaffold: TiO_2 shows a tubular-like honeycomb structure after curing (Figure 4.1b and AFM image in Figure 4.3) and SiO_2 yields a more contiguous honeycomb structure (Figure 4.1c).

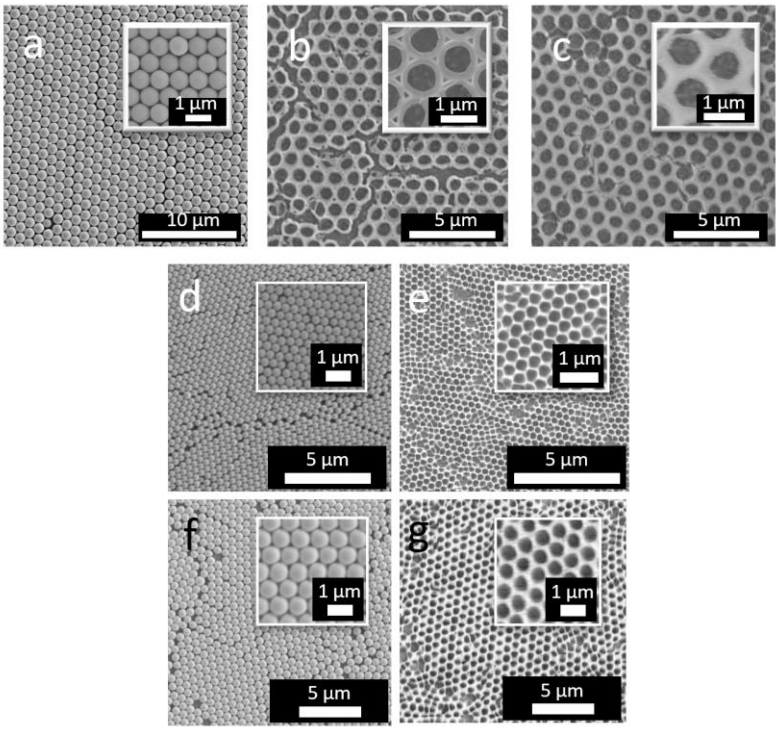


Figure 4.1: SEM images (with magnified insets, scale bar 1 µm) showing a typical highly ordered monolayer of 1 µm diameter PS microspheres (a), cured TiO_2 (b) and SiO_2 (c) honeycomb structure. SEM images of colloidal monolayer (d, f) of PS microspheres with 0.37 and 0.6 µm diameter and corresponding SiO_2 honeycomb scaffold (e, g).

A broad range of other oxides should also be able to be templated following this methodology, provided that the precursor solvent does not dissolve or wash away the PS spheres from the substrate during the spin-coating process[158]. The curing process was

optimised via different heating steps leading to honeycomb structures with open pores at the top and bottom.

A soft baking step for the as-deposited polystyrene spheres was performed at 80 °C for 2 h to dry the films and begin to melt the microspheres to increase the contact area with the c-TiO_2 layer before forming the scaffold. Subsequently a quick temperature increase to 250 °C to rapidly degrade the microspheres and a slow rise to 500 °C to form a stable oxide structure. It is to be noted that the 80 °C step is important to resultantly expose compact TiO_2 at the base of the holes in the as-formed SiO_2 honeycomb. We used PS microspheres with diameters of 0.37 (Figure 4.1d-e), 0.6 (Figure 4.1f-g) and 1 µm (Figure 4.1a-c) to fabricate scaffolds with different pore sizes.

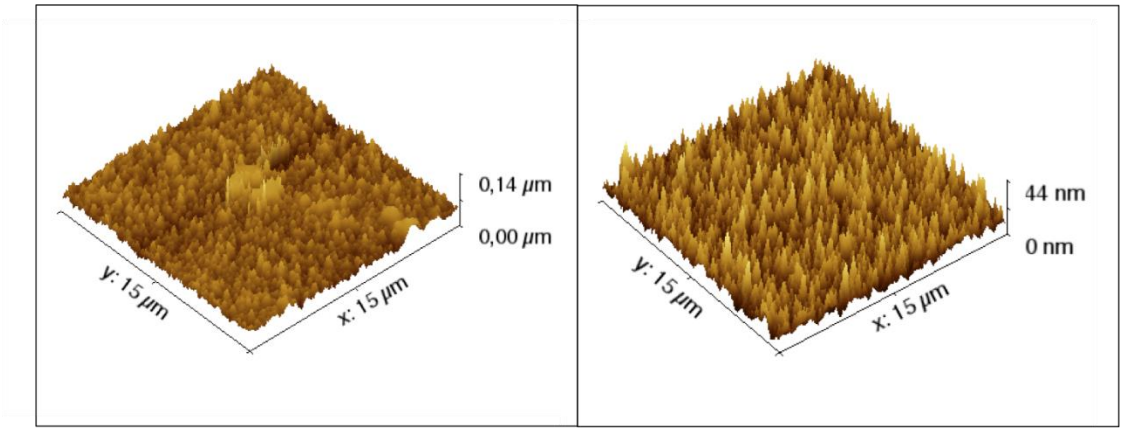


Figure 4.2: AFM measured 3D profile of 15 Ohm/square FTO glass before (left) and after (right) deposition of c-TiO_2. The root mean square roughness was calculated to be 10.5 and 5.2 nm.

4.3.2 Perovskite structuring

In order to template the perovskite material, the pores of the honeycomb structures are filled with $CH_3NH_3PbI_{3-x}Cl_x$ perovskite by spin-coating the precursor solution and annealing in a nitrogen filled glovebox. After annealing, the perovskite films show uniformity over a wide area on the TiO_2 and SiO_2 scaffolds (Figure 4.4a and Figure 4.4b). The perovskite film thickness is controlled within the pores by diluting the precursor

solution. As a control, using the same concentration of precursor solution, perovskite films are fabricated on planar FTO/c-TiO_2 substrates (no scaffold, Figure 4.4c) and mesoporous SiO_2 film (400 nm thick, Figure 4.4d). While the film formation on the patterned honeycomb structures appears to be completely uniform, the films on top of FTO/c-TiO_2 as well as on a mesoporous SiO_2 scaffold show random formations of perovskite domains as has been previously observed[15,154,159]. Since the honeycomb pores are significantly smaller than the randomly forming domains in unstructured substrates (Figure 4.4c), the perovskite growth is bounded by the honeycomb walls.

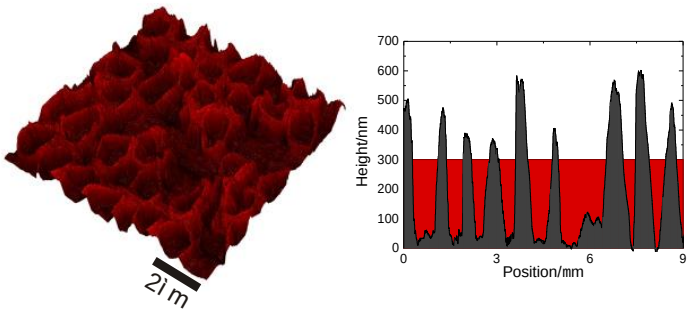


Figure 4.3: AFM measured 3D profile of TiO_2 honeycomb structure (left). Line profile of TiO_2 honeycomb structure with indicated level of 300 nm thick perovskite filling.

This leads to good filling behaviour within the pores and therefore the presented micro-structured oxide scaffold provides controllable perovskite domain size, despite the extremely strong tendency of the material to crystalize[159]. The crystal structure itself does not show a significant change, as shown in Figure 4.5, though the diffraction peak widths are broader for the perovskite processed on the honeycomb structure. This indicates that the crystal domain size is smaller, consistent with confinement of the crystallisation within the honeycomb.

In addition to varying the *pore size* of the honeycomb structure, the height of honeycomb walls can be tuned by changing the PS microsphere size and the concentration of TiO_2 precursor or SiO_2 nanoparticle solution. For example, in this study the honeycomb

structure, which was fabricated from 1 µm PS microspheres, yields 400 nm in wall height. Moreover, by varying the concentration of the perovskite precursor solution, the thickness of the in-filled perovskite domains can be controlled. In Figure 4.4e-h the filling of TiO_2 scaffold pores walls is shown with 20 and 40 wt% perovskite concentrations, respectively. At lower concentration, the perovskite forms only within the pores (Figure 4.4e-f) while at higher concentration an additional capping layer is formed on top of the metal oxide scaffold (Figure 4.4g-h).

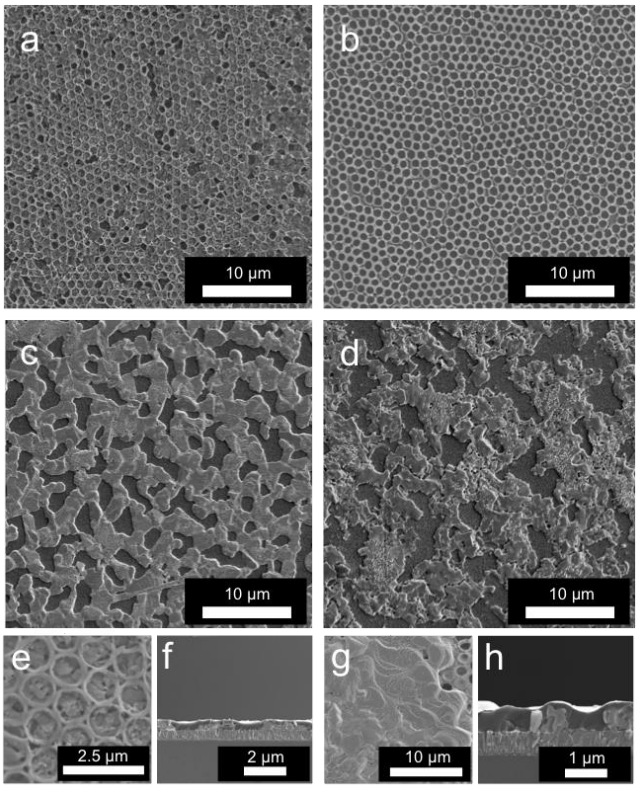


Figure 4.4: SEM images (top view) showing perovskite film formations within TiO_2 (a) and SiO_2 (b) honeycomb scaffolds, on a c-TiO_2 layer (c) and on a mesoporous SiO_2 scaffold of 400 nm thickness (d) produced with 20 wt% perovskite precursor solution. Detailed top view and cross-section SEM images show the filling characteristic of TiO_2 scaffold with 20 wt% (e, f) and 40 wt% (g, h) perovskite precursor solution.

The SiO_2 honeycombs formed from a SiO_2 nanoparticle-solution forms cup-like shapes of mesoporous SiO_2. These SiO_2 structures appear to predominantly coat the entire substrate

at the base of the "cups" and may therefore require interpenetration by the perovskite for the electronic charge to be conducted through the perovskite to the compact TiO_2.

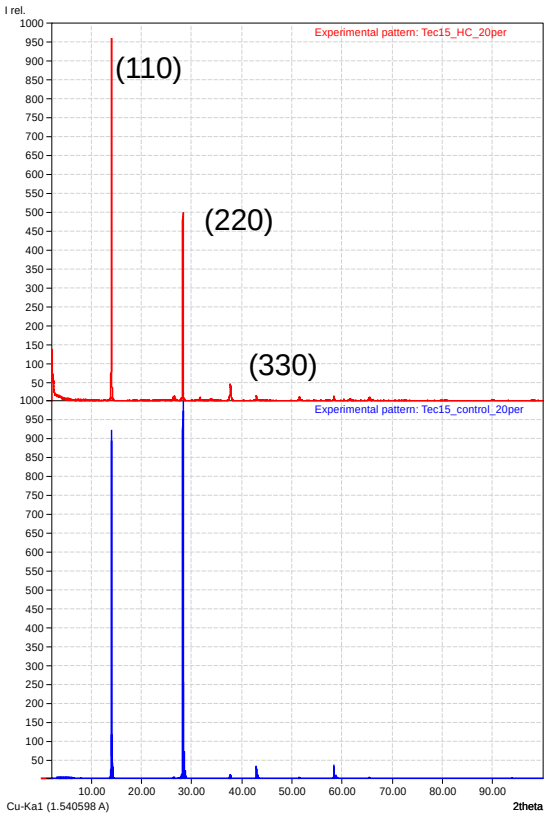


Figure 4.5: XRD patterns of perovskite films within SiO_2 honeycombs (top) or on top of FTO/c-TiO_2 substrates (bottom) deposited from 20 wt% precursor solution. The patterns are showing good similarity with the typical tetragonal $CH_3NH_3PbI_3$ patterns and lattice parameters (a=8.884, c=12.61 and a=8.874, c=12.62) were determined via a Rietveld refinement with χ^2=4.7 and χ^2=9.8). By Scherrer equation, crystallite sizes were estimated to be equal to around 110-120 nm (top) and 150-190 nm (bottom), respectively.

Figure 4.6a shows a comparison of the total transmission spectra of the control substrate (FTO/TiO_2 compact layer) and substrates with additional TiO_2 (FTO/TiO_2 compact layer/TiO_2 honeycomb) or SiO_2 (FTO/TiO_2 compact layer/SiO_2 honeycomb) honeycomb structures. While the TiO_2 honeycomb film appears to reduce the specular transmission in the visible range, the SiO_2 honeycomb shows a considerably different characteristic, since it transmits even more light than the TiO_2 compact layer substrate. We expect the improved

transmittance to be caused by reduced reflectivity that results from a decreased refractive index contrast at the compact TiO_2/Air interface due to the insertion of the porous SiO_2 "interlayer" (n_{air}=1.0, n_{SiO2}=1.5, n_{TiO2}=2.6[160,161]), leading to an anti-reflective character[162].

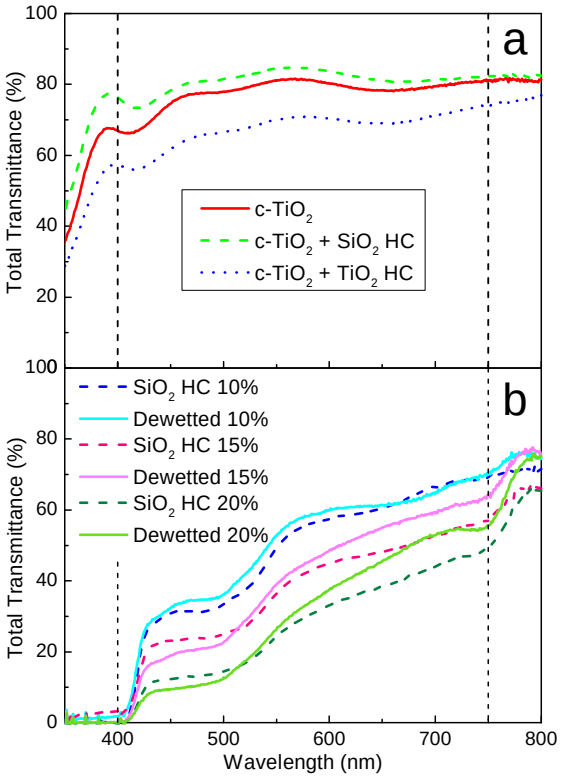


Figure 4.6: Total transmission measurements (a) within the visible spectrum of FTO/c-TiO_2 substrates (solid red line), compared to FTO/c-TiO_2 substrates covered with the SiO_2 honeycomb scaffold (dashed green line) and TiO_2 honeycomb scaffold (dotted blue line). Total transmission measurements (b) within the visible spectrum of top-electrode less devices with (dashed lines) and without SiO_2 honeycomb scaffolds (solid lines) and absorbing layers fabricated with 10 (blue lines), 15 (magenta lines) and 20 wt% (green lines) perovskite solutions.

4.3.3 Semi-transparent solar cell development

As an example application of patterned perovskite thin films, the development of semi-transparent perovskite solar cells was achieved with a focus on the SiO_2 honeycomb structures since they appeared to be more transmissive in the visible spectrum than the TiO_2 honeycomb structure (Figure 4.6a). Figure 4.6b demonstrates the comparison of the

optical properties of these films coated with $CH_3NH_3PbI_{3-x}Cl_x$ and dewet perovskite films with the absence of any scaffold. The transmission through the honeycomb-structured films is similar to that through the dewet perovskite films, but there is a slight flattening of the overall spectra, consistent with some panchromatic light passing un-attenuated through the SiO_2 regions. We note that the honeycomb-structured SiO_2 regions are likely to be mesoporous and hence also contain a small fraction of perovskite. This explains why entirely neutral transmission was not fully achieved with this structure. Despite the lack of neutral transmission, the average visible transmittance (AVT) of around 47 % is reached with the low perovskite concentration (10 wt%), followed by around 37 % and 28 % for medium (15 wt%) and high (20 wt%) perovskite concentrations in the honeycomb structured films.

The fabricated devices exceeded efficiencies of 12% with thicker, less transparent films made from 30 wt% perovskite solution (shown in Figure 4.7). It is noted that 40 wt% solution is usually employed for fully optimized planar heterojunction or meso-superstructured devices, so all the concentrations for semi-transparent solar cells fabricated in this work are lower than those required for maximum performance in solar cells.

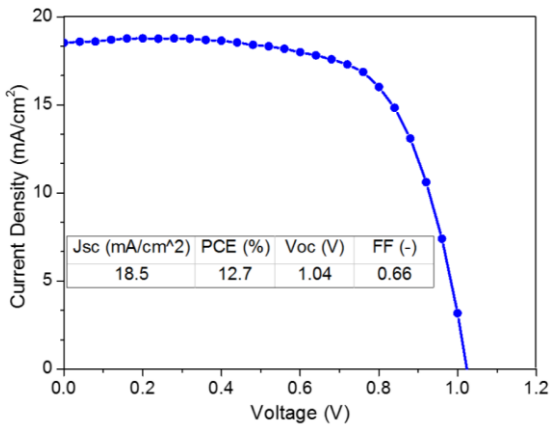


Figure 4.7: J-V characteristic curve for a SiO_2 honeycomb structured perovskite solar cell fabricated with 30 wt % precursor solution, scanning from forward bias to short circuit direction with a scan rate of 0.15 V/s.

The finalised solar cell devices were fabricated by capping the micro-structured perovskite layers with an organic hole-conductor spiro-OMeTAD, and a top electrode (Ag), as shown schematically in Figure 4.8a. Figure 4.8b pictures a colour-enhanced cross-section SEM image of a complete device fabricated from the micro-structured SiO_2 honeycomb and 20 wt% perovskite precursor solution.

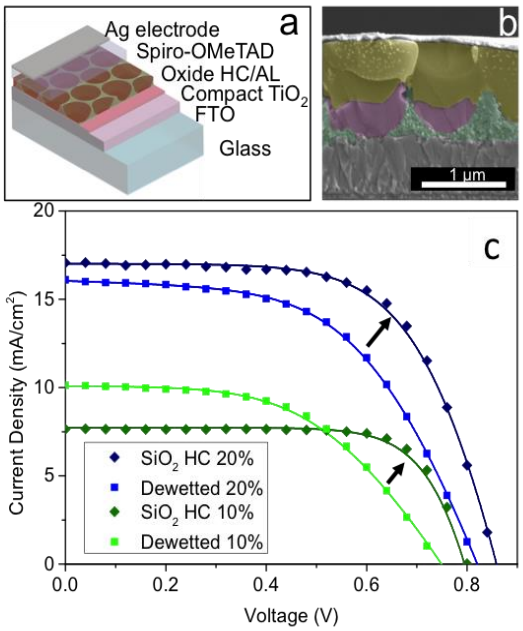


Figure 4.8: Schematic illustration of the device architecture with oxide honeycomb scaffold (a). Colour enhanced cross-section SEM image of a complete device fabricated from the micro-structured SiO_2 honeycomb with 20 wt% perovskite precursor solution (b). Perovskite (purple) is shown in cup-shape SiO_2 scaffold pores (green) and covered with hole transporting layer, spiro-OMeTAD (yellow), below a silver top-electrode (white). Measured (symbols) and one-diode model fitted (lines) J-V characteristics of devices fabricated with and without SiO_2 honeycomb scaffolds and covered with perovskite films processed from 10 and 20 wt% precursor solutions (c). The arrows indicate the obvious change of shape that results in higher open-circuit voltages and fill factors for the SiO_2 honeycomb scaffold devices. The current voltage curves were scanned from forward bias to short-circuit at a rate of 0.15 V/s.

Notably, despite the optimized curing procedure of the honeycomb structure, the perovskite domain on the right side is not in direct contact with the electron-transporting layer. However, the device performance observed is an indication for the partial perovskite infiltration within the thin SiO_2 layer that leads to sufficient charge transport. Devices with and without the honeycomb scaffold were compared at identical perovskite concentrations and the device performance was measured under simulated AM1.5 100 $mWcm^{-2}$ sunlight (see J-V characteristic curves in Figure 4.8c). Observable is an increase in both open-circuit voltage and fill factor for the devices employing micro-structured SiO_2 honeycomb as scaffold. The enhanced V_{oc} and FF can be explained by the suppression of recombination, or "shunting" paths between the hole-blocking layer (c-TiO_2) and the hole-transporting (spiro-OMeTAD) layer by the non-conductive SiO_2 oxide. The shunt resistance and series resistance for devices is shown in Figure 4.8c which were determined by fitting the J-V curves with a one-diode model after Unger *et al.*[163]. The fitted values for the 20 wt% samples were $R_{SH} = 2.5*10^8\ \Omega cm^2$, $R_S = 4.1\ \Omega cm^2$ for the honeycomb structured device and $R_{SH} = 1.1*10^3\ \Omega cm^2$, $R_S = 8.7\ \Omega cm^2$ for the dewet device. A similar trend is found for the 10 wt% devices ($R_{SH} = 1.1*10^8\ \Omega cm^2$, $R_S = 2.7\ \Omega cm^2$ for SiO_2 HC and $R_{SH} = 1.0*10^8\ \Omega cm^2$, $R_S = 15.4\ \Omega cm^2$ for the dewet device). The higher shunting resistance supports the argument that recombination paths are significantly blocked in the honeycomb-structured devices.

The short-circuit current densities (J_{SC}) are slightly lower for devices with honeycomb scaffolds, as compared to dewet perovskite film devices, which is consistent with the previous reports showing lower photocurrents for perovskites infiltrating meso-structured scaffolds[164], presumably due to the electron-hole lifetime being shorter when the material infiltrates the mesoporous oxides[55]. This trend is slightly suppressed at higher perovskite concentration (20 wt%), since the majority of the perovskite film will be formed from

larger crystalline domains for both the dewet perovskite films and honeycomb structured films.

Table 4.1 summarises the solar cell performance parameters. Perovskite solar cells employing micro-structured SiO_2 honeycombs exhibit high power conversion efficiencies (PCEs) while maintaining high optical transparency. PCE of 4.5 % can be reached at 47 % AVT (excluding the absorption in the silver electrode) with perovskite precursor concentration of 10 wt%.

Table 4.1: Solar cell performance parameters of best performing devices without (dewet perovskite films) and with SiO_2 honeycomb scaffolds fabricated from different perovskite precursor concentrations. Values in brackets represent mean values for tested set of devices with standard deviation. Conc. is perovskite precursor solution concentration; AVT is average visible transmission between 380 to 780 nm; AL AVT is the Active Layer AVT, which excludes absorption losses in the FTO/c-TiO_2 anode.

Design	**Conc. (wt%)**	**AVT (%)**	**AL AVT (%)**	**J_{SC} (mA/cm^2)**	**V_{OC} (V)**	**FF (-)**	**PCE (%)**
SiO_2 HC (n=16)	20	28	37	17.1 (14.9±1.6)	0.84 (0.76±0.06)	0.66 (0.63±0.09)	9.5 (7.9±1.2)
Dewet (n=11)	20	31	42	16.1 (16.1±1.3)	0.80 (0.58±0.25)	0.56 (0.43±0.10)	7.2 (5.7±1.9)
SiO_2 HC (n=15)	10	47	63	7.6 (4.8±2.5)	0.80 (0.87±0.04)	0.74 (0.72±0.02)	4.5 (2.8±1.5)
Dewet (n=10)	10	49	65	10.1 (6.1±3.3)	0.76 (0.82±0.22)	0.52 (0.44±0.11)	4.0 (1.9±1.7)

Higher concentrated perovskite (20 wt%) leads to a PCE of 9.5 % at 28 % AVT. Following the method described by Eperon *et al.*[15] the AVT of the photoactive layer (SiO_2/perovskite/spiro-OMeTAD) was calculated to equal 63 and 37 %, respectively, for the lower and higher concentrated micro-structured perovskite films. All the current voltage curves presented here are scanned from forward bias to short-circuit.

There is a certain of hysteresis in the J-V curves and the stabilized power output at the maximum power voltage is lower than that determined from the current voltage curves[165]. For instance, Figure 4.9 shows the forward and backwards current voltage scans for a typical device, which exhibited a J-V derived PCE of 7.5% with a stabilized PCE of just over 5%.

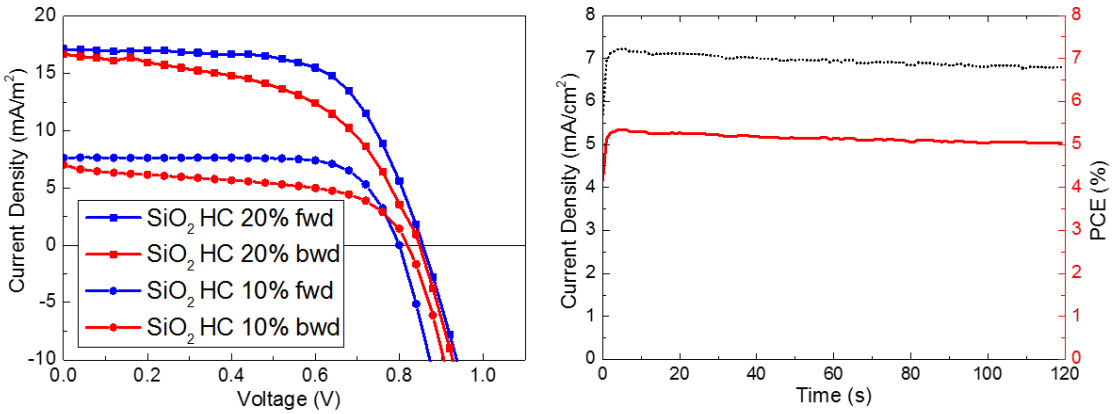


Figure 4.9: J-V characteristic curves for forward and backward scan (scan rate 0.15 V/s) of SiO_2 honeycomb structured perovskite solar cell fabricated with 10 and 20 wt% perovskite precursor solution (left). Stabilized current density and PCE of a SiO_2 honeycomb device fabricated from 20 wt% perovskite precursor solution, held at the maximum power voltage of 0.74 V for 120 seconds (right). This device shows a J_{SC} of 10.5 mA/cm^2, a PCE of 7.5 %, a FF of 0.77 and a V_{OC} of 0.9 V in the J-V measurement scanning from forward bias to short circuit direction under simulated AM1.5 100 mWcm^{-2} simulated sun light.

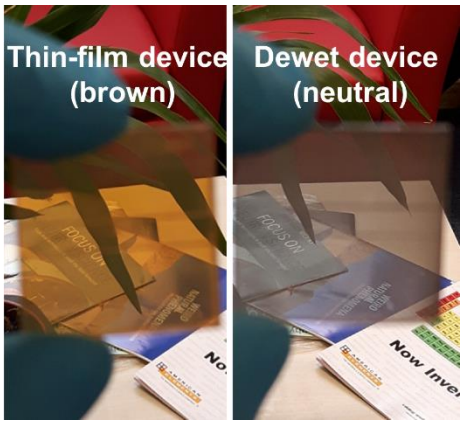
4.4 Conclusion and outlook

In summary, a scalable technique for fabricating highly ordered patterned metal oxide scaffolds was presented that can be used to pattern perovskite thin films on a photonic length scale, despite the tendency for the material to crystalize in much larger domains when unbound. These films were applied for the fabrication of semi-transparent perovskite solar cells, which exhibit very respectable measured efficiencies of over 9 % with relatively high photoactive layer average visible transmission of 37 %. With respect to the semi-transparent solar cells, the key attribute of the honeycomb scaffold is that the electronic contact between the compact TiO_2 and the hole-conductor is suppressed, which otherwise results in a low shunt resistance in the solar cell. For enhancing the use of semi-transparent solar cells, further work should be focused upon more effective segregation of the perovskite from the scaffold region, achieving steeper template walls and focusing on reducing the light scattering by tuning of the template pore size and uniformity. Beyond semi-transparent solar cells, this sort of optical structure may be able to be modified to enhance the overall light absorption and emission from perovskite thin films. Not limited to photovoltaics, this work opens the door for many future applications that involve the controllable patterning of perovskite films for photonics and opto-electronics, relevant to LEDs and lasers.

5 SHUNT-BLOCKING LAYERS FOR SEMI-TRANSPARENT PEROVSKITE SOLAR CELLS

The work presented in this chapter has been published in:

Hörantner, M. T.; Nayak, P. K.; Mukhopadhyay, S.; Wojciechowski, K.; Beck, C.; McMeekin, D.; Kamino, B.; Eperon, G. E.; Snaith, H. J., "Shunt-Blocking Layers for Semitransparent Perovskite Solar Cells", *Adv. Mater. Interfaces* **2016**, *3*, 1500837.



5.1 Context and summary

Perovskite solar cells have shown phenomenal progress and have great potential to be manufactured as low-cost large area modules. However, perovskite films often suffer from pinholes and the resulting contact between hole- and electron transporting layers provides lower resistance (shunt) pathways, leading to decreased open-circuit voltage and fill factor. This problem is even more severe in large area cells and especially in the case of neutral color semi-transparent cells, where a large absorber-free area is required to provide the desired transparency. Herein, a simple, inexpensive, and scalable wet chemical method is

presented to block these "shunting paths" via deposition of transparent, insulating molecular layers, which preferentially bind to the uncovered surface of the electron collecting oxide, without hindering charge extraction from the perovskite to the charge collection layers. It is shown that this method improves the performance in semi-transparent cells, where the enhancement in open-circuit voltage is up to 30 % without negatively impacting the photocurrent. Using this method, an efficiency of 6.1 % was achieved for a neutral colour semi-transparent perovskite cell with 38 % average visible transmittance. This simple shunt blocking technique has applications in improving the yield as well as efficiency of large area perovskite solar cells and light emitting devices.

5.2 Introduction

Organic-inorganic perovskite materials have been proven to be an efficient solar cell photoactive material and devices with power conversion efficiencies exceeding 20% for small area cells have been demonstrated [166]. The crystal formation of the perovskite films is a widely studied topic [167,168], different processing techniques have been used to grow crystalline perovskite films [49,53,139], which makes this material very versatile, also in terms of manufacturing. The thin-film coverage and the morphology have been shown to affect the performance of devices [169]. Single step, solution processed films are prepared from low-viscous ionic solutions where the crystal formation is often very rapid. As a result the films can produce a "dewet" morphology as they grow, leaving pinholes in the thin-films [170].

Pinholes in the absorber thin-films cause a loss in the ability to absorb the full photon flux and therefore reduce the achievable photocurrent density. Moreover, these pinholes allow direct contact between electron (n-type) and hole (p-type) transporting layers. These contacts create shunt paths (reduced shunt resistance) in the solar cell architecture. Lower

R_{SH} in solar cells reduces the fill factor and the open-circuit voltage and thus the PCE of the cell [171]. Improving the coverage of perovskite films by various optimized annealing, solvent dripping or other post treatments typically inhibits the shunting [139,140,154,172,173]. Most of such techniques result in smaller perovskite crystallites, which cover the surface in an improved manner, although this may be detrimental for maximizing device performance; crystal boundaries are thought to be sites that can cause non-radiative recombination [174].

Due to industrial demand for building integrated photovoltaics, a number of reports presenting semi-transparent devices have been published [82,175,176]. One approach is to use a thinner (~80-200 nm) perovskite layer below the absorption depth to enhance the transmission[79,80,82,175,177]. Devices applying this technique have reached efficiencies of 7.8% at an average visible transmittance of 37%[79]. However, such solar cells do not provide colour neutrality, which limits their use in building integrated applications: Due to the nature of the semiconductor absorption with density of states increasing from the bandgap, a continuous thin film of methylammonium lead iodide perovskite (with bandgap ~1.6 eV) will tend to look brown. However, this is not a desirable colour for building-integrated applications, there is most demand for neutral-coloured solar cell windows. An alternative technique to obtain neutral colour semi-transparent perovskite solar cells has been developed by Eperon *et al.* through a perovskite dewetting technique [15,84]. A thick perovskite film is processed in such a way as to create a microstructured array of perovskite 'islands'. Each island is thick enough to absorb the majority of light below the bandgap, so appears black, and is too small to be seen with the bare eye. The combination of fully absorbing islands and transparent regions results in neutral colour devices. Though the reduced coverage of the absorbing layer provides higher transmittance through the device, it has the disadvantage of allowing shunting paths between the perovskite islands.

Consequently, such devices yield low V_{OC} and FF [15,84] when compared to fully covered films [79,178].

As such, a method to selectively fill the regions between the perovskite islands with an electrically insulating material in such semi-transparent devices should greatly increase their open-circuit voltage and fill factor, and thus overall efficiency. In addition, such a "shunt-blocking" technique should be advantageous for opaque devices, filling in pinholes resulting from defects in fabrication to minimise the impact of such pinholes upon device performance. We have previously shown that employing an insulating metal oxide honeycomb architecture, where perovskite material is embedded in the carefully designed pores of the scaffold, can reduce the shunting problem[176]. However, this technique requires multiple fabrication steps and has yet failed to deliver colour neutral transparency.

Alkyl silanes can make well covering molecular monolayers on different semiconductor and metal oxide surfaces, and it has been shown that a monolayer of long alkyl chain silane molecules can act as an electronic insulating barrier for charge transport [179]. Yaffe et al. demonstrated that the conductivity of alkyl based molecular monolayer attached to a silicon surface exponentially decreases with the molecular length [180]. Previous work has also shown that short alkyl silanes with functional groups used as effective interfacial layers in inorganic-organic hybrid solar cell [181] and perovskite solar cells - to modify device performances [182].

In this chapter a simple wet-chemical technique is presented to block shunting paths in partially covered perovskite films via the use of an insulating octadecyl-siloxane molecular layer. It is shown that this layer preferentially attaches to the exposed areas of electron transporting TiO_2, without obstructing the charge transport through the perovskite. As such, this treatment acts to selectively block shunt pathways and resultantly improves the

solar cell performance, leading to increased open-circuit voltage and a PCE of 6.1 % for neutral coloured semi-transparent perovskite cells with a full device AVT close to 40 %.

5.3 Results and Discussion

5.3.1 Self-assembly of shunt-blocking layer

An inexpensive and commercially available molecule Trichloro(octadecyl)silane ($CH_3(CH2)_{17}SiCl_3$; OTS) (Figure 5.1a) was employed as a surface modifier by dissolving it in toluene and immersing the perovskite-coated substrates for 10 minutes with subsequent toluene rinsing and drying at 60 °C (schematic shown in Figure 5.1b). In reaction conditions, OTS molecules hydrolyse to corresponding alkyltrihydroxy silanes (due to presence of about 0.05 % water in the toluene), then intermolecular condensation of -SiOH groups on neighbouring molecules form Si-O-Si (siloxane) bonds [183,184].

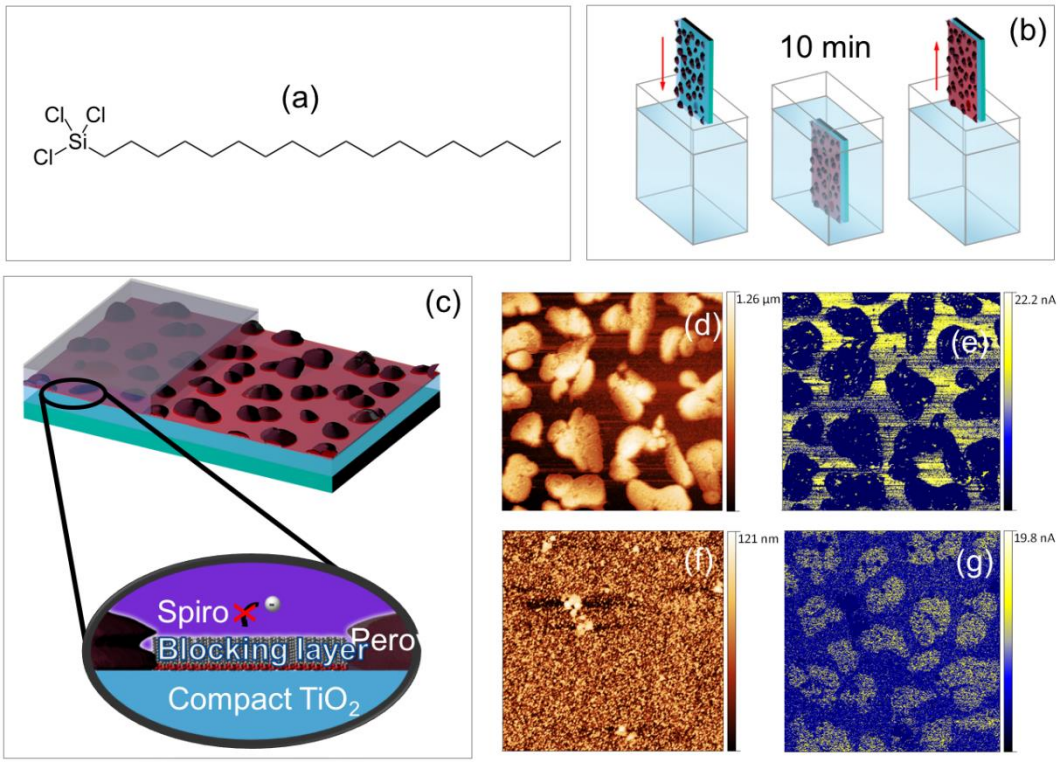


Figure 5.1: Representation of the $CH_3(CH_2)_{17}SiCl_3$ chemical structure (a). Schematic of the dip-coating process for the selective assembly of the Silane blocking layer (b). Sketch of the

components of the island-structured perovskite device with siloxane blocking layer between perovskite domains (c). Conventional (d) and conductive (e) AFM images of dewet perovskite domains on top of compact TiO_2 layer without OTS treatment. Conventional (f) and conductive (g) AFM images of compact TiO_2 layer after OTS treatment and subsequent removal of perovskite domains via DMF immersion. All AFM images represent a 40 x 40 µm scanned area.

The hydroxy groups on TiO_2 surfaces act as anchoring points for the alkylsiloxane or alkyltrihydroxy silanes by formation of Ti-O-Si bonds[185,186]. Due to the condensation reaction between silane molecules and TiO_2 surface, the alkyl chains are expected to be packed as we illustrate in Figure 5.1c. It has been previously reported that assembly of OTS on a TiO_2 surface results in a density of 4.3-4.8 molecules/nm^2 [187], and on SiO_2 this results in a surface which has a water contact angle of 112-120 ° [188]. To confirm that the treatment results in a similar coverage on compact TiO_2, the water contact angle of the TiO_2 films with the OTS treatment is measured, and a value of 112 ° is found (Figure 5.2), in good agreement with previous reports of well-packed monolayers.

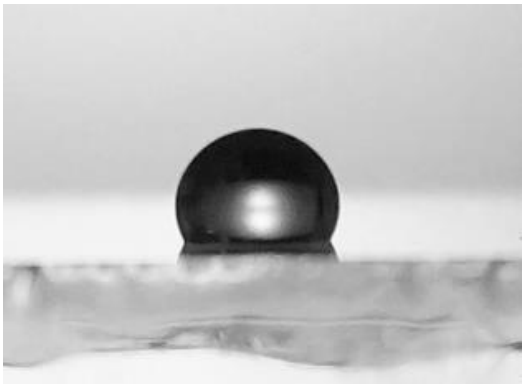


Figure 5.2: Contact angle measurement image of OTS treated FTO/c-TiO_2 surface showing contact angle of around 112 °.

In order to find out whether the insulating alkyl silane binds selectively to the uncovered area between the perovskite islands, conducting atomic force microscopy (c-AFM) was used on the pre and post silane-modified perovskite films on TiO_2 as well as modified TiO_2 surface after removing the perovskite layer. Figure 5.1d shows the topography image of

partially covered perovskite layer; the current mapping of the same area is shown in Figure 5.1e.

Visibly, the current flowing through uncovered area is much higher than that on perovskite islands. In full devices these uncovered areas can act as shunting paths when in contact with hole transporting material. Figure 5.3 shows the c-AFM image of modified perovskite films. The normal topography image reveals that the incubation has not done any detectable modification on the film morphology, on the other hand the c-AFM image shows that the conductivity on the perovskite island area are generally higher or equal to the uncovered area.

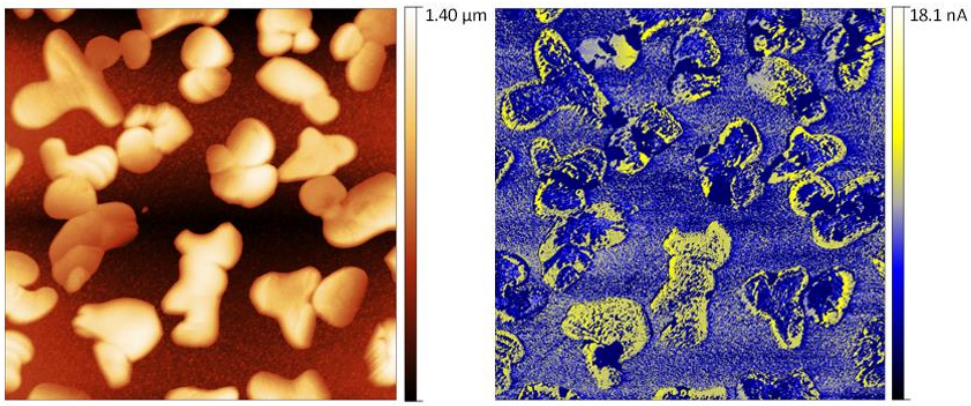


Figure 5.3: AFM (left) and conductive-AFM (right) after OTS treatment.

Figure 5.1f,g show the topography and current mapping of silane-modified surface, after the removal of perovskite with DMF. Even though the topography image does not show any features, the current mapping indicates that the area initially covered with perovskite displays higher current density than the remaining area. That suggests that the silane molecules bind to the exposed TiO_2 surface. The Fourier transform infrared (FTIR) spectrum (see Figure 5.4) of the silane modified surface (after removal of perovskite layer) shows IR features of alkyl chains.

Although it is not expected that the silane molecules rapidly attach to the perovskite film itself, there is a possibility of this happening, which could have the negative impact of inhibiting hole transfer from the perovskite to the hole-conductor. In order to asses if there is any negative influence on hole transfer, a photoluminescence decay study was performed. Continuous perovskite films on glass slides were treated with OTS solution and then coated with the hole conductor, spiro-OMeTAD.

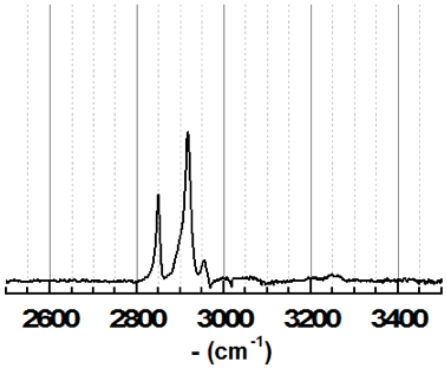


Figure 5.4: Absorption spectrum taken with a Fourier transform infrared (FTIR) spectrometer of the OTS treated substrates.

Figure 5.5 shows the PL decay for the perovskite films with and without OTS treatment, and with and without coating with spiro-OMeTAD. PL decay curves indicate that the quenching of PL due to hole transfer (manifested as sharper decay curves) is similar for both OTS treated and untreated films with even faster decay for the OTS treated device, indicating no negative effect from shunt-blocking treatment. There was no significant evidence found that the siloxane treatment changes the electronic transport properties at the perovskite and hole transporter interface, as reported by Zhang et al. [189].

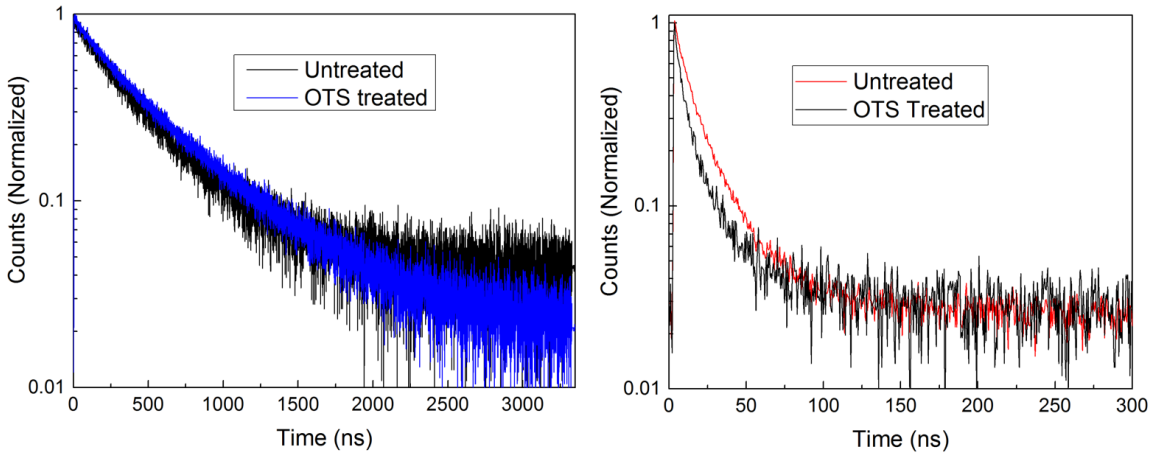


Figure 5.5: Time-resolved photoluminescence response measurement of dewetted semi-transparent perovskite cells without a quenching layer (left) and with Spiro-OMeTAD as a quenching layer (right).

Furthermore, the change in surface energy on TiO_2 and perovskite islands through the attachment of the OTS was compared. Thus, contact angle measurements were carried out with Chlorobenzene on uncovered FTO/c-TiO_2 substrates before and after the OTS treatment and then compared to substrates that were additionally covered with dewet perovskite films. The values and images are depicted in Figure 5.6 and an increase in contact angle on OTS treated TiO_2 surfaces and a significantly lower increase on OTS treated partially covered perovskite films occurs. These findings are consistent with the assumption that the OTS molecules preferentially attach to the uncovered TiO_2 surfaces.

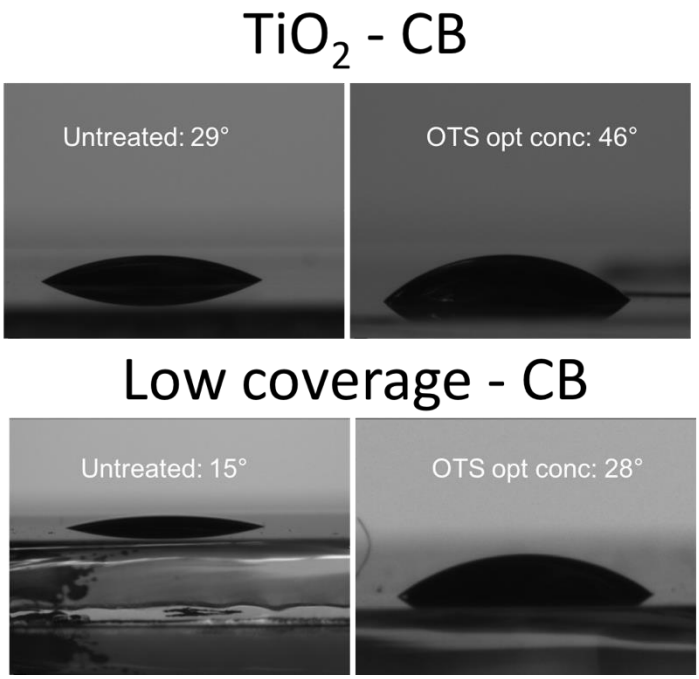


Figure 5.6: Contact angle measurement images of bare compact TiO_2 covered FTO substrates (top row) and compact TiO_2 covered FTO substrates with dewetted low-coverage perovskite (bottom row) before and after different concentrations of OTS treatment.

5.3.2 Solar cell fabrication

To gauge the effect of shunt blocking with the OTS treatment, solar cells were fabricated with spiro-OMeTAD as hole transporting material and evaporated Au as top electrode. Island-structured semi-transparent devices were prepared as described by Eperon et al [15]. In order to observe the effect of the treatment on device reproducibly as well as performance device statistics from a batch of 67 devices are quantified in Figure 5.7a-d. The standard deviation of working devices is much higher for the treated films than for the untreated ones (Figure 5.7a,c). On each substrate 8 different pixels (area 0.09 cm^2) were tested. Data points with very low power conversion efficiency (PCE < 0.1%) were filtered out.

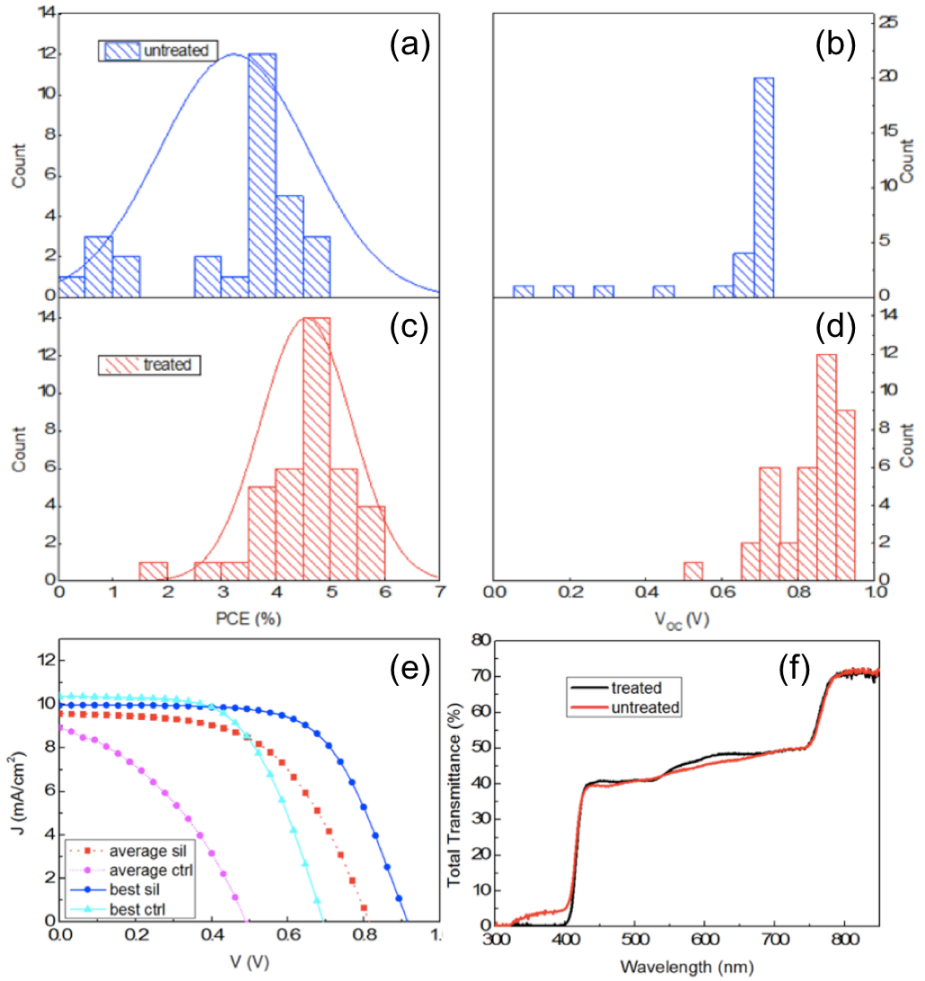


Figure 5.7: Histograms and fitted normal distributions of the measured V_{OC} of semi-transparent dewet perovskite cells before (a) and after (b) OTS treatment. Histograms and fitted normal distributions of the measured PCE of semi-transparent dewet perovskite cells before (c) and after (d) OTS treatment. Averaged J-V curves of 15 semi-transparent perovskite solar cell devices with non-transparent Au top-electrode before (magenta) and after (red) OTS treatment (including all devices above 0.1% PCE). J-V curves (scan speed: 0.38 V/s, scan direction: forward bias to short-circuit) of best preforming semi-transparent perovskite solar cell devices with non-transparent Au top-electrode before (cyan) and after (blue) OTS treatment (e). Total transmittance UV-vis spectra of top-electrode less semi-transparent before (red) and after (blue) OTS treatment (f).

Although several factors other than pinholes can be responsible for lower performance, the general yield of working solar cells was notably improved by 5 % upon treatment. Figure 5.7a and Figure 5.7b show the histograms of the V_{OC} and PCE of all working solar cells.

Not only was the open-circuit voltage and overall power conversion efficiency enhanced, but also the reproducibility of the devices was largely improved, which is evidenced by significantly lower standard deviation of the treated samples. The V_{OC} values of the semi-transparent films reach ~1 V and could so far only be achieved with fully covered perovskite films [15,154].

Figure 5.7e shows the average J-V characteristics of all functioning cells and the single J-V curves for the best performing treated and untreated devices under illumination. The low coverage of perovskite leads to semi-transparent devices with average visible transmittance (AVT) of ca. 45% (see SEM image in Figure 5.8) without top electrode. The J_{SC} of these semi-transparent films correlates with the coverage and therefore results in a trade-off between efficiency and transparency in the devices [15]. Consequently, at a given AVT of the device the J_{SC} will not be improved, as can be seen in the similarity of maximum currents of the different devices in Figure 5.7e. However, upon OTS treatment, it is observable that the V_{OC} and FF are significantly improved to reach a maximum PCE of 5.9 % (average PCE of 4.6 ± 0.8 %) compared to 4.3 % in control cells (average PCE of 3.2 ± 1.4 %). All the characteristic parameters are shown in Table 5.1.

Table 5.1: Average and maximum performance parameters of OTS treated (n = 39) and untreated (n = 28) semi-transparent perovskite devices.

Device type	J_{SC} [mA cm^{-2}]	V_{OC} [V]	FF [-]	PCE [%]
OTS treated avg.	9.6±0.8	0.83±0.09	0.56±0.06	4.6±0.8
Control avg.	8.9±1.4	0.60±0.16	0.52±0.13	3.2±1.4
OTS treated max	10.0	0.92	0.64	5.9
Control max	10.4	0.69	0.60	4.3

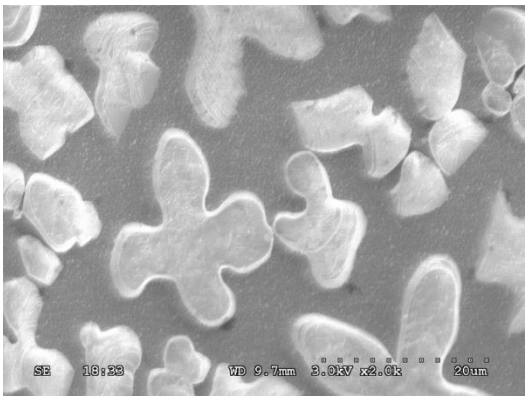


Figure 5.8: Top view SEM image of the dewetted perovskite islands on top of c-TiO_2 coated FTO glass.

Notably, these cells show current-voltage hysteresis with and without the OTS treatment (Figure 5.9), consistent with previously reported results[84], and the steady-state efficiency measured at the maximum power point is lower than the PCE derived from the J-V scan (Figure 5.10). The fact that the OTS treated devices function as solar cells and produce similar photo-current density suggests that the OTS molecules are not preventing the charge collection.

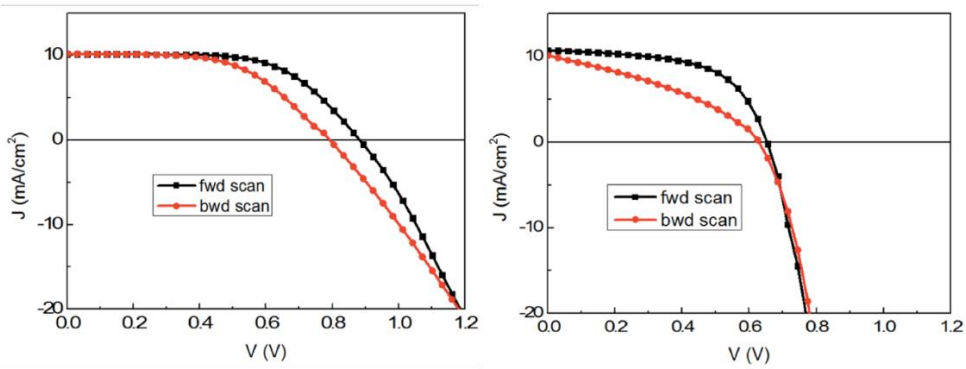


Figure 5.9: J-V characteristic curves of OTS treated device (left) scanned with a speed of 0.38V/s from forward bias to short circuit (black line with squares: J_{SC} = 10.2 $mAcm^{-2}$, V_{OC} = 0.89 V, FF = 0.60, PCE = 5.5%) and from short circuit to forward bias (red line with circles: J_{SC} = 10.2 $mAcm^{-2}$, V_{OC} = 0.80 V, FF = 0.54, PCE = 4.4%) showing hysteresis. J-V characteristic curves of untreated device scanned with equal parameters (black line with squares: J_{SC} = 9.9 $mAcm^{-2}$, V_{OC} = 0.63 V,

FF = 0.69, PCE = 4.3%) and from short circuit to forward bias (red line with circles; J_{SC} = 9.9 $mAcm^{-2}$, V_{OC} = 0.63 V, FF = 0.58, PCE = 3.6%) showing anomalous hysteresis.

The attachment of the long alkyl chains on the perovskite surface would have hindered the contact between perovskite and hole transporting material and extraction of photo-generated holes, in turn lowering the photovoltaic performance of those devices. Furthermore, according to the proposal that the interface between the perovskite domains and the charge collection layers is not affected, the assumption is that hysteresis or stabilized maximum power performance will remain unimproved upon treatment.

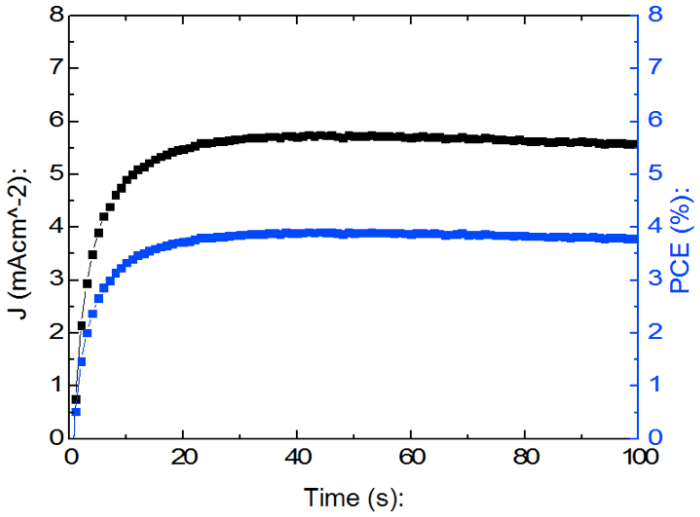


Figure 5.10: Graph showing the current-density (black squares) and PCE (blue squares) measured over time at maximum power point voltage (0.68 V) determined from the reverse scan curve.

The averaged J-V curves of the treated and untreated devices were fitted to a single-diode equivalent circuit model after Unger et al. [163] to determine the series and shunting resistances (see Figure 5.11). Consequently, it was determined that R_S = 3.8 Ωcm^2, R_{SH} = 1.1 x 10^2 Ωcm^2 for the untreated and R_S = 10.9 Ωcm^2, R_{SH} = 4.5 x 10^8 Ωcm^2 for the post-treated cells, revealing a large increase in R_{SH}, which can be attributed to the insulating character of long alkyl chains blocking the contact between electron and hole transporting materials. The slight increase in series resistance could be speculatively caused by

thickness difference in hole-transporting layer, which could stem from a change of the spiro-OMeTAD precursor solution wetting upon treatment[190].

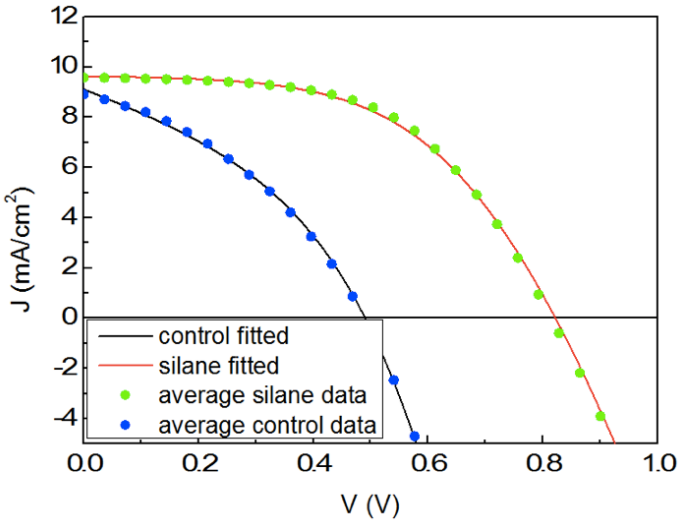


Figure 5.11: Combined J-V curves of untreated and OTS treated semi-transparent perovskite cells and one-diode model fitting comparison.

The real equivalent circuit of the semi-transparent perovskite cells can be modelled as a double heterojunction diode (compact TiO_2/perovskite/spiro-OMeTAD) in parallel with an n-p heterojunction comprising compact TiO_2/spiro-OMeTAD (see Figure 5.12 right). Hence, the shunt resistance, represented by the TiO_2/spiro-OMeTAD junction, is in fact a diode itself and the current which passes through it will have a bias dependence. Therefore, the one diode model, which assumes a fixed bias independent shunt resistance, only gives a first approximation to the changes which occur within the actual cell upon OTS treatment. A measurement of the J-V characteristic curves of TiO_2/spiro-OMeTAD and TiO_2/OTS/spiro-OMeTAD n-p diodes, prepared in the same way as solar cell devices but without the perovskite layer, indicated that the blocking behaviour of the OTS treated diode is extended to much higher voltages when compared to the untreated diode (Figure 5.12 left). Combining these measurements with calculated fractional J-V data from a fully covered well performing device,[173] replicates the significant gain in V_{OC} upon OTS treatment.

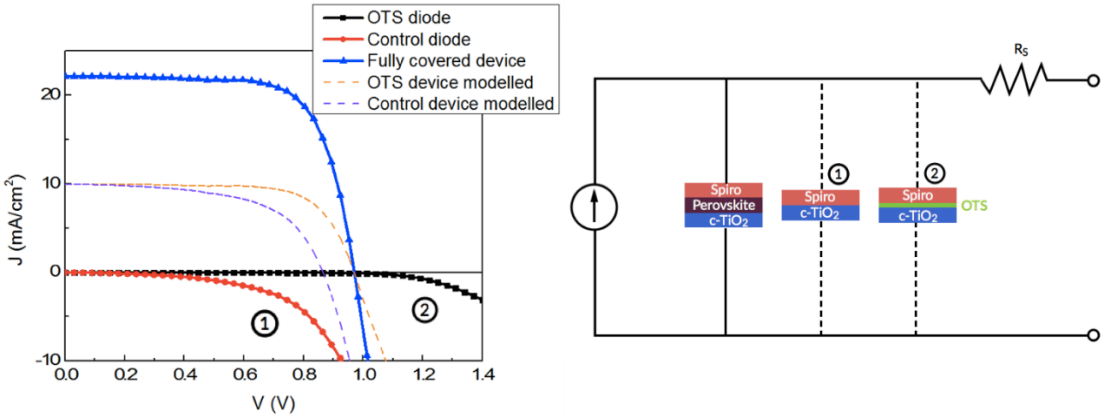


Figure 5.12: Left, J-V curves of a spiro-OMeTAD-compact/OTS/c-TiO_2 diode (black) and spiro-OMeTAD-compact/c-TiO_2 diode (red), fabricated in the same way as the perovskite solar cells but without perovskite layer. Calculated combined J-V curves of a measured fully-covered perovskite cell[173] with the OTS treated diode (dashed orange) and with the untreated diode (dashed purple) by assuming a coverage of 45%. Right, potential equivalent circuit diagram of perovskite solar cell with shunting path through spiro-OMeTAD-compact/c-TiO_2 diode (1) or through spiro-OMeTAD-compact/OTS/c-TiO_2 diode (2).

Beyond the results presented above, the device efficiencies were further improved: The FF was either enhanced with a treatment of the perovskite films with iodopenta-fluorobenzene (IPFB), which was previously reported to reduce the recombination at the interface with the hole-transporting material. [191] Or the J_{SC} and FF was improved with a $TiCl_4$ treatment of the c-TiO_2 layer, prior to perovskite deposition[192]. Figure 5.13 shows the J-V curves of the resulting champion cells, which exhibit a PCE of 6.6 % and 7.4 % for the IPFB and $TiCl_4$ enhanced cells respectively.

5.3.3 Larger active-area solar cells

Large area cells that are required for commercial applications could be more sensitive to the effect of shunting. Consequently, another test was carried out on set of devices with more than 7 times larger area (0.71 cm^2) where the shunting effects are more prominent.

The results are presented in Figure 5.14**,** where the PCE is improved from 4.2 % to 5.2 % comparing cells without and with the OTS treatment. Again, the reason for this enhancement stems from the significantly improved V_{OC} from 0.69 V to 0.89 V.

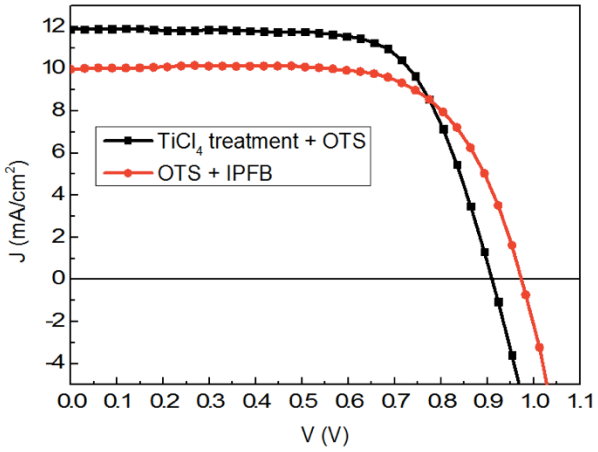


Figure 5.13: J-V curves (scan speed: 0.38 V/s, scan direction: forward bias to short-circuit) of optimized OTS treated semi-transparent perovskite cells with $TiCl_4$ post treatment of the compact TiO_2 layer (black line with squares; J_{SC} = 11.9 mAcm^{-2}, V_{OC} = 0.92 V, FF = 0.68, PCE = 7.4 %) or IPFB passivation treatment (red line with circles; J_{SC} = 10.0 mAcm^{-2}, V_{OC} = 0.98 V, FF = 0.67, PCE = 6.6 %).

5.3.4 Fully transparent device fabrication

The real world application of semi-transparent perovskite solar cells requires both the top and bottom electrodes to be semi-transparent, i.e. in the present case the reflecting top Au electrode needs to be replaced. A set of semi-transparent devices was fabricated using a laminated Nickel micro-grid (with an AVT of 85 %) as a top electrode, as reported previously [86].

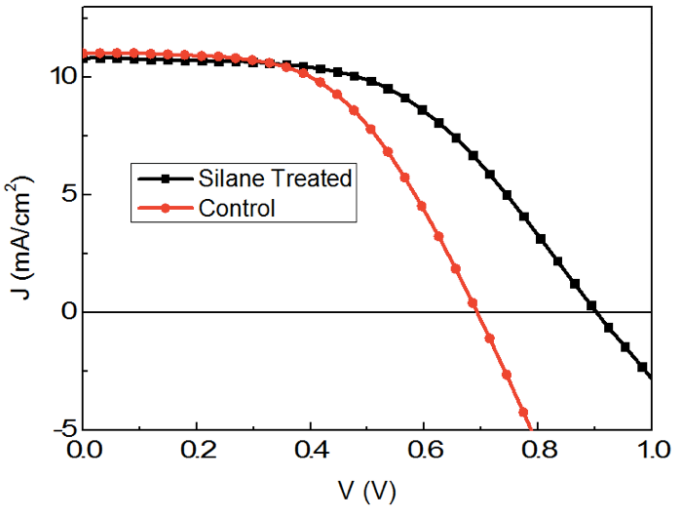


Figure 5.14: J-V curves (scan speed: 0.38 V/s, scan direction: forward bias to short-circuit) of semi-transparent solar cells with (black line with squares; J_{SC} = 10.8 mAcm^{-2}, V_{OC} = 0.89 V, FF = 0.54, PCE = 5.2%) and without OTS treatment (red line with circles; J_{SC} = 11.0 mAcm^{-2}, V_{OC} = 0.69 V, FF = 0.55, PCE = 4.2%) on 0.71 cm^2 exposed devices.

Very little loss in performance is observable, as compared to the devices incorporating a metal electrode, and achieve a record PCE of 6.1 %, which is presented in Figure 5.15a. Notably, in previous reports of employing this gird electrode, especially in semi-transparent perovskite films, the PCE has typically been lower than the control devices, coming mostly from a slight drop in V_{OC} [84,86]. This may be due to the PEDOT employed being especially effective at penetrating pinholes through the perovskite and spiro-OMeTAD layer, which here are blocked by the presence of the OTS layer. The measured total transmittance of the device, which we show in Figure 5.15b, was used to calculate the AVT, which is high at 38 %. At the time of obtaining these results, the performance parameters represent the highest efficiency for a neutral colour semi-transparent perovskite solar cell [80,175]. Thin-film perovskite devices, with brown-tinted colour, have been reported to be more efficient, with AVT of ~37 % and PCE of 7.8 %, but the presented surface-treated solar cells remain neutral coloured (Figure 3b) and are therefore probably more

attractive for building applications. The best performing previous neutral-coloured semi-transparent device had an AVT of ~30 % and PCE of ~5 %.

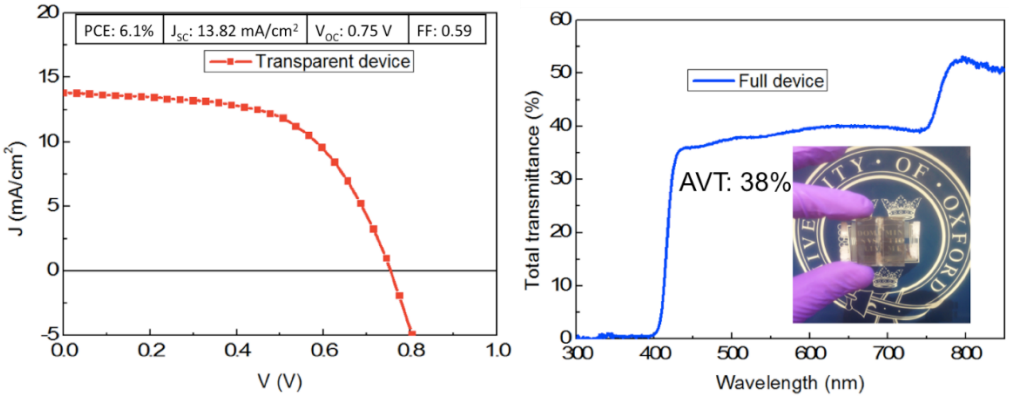


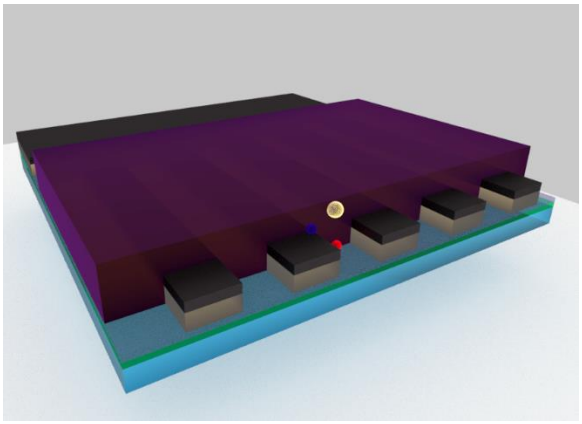
Figure 5.15: Characteristic J-V curve (scan speed: 0.38 V/s, scan direction: forward bias to short-circuit) of best performing semi-transparent dewet perovskite solar cell after OTS treatment with transparent top-electrode (a). Total transmittance UV-vis spectrum of best performing semi-transparent perovskite cell after OTS treatment with transparent top-electrode (b). Photograph of best performing neutral colour semi-transparent device with transparent top-electrode.

5.4 Conclusion and outlook

In summary, it was demonstrated how a simple molecular post-treatment of perovskite films on TiO_2 substrates prevents the formation of shunting paths, which are detrimental for solar cell performance. In this treatment, alkyl-siloxane molecular layers preferentially bind to the TiO_2 surfaces at pinhole sites without hindering charge transport across the active layers. In "island-structured" perovskite solar cells with a low surface coverage, a significant increase in the shunt resistance is reached due to the post treatment, which results in a better solar cell performance and yield. In large area (0.71 cm^2) cells, a relative improvement in PCE by 20 % is observed. Remarkable 6.1 % PCE were achieved for neutral colour semi-transparent (entire cell AVT of 38 %) perovskite cells by using OTS assembly. This low cost and easily scalable shunt path blocking technique will have wide application in improving the yield as well as efficiency of large area perovskite solar cell

and light emitting devices, which is specifically advantageous for commercial exploitation of perovskite solar modules in BIPV applications.

6 Extraordinary Charge Carrier Behaviour in Back-contacted Perovskite Thin-Films



6.1 Context and summary

Lead-halide perovskites have emerged quickly as high-performance photovoltaic materials. For future application in commercial thin-film photovoltaics, it could be beneficial to implement these materials in efficient interdigitated back contact architectures, which are currently the performance-leading technology in silicon-based photovoltaics. Such a device architecture has several advantages, including better light management and better surface passivation strategies. Here, a technique was developed that allows for the simple fabrication of a back-contact device architecture for perovskite solar cells. A testing platform was found that allows to study the recombination at perovskite/electrode interfaces within an operating device and quantifying the effect of

charge carrier transport characteristics on photovoltaic performance. By spatially mapping the external quantum efficiency and photoluminescence it was found that uniform photocurrent generation can be achieved. Furthermore, by varying the pitch distance of the back-contacts the transport characteristics of charges was analysed. Astonishingly, after injection of photo-generated electrons into the electron transporting electrode, holes left in the perovskite layer contribute to substantial photocurrent over distances far exceeding their reported thin-film diffusion lengths. The development of electrodes capable of fast electron extraction opens a pathway to well performing perovskite back-contact devices for large-area fabrication.

6.2 Introduction

Performances of perovskite solar cells have improved quickly from the original device designs that were more similar to dye sensitized solar cells[193,194] than other thin-film technologies. Over time the predominant device architecture emerged from the mesoporous oxide containing design to a planar heterojunction in which the intrinsic semiconducting perovskite layer is sandwiched between n-type electron transporting and p-type hole transporting layers that are again interfaced with planar electrode layers. This design has led to lab cell efficiencies of up to 22% making them comparable to c-Si, after only a few years of development[49,81,139,194,195]. This family of materials is easily processable from solution at low temperature[196], utilizing readily available and earth-abundant materials[197], making them highly attractive for commercial photovoltaics. To this point commercial applications of perovskite solar cells have not reached the market and it remains to be identified which device design will qualify as the most feasible for mass fabrication.

The solar cell material with currently the by far biggest market share remains to be Silicon due to the advantageous abundance of the element and the prices that are dropping significantly as an effect of mass production despite being energy intensive. The economic competitiveness of photovoltaic technologies is predominantly dependent on system cost, the lifetime and the efficiency as these values allow to estimate the price of the energy that the system will generate. The power conversion efficiency has a directly linear effect to the energy price and therefore it is understandable that solar manufacturers have spent many efforts to maximize the efficiency and minimize the production costs to defend their market position.

A large improvement for silicon solar cells has been achieved by using a design that contacts the absorbing layers entirely from the back side opposite of the side exposed to radiation. So called back contact (or rear contact) solar cells, which incorporate such a design, have been explained in section 2.6 and have demonstrated substantial advances for silicon solar cells. A sufficient diffusion length represents the crucial material property to enable rear contact solar cells. The current understanding of charge diffusion and collection within perovskite solar cells leads to the assumption that the distance between the positive and negative electrodes needs to be shorter than the diffusion length of charge carriers to ensure an efficient charge carrier collection. Therefore, thin-film materials that usually have short absorption depths combined with relatively short diffusion lengths would require equally short spacing between the electrodes to efficiently collect charge carriers. Defect-free single crystals of intrinsic silicon with diffusion lengths in the range of 100 – 300 µm consequently have all the right necessities to be back contacted. On the other hand, the grain boundaries in poly-crystalline materials present obstacles for efficient charge diffusion due to recombination at grain boundaries and require therefore a more difficult manufacturing process to reach shorter spacing.

A similar characteristic is present in the well performing perovskite solar cell materials. Single crystal studies suggest charge diffusion lengths as long as 175 μm[198], while vertical diffusion in polycrystalline thin films is reduced to around one micrometre[51,199] due to the presence of grain boundaries that act as recombination centres[200]. In a recent study, it was shown that the diffusion length of electron and hole pairs can greatly exceed predictions, which could be derived from spectroscopic constants, due to the effect of photon recycling[201]. Yet, even in this scenario, the diffusion length of a perovskite solar cell is on the order of a few micrometres. Manufacturing a well performing back-contacted perovskite thin-film is therefore a technical challenge. While solving these challenges the question appeared whether the diffusion length is indeed the main limiting factor for the spacing of the electrodes or if it is possible to introduce a design that can allow for the effective charge collection despite the fundamental limitations of substantial charge carrier recombination at longer distances in perovskites.

It is well known that in hybrid metal-organic perovskites an electron and its corresponding geminate hole become independent from each other within few femtoseconds after generation[144]. However, on average, electron and hole populations are still coupled to each other. This leads to ambipolar transport with a diffusion coefficient given by:

$$D_a = \frac{k_B T}{q} \frac{(n+p)}{\left({}^{n}/_{\mu_p}\right) + \left({}^{p}/_{\mu_n}\right)} \tag{6.1}$$

In the case of balanced mobilities ($\mu_p \approx \mu_n$), which can be assumed to be the case for perovskites due to various reports on effective masses being on a similar order[18,202], e^- and h^+ will simply diffuse following the Einstein relation. Recently it has been demonstrated by Leijtens et al.[203] that evidently electrons tend to be trapped with much higher probabilities than holes. Depending on the charge carrier density, holes could then diffuse

better through perovskite thin-films than electrons. This material property can be used to design the ideal back-contacted perovskite solar cell.

In this chapter, a novel back contacted perovskite solar cell device architecture is introduced, which allows to test several material charge transport and extraction properties and can lead to a back-contacted thin film perovskite solar cell without the sacrifice of involving costly manufacturing processes.

6.3 Results and Discussion

6.3.1 Optical model for absorption improvement estimation

In sandwiched devices, it is a requirement that the perovskite film is covered with a hole or electron transporting material and an additional transparent electrode. Since these materials generally have a specific electronic requirement, their optical properties can usually hardly be engineered for ideal conditions, i.e. minimised reflection and maximised transmission to the absorbing layer. In back contacted devices on the other hand the perovskite layer can be covered with materials that enhance exactly these parameters. To quantify the effect of such an improvement, the reflection, transmission and perovskite absorption spectra were modelled with a transfer matrix model for two common device stacks of each architecture type. The results are plotted in Figure 6.1 and show a big improvement in perovskite absorption for a back contacted device, in which the active layer is covered with a layer of PMMA instead of PEDOT and indium tin oxide (ITO), commonly used in sandwiched devices. The absorption enhancement of over 20 % in some spectral regions comes from reduced reflection of PMMA due to an advantageous refractive of ca. 1.5 lying between perovskite and air. This could lead to a significantly improved photocurrent and therefore PCE and these results are encouraging the efforts to develop back contacted perovskite devices.

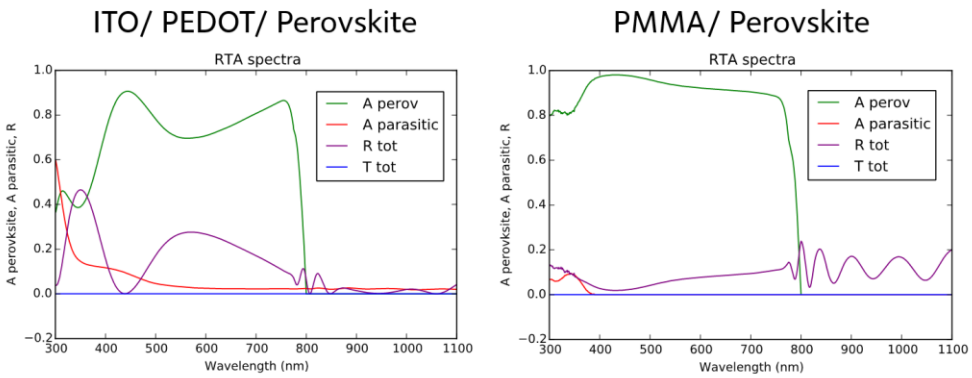


Figure 6.1: Optical model results for absorption in perovskite if covered by PEDOT and ITO as in a commonly found sandwiched devices or covered by PMMA as in a back contacted device.

6.3.2 Architecture and fabrication

To fulfil all the material specific requirements of metal-halide perovskites, an architecture with interdigitated electrodes is desired that would benefit from a simple fabrication process and would allow to be patterned at high enough resolution. With those requirements in mind a design was invented that would include one bottom electrode spreading over the entire substrate area and the other electrode in the shape of fingers to be separated by an insulating material. The design concept is shown in Figure 6.2 and a very similar device architecture has been simultaneously developed by Jumabekov et al.[204], who named it quasi interdigitated back contact (QIBC) design. Diffusion lengths in the order of 1 µm required the finger width and the pitch between the fingers in the original design to be on the same length scale. In principal, the back contacted devices do not require the use of a transparent substrate and bottom electrode as the photons are illuminated from the front side. However, due to the previous device fabrication experience with transparent substrates they were fabricated on top of FTO coated glass substrates. Two different layer stack orders were studied, which are generally referred to as standard and inverted structures in literature[197]. Here, the standard order refers to the stack in which the n-type contact is deposited at the bottom (on top of the FTO/glass substrate) and the p-

type contact is patterned in finger shapes and separated by an insulator. Respectively, the inverted structure involves the p-type contact to be coated throughout the substrate and the n-type contact to be patterned in finger shape.

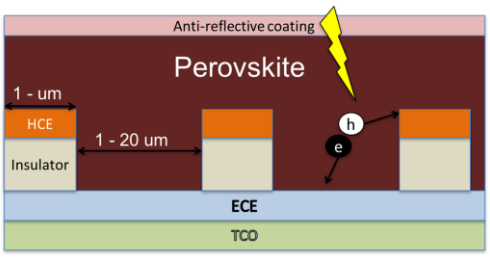


Figure 6.2: Illustration of the back contacted perovskite solar cell architecture.

The fabrication of the all back-contacted devices was achieved via a one-step photolithography process, as illustrated in Figure 6.3. First, a conducting substrate is uniformly coated with n-type or p-type material to act as an electron/hole accepting layer. The counter electrodes were fabricated by depositing a layer of photoresist on top of the bottom selective contact and exposing it via masked UV-light (1). Subsequently, the unexposed resist volumes are removed by immersion into a developer bath (2). An insulating Al_2O_3 layer and a conducting metal layer are coated directionally via electron beam evaporation (3) and then lifted-off in a solvent bath to leave behind the finger pattern of insulator and counter electrode (4). After hole or electron selectivity of the top electrode is attained with different methods, a ca. 300 nm thick continuous film of perovskite is deposited, followed by the deposition of a layer that acts passivating, encapsulating and beneficially also anti-reflecting (5).

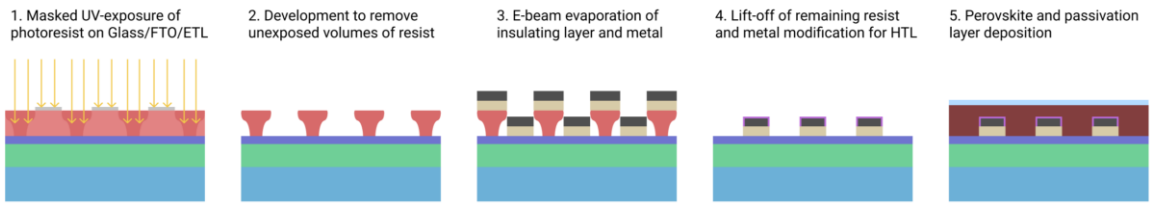


Figure 6.3: Illustration of the processing steps for back contacted perovskite solar cells.

The first fabrication challenge emerged for the lithographic process, as resolutions of 1 µm are difficult to achieve with simple masked photolithography. To avoid interference effects that prevent nanometre precise masked exposure, contact mode is applied. Furthermore, the efficient lift-off of relatively thick layers is difficult to achieve without a suitable undercut profile of the resist side-walls. It is crucial for the solvent to be able to reach and dissolve the remaining resist blocks that lie underneath the evaporated insulator and metal. Such an under-cut profile is visible in the semi-cross sectional SEM image of a patterned resist after development of an image-reversal resist shown in Figure 6.4a. Defect free patterning of the top electrode is a requirement to prevent shunting paths that occur if both electrodes get contacted anywhere within the device. After sufficient optimization of the process, fabricating patterned back contact devices with high quality was possible, as shown in the microscope images in Figure 6.4b, c.

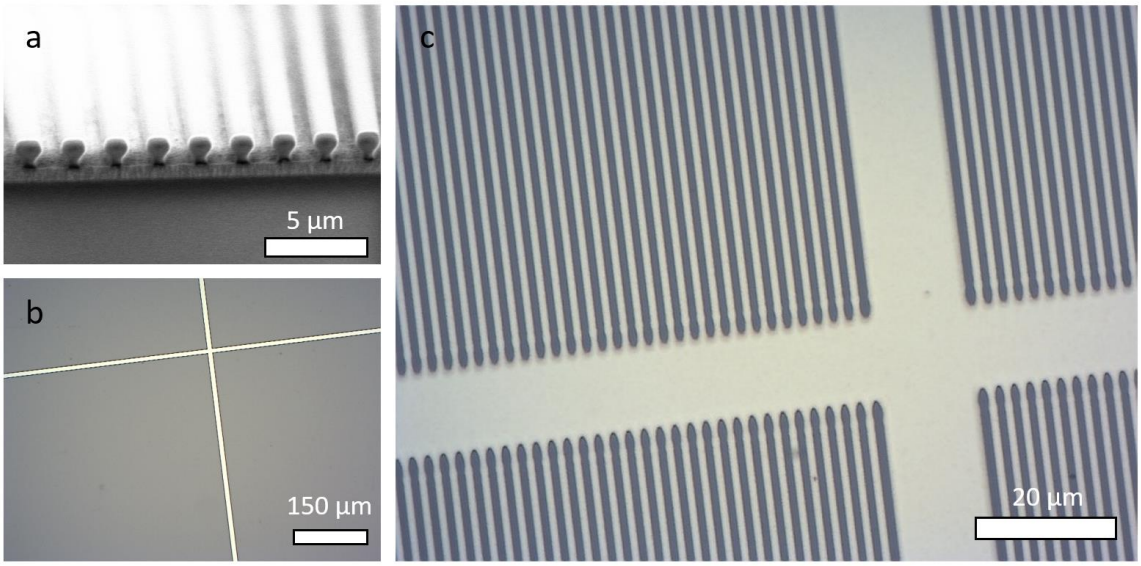


Figure 6.4: Semi-cross sectional SEM image of patterned and developed photoresist with visible undercut profile (a). 10x (b), 100x (c) magnified optical microscope image of patterned finger electrodes.

Several techniques were tried to enable the hole- or electron-selectivity of the patterned top contact. This required the entire exposed surface area of the electrode to be covered

with a p-/n-type material having energy levels that allow for efficient hole/electron extraction. Any area of the interface between the active perovskite layer and the top electrode that is not blocking holes/electrons would represent a centre for recombination and therefore a loss in energy.

6.3.3 Regular device improvements

The initial attempt to fabricate a photovoltaic cell with back contacts involved the use of a compact TiO_2 layer as electron accepting layer at the bottom and bare gold without any coating or modification as the p-type contact. Au has a favourable work function of - 5.1 eV, close to the valence band energy of ~ - 5.5 eV in perovskites[141], to form a Schottky barrier for electrons at the interface. This concept has been proven to work (with severe hysteresis effect and extremely low stabilized power output) within sandwiched devices[205–207].

A ca. 350 nm thick $CH_3NH_3PbI_3$ based perovskite layer was coated over the back-contacting electrodes and subsequently covered with a <50 nm thick layer of PMMA to protect it from moist air (see cross-sectional SEM image in Figure 6.5a). The dimensions can be determined from the image scale and the ~500 nm thick FTO layer appears to be covered with a <50 nm thick layer of compact TiO_2. The patterned electrodes consist of 100 nm thick Al_2O_3 and 100 nm Au and have a width as well as a pitch equal to 1 µm. The result of the J-V measurement with the highest PCE is presented in Figure 6.5b and it was found that it is possible to fabricate a working device (PCE = 1.3 %) with bare Au and no hole selective interfacial layer. However, the low fill factor and the large negative gradient of the light- and dark-current curves is an indicator for significant shunting in the device. The stronger hole-selectivity of the hole-conducting electrode is therefore suggested for the fabrication of better performing back-contact devices. The assumption is that too much recombination of charge carriers occurs at the gold/perovskite interface.

In order to develop an efficient device, the hole transporting material needs coverage of the entire exposed top electrode, without creating shunting paths to the bottom electrode. This proves to be a challenge, as directional deposition techniques such as evaporation can only be used to cover the top surface of the metal, but not the remaining sides, which would still be connected to the surrounding perovskite and allow charge carriers to recombine.

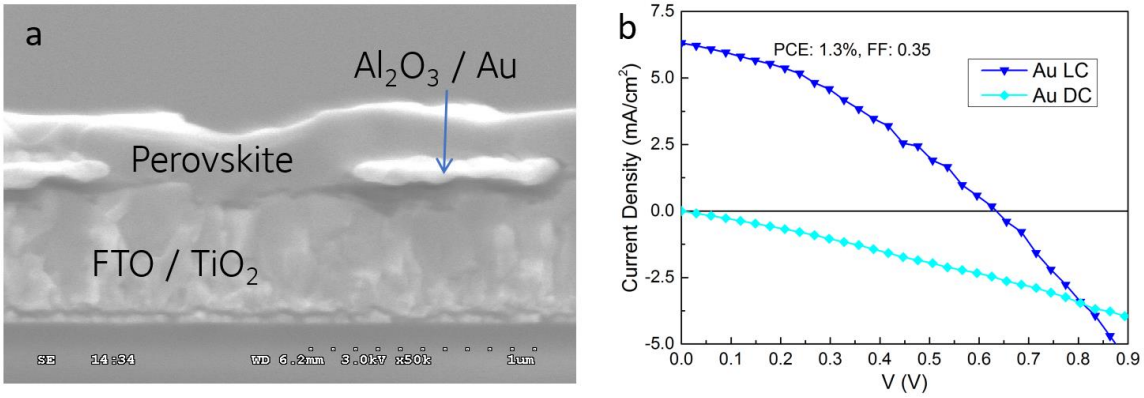


Figure 6.5: Cross sectional SEM image of back contacted perovskite solar cell with Au as anode (a). J-V characteristic of Au based back contacted perovskite solar cell (b).

Therefore, two solutions were proposed to solve this problem. Figure 6.6 shows the schematics of the concepts, which follow two different paths. One path (Figure 6.6a) involved the evaporation of a thin NiO layer as hole transporting material on top of the Au electrode before lifting off the photoresist. The remaining walls of gold would become electrically insulated with the selective self-assembly of a thiol-alkyl monolayer. The thiol head group would preferentially attach to the gold surface upon being immersed into solution and the long alkyl chain would later act as an insulator to block recombination paths that could hinder higher V_{OC}. The other solution of achieving hole selectivity for the patterned top metal electrode involves the use of Ni and the formation of an oxidised NiO shell (Figure 6.6b). The Ni layer could either be oxidised by exposing the electrode to an O_2 plasma treatment or alternatively by annealing at high temperature in air.

Unfortunately, the selective attachment of the insulating SAM lead to wetting difficulties of the perovskite layer and therefore it was impossible to achieve competitive device performances. Consequently, the second solution was chosen for the incorporation of a hole transporting material (HTM).

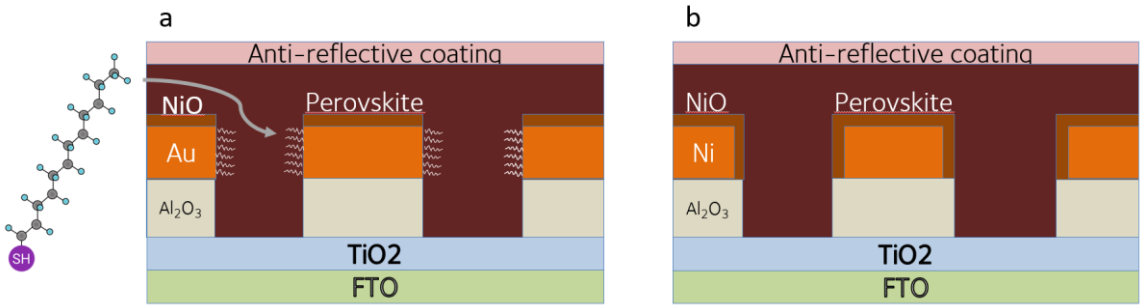


Figure 6.6: Illustrations of designs to modify top electrodes for better hole-selectivity. First design uses evaporated NiO as HTM and insulating SAM to block exposed Au sides (a). Second design incorporates a NiO shell around Ni electrode as HTM (b).

Both Ni/NiO electrode devices, treated either via annealing or O_2 plasma etching, were tested under simulated sunlight at $AM_{1.5}$ and the current voltage characteristics were measured as plotted in Figure 6.7. The devices show photovoltaic feasibility for rear-contacted perovskite solar cells. When scanned in reverse bias direction PCEs of 0.6 % and 3.4 % were achieved for the O_2 plasma etched and annealed devices respectively. A significant difference in short circuit current (4.7 mA/cm^2 and 10.8 mA/cm^2) and fill factor (0.19 and 0.47) is noticeable when comparing the two differently oxidised electrodes. The S-shapes of the O_2 plasma treated J-V curves under light suggest that charge extraction is prohibited by an energetic barrier at the interface. This agrees with the shape of the J-V curve in the dark, which shows that barely any current is leaking at higher bias voltage. Therefore, it is likely that the O_2 plasma treatment leads to a thicker NiO shell, which might prohibit efficient charge extraction.

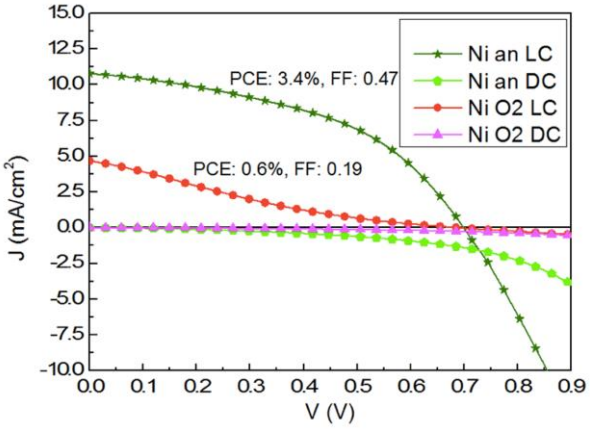


Figure 6.7: J-V characteristics of back contacted devices with oxidised Nickel shell from annealing and O_2 plasma treatment in light and dark.

The charge extraction behaviour was further analysed by spatially resolving the external quantum efficiency (Figure 6.8a, b) and photoluminescence response (Figure 6.8c, d) over a distance of 50 µm across the electrodes when illuminated with a laser wavelength of 510 nm. When comparing the magnitude and the shape of the average projected EQE (ratio between incoming photons from laser to generated electrons in collected photocurrent) of each of the devices a remarkably enhanced charge extraction behaviour is found in the Ni/NiO annealed device. There appears to be much less variation of extraction efficiency for the optimised annealed devices, leading to the conclusion that the hole extraction has been enhanced, while the strong decays above the p-type electrodes within the plasma treated devices suggest poor charge extraction. A similar behaviour is noticeable when comparing the PL emission intensity variations along the electrodes, which appear to be again less for the annealed devices. However, a drop with the same periodicity as the electrode pitch is obvious, which suggests that the electrode type above which the PL intensity is larger allows for more charge recombination and therefore less charge extraction. There appears to be a stronger averaged PL response for the annealed devices and one explanation for this effect could be additional non-radiative recombination in the plasma treated devices. This could be a consequence of increased surface recombination

due to overall weaker extraction behaviour of the electrodes. More spectroscopic analysis is needed to support this theory.

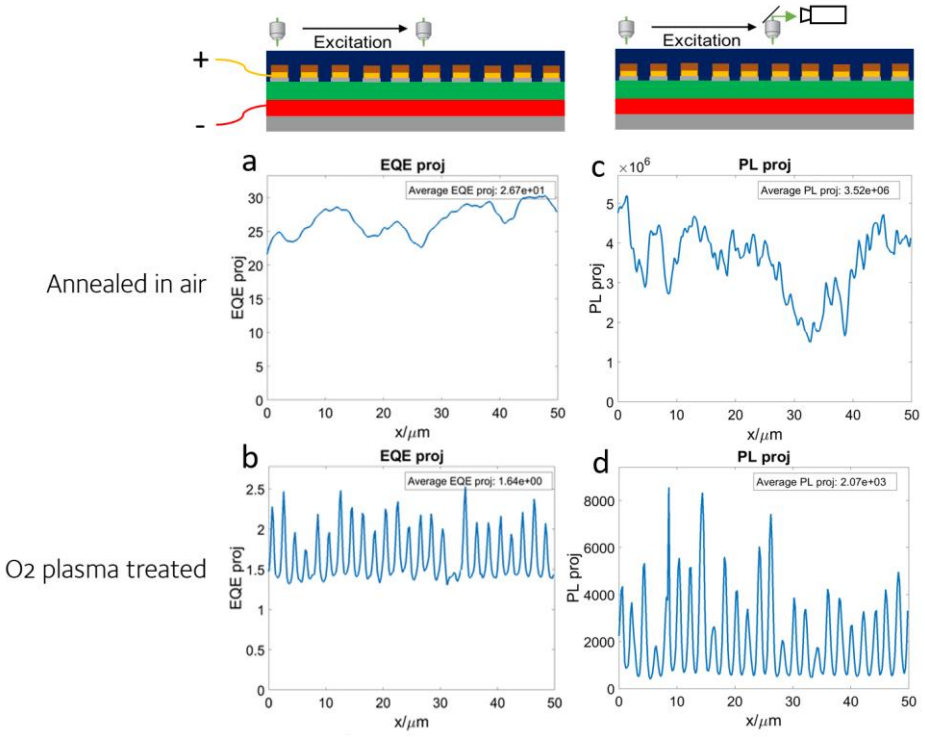


Figure 6.8: Spatially resolved projected EQE (a, b) and PL intensity (c, d) of back contacted devices with oxidised Nickel shell from annealing (a, c) and O_2 plasma treatment (b, d).

6.3.4 Charge transport phenomena

An even more remarkable result was found when the excitation spot was moved beyond the last finger electrode, as plotted in Figure 6.9. Expected was a quick decay in photocurrent, which might be improved by a photon recycling effect that had been found in perovskite films before[208]. Instead the outcome was an unexpectedly low decay, showing that even at distances as far as 200 µm away from the last p-type electrode, the photocurrent only dropped about 4.5 x when compared to the currents measured directly next to the electrode.

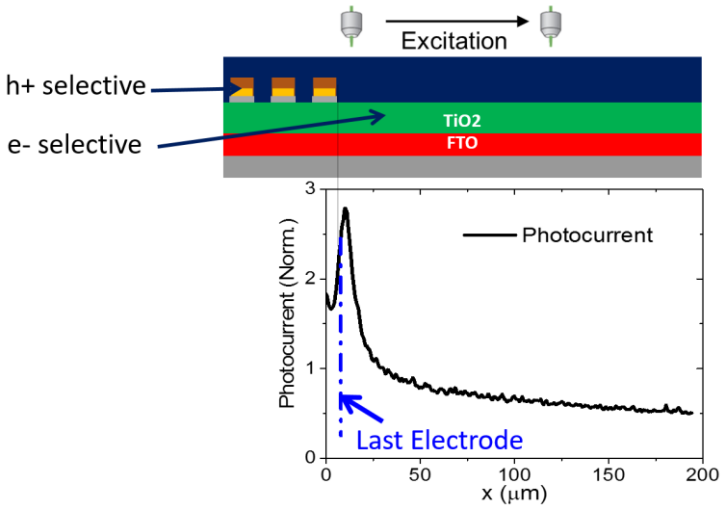


Figure 6.9: Normalised spatially resolved photocurrent when exciting beyond the last p-type electrode.

This finding would open the door for the development of efficient devices with pitch distances a lot longer than the original 1 µm, which was chosen due to diffusion lengths published in literature. Hence, devices with electrode pitch of 5 µm, 10 µm and 20 µm with the same finger width of 1 µm were fabricated (see illustration and microscope images in Figure 6.10a,c,d,e). When testing these devices with coated perovskite under simulated sunlight, the results were not as drastic but showed a similar trend, as photocurrents only dropped ca. 4 x in the devices with pitch of 10 µm and 20 µm (see Figure 6.10b). Notably an analogous behaviour as in the mapped photocurrent measurements occurred, with a quick drop within a short distance and a following almost non-declining tail.

Early reports on charge transport in perovskite have shown that in a single crystal of lead iodide perovskite, diffusion lengths of 175 µm can be achieved, and even transport distances of 3 mm can be found for individual charge carriers[198]. However, in thin films the diffusion length is thought to strongly decrease due to high densities of trap states at the grain boundaries[209,210]. Published measurements indicate that diffusion lengths of 1 µm in a film should be expected[51]. Relating the above results with the one-dimensional charge transport characteristic in sandwiched devices[211,212], allows to state that the photocurrent

is proportional to the negative exponential of the absorber thickness divided by the diffusion length as $J_{photo} \propto \exp(-W/L)$. However, applying this model to the measured decay characteristic in Figure 6.9 or even Figure 6.10b would mean a diffusion length that is orders of magnitude higher than the currently reported values for perovskite thin-films. Furthermore, very slow recombination velocities should be assumed, far beyond the values that have been previously assigned to perovskite thin-films[213–215]. Such recombination has only been observed in some of the best silicon electrodes[94]. A more complex model is therefore needed to describe the unexpected findings.

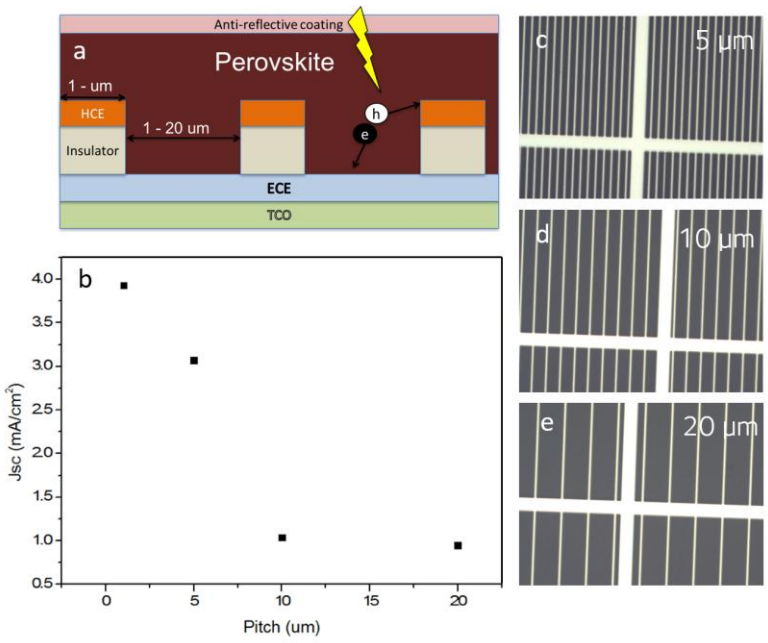


Figure 6.10: Illustration of back-contacted device with extended pitch (a). Short current density of devices with 1 µm, 5 µm, 10 µm and 20 µm pitch (b). Optical microscope image of patterned electrodes with 5 µm (c), 10 µm (d) and 20 µm (e) pitch.

A theory was developed and is in close agreement with a previously published comment about diffusion length determination by Hodes and Kamat[216] (see illustration in Figure 6.11): Photons are absorbed and generate electron-hole pairs in the same way as in sandwiched devices (1). However, after the quick removal of electrons through the electron transporting material and the underlying electrode (TiO_2/FTO) close to the excitation spot

(2), holes can consequently exceed travel distances of 175 µm in a thin film of perovskite to reach the hole-selective electrode (NiO), due to the absence of electrons to recombine with (3). In this scenario, holes can recombine via two different pathways. They can either recombine with electrons in the TiO_2, or they can get trapped into trap-sates of perovskite before reaching the p-type electrode.

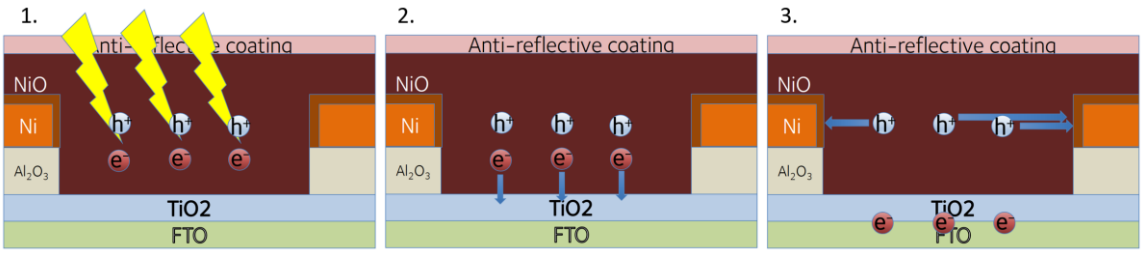


Figure 6.11: Sketch of proposed mechanism for long-distance hole diffusion.

An experiment was designed to support this theory. It was verified whether n-type materials with better electron extraction efficiencies could lead to a rise of the encountered tail. It is well known from literature that the fabrication route of electron transporting layers can lead to highly varying results in performance, even when using the same materials[121,217,218]. TiO_2 and SnO_2, two metal oxides known to work well as n-type materials in perovskite solar cells[121,219,220], were deposited via three different methods with subsequent identical fabrication of insulated top electrodes and perovskite coating. Conformal coating of the compact TiO_2 layer appears to have a good impact due to less thickness variations, that can lead to better charge extraction and reduced charge recombination[218,221]. Therefore, TiO_2 was once deposited via a Titanium isopropoxide based precursor spin-coating (used for all previous experiments of back contacted devices) and once via spray-pyrolysis of a Titanium diisopropoxide bis(acetylacetonate) based solution as a conformal coating technique. SnO_2 was deposited via spin-coating and subsequent chemical bath treatment as reported by Anaraki et al.[121], which showed remarkable performance improvements in sandwiched devices. Further reports showed the

improved extraction efficiency of SnO_2 via solar cell performance measurements and photoluminescence studies[222,223]. The electron quenching efficiency was analysed by depositing a perovskite film on top of the FTO/n-type layers and measuring the transient photoluminescence response. The normalised results are plotted in Figure 6.12a and confirm the statements from literature. The slope of the decay curve can be related to the lifetime of charge carriers[224]. The steeper the curve, the faster the quenching and therefore shorter the lifetime. The slope of the decay curve for the spin-coated SnO_2 layer was the steepest, followed closely by spray-coated TiO_2 and the previously used spin-coated TiO_2 layer, showed the slowest extraction properties.

Testing back-contacted solar cells with these materials and different pitch distances lead to the results shown in Figure 6.12b. The predicted rising of the tail in photocurrent decay over distance could be achieved by introducing different electron extraction layers. The short circuit current densities were normalised to the values measured from the 5 µm pitch devices. Spray-coated TiO_2 yielded the highest enhancement in long distance charge extraction with a decay of only 20 % from 5 µm to 10 µm and no further decline over the next 10 µm. Spin-coated SnO_2 also performed better than spin-coated TiO_2 but dropped by ca. 50 % from 5 µm to 10 µm and another 10 % in the 20 µm pitch device. In this tested batch the devices with spin-coated TiO_2 had a similar decrease of J_{SC} (60 %) from 5 µm to 10 µm as the previously tested devices in Figure 6.10b (ca. 65 %) but the tail did not show a flat behaviour and declined by another 30 % for the 20 µm pitch device. The faster PL decay in spray-coated TiO_2 and spin-coated SnO_2 could be partially used to explain a faster electron extraction and therefore longer hole travel distances. However, as order in PL lifetime and rising tail for long pitch back contacts don't match exactly, it can be concluded that it is not as simple as just relating PL lifetimes to lower electron densities. It is probably one factor, but the recombination from electrons in the electron extraction layer with holes

in the perovskite might vary significantly across the materials and this wasn't yet quantified.

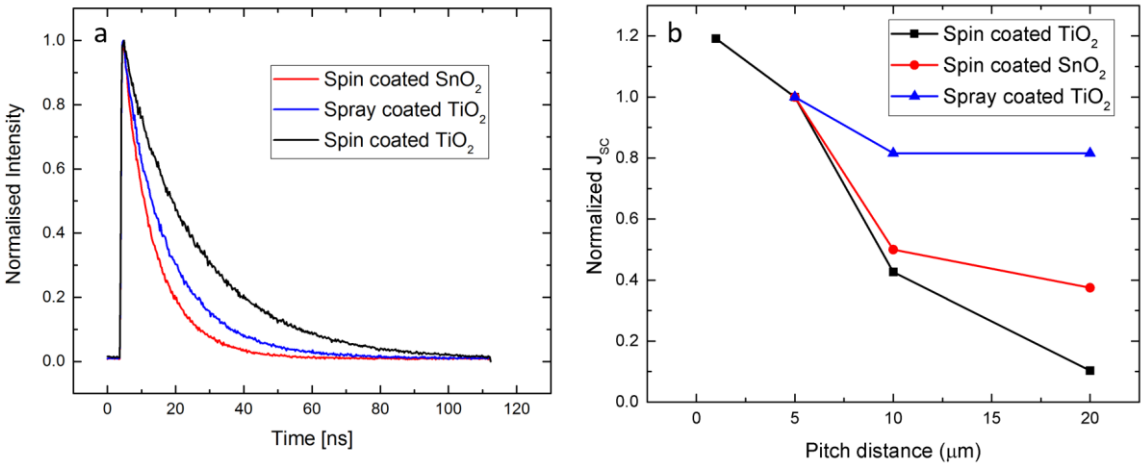


Figure 6.12: Normalised transient PL decay of perovskite thin-films on top of spin-coated TiO_2, spin-coated SnO_2 and spray-coated TiO_2 electron extraction layers on FTO coated class (a). Normalised current density for devices incorporating electron transporting materials of spin-coated TiO_2, spin-coated SnO_2 and spray-coated TiO_2 with various pitch (b).

To better understand the charge extraction behaviour and the comparison between the n-type and p-type electrodes, a simultaneous spatial mapping measurement of the photocurrent, the photoluminescence at short-circuit and the fitted lifetime from transient photoluminescence decay was performed (see Figure 6.13). Figure 6.13b shows the optical microscope image of the analysed area for which the 2D maps of photocurrent (Figure 6.13c) and PL (Figure 6.13d) were taken. The normalised measurements that were taken across the electrodes are plotted together in Figure 6.13e and indicate that the photocurrent rises when the areas above the n-type TiO_2/FTO electrode are illuminated. This suggests worse charge extraction above the p-type NiO/Ni electrode, which is also supported by the fact that the PL response is increased (opposite effect to the photocurrent), an indication for more radiative recombination due to slower extraction. Furthermore, the PL lifetime was extracted from transient PL decay and also demonstrates higher values above the p-

type contact, again a sign for inefficient extraction. Figure 6.13f shows such a transient PL decay plot, measured at the indicated locations in Figure 6.13d, above the n-type and p-type electrode. Analysing the PL lifetime or the slope of the PL decay curve is a common approach in literature to judge the charge extraction capabilities of interface layers. In the current case, the required improvement of the p-type NiO/Ni electrode becomes more clear.

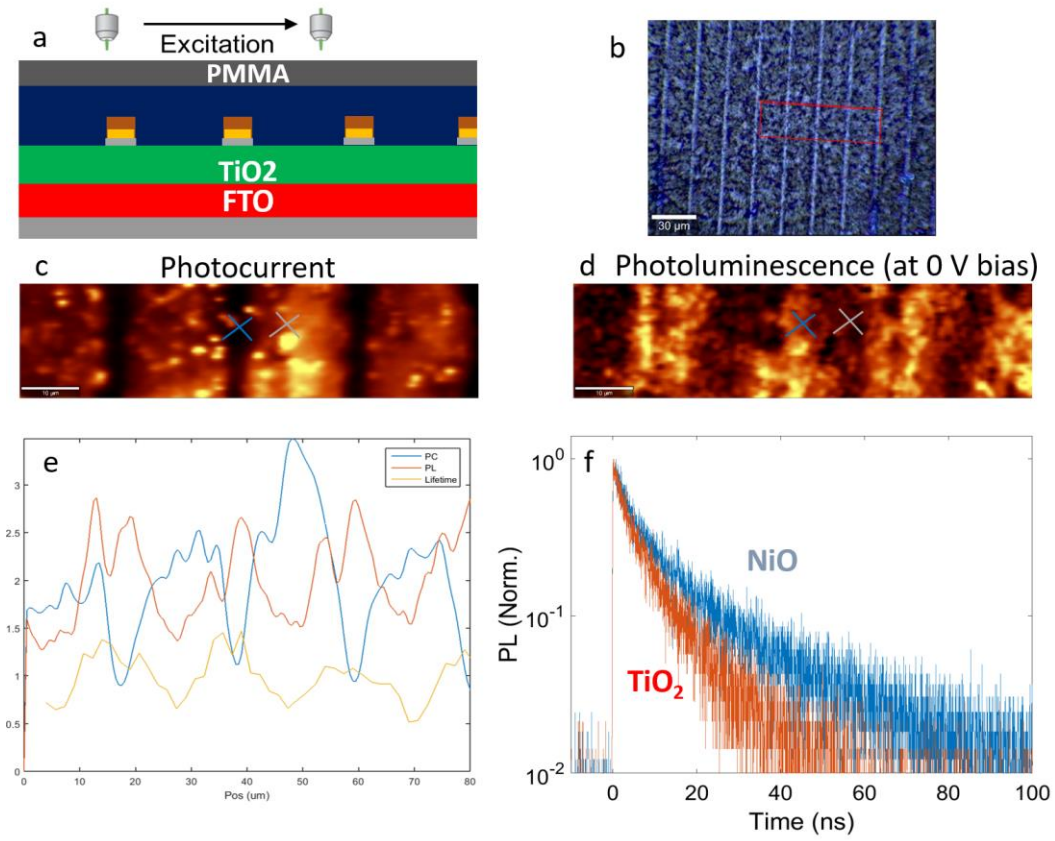


Figure 6.13: Illustration of spatial mapping technique of large pitch device (a). Top view microscope image of spatially analysed area (b). Photocurrent map of device with 20 µm pitch (c) and equivalent photoluminescence map (d) with indicators of the location where photoluminescence decay in (f) was measured. Plot of normalised mapped photocurrent, photoluminescence and estimated lifetime from photoluminescence decay of analysed area in horizontal scan direction. Plot of photoluminescence decay above TiO_2 and NiO electrodes at location indicated in (d).

6.3.5 Inverted devices

Inverted devices with p-type bottom contacts and insulated n-type finger contacts were fabricated with 1 µm pitch to investigate if similar charge transport effects are happening for the opposite charge species. NiO was coated onto the FTO from a Nickel Nitrate hexahydrate based precursor and Ti was evaporated onto the Al_2O_3 insulator instead of Ni, to then oxidise a shell to TiO_2 upon high temperature annealing in air. According to the theory of Leijtens et al.[203], holes are not trapped as much as electrons and should therefore be able to travel longer distances without recombining due to trap defects i.e. in grain boundaries. For that reason, it would be expected that the regular devices would lead to better charge extraction, ergo device performance, than inverted devices. The results of the J-V measurements (see Figure 6.14) show that this is indeed the case. The currents reached in the inverted device are orders of magnitude smaller than the ones reached in regular back-contacted devices. The assumption is that electrons recombine quicker before reaching the appropriate electrode. Therefore it was decided that future efforts should be focused on the architecture incorporating the n-type electrode at the bottom. However, at this point it must be noted that big batch to batch variations occur with back-contacted devices and the source of the problem was not yet discovered. Hence, it might be worth revisiting this experiment for better performances.

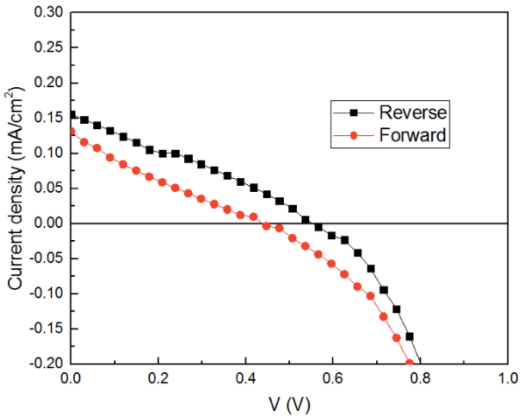


Figure 6.14: J-V characteristic of inverted back contacted device with 1 µm pitch in forward (SC to OC) and reverse (OC to SC) scan direction.

6.3.6 Surface passivation

As introduced earlier, suppressing surface recombination plays an important role for the improvement of back contacted solar cells. deQuilettes et al.[225] have shown recently that the photoluminescence lifetime of perovskite films could be significantly improved upon introducing a ligand passivation to the surface of perovskites. While this technique can hardly be tried in a sandwiched device, as the ligand passivating layer also acts as an insulator and would prohibit charge transport to the HTM, back-contacted perovskite solar cells are ideal devices to test if this surface passivation could improve the device performance through reduced charge carrier recombination.

Trioctylphosphine oxide (TOPO), the material with the highest reported effect was deposited on top of a back-contacted perovskite device (as illustrated in Figure 6.15a) and compared to devices coated with PMMA, which is a typical encapsulation layer and doesn't seem to have a big impact on surface passivation. Furthermore, a recently reported technique for the surface optimisation of the TiO_2 electron extraction layer via an ionic liquid treatment[226] was also tested to analyse the effect in the back contacted devices.

The outcome of the J-V measurements under simulated sunlight are presented in Figure 6.15b and show an encouraging increase of V_{OC} by 140 mV from 820 to 960 mV upon surface passivation. However, the J_{SC} and the FF were particularly low in this tested batch of spin coated TiO_2 based devices. Surprisingly, the ionic liquid treatment appeared to have a bad impact on the overall device performance. One possible reason might stem from the fact that the treatment had to be applied over the entire area of both electrode types and therefore might have created shunting paths.

To better assess the charge extraction and lifetime characteristics of the two well performing n-type layer materials (spray coated TiO_2 and spin coated SnO_2) together with

the surface passivation treatment, the transient photoluminescence decay and photoluminescence quantum efficiency of such devices were measured. The results are demonstrated in Figure 6.15c and show that un-passivated devices have a much faster PL decay and significantly lower PLQE's of 0.4 % for SnO_2 and 1 % for sprayed TiO_2. The TOPO passivated devices show much longer PL lifetimes and PLQEs of 9.3 % for SnO_2 and 11 % for sprayed TiO_2. The significant rise of PL lifetime and PLQE upon passivation is interesting, as this was measured at open circuit and suggests that there is less nonradiative recombination at open circuit. However, since the current does not seem to be reduced by the passivation, it is expected that fast charge extraction would occur at short-circuit, which is closer to the solar cell operation mode.

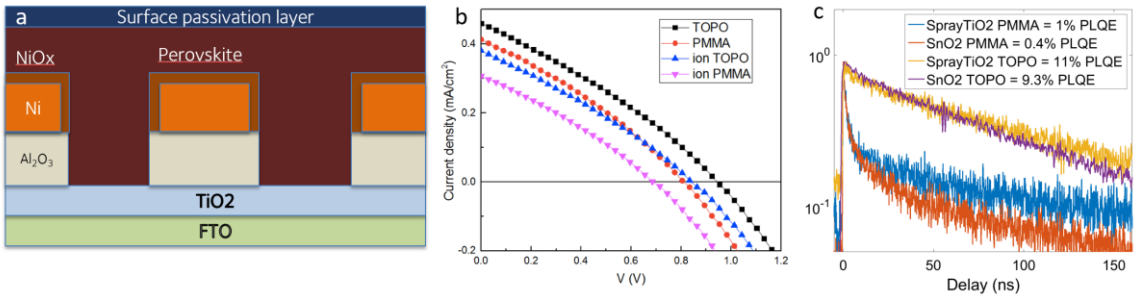


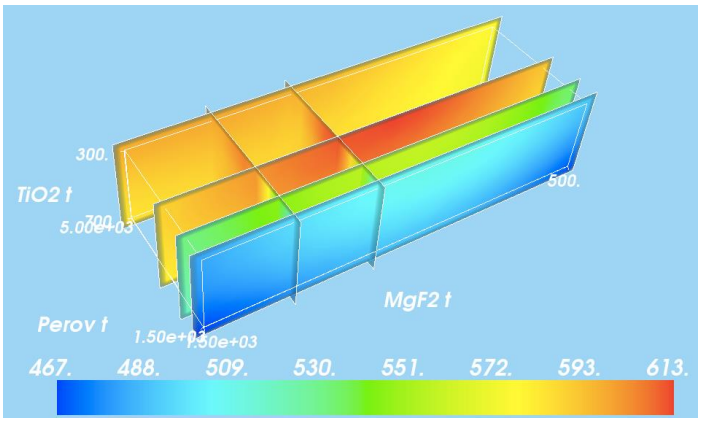
Figure 6.15: Illustration of back contacted perovskite solar cell with surface passivation layer (a). J-V characteristic of surface passivated and un-passivated devices, as well as ionic liquid treated devices (b) in reverse scan direction. Transient PL decay measurements and corresponding PLQEs of passivated and un-passivated SnO_2 and spray coated TiO_2 devices (c).

6.4 Conclusion and outlook

In summary, the limiting factors on the performance of back-contacted perovskite solar cells have been studied. A device architecture was developed, which allows to fabricate back-contacted devices with feasible performance through a simple single-step photolithography technique. The results from J(V) measurements as well as from spatial

photocurrent and photoluminescence mapping suggest that the diffusion length is not the critical parameter for the design of back-contacted devices. Using an insulated back contact architecture, where the whole surface is covered with a carrier selective electrode, the pitch distance of the back-contacted device can be largely increased without affecting its photovoltaic performance. This architecture has proven to be an exceptional platform for the in-situ testing of materials and electrodes. Furthermore, a maximum power conversion efficiency of 3.4 % was reached. It was shown that hole transport over long distances is not significantly hindered by trap states in perovskite and that surface passivation can lead to significantly enhanced V_{OC}. However, limitations were identified to stem mostly from inefficient charge extraction at the p-type electrode, which leaves a lot of room for improvements. Once the challenges are overcome, in-plane tandem devices with prism splitters[227] could be an ideal application enabled by this device architecture. Furthermore, the systematic study of electron or hole transport through crystal grain boundaries, as well as in-situ device performance measurements during thin-film annealing could lead to better insights about perovskite material optimisation.

7 PREDICTING AND OPTIMISING THE ENERGY YIELD OF PEROVSKITE-ON-SILICON TANDEM SOLAR CELLS UNDER REAL WORLD CONDITIONS



7.1 Context and summary

One great advantage of perovskite photovoltaic materials lies in the complementary absorption region when combined with a Silicon solar cell, making it an almost ideal candidate for tandem solar cell applications. The recent demonstration of nearly perfect tunability of the band gap of such perovskites has opened even more possibilities for adjusting the layer stack and the potential to fabricate all-perovskite tandem devices. The development of such solar cells becomes reasonably complicated, considering the multiple

layers that are involved in the design. In this chapter a rigorous optical and device simulation is introduced to optimise perovskite-on-silicon tandem solar cell stacks and identify feasibility of various interface materials, layer thicknesses and bandgaps to achieve the highest possible efficiencies. The annual energy yield under simulated hourly spectrum changes is calculated at different locations with optimised stacks to show that tandem solar cells are yielding up to 30 % more energy output than the single junction silicon cells. Most critically, the standardised air mass (AM) 1.5 efficiency measurement improvements observed for the tandems cells, translate almost entirely to the same fractional improvement in energy yield. Hence, the efficiency of the tandem cell is not significantly "de-rated" by real world spectral variations. Furthermore, the annual energy yield under simulated hourly spectrum changes at different locations is calculated and maximised to show that tandem solar cells are not only yielding up to 30 % more energy output but that they are relatively performing as well as single junction silicon cells. Additionally, it was found that tandem solar cell stacks should be optimized depending on the place of installation to gain up to 3 % more energy output. The results can offer extensive guidance to design the perovskite tandem device of the future and allow estimations for economical perspectives.

7.2 Introduction

Hybrid organic perovskites have optical absorption characteristics that not only make them very interesting for single layer solar cell applications but also for tandem devices. With a bandgap of 1.55 eV the absorption spectrum of typical hybrid metal-halide perovskites is very strong in the ultraviolet and visible light region but transparent for infrared light, which makes it an ideal top absorbing layer for materials that absorb well in the higher wavelength section of the spectrum[141]. Crystalline silicon as well as CIGS have been

identified and already demonstrated[228–234] as feasible candidates with such criteria. Combined power conversion efficiencies of up to 21.2 % in a monolithic configuration[231] and 25.2 % in a 4 terminal configuration[234] on top of Silicon have been achieved experimentally and seem to be improved with a high rate, which is also due to big commercial interest. The cost benefit of increasing the power output per installed photovoltaic module is very attractive, as the installation cost of solar panels usually accounts for a substantial part of the total system cost[10]. The potentially inexpensive manufacturing methods of perovskite solar cells integrated into silicon solar panels make it therefore a great business case, as the added marginal cost would easily be compensated within a short time by more energy production.

The use of perovskite solar absorbers as top cells has become even more interesting since it has been demonstrated that the bandgap can be precisely changed to higher values by adding different halide contents to the MA or FA based perovskite crystals[69,235] and use Caesium to stabilize the phase[73,74,131,236]. A higher bandgap allows for the perfect optimization of a tandem solar cell to reach the maximum achievable efficiency as shown in Figure 2.22. Since the viability of bandgap shifts to lower energies have been shown by using Sn-Pb based perovskites[70,237], this has led to the remarkable development of perovskite-on-perovskite tandem solar cells with efficiencies crossing 20 %[75,238].

Another advantage lies in the fact that bare Silicon is highly reflective in lower wavelength regions and a lot of light, and therefore energy, is lost when no anti-reflective layer is coated onto the device. Perovskite materials show better absorption at higher incident angles due to their lower refractive index[128]. Therefore, the coating of perovskite on top of Silicon could not only benefit the performance from a thermodynamic perspective but also by acting as an anti-reflective coating at the same time.

Engineering a tandem device stack proofs to be challenging, due to the complexity of adding new material layers that need to be energetically optimized. Monolithically integrated stacks, that connect both solar cells in series, need to have well designed recombination layers and 4T devices need to have two transparent electrodes either side to transmit the non-absorbed light to the bottom cell. The additional layers introduce more interference effects that can lead to reduced absorption in the photovoltaic layers and require to be finely tweaked to achieve maximum performance. Particularly in two-terminal tandem devices the highest power output is reached when the currents of the bottom and the top solar cell are well matched. Consequently, the fine tuning of all the layer materials and thicknesses is essential for attaining the highest possible performance. The simulation of theoretically feasible efficiency limits is essential for the evaluation of research and development efforts when compared to single junction solar cell applications. Hence, modelling the variation of the materials, their thicknesses and even the perovskite bandgap plays an important role for the coming research exertions.

When looking at currently published estimations of maximum efficiency limits, we find that often the thermodynamic detailed balance model by Shockley and Queisser[22] is used. The importance when doing so is to bear in mind that the key assumption in this model is that every photon with an energy above the absorbers bandgap, gets absorbed. In other words, this means that the assumed EQE of the absorbing layer equals 100 % in the region below the bandgap and cuts off perfectly at the absorption-edge. Even though perovskites demonstrate a remarkably sharp absorption-edge[61], it is far from perfectly rectangular and this needs to be taken into account when trying to find the optimal bandgap for a top cell.

Lately there have been several reports about attempts to optically model and optimize the thicknesses of Silicon-perovskite tandem solar cell stacks. Filipic et al.[129] compared in a rigorous model, based on the transfer matrix modulation, the maximum efficiencies that

could optically be achieved with two-terminal versus four-terminal tandem devices. They found that efficiencies above 30 % are theoretically feasible and that four-terminal devices show a higher maximum power output. However, the authors did not take into account the optical losses that might be induced by the physical separation of the top and the bottom cell as well as the fact that there might arise additional efficiency losses or illumination area losses due to different interconnection.

Further optical simulation results have been reported that included the comparison of different bandgap perovskite materials. This has been achieved by theoretically shifting the published optical constants of the perovskite along the energy axis of the spectrum[239], as well as by deriving experimentally the optical constants of different perovskite material compositions via fitting experimental reflection and transmission data[240].

Academic research so far has mostly focused on the maximization of power conversion efficiencies under simulated sunlight with the well-known standardized air mass of 1.5. The accepted standard across the research field is an important instrument to be able to compare the results and even get certifications from accredited institutions. However, it is of great importance to not forget the actual purpose of a solar cell, the production of electricity in the real world. Depending on the location of the solar installation, real world conditions contain the change of air mass, appearance of clouds, air-pollution, substantial sun-angle changes subject to seasons and noteworthy temperature variations. All such conditions have quite a significant impact on the energy yield of a solar cell. The two most important factors that must be accounted for in real world conditions is the continuous variation of the solar spectrum and the incident sun angle. It is for example well known that the spectrum appears more reddish in the mornings after sunrise, the evenings before sunset and generally in the winter. This is caused by higher air mass, which leads to Rayleigh scattering[241]. Similarly, cloud coverage will change the fraction of direct

irradiance and diffuse irradiance and can also cause a shifts in the solar spectrum due to light reflection and absorption by the clouds[242–244]. The effect that such spectral fluctuations can have on the performance of amorphous and microcrystalline silicon tandem devices has been studied before and shows variations of up to 20 % over the same time period at different weather conditions[244,245]. Slightly less drastic results of about 4 % variation have been shown for polycrystalline solar cells[246]. It should be noted that not many possibilities exist to improve the energy yield of a single junction solar cell other than changing the bandgap to adjust to a shift of the solar spectrum or to apply an anti-reflective coating to absorb better at steeper solar angles. On the other hand, the layer stacks in tandem solar cells are feasible to be precisely designed for maximum energy yield at a specific location.

Energy yield simulations have been carried out in more and less complex ways for several photovoltaic materials and tandem device architectures[247–249]. Most of the previous work relies on spectra that have been computed with the SMARTS model for clear skies or with the SEDES model for overcast skies, as hourly measured data for the entire wavelength spectrum is rarely available. A common approach to include varying spectra into the calculations is done via binning them by their average photon energy (APE) [250,251]. Futscher and Ehrler [252] have recently carried out such a calculation, in which they modelled the spectral influence on perovskite-on-silicon tandem devices by using the combined detailed balance limit of the absorbers. It was found that specifically 4T and also 2T architectures are not much affected by the spectral variations and would perform relatively as well as the single junction silicon solar cells. A simulation with more rigorous device modelling was carried out for CdTe/CdS tandem applications[248], which lead to the results that 4T configuration are more desirable due to less dependence on the varying spectrum by current matching conditions.

This chapter present the implementation of a rigorous optical/device model, which was used to simulate various silicon-perovskite tandem solar cells in combination with real weather data and complex diffuse light treatment to predict the achievable annual energy yield at specified locations with three different sun tracking systems. Not only is the annual energy yield for a device stack calculated which has been optimized for a single $AM_{1.5}$ solar spectrum and a single specified incident angle but it was managed to develop an ultrafast optimizing algorithm that allows for the maximisation of energy yield for a specific location. Consequently, it is assessed whether the change of materials, a shift of the bandgap and the variation of thicknesses in all layers needs to be carried out for different locations of tandem solar deployments. Additionally, the energy yields of perovskite-on-silicon tandem solar cells and single junction silicon solar cells were compared in relation to their $AM_{1.5}$ irradiance power conversion efficiencies to introduce an "efficiency derating value". It was found that in relative terms, tandem devices can perform as well as, or even better than single junction silicon cells, and the 2T tandem devices are usually with 2% of their expected energy yield. This means that the expected enhancement in energy yield of up to 30 % in tandems over single junction silicon cells should be realised. Furthermore, it was demonstrated that 2T configurations come very close to 4T performances. These results and the introduced simulation methods present a roadmap for the development and evaluation of optimised high energy yield tandem devices that will benefit research and the design strategies for cell manufacturing.

7.3 Results and discussion

7.3.1 Individual cell performance modelling

The model, as described in detail in section 3.6, was performed on three different types of devices as illustrated in Figure 7.1. The monolithically connected 2T stack consists of a

perovskite top cell and a silicon HIT bottom cell, which was changed only slightly for the 4T configuration by virtually electrically detaching the two devices at the indium tin oxide ITO layer. The layers, starting from the top illumination side, are MgF_2 as an anti-reflective coating, ITO, Spiro-OMeTAD, perovskite (varied band-gaps), electron transporting layer (varied between TiO_2, C_{60} and SnO_2), ITO, and then the HIT cell consisting of 10 nm p-type amorphous silicon, 5 nm intrinsic amorphous silicon, 3.5 mm of intrinsic single crystalline silicon, 5 nm intrinsic amorphous silicon and 10 nm of n-type amorphous silicon, with an additional bottom electrode of 300 nm Ag on glass. Notably, the thickness of the single crystalline silicon layer was overestimated to resemble a commonly used efficient back reflector, which increases the path length of light travelled through the absorber. The single junction HIT cell was analysed separately with the only difference that a top layer of MgF_2 was included to reduce reflecting light effects. The upper and lower limits of varied thicknesses and bandgaps (shown in Figure 7.1) were chosen to guarantee feasibility of electrical functionality and manufacturability.

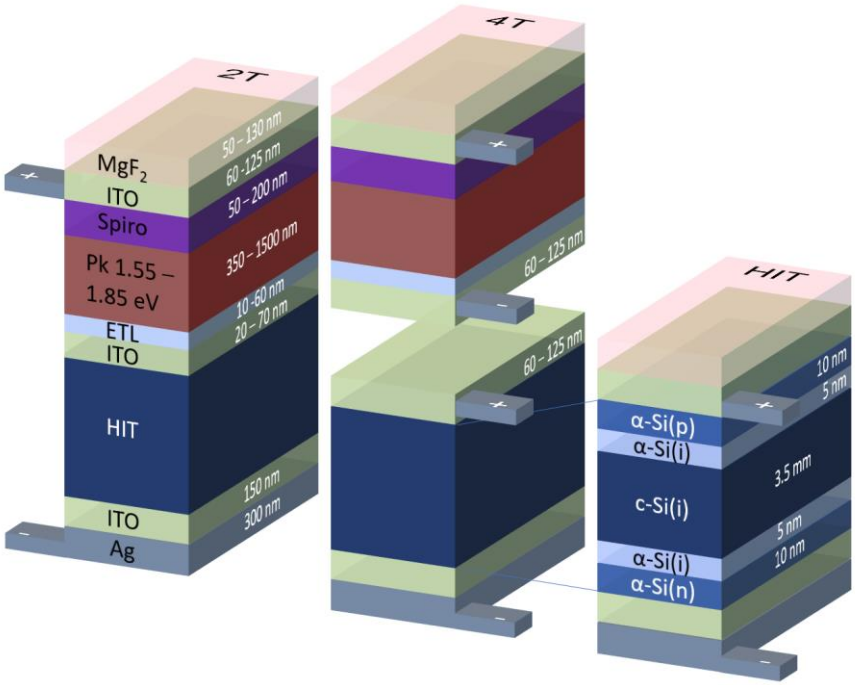


Figure 7.1: Illustration of the 2T/4T tandem stacks and the HIT solar cell, including all materials and layer thicknesses.

Initially as a quality check, a simple device performance simulation was carried out for a single junction perovskite solar cell resembling the stack reported by Saliba et al.[73], as the J-V fitting parameters (found in section 3.6) for the device model were taken from this publication. The simulated EQE spectrum and J-V characteristic are presented in Figure 7.2a, b. Given the fact that the reported solar cell contains a perovskite infiltrated mesoporous scaffold, which is difficult to model optically, the results are sufficiently close to the reported experimental values and allow to confidently carry on with the more complex modelling. The simulated solar cell reached a PCE of 21.2 %, which is not exceeding the most recent experimentally achievable record efficiencies. The modelling was carried out with an $AM_{1.5}$ spectrum and 0° incidence angle (later referred to as $AM_{1.5}$/0° condition) to resemble lab conditions.

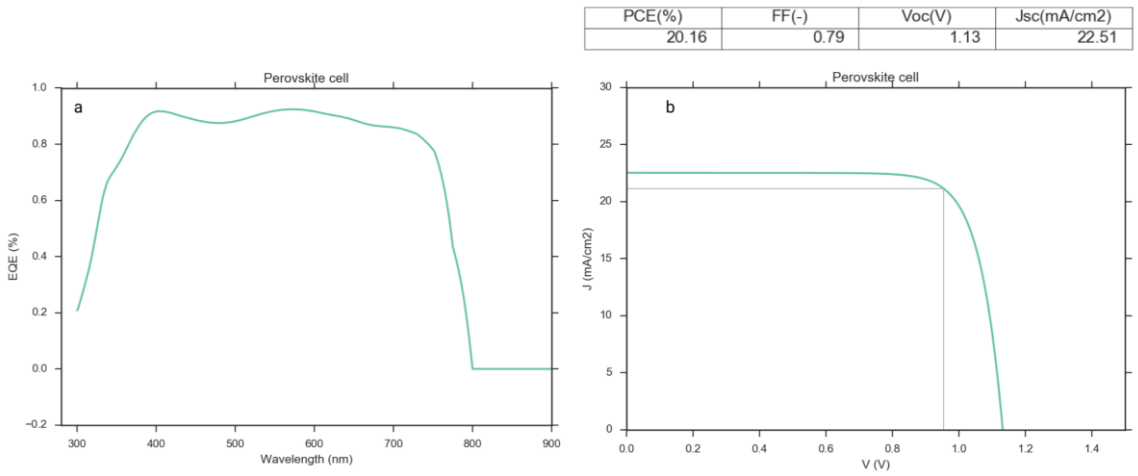


Figure 7.2: Simulated EQE spectrum (a) and J-V characteristic with performance parameters (b) of single junction perovskite solar cell.

A similar approach was taken for the simulation of the single junction HIT cell. However, since reflection losses play a more important role for silicon solar cells, the device was modelled with an anti-reflection layer of MgF_2, and the thicknesses of the top two layers (ITO and MgF_2) were varied through a differential evolution algorithm to maximise the PCE. Thicknesses of 71 nm MgF_2 and 62 nm ITO lead to the highest PCE of 21.6 %. The

simulated EQE spectrum and J-V curve are presented in Figure 7.3 and resemble well the shapes and values shown by others[129]. Here it is important to note that significantly higher J_{SC}s have been experimentally demonstrated by using structured anti-reflective coatings, which are more computationally expensive to include into the model.

The simulated performance values of both individual single junction devices are not unrealistic to achieve, which is the reason why the outcome of the tandem modelling is relevant for currently ongoing experimental research.

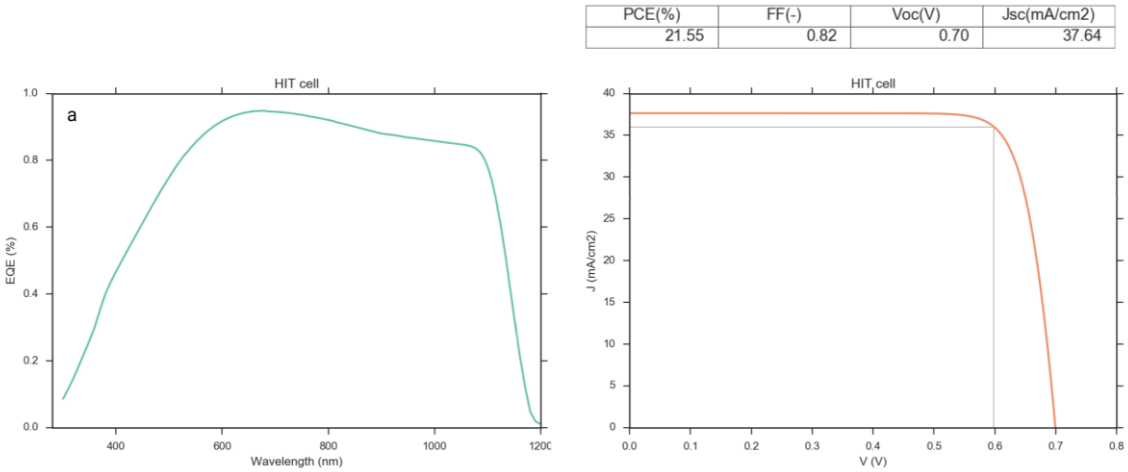


Figure 7.3: Simulated EQE spectrum (a) and J-V characteristic with performance parameters (b) of optimised single junction HIT solar cell.

7.3.2 Optimisation for PCE in lab conditions

In a next step the bandgap of the perovskite material was varied by shifting the absorption coefficient along the energy axis and applying a Kramers-Kronig transformation to calculate the complex refractive index as explained in section 3.6. The results of the original and shifted optical constants is presented in Figure 7.4a. The shifted extinction coefficients appear similar in shape to the published experimental data of absorbance spectra for different perovskite bandgaps[131]. The 2T and 4T stacks were then optimised individually for $AM_{1.5}$/0° condition with the optical constants that correspond to bandgaps

from 1.55 eV to 1.85 eV to determine the maximum achievable efficiencies. The bandgap energies and the resulting maximum PCEs are presented in Figure 7.4b. It is discovered that the optimal top cell bandgap for 2T configurations appears to peak at 1.70 eV, which is slightly different from previously published reports[131,228] that took Shockley-Queisser models (calculated and presented in Figure 2.22) for their conclusion to aim for 1.75 eV as the ideal bandgap for the top absorber. Furthermore, it appears that the perovskite bandgap shift in the 4T configuration has less impact and seems to occur at a slightly higher energy of 1.8 eV. For both architectures PCEs over 30 % are feasible with current technologies and the 4T device appears to perform slightly better.

Another question needing to be answered was how much of an effect different interface materials would have on the overall performance of tandem devices. Therefore, the three different materials C_{60}, to TiO_2 and SnO_2 were compared as electron transporting layers between the perovskite and the ITO interfaces. Again, the same optimisation procedure for $AM_{1.5}$/0° conditions and two different perovskite bandgaps (1.55 eV and 1.70 eV) was performed. The results in Figure 7.4c show the small effect of the material on the maximum PCE and can therefore be almost neglected for optical performance considerations. C_{60} remained as the ETL material for all subsequent simulations.

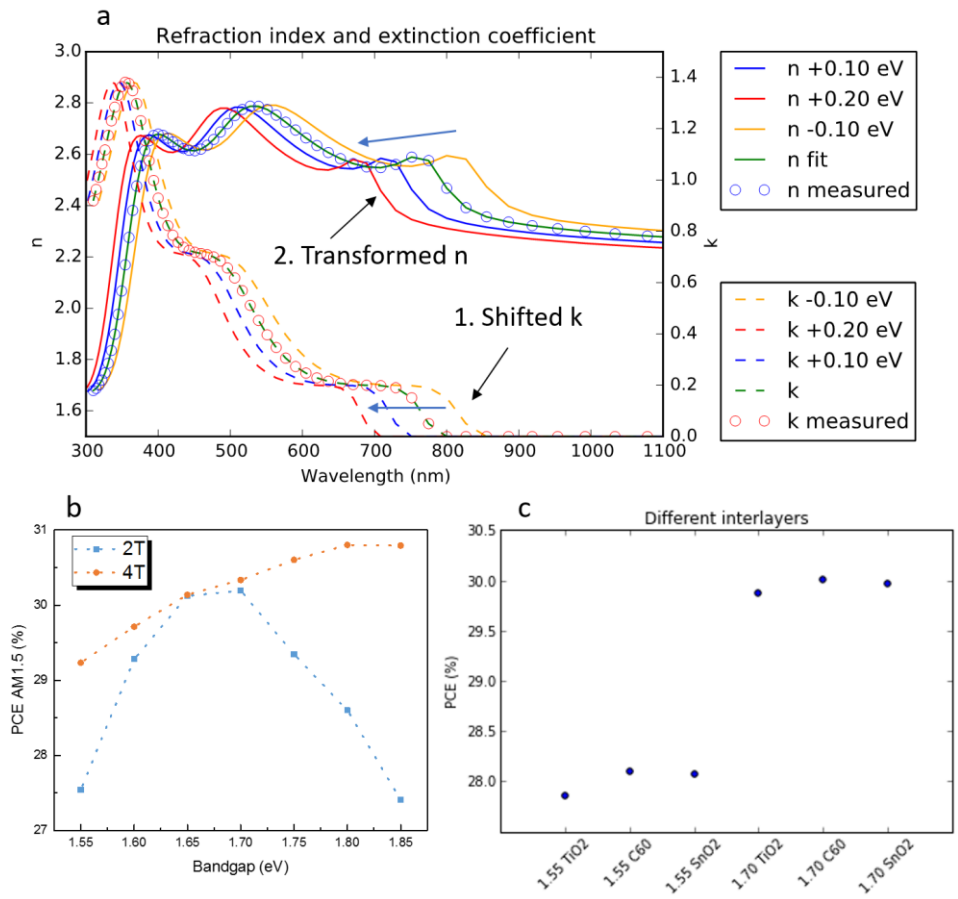
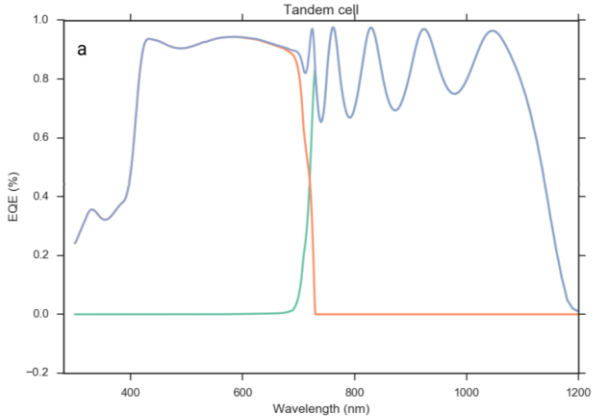


Figure 7.4: Shifted extinction coefficients and corresponding Kramers-Kronig transformed refractive index spectra (a). PCE for optimised 2T and 4T tandem device stacks with C_{60} as ETL for shifted perovskite band-gaps (b). PCE for optimised 2T tandem devices with different ETL for perovskite bandgaps of 1.55 eV and 1.70 eV.

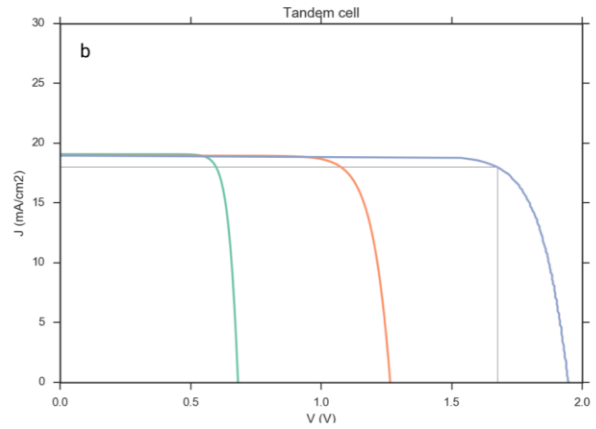
Now that the optimal material composition was found to maximise the PCE, the simulated EQE spectrum (Figure 7.5a) and J-V characteristic curve (Figure 7.5b) was plotted together with the tabulated optimised thicknesses (Figure 7.5c). The highly varying fringes are noticeable in the EQE spectrum in the red region, which are probably a result of interference stemming from reflected light within the many thin layers. Introducing scattering layers to break the coherency of the light could improve this behaviour. Moreover, it can be seen from the J-V curves in Figure 7.5b that the currents from the absorbing layers are very well matched, leading to the optimal device efficiency. The perovskite layer thickness has to maximised almost to its upper limit of 1.5 µm to match

the relatively high current that comes from the transmitted photons absorbed by the silicon cell.



c

MgF2	91.637322 nm
ITO	123.640318 nm
Spiro	55.4303514 nm
Pk	1.47619845 um
C60	23.3908867 nm
ITO	22.1730935 nm
a-Si_p	10.0 nm
a-Si_i	5.0 nm
c-Si	3500.0 um
a-Si_i	5.0 nm
a-Si_n	10.0 nm
ITO	150.0 nm
Ag	300.0 nm



PCE	FF	Voc	Jsc
30.13	0.82	1.95	18.95

Figure 7.5: Simulated EQE spectrum (a) and J-V characteristic with performance parameters (b) of optimised 2T perovskite-on-silicon (1.7 eV) solar device. Table of optimised layer thicknesses (c).

7.3.3 Energy yield simulations

The analysis of optimized tandem stacks under $AM_{1.5}/0°$ conditions is interesting from a research lab perspective because these are the standard conditions, which are generally used to experimentally characterize solar cells. However, for real world applications, and those should be the main focus for the development of solar cells, the annual energy yield at a particular deployment location has a lot more significance for financial and

engineering feasibility analyses. The overall energy yield is heavily dependent on the changes of the solar spectrum and the variations of incidence angles on the installed panel. The influence of the incidence angles is so large that for many photovoltaic technology applications, complex and expensive sun tracking systems have been implemented. Three locations in the USA with significantly different weather conditions were picked for comparison. The detailed location and weather information for the analysed locations Golden (Colorado), Seattle (Washington) and Mohave desert (California) is given in Table 7.1. The solar irradiation characteristic, the precipitation and the temperature vary largely at all locations. It was to be expected that the Mohave desert location is exposed to a lot more direct beam irradiation than diffuse light, caused by less clouds and therefore less scattered light. The least solar energy is received in Seattle, which was predictable due to the heavily overcast skies and the higher latitude. These locations were chosen for the simulations to offer a diverse perspective on the results.

Table 7.1: Tabulated geographic and meteorological data for locations Golden, Seattle and Mohave desert. Data was derived from NREL NSRDB[136] for the year 2015.

Location:	**Golden, CO**	**Seattle, WA**	**Mohave Desert, CA**
Latitude:	39.79°	47.49 °	34.29°
Altitude:	1820 m	139 m	646 m
Annual global horizontal irradiance:	1576 kWh/m^2	1295 kWh/m^2	2140 kWh/m^2
Annual direct normal irradiance:	1863 kWh/m^2	1482 kWh/m^2	2841 kWh/m^2
Annual diffuse horizontal irradiance:	572 kWh/m^2	503 kWh/m^2	452 kWh/m^2
Clear sky sun hours:	1701 h	1684 h	3255 h
Average annual precipitation(cm):	62.2 cm	94.3 cm	11.4 cm
Average temperature:	8.6 °C	13.0 °C	20.5 °C

In order to demonstrate the difference in the solar spectra, the annually averaged spectral components GHI and DHI were individually plotted in Figure 7.6a, b, c. The added 25th - 75th and 5th – 95th percentile plots offer an image how the spectra vary over a year. A better comparison can be made by seeing these spectra plotted in the same graph (Figure 7.6d).

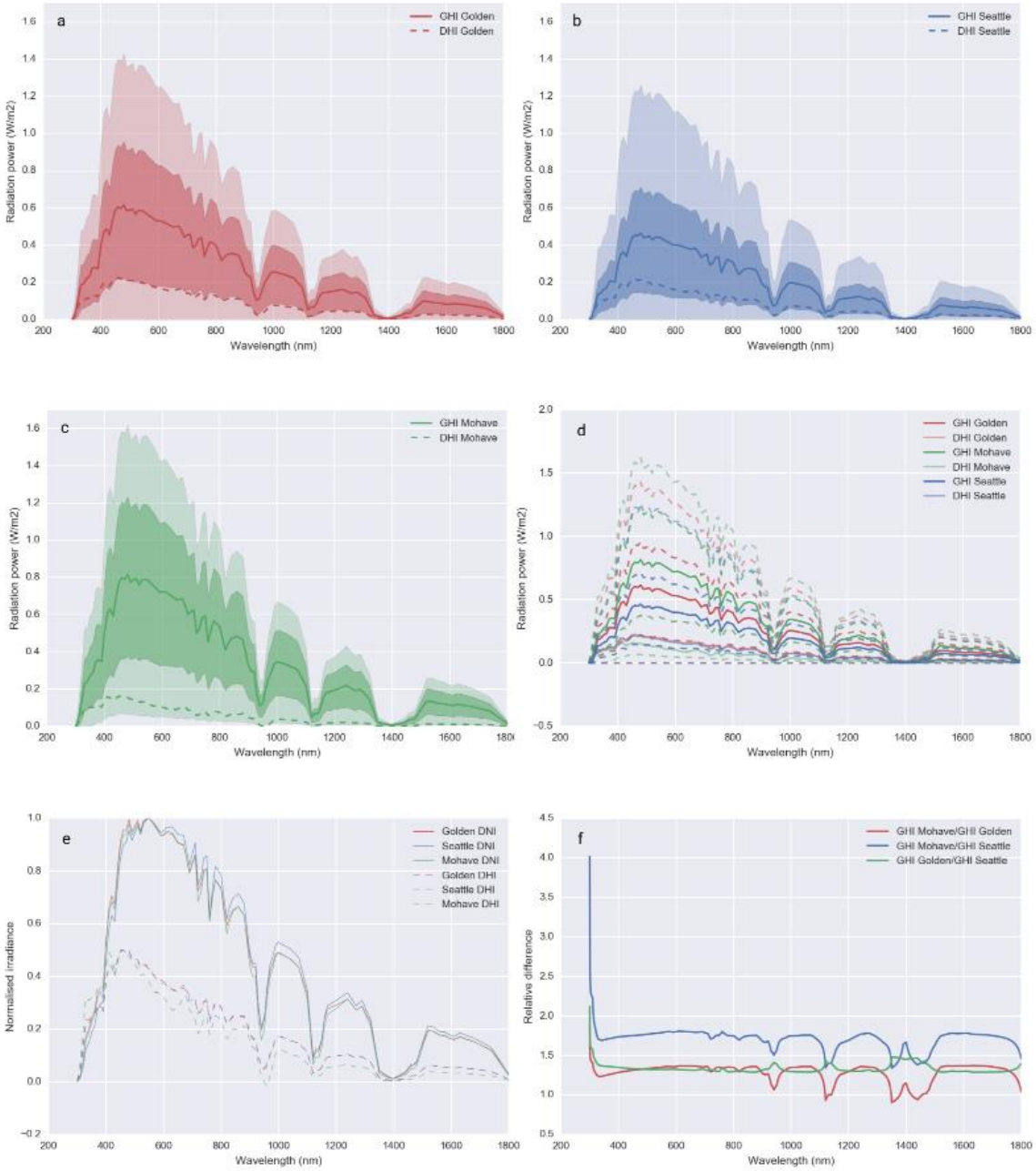


Figure 7.6: Diffuse horizontal irradiance and global horizontal irradiance spectrum with 25th - 75th and 5th – 95th percentile representation in Golden (a), Seattle (b) and Mohave desert (c). Comparison of DHI and GHI spectra of all three locations at correct scale (d) and DHI and DNI

spectra of all three locations at normalised scales (e). Plot of the fractions of GHI spectra pairs to demonstrate non-constant scaling (f).

Mohave desert, unsurprisingly, received significantly higher annual solar irradiation, specifically in the blue. However, from these graphs it is not clear whether the spectra are just scaled by a constant value or if there are substantial changes in different wavelength regions. Therefore the direct normal irradiance and the diffuse horizontal irradiance spectra were normalised (DHI was additionally multiplied by 0.5 to better distinguish) and plotted in Figure 7.6e. Now it is possible to notice significant change in the higher wavelength regions of the spectrum. The direct normal irradiance in Seattle shows nicely the red shift, that is to be expected from Rayleigh scattering due to the higher air mass and humid atmosphere. Figure 7.6f shows the fraction of averaged GHI spectra to visualise substantial disturbances in the scaling of the spectra. The change from the desert spectrum to the more overcast location's spectra is visible in some regions in the red, which can be assigned to absorption by water vapor in clouds.

The effect that such spectral changes have on the performance of the tandem and the HIT devices are demonstrated in Figure 7.7. A typical summer midday spectrum in Mohave desert (plotted in Figure 7.7a) is used to simulate the J-V curves of the HIT cell (Figure 7.7b) and the $AM_{1.5}/0°$ optimised 2T tandem cell (Figure 7.7c). Noticeable is the unmatched current condition in the tandem stack, which presumably comes from the difference in spectral shape, for which the device was not optimised. It probably leads to a larger fraction of blue photons being absorbed by the perovskite.

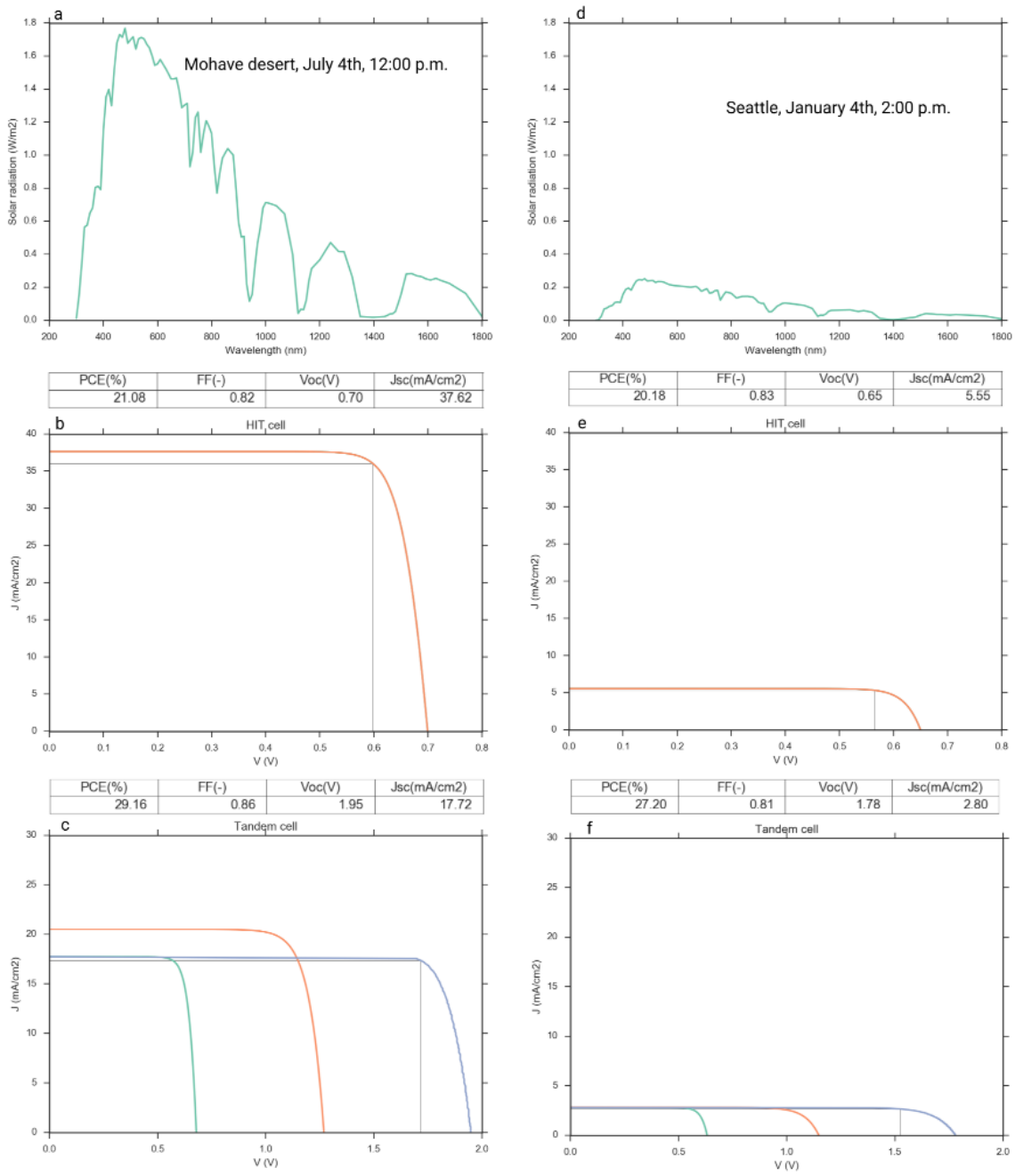


Figure 7.7: Global horizontal irradiance spectrum in Mohave desert on July 4th at 12:00 p.m. (a) and simulated corresponding J-V characteristic of HIT cell (b) and 2T tandem device optimised for $AM_{1.5}/0°$ (c). Global horizontal irradiance spectrum in Seattle on July 4th at 2:00 p.m. (d) and simulated corresponding J-V characteristic of HIT cell (e) and 2T tandem device (f).

However, the drop in PCE from 30.1 % to 29.2 % is bearable and probably due to the higher occurring FF, which can compensate the overall current loss. The same analysis was made for a very weak spectrum in Seattle's wintertime (Figure 7.7d), which lead to a

well current matched tandem stack that still underperformed a bit due to the high voltage loss. It appears that the HIT cell is slightly less prone to spectral changes than the 2T tandem device, but the differences are not significant. The second component influencing the optical model is the incident angle of the photons. Since in real world conditions, the position of the sun towards the solar panel is permanently changing, it will have an important influence on the overall energy yield. The angular dependent performance of the HIT cell and the $AM_{1.5}$/0° optimised 2T tandem cell were simulated and plotted normalised together with the cosine dependence of the intensity in Figure 7.8a. In this graph it is almost impossible to see the difference of performances, which is why the relative difference of normalised PCEs was demonstrated in Figure 7.8b. Even though the differences are generally not large, it is possible to conclude that the HIT cell achieves minimally higher efficiencies (below 1 % difference) for a large range, but at higher angles above 70 ° the gain in performance from the tandem device becomes more noteworthy. It is assumed that the loss comes from lower intensity and unmatched currents, which is later gained by less reflection at high angles, but this has to be analysed in more detail.

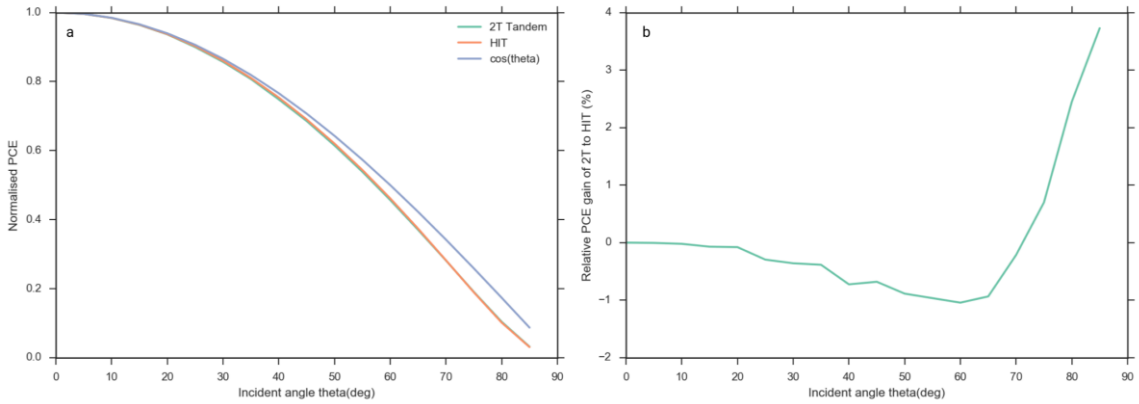


Figure 7.8: Angle dependence of normalised PCE for HIT device and 2T tandem device compared to cosine dependence (a). Angle dependent relative difference in normalised PCE of 2T tandem to HIT device (b).

The fast parallel computability of the simulation program and the use of a high performance computation cluster allows for a complete tandem stack optimisation for maximum annual energy yield at a particular deployment location within only a couple of hours. Analogous to Figure 7.4c, optimisations were carried out to see which bandgap material would yield the highest annual energy output at the three specified U.S. locations and the results for all different tracking systems and tandem architectures are shown in Figure 7.9a, b, c. Interestingly but not too surprisingly we find a very similar bandgap dependence when optimising 2T tandem for energy yield as when optimising for PCE at $AM_{1.5}/0°$ conditions. Even the tracking system does not seem to make a big difference. Only for Seattle the peak appears to be shifted towards a lower bandgap, which can be explained by the red-shift of the spectrum. Thought provoking is also the fact that fixed 4T tandem devices appear to have a peaking bandgap at higher energies. Here the it is assumed that wider bandgaps could lead to more absorption of steeper incoming photons. The highest energy yields for each optimised device stack was inserted into the diagram in Figure 7.9d, which demonstrates perfectly the efficacy of solar tracking systems and the importance of PV deployment location. Energy yields of up to 950 kWh/m^2 can be reached with a 4T tandem device, which is deployed in Mohave desert with a 2-axis tracker, which is reduced by almost 30 % if not solar tracked. Almost exactly half of this energy amount is to be expected from a similar device also 2-axis tracked in Seattle. The important findings are that 1-axis tracking systems are performing nearly as well as 2-axis trackers, especially for locations with more direct spectral distribution. Furthermore, 4T devices are only yielding a couple of percent more energy in all scenarios, and additional losses that come with such configurations have not even been accounted for.

Additionally, it is now possible to compare the annual energy yield at different locations for tandem stacks that were optimized for $AM_{1.5}/0°$ conditions with devices that were

specifically optimized for these deployment locations. The results are presented in Figure 7.9e as relative annual energy yield gains for location optimised devices.

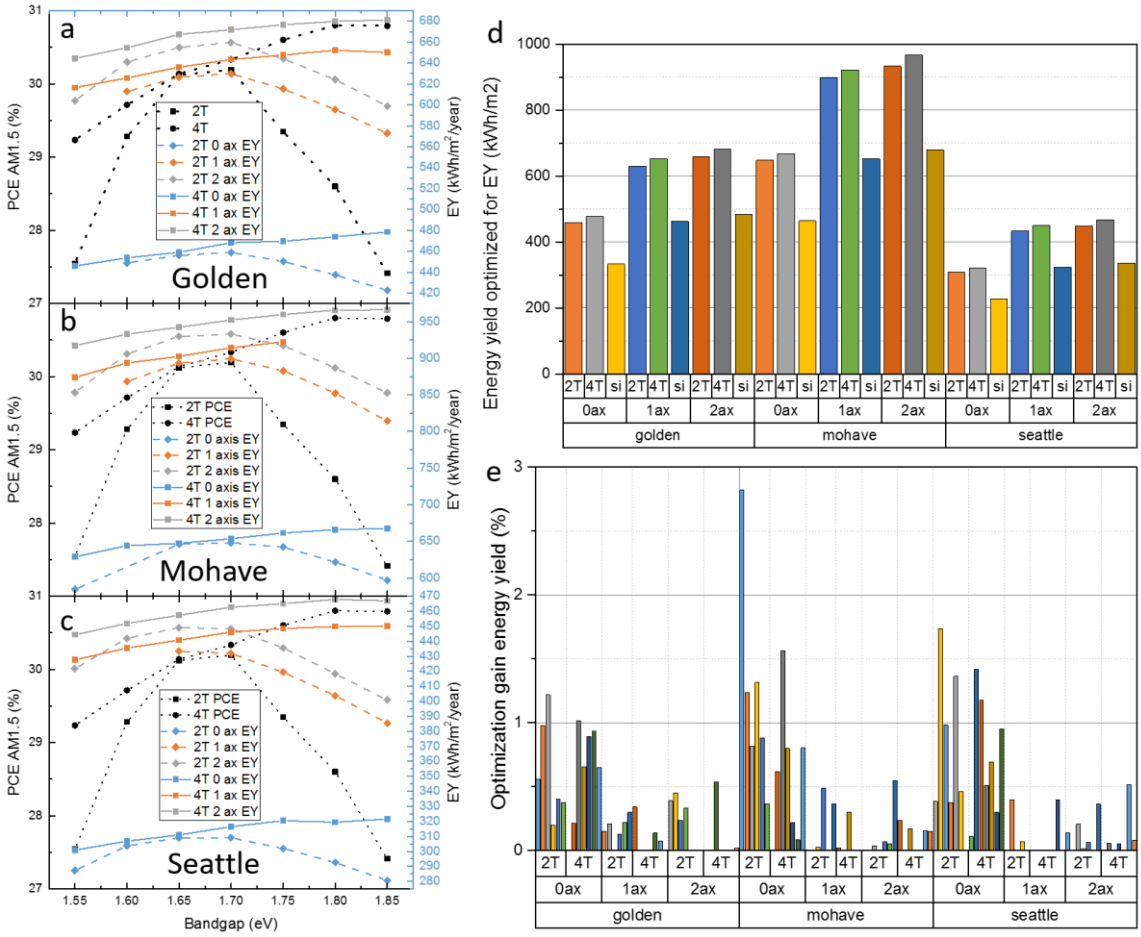


Figure 7.9: PCE and energy yield of optimised 2T and 4T tandem solar cells depending on perovskite bandgap, optimised and calculated with fixed, 1-axis and 2-axis tracking at locations Golden (a), Mohave desert (b) and Seattle (c). Highest achievable annual energy yield for optimised devices with varying tracking system at different locations (d). Relative energy yield gain of devices optimised for energy yield compared to devices optimised for $AM_{1.5}/0°$ PCE.

It needs to be noted that the optimisation for energy yield is a very computationally heavy task that involves billions of calculations, which is the reason why the execution of the differential evolution algorithm not always converges to a maximum with larger energy output than the stack optimised for $AM_{1.5}/0°$ (indicated as 0 % gain in the graph). Calculating the PCE at $AM_{1.5}/0°$ is exponentially faster due to no specular contribution of

irradiance and hence a global maximum is always found. However, the EY gains that have been found show that relative improvements of up to nearly 3 % are possible. This is a remarkable finding, as it indicates that device stacks for future commercial tandem applications should certainly be optimised for every deployment location. The gain can be as large as the improvement of a 30 % PCE solar cell to 31 %.

7.3.4 Efficiency derating factor

The energy yield calculations are required in order to estimate the cost of installed PV power in different locations. However, in the development of the multi-junction technologies it would be useful to have a simple "correction factor" which could be applied to the $AM_{1.5}$/0° PCE measurement in order to be able to make a like-to-like comparison between the perovskite-on-silicon tandem and single junction silicon cells. Therefore an "efficiency derating factor" f_D is introduced, which allows to compare the ratios of annual energy yield to the $AM_{1.5}$/0° PCE of the tandem device against the silicon HIT device:

$$\frac{EY_{tandem}}{PCE_{tandem}} = f_D * \frac{EY_{HIT}}{PCE_{HIT}} \quad (7.1)$$

It follows, that the derating factor is therefore defined as:

$$f_D = \frac{EY_{tandem} * PCE_{HIT}}{EY_{HIT} * PCE_{tandem}} \quad (7.2)$$

Therefore, in order to estimate how much of a real improvement in energy a relative increase in efficiency will deliver via making the tandem solar cells, the measured $AM_{1.5}$/0° PCE of the tandem device should be multiplied by f_D. If $f_D > 1$, the tandem cell will perform even better than expected from the efficiency gain, if $f_D < 1$, the tandem cell with perform less-well than expected from the efficiency gain. The calculated derating factors for all tandem architectures, tracking systems and for the three different locations are presented in Figure 7.10a. The outcome is very encouraging for the future prospects of

perovskite-on-silicon tandem cells, since the de-rating factor is close to unity for most locations, ranging from 0.96 to 1.0. Therefore, on average applying a de-rating factor of ~0.98 appears sensible, which implies that a 30% efficient tandem cell should be considered to be as effective as a ~ 29.3% efficient single junction cell. It is found that the location plays a significant role for the derating factor and the best case for tandem applications appears to be the desert. On fixed systems, tandem solar cells appear to perform more comparable to silicon solar cells than with tracked systems. 4T architectures, which are less prone to spectral changes and angular dependence, outcompete silicon solar cells in the dryer locations with derating factors above 1. These results pave the way for motivated commercial efforts that focus on the introduction of perovskite tandem absorber layers to the photovoltaic market.

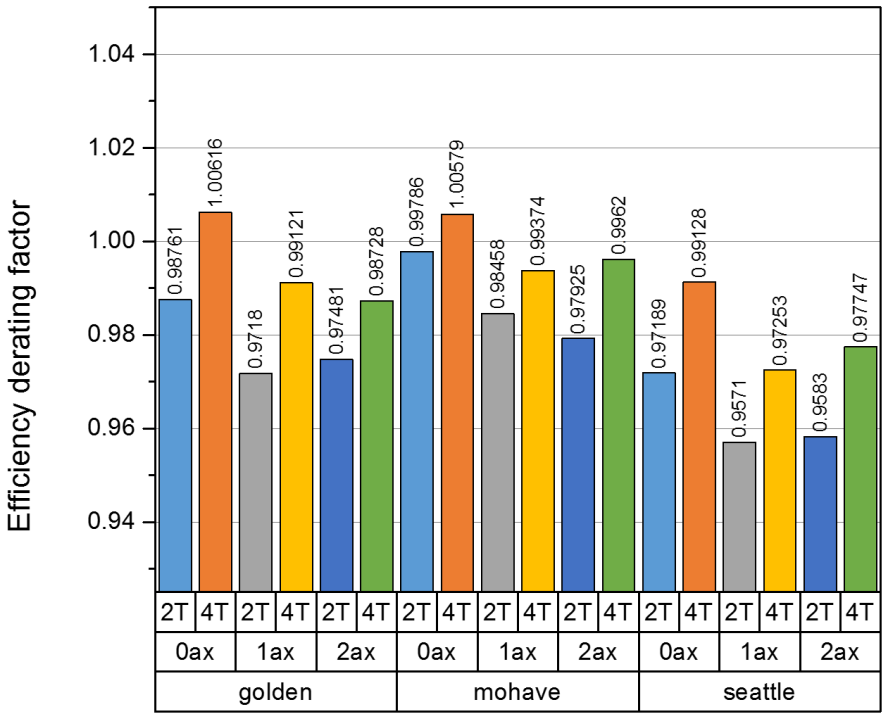


Figure 7.10: Efficiency derating factors for tandem devices with varying tracking systems at different locations.

7.4 Conclusion and outlook

In summary, a rigorous optical model was developed and combined with a solar cell device model to simulate the power conversion efficiency of perovskite-on-silicon tandem stacks. Together with typical meteorological year data for measured solar spectra and the implementation of a diffuse light radiance distribution model, the annual energy yield at chosen locations can be determined. An additional optimisation routine enabled the discovery of the ideal material and thickness combination that would lead to the highest possible energy output. Consequently, it was possible to compare the location dependent performance of a state of the art single junction silicon solar cell to perfectly optimised tandem stacks with two- and four-terminal configurations mounted to various solar tracking systems. It was found that perovskites should have a bandgap close to 1.7 eV in 2T configurations and higher bandgaps of at least 1.85 eV in 4T designs. The use of different electron transporting layers did not lead to big differences. Furthermore, it can be concluded that 2T tandems yield nearly as much energy as 4T designs and that 1-axis tracking systems should be chosen for big improvements that can only be slightly topped by more expensive 2-axis tracking systems. The deployment location plays a very important role, as differences in solar irradiation spectra lead to roughly twice as much energy output for cells, when installed in sunny Mohave desert as compared to cloudy Seattle. Another remarkable finding was the fact that a gain in energy yield of almost 3 % is possible, when certain tandem device stacks are optimised for a maximised energy output at a specific location over devices that were optimised for the lab conditions with an $AM_{1.5}$ spectrum and 0 ° incidence angle. Most critically, it was assessed how the improvement in power conversion efficiency, going from single junction silicon to perovskite-on-silicon tandem cells, translates into improved energy yield. It was found that, depending upon location and style of deployment (fixed or tracked), the perovskite-

on-silicon cells will deliver between 96 and 100 % of the expected energy yield. This implies that when making a side-by-side comparison between single junction silicon and perovskite-on-silicon tandem cells, the measured efficiency of the perovskite-on-silicon tandem cell should be multiplied by a de-rating factor of ~0.98. This is a relatively small de-rating factor, and gives good confidence that 2T perovskite-on-silicon tandem cells will deliver upon their promise of not just very high efficiencies, but also significantly boosted energy yields under real world conditions. These discoveries are strongly encouraging the developments of perovskite solar cells as great companions for silicon solar cells for the future of large scale photovoltaic applications.

The model can be further improved by adding additional ray-tracing capabilities for the inclusion of highly effective anit-reflective coatings. Additionally, the computational algorithms could be adjusted for better multi-node cluster support, or by using graphic processing unit (GPU) enhanced methods to provide fast location optimisation features. Finally, a side-to-side comparison with measured energy yield of real modules could provide a benchmarking method to assess the value of the simulations in more detail.

8 CONCLUSIONS AND OUTLOOK

The work presented in this thesis has been focused on the design, fabrication and analysis of novel concepts for perovskite solar cell device architectures. It was tried to diverge from conventional designs to widen the basic understanding of this new material and open up new perspectives for future perovskite applications. Through the intensive use of lithography and self-assembly techniques, it was managed to structure perovskites and other materials to alter the light interaction and charge carrier behaviour in opto-electronic devices. The lessons learned from this process contributed to the understanding of perovskite crystal growth behaviour, material and chemical compatibility, optical properties as well as charge transport and extraction characteristics. Additionally, modelling the optical behaviour in solar cell stacks and combining it with device and solar radiation theory provided the basis for careful valuation of the performance of solar cells under real world conditions.

More specifically, in Chapter 4, the crystal growth characteristics were studied by confining the perovskite domains into nano-scale templates, formed from metal oxides, which were periodically patterned. Morphology improvements were noticed by the assumed precise seeding of crystallites upon deposition. The three-dimensional geometry control of the photo-active perovskite material could be demonstrated, which enables multiple opto-electronic applications. One of such is the use-case of semi-transparent solar cell devices. The reduced surface coverage of perovskites through the template walls would allow enough light to be transmitted while blocking the contact between the sandwiching interface layers and lead to enhanced devices. The relevance of this work is

underlined by the fact that the idea of this concept has lately been used for demonstrating the highest efficiency per transparency record of 7.5 % PCE/ 42 % AVT in semi-transparent perovskite cells[253], breaking the records of so far unmatched organic photovoltaics[254].

The interest of solving the shunting problem in neutral coloured perovskite solar cells was carried on in Chapter 5. A simple post-treatment was developed for dewet perovskite island films, which lead to a significant performance improvement by the proven ability to electrically insulate the contact areas between hole and electron transporting materials. The self-assembly dynamics and insulation characteristics were probed in much detail. With this technique, the at the time highest neutral coloured semi-transparent solar cells could be fabricated, making it a very promising route for commercialization.

In Chapter 6, an architecture was developed that allows to contact perovskite solar absorbers entirely from the back. Through the simple lithography process working photovoltaic devices were developed. A platform was invented to test the individual charge carrier characteristics, different electrode spacing, interface materials and passivation methods. It was found that holes can travel remarkably long distances in the absence of electrons, which allows to neglect the typical diffusion length and allow for simpler fabrication of back contacts. Concluding that the charge extraction efficiency in the p-type selective materials offers much room for improvement and that passivation can lead to much higher voltages might make back contacted devices catch up with conventionally sandwiched devices soon.

Finally, computational modelling efforts were focused on the simulation of real world energy yield estimations for perovskite-on-silicon tandem solar cells in Chapter 7. For three U.S. locations with contrasting solar irradiation, device stacks with different materials and thicknesses were optimised for maximum annual energy output on fixed or

sun-tracked systems. The outcome guides current tandem researchers to use top cell perovskite absorbers with specified bandgaps, and finds that two-terminal devices are yielding almost as much energy as four-terminal stacks. The most important finding however is the little loss of derating factor for tandem devices, indicating that the energy yields of perovskite-on-silicon tandem solar cells and single junction silicon solar cells in relation to their $AM_{1.5}$ irradiance power conversion efficiencies are very similar. This should be a convincing argument for silicon photovoltaic manufacturers to give perovskites a try as an accompanying top absorber.

All of the device architectures touched upon in this thesis demonstrate the potential to deserve a place in the list of candidates to be considered for future research and commercialization efforts. The possibility to cheaply pattern perovskites to fabricate semi-transparent solar cells with neutral colour, present a feature unmatchable by other materials such as crystalline silicon, and could allow for a quick entry into a niche market. Studying electrodes and interface materials is made possible with the demonstrated back contact devices. Much more exciting results can be expected when these systems are electronically improved, used for in situ studies of perovskite crystal formation with passivation processes and in-plane tandem applications. However, what stand between the lab results and the consumer product are two big aspects: stability and scalable fabrication processes. Analysing and optimising systematically the long-term stability of the presented solar cells was beyond the scope of this thesis and should be carried out to leap closer to feasible and usable applications. The use of more intrinsically stable materials (i.e. FA and Cs containing perovskites) and ensuring their compatibility as well as the development of intelligent packaging designs will enable these. Once made stable, the economic competitiveness will be determined by the capital expenditure of the fabrication process and the resulting cost per watt of power output of the produced solar cell. This topic is of particular interest for the author of this thesis and sparks motivation to focus his future

efforts into this direction of research. With their low-cost processing opportunities and high efficiencies perovskites have all the properties needed to become the new shining star on the clean energy horizon and contribute to alleviate global climate change. It can hardly be argued that we are looking into a bright future for opto-electronic perovskite applications.

9 REFERENCES

(1) Soytas, U.; Sari, R. Energy Consumption and GDP: Causality Relationship in G-7 Countries and Emerging Markets. *Energy Econ.* **2003**, *25*, 33–37.

(2) Keeling, C. D.; Bacastow, R. B.; Bainbridge, A. E.; Ekdahl Jr., C. . A.; Guenther, P. R.; Waterman, L. S.; Chin, J. F. S. Atmospheric Carbon Dioxide Variations at Mauna Loa Observatory, Hawaii. *Tellus A* **1976**, *28*, 538–551.

(3) Tol, R. S. J. Quantifying the Consensus on Anthropogenic Global Warming in the Literature: Rejoinder. *Energy Policy* **2014**, *73*, 709.

(4) Solomon, S.; Plattner, G.-K.; Knutti, R.; Friedlingstein, P. Irreversible Climate Change due to Carbon Dioxide Emissions. *Proc. Natl. Acad. Sci. U.S.A* **2009**, *106*, 1704–1709.

(5) Parmesan, C.; Yohe, G.; Parmesan, C.; Yohe, G.; Yohe, G. A Globally Coherent Fingerprint of Climate Change Impacts across Natural Systems. *Nature* **2003**, *421*, 37–42.

(6) Hughes, T. P. Climate Change, Human Impacts, and the Resilience of Coral Reefs. *Science (80-.).* **2003**, *301*, 929–933.

(7) *Statistical Review of World Energy*; 2016.

(8) Obama, B. The Irreversible Momentum of Clean Energy. *Science (80-.).* **2017**.

(9) Kristin Seyboth; Sverrisson, F.; Appavou, F.; Brown, A.; Epp, B.; Leidreiter, A.; Lins, C.; Musolino, E.; Murdock, H. E.; Petrichenko, K.; *et al. Renewables 2016 Global Status Report*; 2016.

(10) Jean, J.; Brown, P. R.; Jaffe, R. L.; Buonassisi, T.; Bulovic, V. Pathways for Solar Photovoltaics. *Energy Environ. Sci.* **2015**, *8*, 1200–1219.

(11) Schachinger, M. Module price index http://www.pv-magazine.com/investors/module-price-index/#axzz2c79c34GK (accessed Dec 11, 2016).

(12) Powell, D. M.; Fu, R.; Horowitz, K.; Basore, P. A.; Woodhouse, M.; Buonassisi, T. The Capital Intensity of Photovoltaics Manufacturing: Barrier to Scale and Opportunity for Innovation. *Energy Environ. Sci.* **2015**, *8*, 3395–3408.

(13) Schmalensee, R.; Bulović, V.; Armstrong, R.; Batlle, C.; Brown, P.; Deutch, J.; Jacoby, H.; Jaffe, R.; Jean, J.; Miller, R.; *et al. The Future of Solar Energy*; 2015.

(14) Green, M. A.; Emery, K.; Hishikawa, Y.; Warta, W.; Dunlop, E. D. Solar Cell Efficiency Tables (Version 48). *Prog. Photovoltaics Res. Appl.* **2016**, *24*, 905–913.

(15) Eperon, G. E.; Burlakov, V. M.; Goriely, A.; Snaith, H. J. Neutral Color Semitransparent Microstructured Perovskite Solar Cells. *ACS Nano* **2014**, *8*, 591–598.

(16) Griffiths, D. *Introduction to Quantum Mechanics*; Pearson Education India, 2005.

(17) Giorgi, G.; Fujisawa, J. I.; Segawa, H.; Yamashita, K. Small Photocarrier Effective Masses Featuring Ambipolar Transport in Methylammonium Lead Iodide Perovskite: A Density Functional Analysis. *J. Phys. Chem. Lett.* **2013**, *4*, 4213–4216.

(18) Umari, P.; Mosconi, E.; De Angelis, F. Relativistic GW Calculations on CH3NH3PbI3 and CH3NH3SnI3 Perovskites for Solar Cell Applications. *Sci. Rep.* **2014**, *4*, 4467.

(19) Tress, W. *Organic Solar Cells: Theory, Experiment, and Device Simulation*; Springer, 1991; Vol. 3.

(20) Sze, S. M.; Ng, K. K. *Photodetectors and Solar Cells*; John Wiley & Sons, Inc.: Hoboken, NJ, USA, 2007.

(21) Nelson, J. *The Physics of Solar Cells - Nelson.pdf*; Imperial College Press, 2003.

(22) Shockley, W.; Queisser, H. J. Detailed Balance Limit of Efficiency of P-N Junction Solar Cells. *J. Appl. Phys.* **1961**, *32*, 510–519.

(23) Kirchhoff, G. Ueber Das Verhältniss Zwischen Dem Emissionsvermögen Und Dem Absorptionsvermögen Der Körper Für Wärme Und Licht. *Ann. Phys.* **1860**, *185*, 275–301.

(24) Rau, U. Reciprocity Relation between Photovoltaic Quantum Efficiency and Electroluminescent Emission of Solar Cells. *Phys. Rev. B - Condens. Matter Mater. Phys.* **2007**, *76*, 85303.

(25) Christoforo, M.; Hoke, E.; McGehee, M.; Unger, E. Transient Response of Organo-Metal-Halide Solar Cells Analyzed by Time-Resolved Current-Voltage Measurements. *Photonics* **2015**, *2*, 1101–1115.

(26) Pettersson, L. a a; Roman, L. S.; Inganäs, O. Modeling Photocurrent Action Spectra of Photovoltaic Devices Based on Organic Thin Films Modeling Photocurrent Action Spectra of Photovoltaic Devices Based on Organic Thin Films. *J. Appl. Phys.* **2011**, *487*, 487–496.

(27) Cox, L. J. *Ellipsometry and Polarized Light*; North-Holland. sole distributors for the USA and Canada, Elsevier Science Publishing Co., Inc., 1978; Vol. 25.

(28) Centurioni, E. Generalized Matrix Method for Calculation of Internal Light Energy Flux in Mixed Coherent and Incoherent Multilayers. *Appl. Opt.* **2005**, *44*, 7532.

(29) Walraven, R. Calculating the Position of the Sun. *Sol. Energy* **1978**, *20*, 393–397.

(30) Stine, W.; Geyer, M. *Power From The Sun*; 2001.

(31) Lamm, L. O. A New Analytic Expression for the Equation of Time. *Sol. Energy* **1981**, *26*, 465.

(32) Nann, S.; Emery, K. Spectral Effects on PV-Device Rating. *Sol. Energy Mater. Sol. Cells* **1992**, *27*, 189–216.

(33) Gueymard, C. A. *SMARTS, A Simple Model of the Atmospheric Radiative Transfer of Sunshine: Algorithms and Performance Assessment.*; Florida Solar Energy Center Cocoa, FL, 1995.

(34) Mousazadeh, H.; Keyhani, A.; Javadi, A.; Mobli, H.; Abrinia, K.; Sharifi, A. A Review of Principle and Sun-Tracking Methods for Maximizing Solar Systems Output. *Renew. Sustain. Energy Rev.* **2009**, *13*, 1800–1818.

(35) Liu, B. Y. H.; Jordan, R. C. The Interrelationship and Characteristic Distribution of Direct, Diffuse and Total Solar Radiation. *Sol. Energy* **1960**, *4*, 1–19.

(36) Klucher, T. M. Evaluation of Models to Predict Insolation on Tilted Surfaces. *Sol. Energy* **1979**, *23*, 111–114.

(37) Hay, J.; Davies, J. Calculations of the Solar Radiation Incident on an Inclined Surface. In *First Canadian Solar Radiation Data*; 1980; Vol. 59.

(38) Perez, R.; Ineichen, P.; Seals, R.; Michalsky, J.; Stewart, R. Modeling Daylight Availability and Irradiance Components from Direct and Global Irradiance. *Sol. Energy* **1990**, *44*, 271–289.

(39) Loutzenhiser, P. G.; Manz, H.; Felsmann, C.; Strachan, P. A.; Frank, T.; Maxwell, G. M. Empirical Validation of Models to Compute Solar Irradiance on Inclined Surfaces for Building Energy Simulation. *Sol. Energy* **2007**, *81*, 254–267.

(40) Hess, S.; Hanby, V. I. Collector Simulation Model with Dynamic Incidence Angle Modifier for Anisotropic Diffuse Irradiance. *Energy Procedia* **2014**, *48*, 87–96.

(41) Gueymard, C. An Anisotropic Solar Irradiance Model for Tilted Surfaces and Its Comparison with Selected Engineering Algorithms. *Sol. Energy* **1987**, *38*, 367–386.

(42) Perez, R.; Stewart, R.; Arbogast, C.; Seals, R.; Scott, J. An Anisotropic Hourly Diffuse Radiation Model for Sloping Surfaces: Description, Performance Validation, Site Dependency Evaluation. *Sol. Energy* **1986**, *36*, 481–497.

(43) Kim, H.-S.; Mora-Sero, I.; Gonzalez-Pedro, V.; Fabregat-Santiago, F.; Juarez-Perez, E. J.; Park, N.-G.; Bisquert, J. Mechanism of Carrier Accumulation in Perovskite Thin-Absorber Solar Cells. *Nat. Commun.* **2013**, *4*, 2242.

(44) Brunger, A. P.; Hooper, F. C. Anisotropic Sky Radiance Model Based on Narrow Field of View Measurements of Shortwave Radiance. *Sol. Energy* **1993**, *51*, 53–64.

(45) Mitzi, D. B. Synthesis, Structure, and Properties of Organic-Inorganic Perovskites and Related Materials. In *Progress in Inorganic Chemistry*; John Wiley & Sons, Inc., 2007; pp. 1–121.

(46) Kojima, A.; Teshima, K.; Shirai, Y.; Miyasaka, T. Novel Photoelectrochemical Cell with Mesoscopic Electrodes Sensitized by Lead-Halide Compounds (11). In *Meeting Abstracts*; 2008; Vol. MA2008-02, p. 27.

(47) Kojima, A.; Teshima, K.; Shirai, Y.; Miyasaka, T. Organometal Halide Perovskites as Visible-Light Sensitizers for Photovoltaic Cells Organometal Halide Perovskites as Visible-Light Sensitizers for Photovoltaic. *J. Am. Chem. Soc.* **2009**, *131*, 6050–6051.

(48) Kim, H.-S.; Lee, C.-R.; Im, J.-H.; Lee, K.-B.; Moehl, T.; Marchioro, A.; Moon, S.-J.; Humphry-Baker, R.; Yum, J.-H.; Moser, J. E.; *et al.* Lead Iodide Perovskite Sensitized All-Solid-State Submicron Thin Film Mesoscopic Solar Cell with Efficiency Exceeding 9%. *Scientific reports*, 2012, *2*, 591.

(49) Lee J Miyasaka, T Murakami, TN Snaith, HJ, M. M. T. Efficient Hybrid Solar Cells Based on Meso-Superstructured Organometal Halide Perovskites. *Science (80-.).* **2012**, *338*, 647.

(50) Oregan, B.; Gratzel, M. A Low-Cost, High-Efficiency Solar-Cell Based on Dye-Sensitized Colloidal Tio2 Films. *Nature* **1991**, *353*, 737–740.

(51) Alcocer, M. J. P.; Leijtens, T.; Herz, L. M.; Petrozza, A.; Snaith, H. J. Electron-Hole Diffusion Lengths Exceeding 1 Micrometer in an Organometal Trihalide Perovskite Absorber. *Science* **2014**, *342*, 341–344.

(52) Xing, G.; Mathews, N.; Sun, S.; Lim, S. S.; Lam, Y. M.; Gratzel, M.; Mhaisalkar, S.; Sum, T. C. Long-Range Balanced Electron- and Hole-Transport Lengths in Organic-Inorganic CH3NH3PbI3. *Science (80-.).* **2013**, *342*, 344–347.

(53) Liu, M.; Johnston, M. B.; Snaith, H. J. Efficient Planar Heterojunction Perovskite Solar Cells by Vapour Deposition. *Nature* **20139**, *501*, 395–398.

(54) Eperon, G. E.; Burlakov, V. M.; Docampo, P.; Goriely, A.; Snaith, H. J. Morphological Control for High Performance, Solution-Processed Planar Heterojunction Perovskite Solar Cells. *Adv. Funct. Mater.* **2014**, *24*, 151–157.

(55) Leijtens, T.; Lauber, B.; Eperon, G. E.; Stranks, S. D.; Snaith, H. J. The Importance of Perovskite Pore Filling in Organometal Mixed Halide Sensitized TiO2-Based Solar Cells. *J. Phys. Chem. Lett.* **2014**, *5*, 1096–1102.

(56) Wehrenfennig, C.; Eperon, G. E.; Johnston, M. B.; Snaith, H. J.; Herz, L. M. High Charge Carrier Mobilities and Lifetimes in Organolead Trihalide Perovskites. *Adv. Mater.* **2014**, *26*, 1584–1589.

(57) Oga, H.; Saeki, A.; Ogomi, Y.; Hayase, S.; Seki, S. Improved Understanding of the Electronic and Energetic Landscapes of Perovskite Solar Cells: High Local Charge Carrier Mobility, Reduced Recombination, and Extremely Shallow Traps. *J. Am. Chem. Soc.* **2014**, *136*, 13818–13825.

(58) Ponseca, C. S.; Savenije, T. J.; Abdellah, M.; Zheng, K.; Yartsev, A.; Pascher, T.; Harlang, T.; Chabera, P.; Pullerits, T.; Stepanov, A.; *et al.* Organometal Halide Perovskite Solar Cell Materials Rationalized: Ultrafast Charge Generation, High and Microsecond-Long Balanced Mobilities, and Slow Recombination. *J. Am. Chem. Soc.* **2014**, *136*, 5189–5192.

(59) Tvingstedt, K.; Malinkiewicz, O.; Baumann, A.; Deibel, C.; Snaith, H. J.; Dyakonov, V.; Bolink, H. J. Radiative Efficiency of Lead Iodide Based Perovskite Solar Cells. *Nat. Sci. Reports* **2014**, *4*, 1–7.

(60) Tress, W.; Marinova, N.; Ingans, O.; Nazeeruddin, M. K.; Zakeeruddin, S. M.; Graetzel, M. Predicting the Open-Circuit Voltage of CH3NH3PbI3 Perovskite Solar Cells Using Electroluminescence and Photovoltaic Quantum Efficiency Spectra: The Role of Radiative and Non-Radiative Recombination. *Adv. Energy Mater.* **2015**, *5*, 1400812.

(61) De Wolf, S.; Holovsky, J.; Moon, S. J.; Löper, P.; Niesen, B.; Ledinsky, M.; Haug, F. J.; Yum, J. H.; Ballif, C. Organometallic Halide Perovskites: Sharp Optical Absorption Edge and Its Relation to Photovoltaic Performance. *J. Phys. Chem. Lett.* **2014**, *5*, 1035–1039.

(62) Hirasawa, M.; Ishihara, T.; Goto, T.; Uchida, K.; Miura, N. Magnetoabsorption of the Lowest Exciton in Perovskite-Type Compound (CH3NH3)PbI3. *Phys. B Phys. Condens. Matter* **1994**, *201*, 427–430.

(63) Tanaka, K.; Takahashi, T.; Ban, T.; Kondo, T.; Uchida, K.; Miura, N. Comparative Study on the Excitons in Lead-Halide-Based Perovskite-Type Crystals CH3NH3PbBr3 CH3NH 3PbI3. *Solid State Commun.* **2003**, *127*, 619–623.

(64) D'Innocenzo, V.; Grancini, G.; Alcocer, M. J. P.; Kandada, A. R. S.; Stranks, S. D.; Lee, M. M.; Lanzani, G.; Snaith, H. J.; Petrozza, A. Excitons versus Free Charges in Organo-Lead Tri-Halide Perovskites. *Nat. Commun.* **2014**, *5*, 3586.

(65) Sun, S.; Salim, T.; Mathews, N.; Duchamp, M.; Boothroyd, C.; Xing, G.; Sum, T. C.; Lam, Y. M. The Origin of High Efficiency in Low-Temperature Solution-Processable Bilayer Organometal Halide Hybrid Solar Cells. *Energy Environ. Sci.* **2014**, *7*, 399.

(66) Lin, Q.; Armin, A.; Chandra, R.; Nagiri, R.; Burn, P. L.; Meredith, P. Electro-Optics of Perovskite Solar Cells. *Nat. Photonics* **2014**, *9*, 106–112.

(67) Miyata, A.; Mitioglu, A.; Plochocka, P.; Portugall, O.; Wang, J. T.; Stranks, S. D.; Snaith, H. J.; Nicholas, R. J. Direct Measurement of the Exciton Binding Energy and Effective Masses for Charge Carriers in Organic-Inorganic Tri-Halide Perovskites. *Nat. Phys.* **2015**, *11*, 582–587.

(68) Noh, J. H.; Im, S. H.; Heo, J. H.; Mandal, T. N.; Seok, S. Il. Chemical Management for Colorful, Efficient, and Stable Inorganic-Organic Hybrid Nanostructured Solar Cells. *Nano Lett.* **2013**, *13*, 1764–1769.

(69) Eperon, G. E.; Stranks, S. D.; Menelaou, C.; Johnston, M. B.; Herz, L. M.; Snaith, H. J. Supplementary Information Formamidinium of Formamidinium Lead Trihalide: A Broadly Tunable Perovskite for Efficient Planar Heterojunction Solar Cells. *Energy Environ. Sci.* **2014**, *7*, 982.

(70) Hao, F.; Stoumpos, C. C.; Chang, R. P. H.; Kanatzidis, M. G. Anomalous Band Gap Behavior in Mixed Sn and Pb Perovskites Enables Broadening of Absorption Spectrum in Solar Cells. *J. Am. Chem. Soc.* **2014**, *136*, 8094–8099.

(71) Noel, N. K.; Stranks, S. D.; Abate, A.; Wehrenfennig, C.; Guarnera, S.; Haghighirad, A.-A.; Sadhanala, A.; Eperon, G. E.; Pathak, S. K.; Johnston, M. B.; *et al.* Lead-Free Organic-Inorganic Tin Halide Perovskites for Photovoltaic Applications. *Energy Environ. Sci.* **2014**, *7*, 3061–3068.

(72) McMeekin, D. P.; Sadoughi, G.; Rehman, W.; Eperon, G. E.; Saliba, M.; Horantner, M. T.; Haghighirad, A.; Sakai, N.; Korte, L.; Rech, B.; *et al.* A Mixed-Cation Lead Mixed-Halide Perovskite Absorber for Tandem Solar Cells. *Science (80-.).* **2016**, *351*, 151–155.

(73) Saliba, M.; Matsui, T.; Seo, J.-Y.; Domanski, K.; Correa-Baena, J.-P.; Nazeeruddin, M. K.; Zakeeruddin, S. M.; Tress, W.; Abate, A.; Hagfeldt, A.; *et al.* Cesium-Containing Triple Cation Perovskite Solar Cells: Improved Stability, Reproducibility and High Efficiency. *Energy Environ. Sci.* **2016**, *9*, 1989–1997.

(74) Yi, C.; Luo, J.; Meloni, S.; Boziki, A.; Ashari-Astani, N.; Grätzel, C.; Zakeeruddin, S. M.; Röthlisberger, U.; Grätzel, M. Entropic Stabilization of Mixed A-Cation ABX 3 Metal Halide Perovskites for High Performance Perovskite Solar Cells. *Energy Environ. Sci.* **2016**, *9*, 656–662.

(75) Yang, Z.; Rajagopal, A.; Chueh, C. C.; Jo, S. B.; Liu, B.; Zhao, T.; Jen, A. K. Y. Stable Low-Bandgap Pb/Sn Binary Perovskites for Tandem Solar Cells. *Adv. Mater.* **2016**, *28*, 8990–8997.

(76) Richard, R.; Transparent, V. B.; Link, C. Transparent , near-Infrared Organic Photovoltaic Solar Cells for Window and Energy-Scavenging Applications Citation Accessed Transparent , near-Infrared Organic Photovoltaic Solar Cells for Window and Energy-Scavenging Applications. *Appl. Phys. Lett.* **2016**, *98*, 113305.

(77) Park, N. G.; Kim, K. Transparent Solar Cells Based on Dye-Sensitized Nanocrystalline Semiconductors. *Phys. Status Solidi Appl. Mater. Sci.* **2008**, *205*, 1895–1904.

(78) Chen, C.-C.; Dou, L.; Gao, J.; Chang, W.-H.; Li, G.; Yang, Y. High-Performance Semi-Transparent Polymer Solar Cells Possessing Tandem Structures. *Energy Environ. Sci.* **2013**, *6*, 2714–2720.

(79) Jung, J. W.; Chueh, C. C.; Jen, A. K. Y. High-Performance Semitransparent Perovskite Solar Cells with 10% Power Conversion Efficiency and 25% Average Visible Transmittance Based on Transparent CuSCN as the Hole-Transporting Material. *Adv. Energy Mater.* **2015**, *5*.

(80) Ramírez Quiroz, C. O.; Levchuk, I.; Bronnbauer, C.; Salvador, M.; Forberich, K.; Heumüller, T.; Hou, Y.; Schweizer, P.; Spiecker, E.; Brabec, C. J. Pushing Efficiency Limits for Semitransparent Perovskite Solar Cells. *J. Mater. Chem. A* **2015**, *3*, 24071–24081.

(81) Liu, M.; Johnston, M. B.; Snaith, H. J. Efficient Planar Heterojunction Perovskite Solar Cells by Vapour Deposition. *Nature* **20139**, *501*, 395–398.

(82) Roldán-Carmona, C.; Malinkiewicz, O.; Betancur, R.; Longo, G.; Momblona, C.; Jaramillo, F.; Camacho, L.; Bolink, H. J. High Efficiency Single-Junction Semitransparent Perovskite Solar Cells. *Energy Environ. Sci.* **2014**, *7*, 2968.

(83) Della Gaspera, E.; Peng, Y.; Hou, Q.; Spiccia, L.; Bach, U.; Jasieniak, J. J.; Cheng, Y. B. Ultra-Thin High Efficiency Semitransparent Perovskite Solar Cells. *Nano Energy* **2015**, *13*, 249–257.

(84) Eperon, G. E.; Bryant, D.; Troughton, J.; Stranks, S. D.; Johnston, M. B.; Watson, T.; Worsley, D. A.; Snaith, H. J. Efficient, Semitransparent Neutral-Colored Solar Cells Based on Microstructured Formamidinium Lead Trihalide Perovskite. *J. Phys. Chem. Lett.* **2015**, *6*, 129–138.

(85) Hoerantner, M. T.; Nayak, P. K.; Mukhopadhyay, S.; Wojciechowski, K.; Beck, C.; McMeekin, D.; Kamino, B.; Eperon, G. E.; Snaith, H. J. Shunt-Blocking Layers for Semitransparent Perovskite Solar Cells. *Adv. Mater. Interfaces* **2016**, *3*.

(86) Bryant, D.; Greenwood, P.; Troughton, J.; Wijdekop, M.; Carnie, M.; Davies, M.; Wojciechowski, K.; Snaith, H. J.; Watson, T.; Worsley, D. A Transparent Conductive Adhesive Laminate Electrode for High-Efficiency Organic-Inorganic Lead Halide Perovskite Solar Cells. *Adv. Mater.* **2014**, *26*, 7499–7504.

(87) Li, Y.; Meng, L.; Yang, Y. (Michael); Xu, G.; Hong, Z.; Chen, Q.; You, J.; Li, G.; Yang, Y.; Li, Y. High-Efficiency Robust Perovskite Solar Cells on Ultrathin Flexible Substrates. *Nat. Commun.* **2016**, *7*, 10214.

(88) Peters, I. M.; Sofia, S.; Mailoa, J.; Buonassisi, T. Techno-Economic Analysis of Tandem Photovoltaic Systems. *RSC Adv.* **2016**, *6*, 66911–66923.

(89) Kayes, B. M.; Zhang, L.; Twist, R.; Ding, I.; Higashi, G. S. Flexible Thin-Film Tandem Solar Cells With >30% Efficiency. *IEEE J. Photovoltaics* **2014**, *4*, 729–733.

(90) Van Kerschaver, E.; Beaucarne, G. Back-Contact Solar Cells: A Review. *Prog. Photovoltaics Res. Appl.* **2006**, *14*, 107–123.

(91) Schwartz, R. J.; Lammert, M. D. Silicon Solar Cells for High Concentration Applications. In *1975 International Electron Devices Meeting*; IRE, 1975; Vol. 21, pp. 350–352.

(92) Savin, H.; Repo, P.; von Gastrow, G.; Ortega, P.; Calle, E.; Garín, M.; Alcubilla, R. Black Silicon Solar Cells with Interdigitated Back-Contacts Achieve 22.1% Efficiency. *Nat. Nanotechnol.* **2015**, *10*, 1–6.

(93) Neuhaus, D. H.; Münzer, A. Industrial Silicon Wafer Solar Cells. *Adv. Optoelectron.* **2007**, *2007*, 1–15.

(94) Masuko, K.; Shigematsu, M.; Hashiguchi, T.; Fujishima, D.; Kai, M.; Yoshimura, N.; Yamaguchi, T.; Ichihashi, Y.; Mishima, T.; Matsubara, N.; *et al.* Achievement of More than 25% Conversion Efficiency with Crystalline Silicon Heterojunction Solar Cell. *IEEE J. Photovoltaics* **2014**, *4*, 1433–1435.

(95) Saomoto, S. World's Highest Conversion Efficiency of 26.33% Achieved in a Crystalline Silicon Solar Cell. *New Energy and Industrial Technology Development Organization (NEDO) Kaneka Corporation*, 2016, 1–3.

(96) Gee, J. M.; Schubert, W. K.; Basore, P. A. Emitter Wrap-through Solar Cell. *IEEE* **1993**, 265–270.

(97) Hangarter, C. M.; Hamadani, B. H.; Guyer, J. E.; Xu, H.; Need, R.; Josell, D. Three Dimensionally Structured Interdigitated Back Contact Thin Film Heterojunction Solar Cells. *J. Appl. Phys.* **2011**, *109*.

(98) Hangarter, C. M.; Debnath, R.; Ha, J. Y.; Sahiner, M. A.; Reehil, C. J.; Manners, W. A.; Josell, D. Photocurrent Mapping of 3D CdSe/CdTe Windowless Solar Cells. *ACS Appl. Mater. Interfaces* **2013**, *5*, 9120–9127.

(99) Josell, D.; Debnath, R.; Ha, J. Y.; Guyer, J.; Sahiner, M. A.; Reehil, C. J.; Manners, W. A.; Nguyen, N. V. Windowless CdSe/CdTe Solar Cells with Di Ff Erentiated Back Contacts: J − V , EQE, and Photocurrent Mapping. **2014**.

(100) Fu, D.; Li Zhang, X.; Barber, R. L.; Bach, U. Dye-Sensitized Back-Contact Solar Cells. *Adv. Mater.* **2010**, *22*, 4270–4274.

(101) Nagata, S.; Atkinson, G. M.; Pestov, D.; Tepper, G. C.; McLeskey, J. T. Co-Planar Bi-Metallic Interdigitated Electrode Substrate for Spin-Coated Organic Solar Cells. *Sol. Energy Mater. Sol. Cells* **2011**, *95*, 1594–1597.

(102) Gatzen, H. H.; Saile, V.; Leuthold, J. *Micro and Nano Fabrication Tools and Processes*; Springer-Verlag GmbH.

(103) Streetman, B. G. *Solid State Electronic Devices*; Prentice Hall, 2005.

(104) Yu, B.; Pan, D. Z. *Design for Manufacturability with Advanced Lithography*; Springer.

(105) Lim, H.; Choi, K. B.; Kim, G.; Lee, S.; Park, H.; Ryu, J.; Jung, S.; Lee, J. Roll-to-Roll Nanoimprint Lithography for Patterning on a Large-Area Substrate Roll. *Microelectron. Eng.* **2014**, *123*, 18–22.

(106) Kooy, N.; Mohamed, K.; Pin, L. T.; Guan, O. S. A Review of Roll-to-Roll Nanoimprint Lithography. *Nanoscale Res. Lett.* **2014**, *9*, 320.

(107) Ye, X.; Qi, L. Two-Dimensionally Patterned Nanostructures Based on Monolayer Colloidal Crystals: Controllable Fabrication, Assembly, and Applications. *Nano Today* **2011**, *6*, 608–631.

(108) Denkov, N.; Velev, O.; Kralchevski, P.; Ivanov, I.; Yoshimura, H.; Nagayama, K. Mechanism of Formation of Two-Dimensional Crystals from Latex Particles on Substrates. *Langmuir* **1992**, *8*, 3183–3190.

(109) Dimitrov, A. S.; Nagayama, K. Continuous Convective Assembling of Fine Particles into Two-Dimensional Arrays on Solid Surfaces. *Langmuir* **1996**, *12*, 1303–1311.

(110) Jiang, P.; Prasad, T.; McFarland, M. J.; Colvin, V. L. Two-Dimensional Non Close-Packed Colloidal Crystals Formed by Spincoating. *Appl. Phys. Lett.* **2006**, *89*, 11908.

(111) Jiang, P.; McFarland, M. J. Wafer-Scale Periodic Nanohole Arrays Templated from Two-Dimensional Nonclose-Packed Colloidal Crystals. *J. Am. Chem. Soc.* **2005**, *127*, 3710–3711.

(112) Li, Y.; Cai, W.; Duan, G. Ordered Micro/nanostructured Arrays Based on the Monolayer Colloidal Crystals. *Chem. Mater.* **2008**, *20*, 615–624.

(113) Gunnarsson, L.; Bjerneld, E. J.; Xu, H.; Petronis, S.; Kasemo, B.; Käll, M. Interparticle Coupling Effects in Nanofabricated Substrates for Surface-Enhanced Raman Scattering. *Appl. Phys. Lett.* **2001**, *78*, 802–804.

(114) Kolle, M.; Salgard-Cunha, P. M.; Scherer, M. R. J.; Huang, F.; Vukusic, P.; Mahajan, S.; Baumberg, J. J.; Steiner, U. Mimicking the Colourful Wing Scale Structure of the Papilio Blumei Butterfly. *Nat. Nanotechnol.* **2010**, *5*, 511–515.

(115) Wijnhoven, J. E. G. J.; Vos, W. L. Preparation of Photonic Crystals Made of Air Spheres in Titania. *Science (80-.).* **1998**, *281*, 802–804.

(116) Farcau, C.; Astilean, S. 4.Probing the Unusual Optical Transmission of Silver Films Deposited on Two-Dimensional Regular Arrays of Polystyrene Microspheres. *J. Opt. A Pure Appl. Opt.* **2007**, *9*, S345–S349.

(117) Zhang, J.; Li, Y.; Zhang, X.; Yang, B. Colloidal Self-Assembly Meets Nanofabrication: From Two-Dimensional Colloidal Crystals to Nanostructure Arrays. *Adv. Mater.* **2010**, *22*, 4249–4269.

(118) Ulman, a. Formation and Structure of Self-Assembled Monolayers. *Chem. Rev.* **1996**, *96*, 1533–1554.

(119) Calame, K. L.; Lin, K.-I.; Tunyaplin, C. REGULATORY MECHANISMS THAT DETERMINE THE DEVELOPMENT AND FUNCTION OF PLASMA CELLS. *Annu. Rev. Immunol.* **2003**, *21*, 205–230.

(120) Koh, S. J. Strategies for Controlled Placement of Nanoscale Building Blocks. *Nanoscale Res. Lett.* **2007**, *2*, 519–545.

(121) Anaraki, E. H.; Kermanpur, A.; Steier, L.; Domanski, K.; Matsui, T.; Tress, W.; Saliba, M.; Abate, A.; Grä, M.; Hagfeldt, A.; *et al.* Highly Efficient and Stable Planar Perovskite Solar Cells by Solution-Processed Tin Oxide. *Energy Environ. Sci. Energy Environ. Sci* **2016**, *3128*, 3128–3134.

(122) Hulteen, J. C. Nanosphere Lithography: A Materials General Fabrication Process for Periodic Particle Array Surfaces. *J. Vac. Sci. Technol. A Vacuum, Surfaces, Film.* **1995**, *13*, 1553.

(123) Cheung, C. L.; Nikolic, R. J.; Reinhardt, C. E.; Wang, T. F. Fabrication of Nanopillars by Nanosphere Lithography. *Nanotechnology* **2006**, *17*, 1339–1343.

(124) Bogush, G. H.; Tracy, M. A.; Zukoski IV, C. F. Preparation of Monodisperse Silica Particles: Control of Size and Mass Fraction. *J. Non. Cryst. Solids* **1988**, *104*, 95–106.

(125) Snaith, H. J. How Should You Measure Your Excitonic Solar Cells? *Energy Environ. Sci.* **2012**, *5*, 6513.

(126) de Mello, J. C.; Wittmannn, H. F.; Friend, R. H. An Improved Experimental Determination of External Photoluminescence Quantum Efficiency. *Adv. Mater.* **1997**, *9*, 230.

(127) Centurioni, E. Generalized Matrix Method for Calculation of Internal Light Energy Flux in Mixed Coherent and Incoherent Multilayers. *Appl. Opt.* **2005**, *44*, 7532.

(128) Ball, J. M.; Stranks, S. D.; Hörantner, M. T.; Hüttner, S.; Zhang, W.; Crossland, J. W.; Ramirez, I.; Riede, M.; Johnston, M. B.; Steiner, U.; *et al*. Optical Properties and Limiting Photocurrent of Thin-Film Perovskite Solar Cells. *Energy Environ. Sci.* **2015**, *8*, 602–609.

(129) Filipic, M.; Loper, P.; Niesen, B.; De Wolf, S.; Krc, J.; Ballif, C.; Topic, M. CH3NH3PbI3 Perovskite / Silicon Tandem Solar Cells: Characterization Based Optical Simulations. *Opt Express* **2015**, *23*, A263-78.

(130) Löper, P.; Stuckelberger, M.; Niesen, B.; Werner, J.; Filipič, M.; Moon, S.-J.; Yum, J.-H.; Topič, M.; De Wolf, S.; Ballif, C. Complex Refractive Index Spectra of CH 3 NH 3 PbI 3 Perovskite Thin Films Determined by Spectroscopic Ellipsometry and Spectrophotometry. *J. Phys. Chem. Lett.* **2015**, *6*, 66–71.

(131) McMeekin, D. P.; Sadoughi, G.; Rehman, W.; Eperon, G. E.; Saliba, M.; Horantner, M. T.; Haghighirad, A.; Sakai, N.; Korte, L.; Rech, B.; *et al.* A Mixed-Cation Lead Mixed-Halide Perovskite Absorber for Tandem Solar Cells. *Science (80-.).* **2016**, *351*, 151–155.

(132) Stern, F. Dispersion of the Index of Refraction near the Absorption Edge of Semiconductors. *Phys. Rev.* **1964**, *133*, A1653–A1664.

(133) Ohta, K.; Ishida, H. Comparison among Several Numerical Integration Methods for Kramers-Kronig Transformation. *Appl. Spectrosc.* **1988**, *42*, 952–957.

(134) Jain, A.; Kapoor, A. Exact Analytical Solutions of the Parameters of Real Solar Cells Using Lambert W-Function. *Sol. Energy Mater. Sol. Cells* **2004**, *81*, 269–277.

(135) Hadipour, A.; de Boer, B.; Blom, P. W. M. Device Operation of Organic Tandem Solar Cells. *Org. Electron. physics, Mater. Appl.* **2008**, *9*, 617–624.

(136) NREL - National Solar Radiation Database (NSRDB) https://nsrdb.nrel.gov/ (accessed Jan 6, 2017).

(137) Landau, C. R. Optimum Tilt of Solar Panels http://www.macslab.com/optsolar.html (accessed Jan 13, 2017).

(138) Storn, R.; Price, K. Differential Evolution – A Simple and Efficient Heuristic for Global Optimization over Continuous Spaces. *J. Glob. Optim.* **1997**, *11*, 341–359.

(139) Burschka, J.; Pellet, N.; Moon, S.-J.; Humphry-Baker, R.; Gao, P.; Nazeeruddin, M. K.; Grätzel, M. Sequential Deposition as a Route to High-Performance Perovskite-Sensitized Solar Cells. *Nature* **2013**, *499*, 316–320.

(140) Jeon, N. J.; Noh, J. H.; Kim, Y. C.; Yang, W. S.; Ryu, S.; Seok, S. Il. Solvent Engineering for High-Performance Inorganic–organic Hybrid Perovskite Solar Cells. *Nat Mater* **2014**, *13*, 897–903.

(141) Green, M. A.; Ho-Baillie, A.; Snaith, H. J. The Emergence of Perovskite Solar Cells. *Nat. Photonics* **2014**, *8*, 506–514.

(142) Mitzi, D. B.; Feild, C. A.; Harrison, W. T. A.; Guloy, A. M.; Kagan, C. R.; Mitzi, D. B.; Dimitrakopoulos, C. D. Organic-Inorganic Hybrid Materials as Semiconducting Channels in Thin-Film Field-Effect Transistors. *Nature* **1994**, *369*, 467–469.

(143) Xing, G.; Mathews, N.; Lim, S. S.; Yantara, N.; Liu, X.; Sabba, D.; Grätzel, M.; Mhaisalkar, S.; Sum, T. C. Low-Temperature Solution-Processed Wavelength-Tunable Perovskites for Lasing. *Nat. Mater.* **2014**, *13*, 476–480.

(144) Deschler, F.; Price, M.; Pathak, S.; Klintberg, L. E.; Jarausch, D. D.; Higler, R.; Hüttner, S.; Leijtens, T.; Stranks, S. D.; Snaith, H. J.; *et al.* High Photoluminescence Efficiency and Optically Pumped Lasing in Solution-Processed Mixed Halide Perovskite Semiconductors. *J. Phys. Chem. Lett.* **2014**, *5*, 1421–1426.

(145) Tan, Z.-K.; Moghaddam, R. S.; Lai, M. L.; Docampo, P.; Higler, R.; Deschler, F.; Price, M.; Sadhanala, A.; Pazos, L. M.; Credgington, D.; *et al.* Bright Light-Emitting Diodes Based on Organometal Halide Perovskite. *Nat. Nanotechnol.* **2014**, *9*, 1–6.

(146) Song, M. H.; Kabra, D.; Wenger, B.; Friend, R. H.; Snaith, H. J. Optically-Pumped Lasing in Hybrid Organic-Inorganic Light-Emitting Diodes. *Adv. Funct. Mater.* **2009**, *19*, 2130–2136.

(147) Fang, H. H.; Ding, R.; Lu, S. Y.; Yang, J.; Zhang, X. L.; Yang, R.; Feng, J.; Chen, Q. D.; Song, J. F.; Sun, H. B. Distributed Feedback Lasers Based on Thiophene/phenylene Co-Oligomer Single Crystals. *Adv. Funct. Mater.* **2012**, *22*, 33–38.

(148) Mahler, L.; Tredicucci, A.; Beltram, F.; Walther, C.; Beere, H. E.; Ritchie, D. A.; Wiersma, D. S. Quasi-Periodic Distributed Feedback Laser. *Nat. Photonics* **2010**, *4*, 165–169.

(149) Pavesi, L.; Mazzoleni, C.; Tredicucci, A.; Pellegrini, V. Controlled Photon Emission in Porous Silicon Microcavities. *Appl. Phys. Lett.* **1995**, *67*, 3280.

(150) Koo, W. H.; Youn, W.; Zhu, P.; Li, X. H.; Tansu, N.; So, F. Light Extraction of Organic Light Emitting Diodes by Defective Hexagonal-Close-Packed Array. *Adv. Funct. Mater.* **2012**, *22*, 3454–3459.

(151) Li, X. H.; Song, R.; Ee, Y. K.; Kumnorkaew, P.; Gilchrist, J. F.; Tansu, N. Light Extraction Efficiency and Radiation Patterns of III-Nitride Light-Emitting Diodes with Colloidal Microlens Arrays with Various Aspect Ratios. *IEEE Photonics J.* **2011**, *3*, 489–499.

(152) Snaith, H. J. Perovskites: The Emergence of a New Era for Low-Cost, High-Efficiency Solar Cells. *J. Phys. Chem. Lett.* **2013**, *4*, 3623–3630.

(153) Kagan, C. R.; Breen, T. L.; Kosbar, L. L. Patterning Organic – Inorganic Thin-Film Transistors Using Microcontact Printed Templates Patterning Organic – Inorganic Thin-Film Transistors Using Microcontact Printed Templates. *Appl. Phys. Lett.* **2007**, *3536*, 1–4.

(154) Eperon, G. E.; Burlakov, V. M.; Docampo, P.; Goriely, A.; Snaith, H. J. Morphological Control for High Performance, Solution-Processed Planar Heterojunction Perovskite Solar Cells. *Adv. Funct. Mater.* **2014**, *24*, 151–157.

(155) Jang, J.; Hwang, S. H.; Roh, J.; Lee, J.; Ryu, J.; Yun, J. Size-Controlled SiO2 Nanoparticles as Scaffold Layers in Thin-Film Perovskite Solar Cells. *J. Mater. Chem. A* **2014**, *2*, Ahead of Print.

(156) Chou, T. P.; Zhang, Q.; Fryxell, G. E.; Cao, G. Hierarchically Structured ZnO Film for Dye-Sensitized Solar Cells with Enhanced Energy Conversion Efficiency. *Adv. Mater.* **2007**, *19*, 2588–2592.

(157) Yuan, W.; Zhao, H.; Hu, H.; Wang, S.; Baker, G. L. Synthesis and Characterization of the Hole-Conducting Silica/polymer Nanocomposites and Application in Solid-State Dye-Sensitized Solar Cell. *ACS Appl. Mater. Interfaces* **2013**, *5*, 4155–4161.

(158) Hench, L. L.; West, J. K. The Sol-Gel Process. *Chem. Rev.* **1990**, *90*, 33–72.

(159) Burlakov, V. M.; Eperon, G. E.; Snaith, H. J.; Chapman, S. J.; Goriely, A. Controlling Coverage of Solution Cast Materials with Unfavourable Surface Interactions. *Appl. Phys. Lett.* **2014**, *104*, 91602.

(160) Devore, J. R. Refractive Indices of Rutile and Sphalerite. *J. Opt. Soc. Am.* **1951**, *41*, 416.

(161) Ghosh, G. Dispersion-Equation Coefficients for the Refractive Index and Birefringence of Calcite and Quartz Crystals. *Opt. Commun.* **1999**, *163*, 95–102.

(162) Optics, H. O. F.; Library, D. E.; Companies, T. M. Optical Properties of Films and Coatings. *Handb. Opt.* **2004**, *1*, 41–42.

(163) Unger, E. L.; Hoke, E. T.; Bailie, C. D.; Nguyen, W. H.; Bowring, A. R.; Heumüller, T.; Christoforo, M. G.; McGehee, M. D. Hysteresis and Transient Behavior in Current–voltage Measurements of Hybrid-Perovskite Absorber Solar Cells. *Energy Environ. Sci.* **2014**, *7*, 3690–3698.

(164) Mauro, J. C. Topological Constraint Theory of Glass. *Am. Ceram. Soc. Bull.* **2011**, *90*, 31–37.

(165) Snaith, H. J.; Abate, A.; Ball, J. M.; Eperon, G. E.; Leijtens, T.; Noel, N. K.; Stranks, S. D.; Wang, J. T. W.; Wojciechowski, K.; Zhang, W. Anomalous Hysteresis in Perovskite Solar Cells. *J. Phys. Chem. Lett.* **2014**, *5*, 1511–1515.

(166) Green, M. A.; Emery, K.; Hishikawa, Y.; Warta, W.; Dunlop, E. D. Solar Cell Efficiency Tables (Version 45). *Prog. Photovoltaics Res. Appl.* **2015**, *23*, 1–9.

(167) Eperon, G. E.; Burlakov, V. M.; Docampo, P.; Goriely, A.; Snaith, H. J. Morphological Control for High Performance, Solution-Processed Planar Heterojunction Perovskite Solar Cells. *Afm* **2014**, *24*, 151–157.

(168) Xiao, M.; Huang, F.; Huang, W.; Dkhissi, Y.; Zhu, Y.; Etheridge, J.; Gray-Weale, A.; Bach, U.; Cheng, Y.-B.; Spiccia, L. A Fast Deposition-Crystallization Procedure for Highly Efficient Lead(supporting). *Angew. Chemie* **2014**, *126*, 10056–10061.

(169) Stranks, S. D.; Nayak, P. K.; Zhang, W.; Stergiopoulos, T.; Snaith, H. J. Formation of Thin Films of Organic-Inorganic Perovskites for High-Efficiency Solar Cells. *Angew. Chemie - Int. Ed.* **2015**, *54*, 3240–3248.

(170) McGehee, M. D. Perovskite Solar Cells: Continuing to Soar. *Nat. Mater.* **2014**, *13*, 845–846.

(171) Nelson, J. *The Physics of Solar Cells - Nelson.pdf*; Series on Properties of Semiconductor Materials; Imperial College Press, 2003.

(172) Xiao, M.; Huang, F.; Huang, W.; Dkhissi, Y.; Zhu, Y.; Etheridge, J.; Gray-Weale, A.; Bach, U.; Cheng, Y. B.; Spiccia, L. A Fast Deposition-Crystallization Procedure for Highly Efficient Lead Iodide Perovskite Thin-Film Solar Cells. *Angewandte Chemie - International Edition*, 2014, *53*, 9898–9903.

(173) Zhang, W.; Saliba, M.; Moore, D. T.; Pathak, S. K.; Horantner, M. T.; Stergiopoulos, T.; Stranks, S. D.; Eperon, G. E.; Alexander-Webber, J. A.; Abate, A.; *et al.* Ultrasmooth Organic-Inorganic Perovskite Thin-Film Formation and Crystallization for Efficient Planar Heterojunction Solar Cells. *Nat Commun* **2015**, *6*, 6142.

(174) de Quilettes, D. W.; Vorpahl, S. M.; Stranks, S. D.; Nagaoka, H.; Eperon, G. E.; Ziffer, M. E.; Snaith, H. J.; Ginger, D. S. Impact of Microstructure on Local Carrier Lifetime in Perovskite Solar Cells. *Science (80-.).* **2015**, *348*, 683–686.

(175) Della Gaspera, E.; Peng, Y.; Hou, Q.; Spiccia, L.; Bach, U.; Jasieniak, J. J.; Cheng, Y. B. Ultra-Thin High Efficiency Semitransparent Perovskite Solar Cells. *Nano Energy* **2015**, *13*, 249–257.

(176) Hörantner, M. T.; Zhang, W.; Saliba, M.; Wojciechowski, K.; Snaith, H. J. Templated Microstructural Growth of Perovskite Thin Films via Colloidal Monolayer Lithography. *Energy Environ. Sci.* **2015**, *8*, 2041–2047.

(177) Chang, C. Y.; Lee, K. T.; Huang, W. K.; Siao, H. Y.; Chang, Y. C. High-Performance, Air-Stable, Low-Temperature Processed Semitransparent Perovskite Solar Cells Enabled by Atomic Layer Deposition. *Chem. Mater.* **2015**, *27*, 5122–5130.

(178) Roldan-Carmona, C.; Malinkiewicz, O.; Soriano, A.; Minguez Espallargas, G.; Garcia, A.; Reinecke, P.; Kroyer, T.; Dar, M. I.; Nazeeruddin, M. K.; Bolink, H. J. Flexible High Efficiency Perovskite Solar Cells. *Energy Environ. Sci.* **2014**, *7*, 994–997.

(179) DiBenedetto, S. A.; Facchetti, A.; Ratner, M. A.; Marks, T. J. Molecular Self-Assembled Monolayers and Multilayers for Organic and Unconventional Inorganic Thin-Film Transistor Applications. *Adv. Mater.* **2009**, *21*, 1407–1433.

(180) Yaffe, O.; Qi, Y.; Scheres, L.; Puniredd, S. R.; Segev, L.; Ely, T.; Haick, H.; Zuilhof, H.; Vilan, A.; Kronik, L.; *et al.* Charge Transport across Metal/molecular (Alkyl) Monolayer-Si Junctions Is Dominated by the LUMO Level. *Phys. Rev. B - Condens. Matter Mater. Phys.* **2012**, *85*, 45433.

(181) Nayak, P. K.; Barnea-Nehoshtan, L.; Kim, R. S.; Shu, A.; Man, G.; Kahn, A.; Lederman, D.; Feldman, Y.; Cahen, D. The Effect of Structural Order on Solar Cell Parameters, as Illustrated in a SiC-Organic Junction Model. *Energy Environ. Sci.* **2013**, *6*, 3272.

(182) Zuo, L.; Gu, Z.; Ye, T.; Fu, W.; Wu, G.; Li, H.; Chen, H. Enhanced Photovoltaic Performance of CH3NH3PbI3 Perovskite Solar Cells through Interfacial Engineering Using Self-Assembling Monolayer. *J. Am. Chem. Soc.* **2015**, *137*, 2674–2679.

(183) Parikh, A. N.; Schivley, M. A.; Koo, E.; Seshadri, K.; Aurentz, D.; Mueller, K.; Allara, D. L. N-Alkylsiloxanes: From Single Monolayers to Layered Crystals. The Formation of Crystalline Polymers from the Hydrolysis of N-Octadecyltrichlorosilane. *J. Am. Chem. Soc.* **1997**, *119*, 3135–3143.

(184) Allara, D. L.; Parikh, A. N.; Rondelez, F. Evidence for a Unique Chain Organization in Long Chain Silane Monolayers Deposited on Two Widely Different Solid Substrates. *Langmuir* **1995**, *11*, 2357–2360.

(185) Iguchi, N.; Cady, C.; Snoeberger, R. C.; Hunter, B. M.; Sproviero, E. M.; Schmuttenmaer, C. a; Crabtree, R. H.; Brudvig, G. W.; Batista, V. S. Characterization of Siloxane Adsorbates Covalently Attached to TiO2 - Art. No. 70340C. In *Physical Chemistry of Interfaces and Nanomaterials Vii*; 2008; Vol. 7034, pp. C340–C340.

(186) Zhao, J.; Milanova, M.; Warmoeskerken, M. M. C. G.; Dutschk, V. Surface Modification of TiO2 Nanoparticles with Silane Coupling Agents. *Colloids Surfaces A Physicochem. Eng. Asp.* **2012**, *413*, 273–279.

(187) Helmy, R.; Fadeev, A. Y. Self-Assembled Monolayers Supported on TiO2: Comparison of C18H37SiX3 (X = H, Cl, OCH3), C18H37Si(CH3)2Cl, and C18H37PO(OH)2. *Langmuir* **2002**, *18*, 8924–8928.

(188) Wang, Y.; Lieberman, M. Growth of Ultrasmooth Octadecyltrichlorosilane Self-Assembled Monolayers on SiO2. *Langmuir* **2003**, *19*, 1159–1167.

(189) Zhang, J.; Hu, Z.; Huang, L.; Yue, G.; Liu, J.; Lu, X.; Hu, Z.; Shang, M.; Han, L.; Zhu, Y. Bifunctional Alkyl Chain Barriers for Efficient Perovskite Solar Cells. *Chem. Commun. Chem. Commun* **2015**, *51*, 7047–7050.

(190) Marinova, N.; Tress, W.; Humphry-Baker, R.; Dar, M. I.; Bojinov, V.; Zakeeruddin, S. M.; Nazeeruddin, M. K.; Grätzel, M. Light Harvesting and Charge Recombination in CH 3 NH 3 PbI 3 Perovskite Solar Cells Studied by Hole Transport Layer Thickness Variation. *ACS Nano* **2015**, *9*, 4200–4209.

(191) Abate, A.; Saliba, M.; Hollman, D. J.; Stranks, S. D.; Wojciechowski, K.; Avolio, R.; Grancini, G.; Petrozza, A.; Snaith, H. J. Supramolecular Halogen Bond Passivation of Organic-Inorganic Halide Perovskite Solar Cells. *Nano Lett.* **2014**, *14*, 3247–3254.

(192) Sommeling, P. M.; O'Regan, B. C.; Haswell, R. R.; Smit, H. J. P.; Bakker, N. J.; Smits, J. J. T.; Kroon, J. M.; Van Roosmalen, J. A. M. Influence of a TiCl4 Post-Treatment on Nanocrystalline TiO 2 Films in Dye-Sensitized Solar Cells. *J. Phys. Chem. B* **2006**, *110*, 19191–19197.

(193) Kojima, A.; Teshima, K.; Shirai, Y.; Miyasaka, T. Organometal Halide Perovskites as Visible-Light Sensitizers for Photovoltaic Cells. *J. Am. Chem. Soc.* **2009**, *131*, 6050–6051.

(194) Im, J.-H.; Lee, C.-R.; Lee, J.-W.; Park, S.-W.; Park, N.-G.; Sargent, E. H.; Cho, K.-S.; Lee, E. K.; Joo, W.-J.; Jang, E.; *et al.* 6.5% Efficient Perovskite Quantum-Dot-Sensitized Solar Cell. *Nanoscale* **2011**, *3*, 4088.

(195) Kim, H.-S.; Lee, C.-R.; Im, J.-H.; Lee, K.-B.; Moehl, T.; Marchioro, A.; Moon, S.-J.; Humphry-Baker, R.; Yum, J.-H.; Moser, J. E.; *et al.* Lead Iodide Perovskite Sensitized All-Solid-State Submicron Thin Film Mesoscopic Solar Cell with Efficiency Exceeding 9%. *Sci. Rep.* **2012**, *2*, 591.

(196) You, J.; Hong, Z.; Yang, Y. M.; Chen, Q.; Cai, M.; Song, T.; Chen, C. Perovskite Solar Cells with High Efficiency and Flexibility. *ACS Nano* **2014**, *8*, 1674–1680.

(197) Docampo, P.; Ball, J. M.; Darwich, M.; Eperon, G. E.; Snaith, H. J. Efficient Organometal Trihalide Perovskite Planar-Heterojunction Solar Cells on Flexible Polymer Substrates. *Nat. Commun.* **2013**, *4*, 2761.

(198) Dong, Q.; Fang, Y.; Shao, Y.; Mulligan, P.; Qiu, J.; Cao, L.; Huang, J. Electron-Hole Diffusion Lengths > 175 Um in Solution-Grown CH 3 NH 3 PbI 3 Single Crystals. *Science* **2015**, *347*, 967–970.

(199) Xing, G.; Mathews, N.; Sun, S.; Lim, S. S.; Lam, Y. M.; Grätzel, M.; Mhaisalkar, S. G.; Sum, T. C. Long-Range Balanced Electron- and Hole-Transport Lengths in Organic-Inorganic CH3NH3PbI3. *Science (80-.).* **2013**, *342*, 344–347.

(200) de Quilettes, D. W.; Vorpahl, S. M.; Stranks, S. D.; Nagaoka, H.; Eperon, G. E.; Ziffer, M. E.; Snaith, H. J.; Ginger, D. S. Impact of Microstructure on Local Carrier Lifetime in Perovskite Solar Cells. *Science (80-.).* **2015**, *348*, 683–686.

(201) Pazos-Outon, L. M.; Szumilo, M.; Lamboll, R.; Richter, J. M.; Crespo-Quesada, M.; Abdi-Jalebi, M.; Beeson, H. J.; Vru ini, M.; Alsari, M.; Snaith, H. J.; *et al.* Photon Recycling in Lead Iodide Perovskite Solar Cells. *Science (80-.).* **2016**, *351*, 1430–1433.

(202) Menéndez-Proupin, E.; Palacios, P.; Wahnón, P.; Conesa, J. C. Self-Consistent Relativistic Band Structure of theCH3NH3PbI3. *Phys. Rev. B* **2014**, *90*, 45207.

(203) Leijtens, T.; Eperon, G. E.; Barker, A. J.; Grancini, G.; Zhang, W.; Ball, J. M.; Kandada, A. R. S.; Snaith, H. J.; Petrozza, A. Carrier Trapping and Recombination: The Role of Defect Physics in Enhancing the Open Circuit Voltage of Metal Halide Perovskite Solar Cells. *Energy Environ. Sci.* **2016**, *9*, 3472–3481.

(204) Jumabekov, A. N.; Della Gaspera, E.; Xu, Z.-Q.; Chesman, A. S. R.; van Embden, J.; Bonke, S. A.; Bao, Q.; Vak, D.; Bach, U. Back-Contacted Hybrid Organic–inorganic Perovskite Solar Cells. *J. Mater. Chem. C* **2016**, *4*, 3125–3130.

(205) Etgar, L.; Gao, P.; Xue, Z.; Peng, Q.; Chandiran, A. K.; Liu, B.; Nazeeruddin, M. K.; Grätzel, M. Mesoscopic CH 3NH 3PbI 3/TiO 2 Heterojunction Solar Cells. *J. Am. Chem. Soc.* **2012**, *134*, 17396–17399.

(206) Laban, W. A.; Etgar, L. Depleted Hole Conductor-Free Lead Halide Iodide Heterojunction Solar Cells. *Energy Environ. Sci.* **2013**, *6*, 3249–3253.

(207) Zhang, Y.; Liu, M.; Eperon, G. E.; Leijtens, T. C.; McMeekin, D.; Saliba, M.; Zhang, W.; de Bastiani, M.; Petrozza, A.; Herz, L. M.; *et al.* Charge Selective Contacts, Mobile Ions and Anomalous Hysteresis in Organic–inorganic Perovskite Solar Cells. *Mater. Horiz.* **2015**, *1*, 96.

(208) Pazos-Outon, L. M.; Szumilo, M.; Lamboll, R.; Richter, J. M.; Crespo-Quesada, M.; Abdi-Jalebi, M.; Beeson, H. J.; Vru ini, M.; Alsari, M.; Snaith, H. J.; *et al.* Photon Recycling in Lead Iodide Perovskite Solar Cells. *Science (80-.).* **2016**, *351*, 1430–1433.

(209) Noel, N. K.; Abate, A.; Stranks, S. D.; Parrott, E. S.; Burlakov, V. M.; Goriely, A.; Snaith, H. J.; Al, N. E. T. Enhanced Photoluminescence and Solar Cell Performance via Lewis Base Passivation of Organic À Inorganic Lead Halide Perovskites. **2014**, 9815–9821.

(210) Shkrob, I. A.; Marin, T. W. Charge Trapping in Photovoltaically Active Perovskites and Related Halogenoplumbate Compounds. *J. Phys. Chem. Lett.* **2014**, *5*, 1066–1071.

(211) John Wilfred Orton, P. B. The Electrical Characterization of Semiconductors: Measurement of Minority Carrier Properties. *Electr. Charact. Semicond. Meas. Minor. Carr. Prop.* **1990**, 71–96.

(212) Pala, R. A.; Leenheer, A. J.; Lichterman, M.; Atwater, H. A.; Lewis, N. S. Measurement of Minority-Carrier Diffusion Lengths Using Wedge-Shaped Semiconductor Photoelectrodes. *Energy Environ. Sci.* **2014**, *7*, 3424.

(213) Yang, Y.; Yan, Y.; Yang, M.; Choi, S.; Zhu, K.; Luther, J. M.; Beard, M. C. Low Surface Recombination Velocity in Solution-Grown CH3NH3PbBr3 Perovskite Single Crystal. *Nat Commun* **2015**, *6*, 7961.

(214) Yang, Y.; Yang, M.; Li, Z.; Crisp, R.; Zhu, K.; Beard, M. C. Comparison of Recombination Dynamics in CH3NH3PbBr3 and CH3NH3PbI3 Perovskite Films: Influence of Exciton Binding Energy. *J. Phys. Chem. Lett.* **2015**, *6*, 4688–4692.

(215) Staub, F.; Hempel, H.; Hebig, J. C.; Mock, J.; Paetzold, U. W.; Rau, U.; Unold, T.; Kirchartz, T. Beyond Bulk Lifetimes: Insights into Lead Halide Perovskite Films from Time-Resolved Photoluminescence. *Phys. Rev. Appl.* **2016**, *6*, 44017.

(216) Hodes, G.; Kamat, P. V. Understanding the Implication of Carrier Diffusion Length in Photovoltaic Cells. *J. Phys. Chem. Lett.* **2015**, *6*, 4090–4092.

(217) Wojciechowski, K.; Saliba, M.; Leijtens, T.; Abate, A.; Snaith, H. J. Sub-150 [degree]C Processed Meso-Superstructured Perovskite Solar Cells with Enhanced Efficiency. *Energy Environ. Sci.* **2014**, *7*, 1142–1147.

(218) Choi, J.; Song, S.; Hörantner, M. T.; Snaith, H. J.; Park, T. Well-Defined Nanostructured, Single-Crystalline TiO2 Electron Transport Layer for Efficient Planar Perovskite Solar Cells. *ACS Nano* **2016**, *10*, 6029–6036.

(219) Choi, J.; Song, S.; Hörantner, M. T.; Snaith, H. J.; Park, T. Well-Defined Nanostructured, Single-Crystalline TiO2 Electron Transport Layer for Efficient Planar Perovskite Solar Cells. *ACS Nano* **2016**, *10*, 6029–6036.

(220) Song, S.; Hörantner, M. T.; Choi, K.; Snaith, H. J.; Park, T. Inducing Swift Nucleation Morphology Control for Efficient Planar Perovskite Solar Cells by Hot-Air Quenching. *J. Mater. Chem. A* **2017**, *131*, 6050.

(221) Li, Y.; Cooper, J. K.; Liu, W.; Sutter-Fella, C. M.; Amani, M.; Beeman, J. W.; Javey, A.; Ager, J. W.; Liu, Y.; Toma, F. M.; *et al.* Defective TiO2 with High Photoconductive Gain for Efficient and Stable Planar Heterojunction Perovskite Solar Cells. *Nat. Commun.* **2016**, *7*, 12446.

(222) Baena, J. P. C.; Steier, L.; Tress, W.; Saliba, M.; Neutzner, S.; Matsui, T.; Giordano, F.; Jacobsson, T. J.; Kandada, A. R. S.; Zakeeruddin, S. M.; *et al.* Highly Efficient Planar Perovskite Solar Cells through Band Alignment Engineering. *Energy Environ. Sci.* **2015**, *8*, 2928–2934.

(223) Dong, Q.; Shi, Y.; Wang, K.; Li, Y.; Wang, S.; Zhang, H.; Xing, Y.; Du, Y.; Bai, X.; Ma, T. Insight into Perovskite Solar Cells Based on SnO2 Compact Electron-Selective Layer. *J. Phys. Chem. C* **2015**, *119*, 150415040655003.

(224) Shaw, P. E.; Ruseckas, A.; Samuel, I. D. W. Exciton Diffusion Measurements in Poly(3-Hexylthiophene). *Adv. Mater.* **2008**, *20*, 3516–3520.

(225) deQuilettes, D. W.; Koch, S.; Burke, S.; Paranji, R.; Shropshire, A. J.; Ziffer, M. E.; Ginger, D. S. Photoluminescence Lifetimes Exceeding 8 Ms and Quantum Yields Exceeding 30% in Hybrid Perovskite Thin Films by Ligand Passivation. *ACS Energy Lett.* **2016**, *1*, 1–7.

(226) Yang, D.; Zhou, X.; Yang, R.; Yang, Z.; Yu, W.; Wang, X.; Li, C.; Liu, S. F.; Chang, R. P. H. Surface Optimization to Eliminate Hysteresis for Record Efficiency Planar Perovskite Solar Cells. *Energy Environ. Sci.* **2016**, *9*, 3071–3078.

(227) Barnett, A.; Honsberg, C.; Kirkpatrick, D.; Kurtz, S.; Moore, D.; Salzman, D.; Schwartz, R.; Gray, J.; Bowden, S.; Goossen, K.; *et al.* 50% Efficient Solar Cell Architectures and Designs. In *Conference Record of the 2006 IEEE 4th World Conference on Photovoltaic Energy Conversion, WCPEC-4*; IEEE, 2007; Vol. 2, pp. 2560–2564.

(228) Bailie, C. D.; Christoforo, M. G.; Mailoa, J. P.; Bowring, A. R.; Unger, E. L.; Nguyen, W. H.; Burschka, J.; Pellet, N.; Lee, J. Z.; Grätzel, M.; *et al.* Semi-Transparent Perovskite Solar Cells for Tandems with Silicon and CIGS. *Energy Environ. Sci.* **2014**, *8*, 956–963.

(229) Mailoa, J. P.; Bailie, C. D.; Johlin, E. C.; Hoke, E. T.; Akey, A. J.; Nguyen, W. H.; McGehee, M. D.; Buonassisi, T. A 2-Terminal Perovskite/silicon Multijunction Solar Cell Enabled by a Silicon Tunnel Junction. *Appl. Phys. Lett.* **2015**, *106*, 121105.

(230) Albrecht, S.; Saliba, M.; Correa Baena, J. P.; Lang, F.; Kegelmann, L.; Mews, M.; Steier, L.; Abate, A.; Rappich, J.; Korte, L.; *et al.* Monolithic Perovskite/silicon-Heterojunction Tandem Solar Cells Processed at Low Temperature. *Energy Environ. Sci.* **2016**, *9*, 81–88.

(231) Werner, J.; Weng, C.-H.; Walter, A.; Fesquet, L.; Seif, J. P.; De Wolf, S.; Niesen, B.; Ballif, C. Efficient Monolithic Perovskite/Silicon Tandem Solar Cell With Cell Area > 1 Cm 2. *J. Phys. Chem. Lett.* **2015**, *7*, acs.jpclett.5b02686.

(232) Chen, B.; Bai, Y.; Yu, Z.; Li, T.; Zheng, X.; Dong, Q.; Shen, L.; Boccard, M.; Gruverman, A.; Holman, Z.; *et al.* Efficient Semitransparent Perovskite Solar Cells for 23.0%-Efficiency Perovskite/Silicon Four-Terminal Tandem Cells. *Adv. Energy Mater.* **2016**, *6*, 1601128.

(233) Lang, F.; Gluba, M. a.; Albrecht, S.; Rappich, J.; Korte, L.; Rech, B.; Nickel, N. H. Perovskite Solar Cells with Large-Area CVD-Graphene for Tandem Solar Cells. *J. Phys. Chem. Lett.* **2015**, *6*, 2745–2750.

(234) Werner, J.; Barraud, L.; Walter, A.; Bräuninger, M.; Sahli, F.; Sacchetto, D.; Tétreault, N.; Paviet-Salomon, B.; Moon, S.-J.; Allebé, C.; *et al.* Efficient Near-Infrared-Transparent Perovskite Solar Cells Enabling Direct Comparison of 4 -Terminal and Monolithic Perovskite/Silicon Tandem Cells. *ACS energy Lett.* **2016**, *1*, 474−480.

(235) Noh, J. H.; Im, S. H.; Heo, J. H.; Mandal, T. N.; Seok, S. Il. Chemical Management for Colorful, Efficient, and Stable Inorganic-Organic Hybrid Nanostructured Solar Cells. *Nano Lett.* **2013**, *13*, 1764–1769.

(236) Lee, J. W.; Kim, D. H.; Kim, H. S.; Seo, S. W.; Cho, S. M.; Park, N. G. Formamidinium and Cesium Hybridization for Photo- and Moisture-Stable Perovskite Solar Cell. *Adv. Energy Mater.* **2015**, *5*, 1501310.

(237) Liao, W.; Zhao, D.; Yu, Y.; Shrestha, N.; Ghimire, K.; Grice, C. R.; Wang, C.; Xiao, Y.; Cimaroli, A. J.; Ellingson, R. J.; *et al.* Fabrication of Efficient Low-Bandgap Perovskite Solar Cells by Combining Formamidinium Tin Iodide with Methylammonium Lead Iodide. *J. Am. Chem. Soc.* **2016**, *138*, 12360–12363.

(238) Eperon, G. E.; Leijtens, T.; Bush, K. A.; Prasanna, R.; Green, T.; Wang, J. T.-W.; McMeekin, D. P.; Volonakis, G.; Milot, R. L.; May, R.; *et al.* Perovskite-Perovskite Tandem Photovoltaics with Optimized Band Gaps. *Science (80-.).* **2016**, *354*, 861–865.

(239) Albrecht, S.; Saliba, M.; Jäger, K.; Korte, L.; Hagfeldt, A.; Grätzel, M.; Rech, B. Towards Optical Optimization of Planar Monolithic Perovskite / Silicon-Heterojunction Tandem Solar Cells. *J. Opt.* **2016**, *18*, 1–10.

(240) Anaya, M.; Correa-Baena, J. P.; Lozano, G.; Saliba, M.; Anguita, P.; Roose, B.; Abate, A.; Steiner, U.; Grätzel, M.; Calvo, M. E.; *et al.* Optical Analysis of $CH_3NH_3Sn_xPb_{1-x}I_3$ Absorbers: A Roadmap for Perovskite-on-Perovskite Tandem Solar Cells. *J. Mater. Chem. A* **2016**, *60–61*, 269.

(241) Strutt, J. W. XV. On the Light from the Sky, Its Polarization and Colour. *London, Edinburgh, Dublin Philos. Mag. J. Sci.* **1871**, *41*, 1.

(242) Gottschalg, R.; Infield, D. G.; Kearney, M. J. Experimental Study of Variations of the Solar Spectrum of Relevance to Thin Film Solar Cells. *Sol. Energy Mater. Sol. Cells* **2003**, *79*, 527–537.

(243) Pérez-López, J. J.; Fabero, F.; Chenlo, F. Experimental Solar Spectral Irradiance until 2500 Nm: Results and Influence on the PV Conversion of Different Materials. *Prog. Photovoltaics Res. Appl.* **2007**, *15*, 303–315.

(244) Ishii, T.; Otani, K.; Takashima, T.; Xue, Y. Solar Spectral Influence on the Performance of Photovoltaic (PV) Modules under Fine Weather and Cloudy Weather Conditions. *Prog. Photovoltaics Res. Appl.* **2013**, *21*, 481–489.

(245) Virtuani, A.; Fanni, L. Seasonal Power Fluctuations of Amorphous Silicon Thin-Film Solar Modules: Distinguishing between Different Contributions. *Prog. Photovoltaics Res. Appl.* **2014**, *22*, 208–217.

(246) Hirata, Y.; Tani, T. Output Variation of Photovoltaic Modules with Environmental Factors - I. The Effect of Spectral Solar Radiation on Photovoltaic Module Output. *Sol. Energy* **1995**, *55*, 463–468.

(247) Liu, H.; Ren, Z.; Liu, Z.; Aberle, A. G.; Buonassisi, T.; Peters, I. M. The Realistic Energy Yield Potential of GaAs-on-Si Tandem Solar Cells: A Theoretical Case Study. *Opt. Express* **2015**, *23*, A382.

(248) Mailoa, J. P.; Lee, M.; Peters, I. M.; Buonassisi, T.; Panchula, A.; Weiss, D. N. Energy-Yield Prediction for II–VI-Based Thin-Film Tandem Solar Cells. *Energy Environ. Sci. Energy Environ. Sci* **2644**, *9*, 2644–2653.

(249) Liu, H.; Aberle, A. G.; Buonassisi, T.; Peters, I. M. On the Methodology of Energy Yield Assessment for One-Sun Tandem Solar Cells. *Sol. Energy* **2016**, *135*, 598–604.

(250) Betts, T. R.; Jardine, Christian, N.; Gottschalg, R.; Infield, D. G.; Lane, K. Impact of Spectral Effects on the Electrical Parameters of Multijunction Amorphous Silicon Cells. In *3rd World Conference on Photovoltaic Energy Conversion*; 2003; pp. 1–3.

(251) Williams, S. R.; Betts, T. R.; Helf, T.; Gottschalg, R.; Beyer, H. G.; Infield, D. G. Modelling Long-Term Module Performance Based on Realistic Reporting Conditions with Consideration to Spectral Effects. In *Proceedings of the 3rd World Conference on Photovoltaic Energy Conversion*; 2003; Vol. B, pp. 1908–1911.

(252) Futscher, M. H.; Ehrler, B. Efficiency Limit of Perovskite/Si Tandem Solar Cells. *ACS Energy Lett.* **2016**, *1*, 2–7.

(253) Kwon, H. C.; Kim, A.; Lee, H.; Lee, D.; Jeong, S.; Moon, J. Parallelized Nanopillar Perovskites for Semitransparent Solar Cells Using an Anodized Aluminum Oxide Scaffold. *Adv. Energy Mater.* **2016**, *6*, 1601055.

(254) Do, W. W. E.; Pv, O.; Heliatek, W. H. Y.; Opportunities, J. O. B.; Hello, S. A. Y.; Info, P. *Heliatek Reaches Efficiency Record With 40% Transparent Organic Solar Cells*; 2014.